OUKA
The University of Osaka
Institutional Knowledge Archive

Title	Electron Beam Driven In situ Synthesis of NiTi Coatings on Titanium from Electroplated Nickel Precursors for Enhanced Wear Resistance
Author(s)	王, 雷
Citation	大阪大学, 2026, 博士論文
Version Type	VoR
URL	https://doi.org/10.18910/105445
rights	
Note	

The University of Osaka Institutional Knowledge Archive : OUKA

https://ir.library.osaka-u.ac.jp/

The University of Osaka

Doctoral Dissertation

Electron Beam Driven *In situ* Synthesis of NiTi Coatings on Titanium from Electroplated Nickel Precursors for Enhanced Wear Resistance

(耐摩耗性向上のための電析ニッケル前駆体を用いた電子ビーム駆動チタン上 NiTi コーティングのその場合成に関する研究)

Lei Wang
(王　雷)

December 2025

Graduate School of Engineering,
The University of Osaka

Abstract

Commercially pure titanium (CP-Ti) is extensively utilized in aerospace and biomedical industries due to its superior corrosion resistance, excellent biocompatibility, and high specific strength. However, its application in critical transmission components and load-bearing implants is severely restricted by its inferior tribological properties. These limitations often lead to catastrophic failure through mechanisms such as abrasive wear, fretting, and oxidation. Conversely, Nickel Titanium (NiTi/Nitinol) exhibit exceptional wear and cavitation erosion resistance. This superior performance is primarily attributed to their unique superelasticity property, which enable the material to absorb impact energy through reversible deformation. Nevertheless, the widespread adoption of bulk Nitinol is hindered by high material costs, poor machinability, and challenges associated with welding.

Consequently, depositing NiTi coatings on CP-Ti substrates emerges as a viable strategy to synergize the surface durability of Nitinol with the bulk formability and cost-effectiveness of CP-Ti. Although conventional coating techniques have demonstrated the potential for depositing NiTi as a wear- or cavitation-resistant coating, significant technical hurdles remain. Thermal spraying often yields coatings plagued by porosity, oxidation, and weak bonding strength ; physical vapor deposition (PVD) is typically limited by slow deposition rates, insufficient coating thickness for heavy-load applications, and compositional deviations due to the differing evaporation rates of nickel and titanium. To address these persistent limitations, the author proposes a novel hybrid manufacturing methodology: the *in situ* synthesis of NiTi coatings via electron beam (EB) melting of electroplated nickel layers on CP-Ti substrates. This approach leverages the precise energy control of additive manufacturing to tailor the microstructure and composition, aiming to produce coatings with wear resistance

comparable to bulk Nitinol.

Before researching these two materials (Ni and Ti), in this dissertation the author first conducts single-track electron beam scanning experiments on 316L stainless steel, in order to elucidate the effects of processing parameters on melt-pool geometry and surface morphology. Results indicate that increasing line energy density expands melt dimensions—particularly depth—while surface morphology of melt tracks confirm that Marangoni convection drives fluid flow. These dynamics provide essential physical insights for the subsequent NiTi coating formation.

Having gained such initial understanding of melt pool dynamics in metals under electron beam irradiation, the fundamental feasibility of this novel NiTi coating process was validated through single-track electron beam scanning experiments. The investigation demonstrates that the nickel concentration within the melt track can be precisely modulated by adjusting the electron beam power. Specifically, varying the power input allows the composition to be tuned closer to the stoichiometric NiTi ratio. Furthermore, cross-sectional analysis reveals a uniform elemental distribution along the normal direction of the melt track. This homogeneity is attributed to the Marangoni effect and vigorous thermal convection within the melt pool, which effectively promote the mixing of the electroplated nickel layer and the titanium substrate, thereby satisfying the prerequisite conditions for *in situ* NiTi phase synthesis.

Building upon these feasibility studies, the research then advances to the fabrication of practical coatings using multi-track scanning strategies. A comparative analysis between continuous scanning (CS) and intermittent scanning (IS) modes reveals that IS-coatings exhibit significantly lower surface roughness and compositions much closer to the stoichiometric NiTi ratio. Microstructural characterization confirms that while CS-coatings are dominated by the brittle *C*15-$NiTi_2$ phase, IS-coatings

successfully form the superelastic *B*2-NiTi phase and the strengthening $D0_{24}$-Ni_3Ti phase. Consequently, the IS-coatings demonstrate a superior hardness-to-modulus ratio (*H/E* ratio) and indentation depth recovery ratio compared to the substrate. Tribological testing corroborates these findings, showing a specific wear rate reduction of approximately 80%, achieving performance levels similar to superelastic bulk Nitinol. However, local compositional inhomogeneities persist as a limiting factor preventing further performance enhancement.

To mitigate these inhomogeneities and further optimize coating performance, the author investigates the efficacy of a dual-stage post-process heat treatment, comprising annealing at 900 ℃ followed by ageing at 400 ℃. The treatment successfully homogenizes the microstructure and composition of the Ti-rich and Ni-rich coatings. The annealing process facilitates the redistribution of the $D0_{24}$-Ni_3Ti phase, while subsequent ageing induces the precipitation of the Ni_4Ti_3 phase, contributing to significant precipitation hardening. Nanoindentation and sliding wear tests confirm that this heat treatment significantly narrows the performance gap between varying compositional coatings. The resulting mechanical properties and wear resistance of the heat-treated coatings are found to be comparable to those of superelastic Nitinol.

Finally, seeking a more time-efficient alternative to complex post-process heat treatments, in the dissertation the author introduces a novel point-wise electron beam scanning strategy. Inspired by advanced additive manufacturing techniques, this strategy utilizes multiple remelting cycles to achieve *in situ* homogenization. A machine learning model is developed to elucidate the non-linear interactions between key scanning parameters—such as step size, point spacing, dwell time, and power—and the resulting coating composition. Optimization results indicate that specific dwell times effectively eliminate the brittle $NiTi_2$ phase and achieve target nickel concentrations

comparable to multi-track scanned coatings. The point-wise scanning strategy successfully produces coatings with uniform mechanical properties, characterized by high *H/E* ratios and indentation depth recovery ratios that match the heat-treated samples. This confirms that process parameter optimization can effectively replace post-process heat treatment, offering a streamlined and efficient route for the fabrication of high-performance, wear-resistant NiTi coatings on titanium substrates.

In conclusion, in this dissertation the author establishes a robust methodology for the *in situ* synthesis of high-performance NiTi coatings on CP-Ti. By synergizing electroplating with precision electron beam processing, the study overcomes traditional fabrication limitations, offering a scalable, cost-effective solution for enhancing the surface durability of critical titanium components in aerospace and biomedical applications.

Contents

Chapter 1 General introduction 6

1.1 Concerned materials 6

1.1.1 Commercially pure titanium (CP-Ti) 6

1.1.2 Nickel titanium (NiTi/Nitinol) 8

1.2 Conventional methods for the formation of NiTi coating 11

1.2.1 Thermal spraying 11

1.2.2 Physical vapor deposition 13

1.2.3 Electroplating 15

1.3 Formation of multi-material structure by additive manufacturing 17

1.4 Outline of the present study 19

References 24

Chapter 2 Electron-beam melting behavior of metallic materials.. 33

2.1 Introduction 33

2.2 Experimental and Simulation Methods 34

2.2.1 Material 34

2.2.2 Electron-Beam Irradiation 34

2.2.3 Surface Profilometry 35

2.2.4 Cross-Sectional Microstructural Characterization 35

2.3 Results 36

2.3.1 Surface Morphology of Melt Tracks 36

2.3.2 Cross-Sectional Melt-Pool Geometry 39

2.4 Conclusions 41

Reference 42

Chapter 3 *In Situ* Synthesis of NiTi via Single-Track Electron Beam Scanning on Ni-Plated Ti 43

3.1 Introduction 43

3.2 Methods 44

3.1.1 Preparation of substrate and Ni-plate 44

3.1.2 Electron beam irradiation 45

3.2.3 Microstructural characterization 46

3.3 Results 46

3.3.1 Surface morphology 46

3.3.2 Cross-sectional observation and compositional analysis 49

3.3.3 Microstructures and local inhomogeneities 57

3.4 Discussion 62

3.4.1 Inhomogeneous formation under low beam power conditions 62

3.4.2 Strategy for fabrication of NiTi coating 65

3.5 Conclusions 66

Reference 66

Chapter 4 Formation of NiTi Coatings on Ti via Multi-Track Electron Beam Scanning for Enhanced Wear Resistance 75

4.1 Introduction 75

4.2 Methods 76

4.2.1 Preparation of substrate and Ni-plate 76

4.2.2 Electron beam irradiation 77

4.2.3 Microstructural characterization 78

4.2.4 Nanoindentation tests 78

4.2.5 Sliding wear tests 79

4.3 Results and discussion 80

4.3.1 Surface morphology and roughness 80

4.3.2 Cross-sectional morphology and elemental distribution 84

4.3.3 Phase identification 92

4.3.4 Indentation properties 96

4.3.5 Frictional wear properties 101

4.4 Conclusion 107

References 108

Chapter 5 Heat Treatment of NiTi Coatings for Compositional Homogenization and Wear Resistance Improvement 116

5.1 Introduction 116

5.2 Methods 117

5.2.1 Preparation of multi-track scanned NiTi coatings 117

5.2.3 Heat treatment 117

5.2.4 Microstructural characterization 117

5.2.5 Nanoindentation tests 118

5.2.6 Sliding wear tests 119

5.3 Results and discussions 120

5.3.1 Phase evolution during heat treatment 120

5.3.2 Evolution of microstructure and elemental distribution 123

5.3.3 Enhancement of indentation properties by heat treatment 131

5.3.4 Improvement of wear resistance by heat treatment 135

5.4 Conclusions 140

References 141

Chapter 6 Point-Wise Electron Beam Scanning Strategy for Homogeneous NiTi Coatings and Improved Mechanical Performance **149**

6.1 Introduction 149

6.2 Methods 150

6.2.1 Preparation of substrate and Ni-plate 150

6.2.2 Electron beam point-wise scanning 152

6.2.3 Microstructural characterization 159

6.2.4 Training of machine learning model 159

6.2.5 Nanoindentation tests 160

6.3 Results and discussion 161

6.3.1 Surface morphology and roughness 161

6.3.2 Phase distribution and homogeneity 163

6.3.3 Elemental composition 175

6.3.4 Microstructural size and crystal orientation 178

6.3.5 Indentation properties 183

6.4 Conclusions 186

References 188

Chapter 7 Concluding remarks **194**

Achievement **199**

Acknowledgment 201

Chapter 1

General introduction

1.1 Concerned materials

1.1.1 Commercially pure titanium (CP-Ti)

Commercially pure titanium , also known as CP-Ti, is a widely used metallic material characterized by corrosion resistance, excellent biocompatibility, low density and high specific strength [1]. Thanks to its favourable formability, low density and corrosion resistance, CP-Ti is used in the aerospace industry to manufacture piping systems for environmental control, hydraulics and fuel systems [2]. The fabrication of these pipes requires complex bending and forming processes. The outstanding ductility and cold-working capability of CP-Ti significantly reduce the risk of cracking during machining — a performance level that is unmatched by many high-strength alloys [3]. Its exceptional biocompatibility and chemical stability also make CP-Ti a common material for orthopedic and dental implants [4]. This is because CP-Ti forms a dense, chemically stable titanium dioxide (TiO_2) passivation layer on its surface. This layer effectively isolates the base metal from the physiological environment, significantly suppressing the leaching of harmful metal ions and thereby reducing the risk of inflammatory reactions and immune rejection [5]. Additionally, while its Young's modulus of approximately 100–120 GPa is higher than that of human cortical bone (10–30 GPa), it is substantially lower than that of stainless steel (approximately 200 GPa) and cobalt-chromium alloys (approximately 230 GPa). This mitigates the mismatch in elastic modulus between the implant and bone, alleviating stress shielding and preventing bone loss and peri-prosthetic fractures caused by inadequate bone loading

[6].

However, the inferior wear resistance of CP-Ti restricts its use in critical transmission components, such as engines and pumps [7,8]. Its lower wear resistance may also lead to synergistic effects between corrosion and wear, resulting in a reduced service life and premature failure of orthopedic implants [9]. Fig. 1.1 shows a CP-Ti hip joint implant that was severely degraded due to a combination of fretting and corrosion/oxidation. The implant fractured catastrophically just two years after implantation [9]. Alloying can enhance wear resistance to a certain degree; however, it impacts the bulk properties. For example, Ti-6Al-4V alloys show a wear rate under dry friction conditions that is approximately 50% lower than that of CP-Ti [10,11]. However, this improvement is not adequate, as alloying compromises ductility. The tensile elongation of Ti-6Al-4V is reduced to approximately 10% [12], which is nearly half that of CP-Ti. Kumar et al. [3] employed large strain extrusion (LSEM) techniques, while La et al. [10] investigated equal channel angular pressing (ECAP) techniques, to refine the grain structure of CP-Ti. The aim was to enhance hardness and wear resistance while maintaining a certain degree of ductility. Nevertheless, regardless of whether alloying or grain refinement strengthening is employed, the resulting performance improvements still fall significantly short of those of wear-resistant materials such as carburized steel [13] and cemented carbides [14].



Fig. 1.1 A severely degraded CP-Ti hip joint plant. It is failed catastrophically and fractured two years after implantation in the patient, and was subsequently removed surgically. Reproduced with permission from Ref. [9]

1.1.2 Nickel titanium (NiTi/Nitinol)

Nickel titanium (NiTi) is a widely used shape memory alloy composed of nickel and titanium in nearly equal atomic ratios [15]. It is also known as Nitinol, a name derived from a combination of the elements in its composition and the place of its discovery — a combination of NiTi and the Naval Ordnance Laboratory. Throughout this dissertation, the term Nitinol is used to refer to the bulk nickel titanium as an engineering material. In contrast, the term NiTi is used when describing coatings or films composed of nickel titanium.

The two core properties of Nitinol are the shape memory effect (SME) and superelasticity (SE) [15]. These properties stem from the NiTi phase's unique thermoelastic martensitic phase transformation behaviour. The NiTi phase is the primary phase in Nitinol. At ambient temperatures, when SME-Nitinol undergoes deformation under mechanical loading, its martensitic (*B*19') NiTi phase reorients. When heated above the phase transition temperature, these *B*19'-NiTi phases transform into the austenitic (*B*2) NiTi phase, thereby reverting to their original shape. This is

known as the “shape memory” effect [16]. In contrast, the phase transition temperature of SE-Nitinol is below room temperature, meaning that it primarily consists of the *B*2-NiTi phase under ambient conditions. When SE-Nitinol deforms under mechanical loading, the phase transformation from *B*2-NiTi to *B*19’-NiTi can be induced by stress. Once the load is removed, the *B*19’-NiTi phase rapidly reverts to the *B*2-NiTi phase, restoring the material to its original shape. This manifests macroscopically as superelasticity [16]. Nitinol actuators manufactured based on these properties offer advantages such as a high power-to-weight ratio, a low drive voltage and silent operation. This makes them suitable for precision control tasks in space-constrained environments [17]. Consequently, these actuators are widely used in the automotive [18], aerospace [17,19] and micro-electromechanical systems (MEMS) [20] industries. Furthermore, due to its excellent corrosion resistance and biocompatibility, similar to CP-Ti, Nitinol is also used in the manufacture of medical devices such as orthodontic archwires [21], orthopedic compression staples [22], and endovascular stents [23].

However, researchers and relevant industry personnel rarely mention that Nitinol exhibits excellent wear [24] and cavitation erosion resistance [25]. Jin et al. compared the dry abrasion losses of Nitinol, Co45 (a cobalt-based, wear-resistant alloy) and nitrided 38CrMoAlA steel in a sliding wear test [26]. As shown in Fig. 1.2, at loads below 10 kg, Nitinol's mass loss was lower than that of 38CrMoAlA steel, but higher than that of Co45 alloy. As the load increased, the mass loss of the other two materials increased significantly faster than that of Nitinol. At a load of 20 kg, Nitinol’s mass loss had fallen below that of Co45, and this difference continued to increase as the load increased further. This demonstrates that Nitinol exhibits superior wear resistance to conventional structural metals and wear-resistant alloys, an advantage that becomes even more pronounced under heavy load conditions. Cheng et al. [25] investigated the

cavitation erosion resistance of heat-treated Nitinol. As illustrated in Fig. 1.3, even after 30 hours of cavitation erosion testing, heat-treated Nitinol exhibited minimal surface damage, whereas 304 stainless steel displayed severe surface damage after just 3 hours of testing. This demonstrates that Nitinol's cavitation erosion resistance is significantly superior to that of 304 stainless steel. The mechanism responsible for Nitinol's superior wear and cavitation erosion resistance derives from its superelasticity. Put simply, its extremely high elastic strain limit enables Nitinol to absorb impact energy through surface elastic deformation when it comes into contact with friction pairs or is subjected to cavitation impacts. This prevents plastic deformation and therefore reduces wear caused by friction or cavitation [24–26].

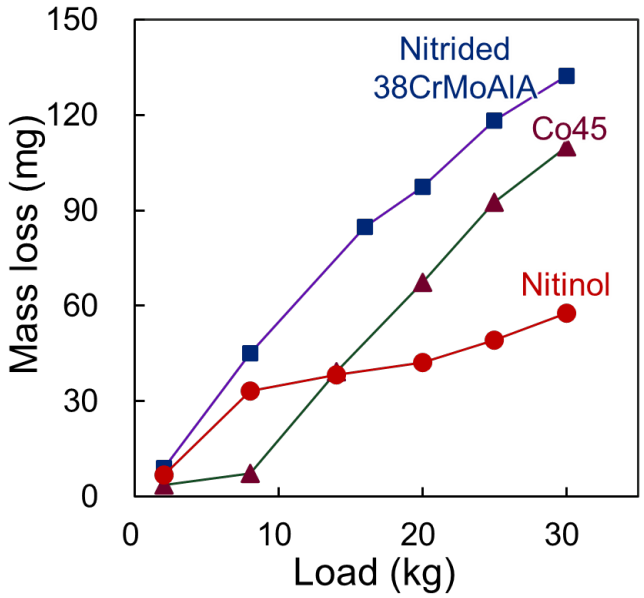

Fig. 1.2. Dry abrasion losses of Nitinol, Co45 (a cobalt-based wear-resistant alloy), and nitrided 38CrMoAlA steel in sliding wear test. Sliding distances 704 m and rotation rates 200 rpm. Reproduced with permission from Ref. [24]

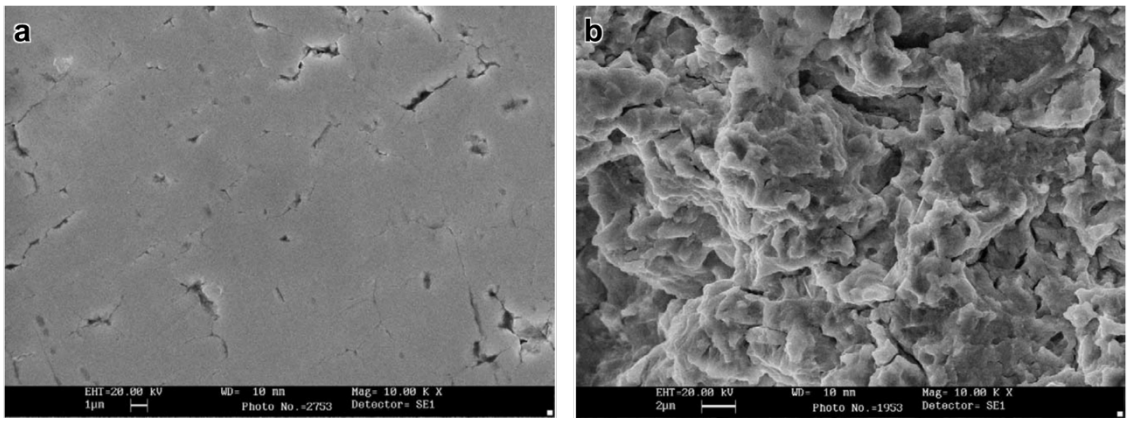

Fig. 1.3. SEM micrographs of cavitated surface of (a) heat-treated Nitinol, cavitated for 30 h and of (b) 304 stainless steel, cavitated for 3 h. Reproduced with permission from Ref. [25]

However, the widespread use of Nitinol remains challenging. Its high cost, complex phase-transition kinetics and tendency to form brittle intermetallic compounds during welding compromise the reliability of structural components and make the fabrication of large-scale or complex structures extremely difficult [27]. Against this backdrop, depositing Nitinol coatings (commonly termed NiTi coatings) onto CP-Ti surfaces emerge as a viable strategy. This approach significantly enhances wear resistance while preserving the excellent machinability of CP-Ti, and effectively reduces costs and weight compared to using bulk Nitinol materials directly.

1.2 Conventional methods for the formation of NiTi coating

1.2.1 Thermal spraying

Thermal spraying is a well-established coating formation method with a long history and a wide range of applications [28]. The principle of all kinds of thermal spraying are the same: A heat source heats the feedstock material, which is then propelled at high velocity by a jet onto the substrate surface. During rapid cooling, the heated particles form a coating through successive deposition [28]. The most widely used thermal spray

coatings include wear-resistant coatings [29], corrosion-resistant coatings [30], and thermal barrier coatings [31]. Therefore, thermal spraying has also become the most commonly chosen method by researchers for producing NiTi coatings.

Thermal sprayed NiTi coatings have been deposited using methods such as low-pressure plasma spraying [32], vacuum plasma spraying [33,34], atmospheric plasma spraying [35,36], cold spraying [37–39]. Bitzer et al. [31] developed a cavitation-resistant NiTi coating using the low-pressure plasma spraying (LPPS) technique. Cavitation test results in this study show that, the mass loss of the LPPS-produced NiTi coating is improved when compared to bulk UTP 730 (usually applied as a wear-resistant build-up weld). However it is still as at least twice that of bulk Nitinol. This indicate that defects in the coatings have negatively impacted the cavitation resistance. Fig. 1.3 shows cross-sectional micrographs and EDS analysis results of the coating. As Fig. 1.3a shows, porosities are distributed within the coating. EDS analysis (Fig. 1.3b) also indicates that the interlayer of sprayed splats contains a higher concentration of oxygen, suggesting that oxidation occurred during the spraying process. These two defects are suggested by authors to be the cause of reduction in the cavitation resistance [31]. Fig. 1.3c shows that porosities are also present at the coating-substrate interface, which prevents proper bonding between the two at these locations. Although these porosities do not directly affect cavitation resistance, they reduce the bonding strength between the coating and the substrate. This increases the risk of delamination. Tria et al. [37] produced NiTi coatings by cold spraying. Fig. 1.4 shows that their coatings also contain defects such as porosities and cracks. Furthermore, the thickness of the cold-sprayed coatings is highly non-uniform, with measurements indicating a maximum thickness of over 30 μm and a minimum thickness of under 20 μm.

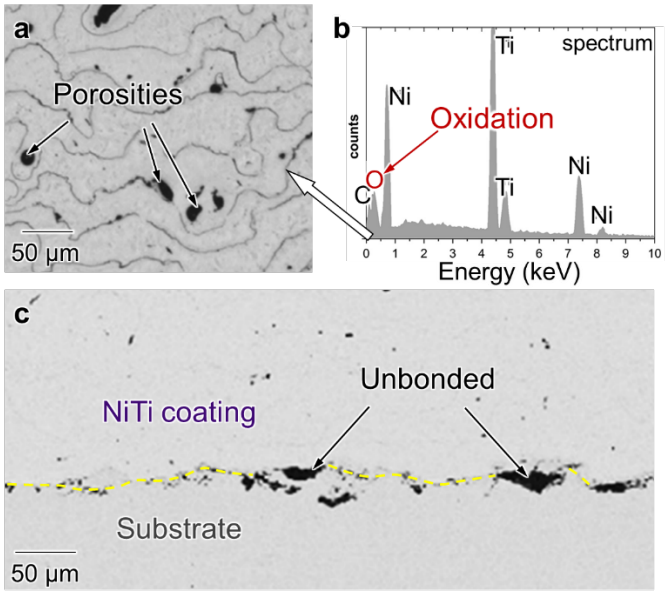

Fig. 1.4. Cross-sectional micrographs and EDS analysis result of low-pressure plasma sprayed NiTi coating. (a) Optical image of the coating. (b) EDS spectrum of the interlayer of splats in (a). (c) SEM image near the interface of the coating. Reproduced with permission from Ref. [32]

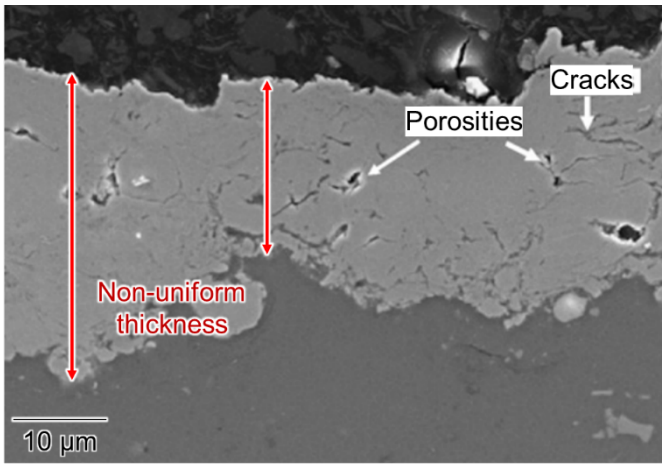

Fig. 1. 5. Cross-sectional SEM micrograph of cold sprayed NiTi coating. Reproduced with permission from Ref. [38]

1.2.2 Physical vapor deposition

Physical vapor deposition (PVD) technology is based on the principle of vaporizing atoms or molecules from a solid target material in a vacuum environment. These atoms or molecules are then transported to the substrate surface, where they condense to form

a coating/thin film [40]. This technology has advanced rapidly in recent years and now has numerous applications, including in cutting tools [40], micro electro mechanical systems and micro actuators[41], and medical devices [42]. Compared to thermal spray coatings, PVD coatings or films have a denser microstructure, are more uniform, and can be made to a precise thickness [40]. Researchers in this field have also recognized the shape memory and superelastic properties of nickel-titanium alloys, resulting in numerous reports on NiTi coatings prepared via PVD [43–49]. Ho et al. [43] investigated and developed a method for preparing NiTi coatings via DC sputtering. While they ultimately succeeded in obtaining NiTi coatings with the desired shape memory effects, the authors of the study noted that "Sputtering processes typically produce films with reduced transformation temperatures (i.e. below room temperature), prohibiting its use as a practical actuator material.". This is attributed to two factors causing Ti deficiency during sputtering: the facile oxidation of titanium, and differing angular flux distributions of Ni and Ti. These ultimately affect the phase transformation temperature of the NiTi coating. Consequently, measures are typically required during the fabrication of sputtered NiTi coatings to compensate for this titanium deficiency [47,48]. Cameron et al. [49] investigated a method of producing Ni/Ti nanolaminate precursors using magnetron sputtering, followed by heat treatment in order to obtain superelastic NiTi coatings. However, as Fig. 1.6 shows, the Ni/Ti nanolaminate precursor produced in this study delaminated from the substrate due to residual stresses, indicating poor adhesion between the sputtered coating and the substrate. Furthermore, the coating thickness produced by magnetron sputtering was only 1 μm, which is insufficient for heavy-load applications.

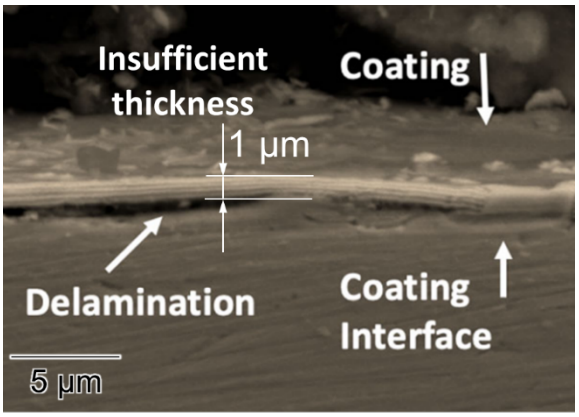

Fig. 1.6. Cross-section micrograph of the magnetron sputtered Ni/Ti nanolaminate as a precursor for the formation of NiTi coating. Reproduced with permission from Ref. [49]

1.2.3 Electroplating

Electroplating is a technique that uses an external current to deposit metal or alloy layers onto substrate surfaces. It features well-established processes, is cost-effective, and can achieve uniform coatings on complex shapes [50]. Modern electroplating has expanded beyond traditional protective and decorative applications to include functionalization for properties such as wear resistance [51], corrosion resistance [52] and composite coating fabrication [53]. It is now widely used in the automotive [54], electronics [55] and aerospace [54] industries. However, the direct formation of NiTi coatings via electroplating remains challenging. Although Ni electroplating methods are well established, Ti is difficult to reduce and deposit in conventional aqueous solutions. This is because Ti possesses a highly negative reduction potential and readily forms a dense oxide film, making it difficult to reduce enough Ti in standard electroplating baths to achieve a near 1:1 atomic ratio with nickel.

Harshini Sai et al. [56] tried to deposit Ni-Ti alloy coatings on mild steel (MS) from citrate bath having nickel sulphate and titanium oxysulphate as salts, tri-sodium citrate as complexing agent. However, the measurement results showed that the maximum mass fraction of Ti in the coating was only 3.5 wt.%, which is far below the proportion

required for nickel titanium. Hasannaeimi et al. [57] synthesized NiTi coatings by means of co-electrodeposition of Ti particles in Ni matrix and subsequent heat treatment. As shown in Fig. 1.7, they successfully deposited a Ni plating layer containing Ti particles with an equivalent atomic percentage of 49% by applying a Ti particle concentration of 5 g/l and a current density of 2 A/dm². Following heat treatment at 1150 °C for four hours, the Ni coating and Ti particles formed a NiTi coating (see Fig. 1.7b). XRD analysis (Fig. 1.7c) revealed significant oxidation of the coating during heat treatment. This coating also exhibits issues such as porosity and compositional inhomogeneity. Despite these shortcomings, this study is valuable as it demonstrates a method for the *in situ* synthesis of NiTi coatings.

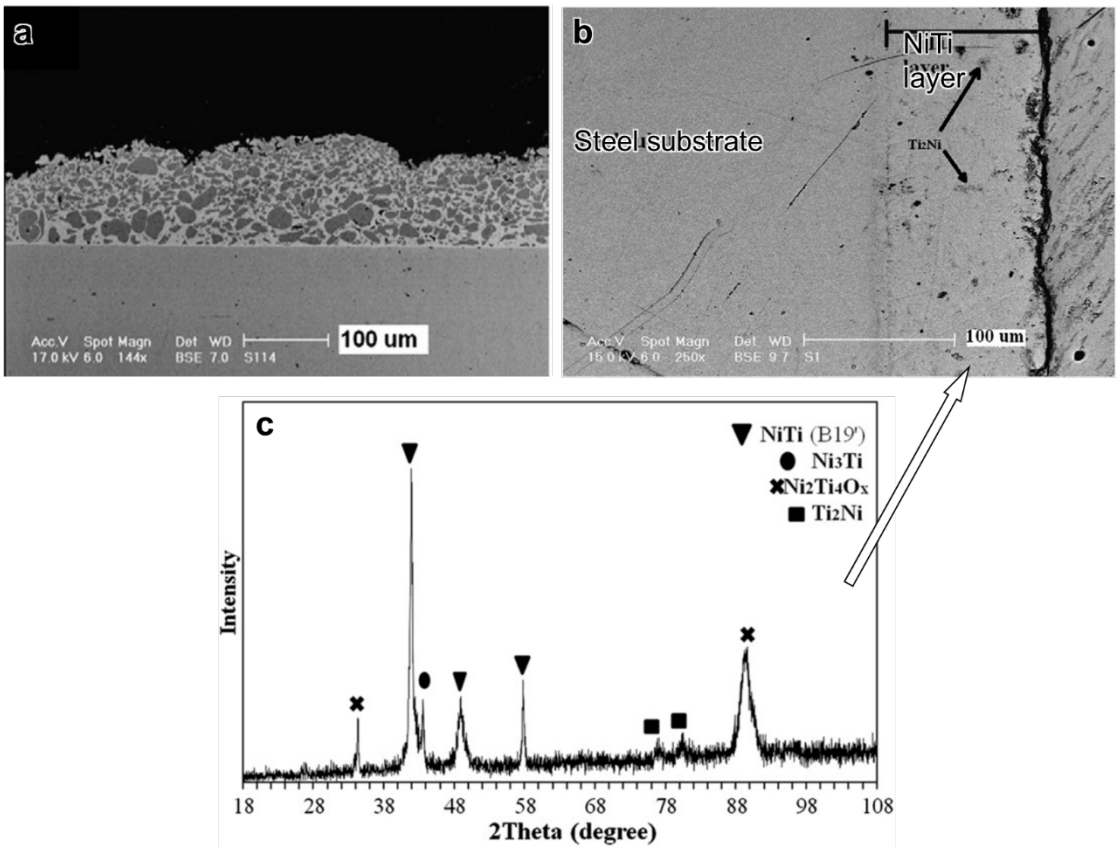

Fig. 1.7. Micrographs of: (a) an as-deposited Ni plating layer with Ti particles embedded; (b) the NiTi coating synthesized by heat treatment; and (c) the XRD analysis result of (b). Reproduced with permission from Ref. [57]

1.3 Formation of multi-material structure by additive manufacturing

Additive manufacturing (AM) is a manufacturing method in which material is deposited sequentially, guided by 3D model data, in layers to generate the target structure [58]. This approach enables the production of complex geometries that are unattainable through conventional methods, and it possesses rapid prototyping capabilities [59]. Furthermore, AM technology offers unparalleled control over the microstructure of target materials, allowing for precise adjustment of the mechanical properties of printed structures [60].

Additive manufacturing processes usually only use one material. However, continuous technological advancements mean that reports of multi-material structures produced using AM techniques are increasingly emerging [61]. Although this area of research is still in its infancy, it offers the possibility of integrating multiple materials with vastly different properties into a single component. This would enable the mechanical characteristics or environmental adaptability of distinct regions to be defined independently, as required.

Mao et al. [62] fabricated 316L/CuCrZr functionally graded materials (FGM) by selective laser melting (LPBF) and investigated the effects of process parameters on interfacial characterization. Although cracks, pores and other defects appeared at the interface of LPBF-manufactured 316L/CuCrZr FGMs when non-optimal parameters are used (see Fig. 1.8a, 1.8b and 1.8d), defect-free interfaces with tight bonding can be achieved when optimal parameters are used (see Fig. 1.8c). Bartolomeu et al. [63] fabricated NiTi-Ti6Al4V multi-material lattice structures by selective laser melting. The authors propose applying this structure to orthopedic implants to reduce stress shielding and wear debris release by using the lower elastic modulus and superior wear resistance of NiTi compared to Ti6Al4V [21]. As illustrated in Fig. 1.9, the two

materials are effectively bonded in the transition region. Furthermore, nanoindentation test results (Fig. 1.9c) confirm that this structure achieves a transition from high to low modulus.

Although the above research does not directly involve the manufacture of coatings, the AM technologies developed in this field should also be applicable to the manufacture of coatings if the structure composed of the coating and substrate is considered a generalized multi-material structure. Additionally, applying AM technology to coating manufacturing would enable the fine-tuning of coating microstructure and mechanical properties.

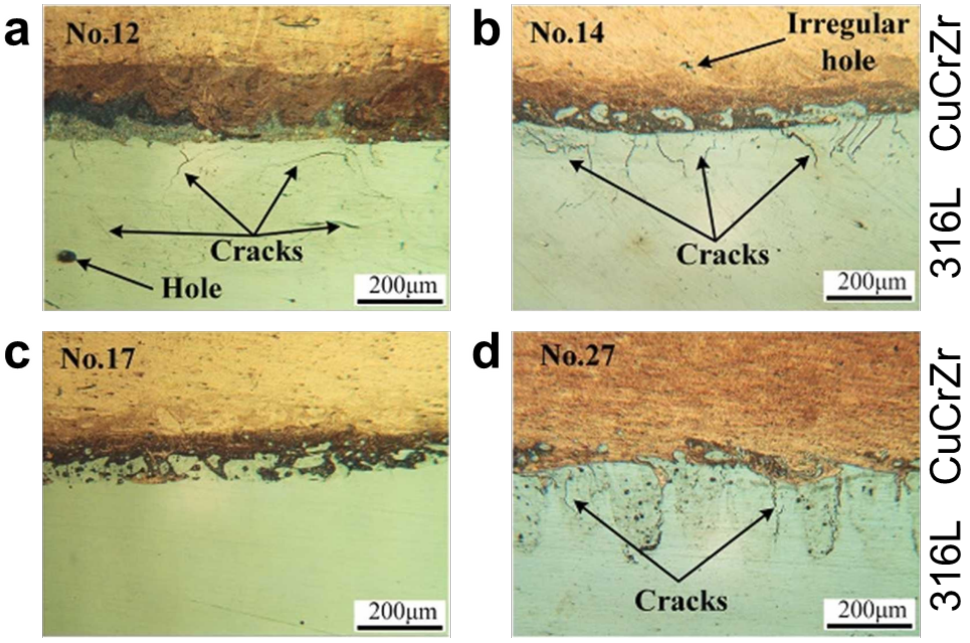

Fig. 1.8. Optical microscope images of the interface the 316L/CuCrZr functionally gradient material by selective laser melting. The process parameters in each image are (a) P = 400 W, v = 700 m/s, H = 50 μm, (b) P = 400 W, v = 700 m/s, H = 110 μm, (c) P = 425 W, v = 700 m/s, H = 140 μm, (d) P = 400 W, v = 1000 m/s, H = 140 μm. Reproduced with permission from Ref. [62]

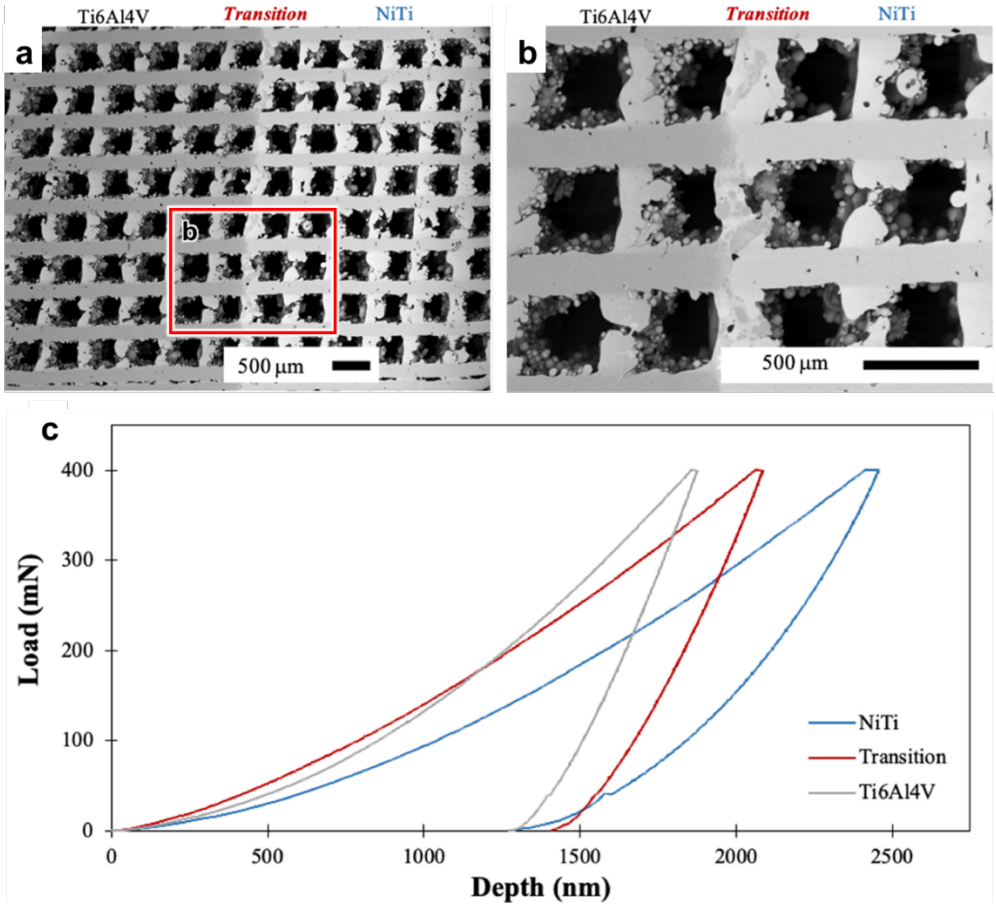

Fig. 1.9. (a) Cross-sectional SEM image; (b) locally magnified image of (a); and (c) nanoindentation results for the NiTi-Ti6Al4V multi-material lattice structure produced by selective laser melting. Reproduced with permission from Ref. [63]

1.4 Outline of the present study

Drawing inspiration from the studies outlined in the preceding sections, a new method combining electroplating and AM (specifically electron beam melting, EBM) was proposed to produce NiTi coatings on CP-Ti surfaces. This method consists of two primary steps: electroplating pure Ni onto the CP-Ti and scanning the Ni plating layer with an electron beam (EB). The primary objective of this study is to develop a viable technical approach for this method. It involves: developing process steps which are practicable in the laboratory, controlling the composition and microstructure of the coatings by adjusting the EB scanning parameters, scanning strategies and post-

processes and ultimately producing NiTi coatings with wear resistance comparable to that of bulk Nitinol. The outline of the present dissertation is shown in Fig. 1.10. The content of each chapter is outlined below:

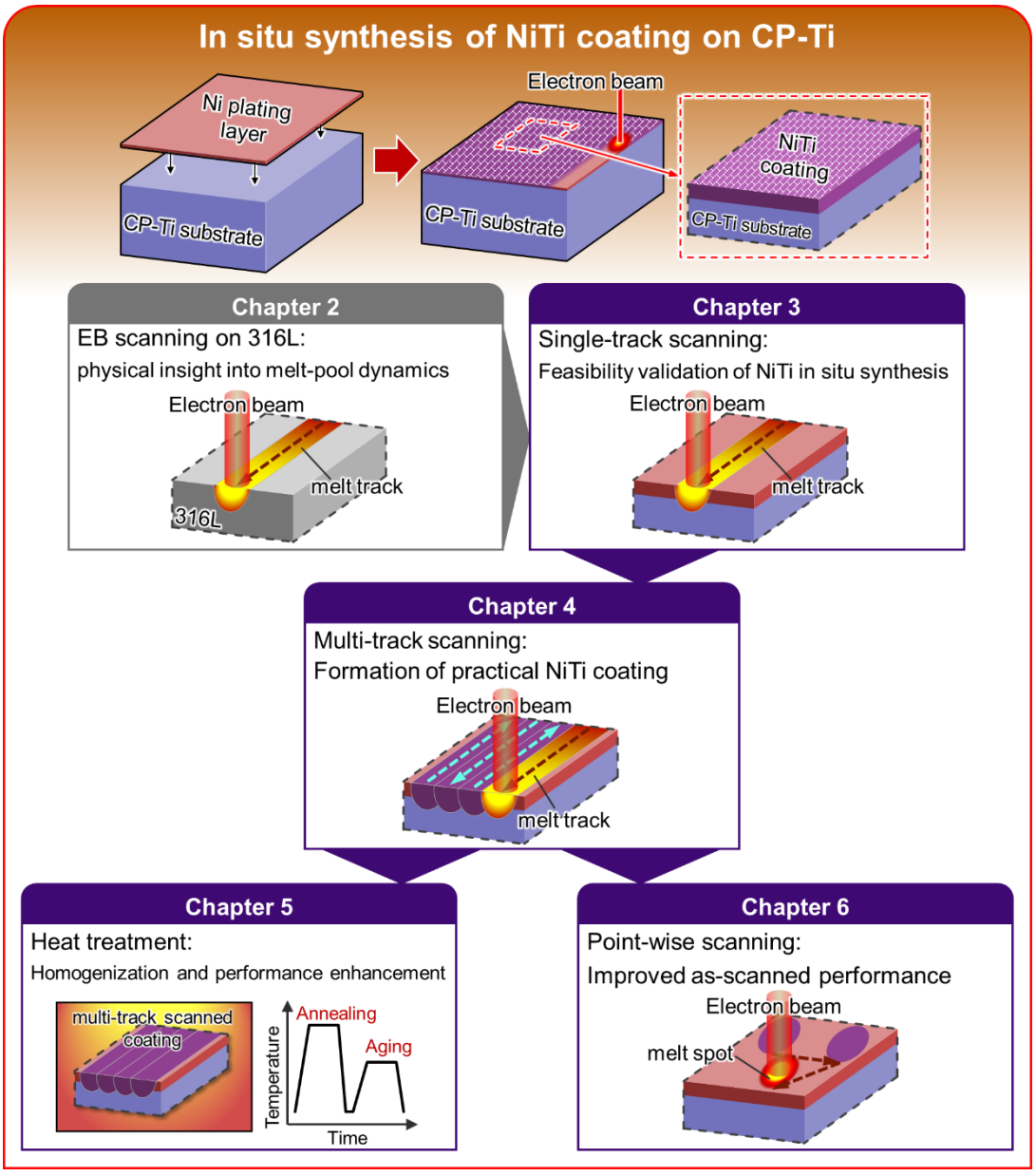

Fig. 1.10. Outline of the present dissertation.

Chapter 2: To understand the melting and resolidification behavior of metallic materials under the irradiation of EB, single-track EB scanning experiments were conducted on 316L stainless steel. The effect of parameters on the surface morphology and melt-pool geometry of the melt tracks was investigated by irradiating 316L stainless steel with the EB at four beam powers (300 W, 600 W, 900 W and 1200 W) and four scan speeds (100 mm/s, 300 mm/s, 1000 mm/s and 3000 mm/s).

Experimental results indicate that melt-track geometry is critically governed by line energy density, where increasing energy input leads to a monotonic expansion in both width and depth. Notably, the depth increases more rapidly than the width, resulting in a higher aspect ratio that suggests a transition toward dominant vertical heat dissipation. Furthermore, the observation of surface chevron patterns confirms that thermocapillary forces (Marangoni effect) play a primary role in redistributing the molten material prior to rapid resolidification. These universal melt-pool dynamics provide essential physical insights for the NiTi coating formation discussed in Chapters 3–6.

Chapter 3: Before conducting a comprehensive study on the new NiTi coating fabrication method, its feasibility must first be confirmed. Therefore, single-track EB scanning experiments were conducted on the Ni-plated CP-Ti substrate, and the composition and elemental distribution of the melt tracks were analyzed in Chapter 2. Experiments were conducted at a fixed scanning speed of 100 mm/s, with varying EB powers, to evaluate the effect of power on the morphology, composition and elemental distribution of the melt tracks.

The results suggest that adjusting the EB power can control the composition of the melt track within a range close to the NiTi stoichiometric ratio, thereby meeting the conditions necessary for NiTi phase synthesis. Cross-sectional observations also revealed a generally uniform distribution of elements along the normal direction of the

melt track, with no significant segregation. This demonstrates that the Marangoni effect and thermal convection-driven melt pool flow effectively promote mixing of Ni and Ti, providing another key condition for NiTi phase synthesis. In summary, the experimental results demonstrate the feasibility of synthesizing NiTi coatings *in situ* via EB irradiation on Ni-plated Ti substrates.

Chapter 4: Chapter 3 demonstrated the feasibility of *in situ* synthesis NiTi coatings on Ti via single-track scanning. Therefore, the aim of Chapter 4 is to prepare practical NiTi coatings via multi-track scanning while controlling their surface roughness, composition, microstructure and wear resistance by adjusting scanning parameters. Electron beam scanning experiments employed both continuous scanning (CS) and intermittent scanning (IS) modes in this chapter, with the EB power set at four levels (126, 132, 138 and 144 W) and the scanning speed fixed at 100 mm/s.

Results from surface observation indicate that IS-coatings exhibit roughness that is approximately 60% lower than that of CS-coatings. Composition analysis and XRD results show that IS-coating scanned at an optimum EB power exhibited a Ni concentration exceeding 50 at.% and consist of the superelastic *B*2-NiTi phase, reinforced by the $D0_{24}$-Ni_3Ti phase. Nanoindentation test and sliding wear test indicate that IS-coating presents enhanced mechanical properties and wear resistance relative to CP-Ti, achieving performance similar to that of superelastic Nitinol. These results demonstrate that multi-track EB scanning can be used to successfully synthesize NiTi coatings *in situ* on Ti, and that the composition and microstructure of these coatings can be controlled by adjusting the scanning parameters to achieve a level of wear resistance similar to that of superelastic Nitinol. However, local inhomogeneities still limit the wear resistance of the IS-coating, indicating a need for further optimization in subsequent chapters to fully match the performance of bulk superelastic Nitinol.

Chapter 5:

In Chapter 4, NiTi coatings were synthesized *in situ* on Ti substrates via multi-track EB scanning. However, the resulting coatings exhibited compositional and microstructural inhomogeneities, which were suggested to reduce their wear resistance. The aim of this chapter is to enhance wear resistance by reducing coating inhomogeneity through a two-step heat treatment consisting of annealing at 900 °C for 10 minutes, followed by ageing at 400 °C for 60 minutes. Two coatings fabricated in Chapter 4 were selected for study and designated Ni-rich and Ti-rich based on their composition.

The experimental results show that heat treatment substantially enhanced the compositional and microstructural homogeneity of both coatings. In the Ni-rich coating, the $D0_{24}$-Ni_3Ti phase coarsened and became uniformly distributed as strengthening particles. Although only limited microstructural evolution occurred during subsequent ageing, XRD still confirmed the precipitation of the Ni_4Ti_3 phase, which further improved the mechanical properties. After annealing and ageing, both coatings showed clear improvements in their mechanical property indicators, and the performance gap between them was significantly reduced. Wear tests displayed the same trend: heat treatment lowered the specific wear rates of both coatings and substantially diminished the difference between them. Moreover, the wear resistance of both coatings after heat treatment approached that of superelastic Nitinol.

Chapter 6:

This chapter presents a novel point-wise EB scanning strategy originating from additive manufacturing research, aimed to explore another effective method for eliminating compositional and microstructural inhomogeneities in NiTi coatings. The point-wise EB scanning experiments involved five parameters: the step size (l_s) for

scanning grid, the spacing between points (l_t) in the scanning grid, the time period (τ) for each point, the dwell time (t_d) of the EB at each point and the average EB power (P_{avg}) during scanning. The l_t was varied across four levels (83, 100, 124 and 167 μm), while the t_d was varied across three levels (2, 5 and 10 ms) with l_s and τ fixed at 1 mm and 10 ms, respectively. The general range of P_{avg} is 20–60, though it varies specifically in each parameter set.

The experimental results demonstrate that, when the parameters are optimized, point-wise scanning effectively homogenized the NiTi coating while achieving a Ni concentrations comparable to multi-track scanned coatings. In order to predict the Ni concentration in the coating, a machine learning model was developed. The model coefficients indicate that P_{avg} and l_t significantly contribute to variations in Ni concentration, whereas t_d's contribution is negligible. With the help of this machine learning model, coatings with a composition similar to that of multi-track scanned coatings were successfully fabricated under multiple parameter sets. Comparing the nanoindentation results of these coatings with those in Chapters 4 and 5 revealed that, point-wise scanned coatings achieved levels comparable to or exceeding those of multi-track scanned coatings after annealing. Moreover, point-wise scanning significantly reduced the standard deviation of mechanical property indicators, indicating that improved composition uniformity enhances uniformity of mechanical properties and contributes to the improved wear resistance of the coatings.

In concluding remarks, the methodology, achievement, and implications of the present study will be briefly reviewed.

References

[1] G. Welsch, R. Boyer, E.W. Collings, Materials Properties Handbook: Titanium

Alloys, ASM International, 1993.

[2] R.R. Boyer, An overview on the use of titanium in the aerospace industry, Mater. Sci. Eng. -Struct. Mater. Prop. Microstruct. Process. 213 (1996) 103–114. https://doi.org/10.1016/0921-5093(96)10233-1.

[3] P. Kumar, V.K. Sharma, R.S. Joshi, R.K. Singla, Exploring Tribological and Metallurgical Properties of Commercially Pure Titanium, Ti-6Al-4 V, and Ti-6Al-7Nb Laminates using Large Strain Extrusion Machining Technology, J. Mater. Eng. Perform. (2025). https://doi.org/10.1007/s11665-025-12691-4.

[4] F.A. Shah, M. Trobos, P. Thomsen, A. Palmquist, Commercially pure titanium (cp-Ti) versus titanium alloy (Ti6Al4V) materials as bone anchored implants — Is one truly better than the other?, Mater. Sci. Eng. C 62 (2016) 960–966. https://doi.org/10.1016/j.msec.2016.01.032.

[5] B.B. Zhang, K.J. Qiu, B.L. Wang, L. Li, Y.F. Zheng, Surface Characterization and Cell Response of Binary Ti-Ag Alloys with CP Ti as Material Control, J. Mater. Sci. Technol. 28 (2012) 779–784. https://doi.org/10.1016/S1005-0302(12)60130-3.

[6] E. dos Santos Monteiro, C.N. Elias, F.M. de Souza Soares, K.S. Ribeiro, A.I. de Carvalho Santana, C. dos Santos, Influence of heat treatment on the microstructure, wettability, and corrosion resistance of a Ti–30Nb–7Zr alloy used in biomedical applications, J. Mater. Res. Technol. 29 (2024) 1683–1690. https://doi.org/10.1016/j.jmrt.2024.01.250.

[7] Y. Qin, L. Geng, D. Ni, Dry sliding wear behavior of extruded titanium matrix composite reinforced by in situ TiB whisker and TiC particle, J. Mater. Sci. 46 (2011) 4980–4985. https://doi.org/10.1007/s10853-011-5415-x.

[8] H. Attar, K.G. Prashanth, A.K. Chaubey, M. Calin, L.C. Zhang, S. Scudino, J.

Eckert, Comparison of wear properties of commercially pure titanium prepared by selective laser melting and casting processes, Mater. Lett. 142 (2015) 38–41. https://doi.org/10.1016/j.matlet.2014.11.156.

[9] E. Marin, R. Offoiach, A. Lanzutti, M. Regis, S. Fusi, L. Fedrizzi, Hybrid diffusive/PVD treatments to improve the tribological resistance of Ti-6Al-4V, Biomed. Mater. Eng. (2014). https://doi.org/10.3233/BME-130845.

[10] P. La, J. Ma, Y.T. Zhu, J. Yang, W. Liu, Q. Xue, R.Z. Valiev, Dry-sliding tribological properties of ultrafine-grained Ti prepared by severe plastic deformation, Acta Mater. 53 (2005) 5167–5173. https://doi.org/10.1016/j.actamat.2005.07.031.

[11] G. Straffelini, A. Molinari, Mild Sliding Wear of Fe–0.2%C, Ti–6%Al–4%V and Al-7072: A comparative study, Tribol. Lett. 41 (2011) 227–238. https://doi.org/10.1007/s11249-010-9705-2.

[12] Y. Harada, Y. Ishida, D. Miura, S. Watanabe, H. Aoki, T. Miyasaka, A. Shinya, Mechanical properties of selective laser sintering pure titanium and Ti-6Al-4V, and its anisotropy, Materials 13 (2020) 5081. https://doi.org/10.3390/ma13225081.

[13] J.N. Sultan, E.T. Karash, M.T.E. Kassim, A.M. Ali, H.A. Ibrhim, Effects of Repeated Heat Treatments on the Wear Resistance of Pre-Carburized Steel, Int. J. Heat Technol. 41 (2023) 1083–1095. https://doi.org/10.18280/ijht.410429.

[14] J.Y. Yi, Y.C. Xu, J.H. Yan, Y. Liu, Y.J. Zhou, Effect of Heat Treatment on Wear Resistance of WC-Co and TiAlN-Coated Cemented Carbides, J. Mater. Eng. Perform. (2025). https://doi.org/10.1007/s11665-025-12473-y.

[15] J. Mohd Jani, M. Leary, A. Subic, M.A. Gibson, A review of shape memory alloy research, applications and opportunities, Mater. Des. 1980-2015 56 (2014) 1078–1113. https://doi.org/10.1016/j.matdes.2013.11.084.

[16]K. Otsuka, X. Ren, Physical metallurgy of Ti–Ni-based shape memory alloys, Prog. Mater. Sci. 50 (2005) 511–678. https://doi.org/10.1016/j.pmatsci.2004.10.001.

[17] D.J. Hartl, D.C. Lagoudas, Aerospace applications of shape memory alloys, Proc. Inst. Mech. Eng. Part G J. Aerosp. Eng. 221 (2007) 535–552. https://doi.org/10.1243/09544100JAERO211.

[18] D. Stoeckel, Shape memory actuators for automotive applications, Mater. Des. 11 (1990) 302–307. https://doi.org/10.1016/0261-3069(90)90013-A.

[19] L. McDonald Schetky, Shape memory alloy applications in space systems, Mater. Des. 12 (1991) 29–32. https://doi.org/10.1016/0261-3069(91)90089-M.

[20] H. Kahn, M.A. Huff, A.H. Heuer, The TiNi shape-memory alloy and its applications for MEMS, J. Micromechanics Microengineering 8 (1998) 213. https://doi.org/10.1088/0960-1317/8/3/007.

[21] W.A. Brantley, Evolution, clinical applications, and prospects of nickel-titanium alloys for orthodontic purposes, J. World Fed. Orthod. 9 (2020) S19–S26. https://doi.org/10.1016/j.ejwf.2020.08.005.

[22] O.N. Schipper, J.K. Ellington, Nitinol Compression Staples in Foot and Ankle Surgery, Orthop. Clin. North Am. 50 (2019) 391–399. https://doi.org/10.1016/j.ocl.2019.02.003.

[23] F. Hoseini, A. Bellelli, L. Mizzi, F. Pecoraro, A. Spaggiari, Self-expanding Nitinol stents for endovascular peripheral applications: A review, Mater. Today Commun. 41 (2024) 111042. https://doi.org/10.1016/j.mtcomm.2024.111042.

[24] D.Y. Li, A new type of wear-resistant material: pseudo-elastic TiNi alloy, Wear 221 (1998) 116–123. https://doi.org/10.1016/S0043-1648(98)00269-5.

[25] F.T. Cheng, P. Shi, H.C. Man, Cavitation erosion resistance of heat-treated NiTi, Mater. Sci. Eng. A 339 (2003) 312–317. https://doi.org/10.1016/S0921-

5093(02)00162-4.

[26] J. Jin, H. Wang, WEAR RESISTANCE OF Ni-Ti ALLOY, Acta Metall. Sin. 24 (1988) 66–70.

[27] J.P. Oliveira, R.M. Miranda, F.M. Braz Fernandes, Welding and Joining of NiTi Shape Memory Alloys: A Review, Prog. Mater. Sci. 88 (2017) 412–466. https://doi.org/10.1016/j.pmatsci.2017.04.008.

[28] D. Tejero-Martin, M. Rezvani Rad, A. McDonald, T. Hussain, Beyond Traditional Coatings: A Review on Thermal-Sprayed Functional and Smart Coatings, J. Therm. Spray Technol. 28 (2019) 598–644. https://doi.org/10.1007/s11666-019-00857-1.

[29] H. Bai, L. Zhong, L. Kang, J. Liu, W. Zhuang, Z. Lv, Y. Xu, A review on wear-resistant coating with high hardness and high toughness on the surface of titanium alloy, J. Alloys Compd. 882 (2021) 160645. https://doi.org/10.1016/j.jallcom.2021.160645.

[30] M. Wu, L. Pan, H. Duan, C. Wan, T. Yang, M. Gao, S. Yu, Study on Wear Resistance and Corrosion Resistance of HVOF Surface Coating Refabricate for Hydraulic Support Column, Coatings 11 (2021) 1457. https://doi.org/10.3390/coatings11121457.

[31] H. Kim, K. Praveen, M.W. Lee, J. Lee, Performance-tunable thermal barrier coating for carbon fiber-reinforced plastic composites via flame spraying, Compos. Part B Eng. 287 (2024) 111842. https://doi.org/10.1016/j.compositesb.2024.111842.

[32] M. Bitzer, N. Rauhut, G. Mauer, M. Bram, R. Vaßen, H.-P. Buchkremer, D. Stöver, M. Pohl, Cavitation-resistant NiTi coatings produced by low-pressure plasma spraying (LPPS), Wear 328–329 (2015) 369–377. https://doi.org/10.1016/j.wear.2015.03.003.

[33] A.P. Jardine, Y. Field, H. Herman, Shape memory effect in vacuum plasma sprayed NiTi, J. Mater. Sci. Lett. 10 (1991) 943–945. https://doi.org/10.1007/BF00722140.

[34] M. Bram, A. Ahmad-Khanlou, H.P. Buchkremer, D. Stöver, Vacuum plasma spraying of NiTi protection layers, Mater. Lett. 57 (2002) 647–651. https://doi.org/10.1016/S0167-577X(02)00847-9.

[35] B. Swain, S. Mantry, S.S. Mohapatra, S.C. Mishra, A. Behera, Investigation of tribological behavior of plasma sprayed NiTi coating for aerospace application, J. Therm. Spray Technol. 31 (2022) 2342–2369. https://doi.org/10.1007/s11666-022-01452-7.

[36] N. Cinca, A. Isalgué, J. Fernández, J.M. Guilemany, Structure characterization and wear performance of NiTi thermal sprayed coatings, Smart Mater. Struct. 19 (2010) 085011. https://doi.org/10.1088/0964-1726/19/8/085011.

[37] S. Tria, O. Elkedim, W.Y. Li, H. Liao, Ball milled Ni–Ti powder deposited by cold spraying, J. Alloys Compd. 483 (2009) 334–336. https://doi.org/10.1016/j.jallcom.2008.08.092.

[38] S. Tria, O. Elkedim, R. Hamzaoui, X. Guo, F. Bernard, N. Millot, O. Rapaud, Deposition and characterization of cold sprayed nanocrystalline NiTi, Powder Technol. 210 (2011) 181–188. https://doi.org/10.1016/j.powtec.2011.02.026.

[39] G. Mauer, K.-H. Rauwald, Y.J. Sohn, T.E. Weirich, Cold gas spraying of nickel-titanium coatings for protection against cavitation, J. Therm. Spray Technol. 30 (2021) 131–144. https://doi.org/10.1007/s11666-020-01139-x.

[40] Y. Deng, W. Chen, B. Li, C. Wang, T. Kuang, Y. Li, Physical vapor deposition technology for coated cutting tools: A review, Ceram. Int. 46 (2020) 18373–18390. https://doi.org/10.1016/j.ceramint.2020.04.168.

[41] G. Piazza, V. Felmetsger, P. Muralt, R.H. Olsson Iii, R. Ruby, Piezoelectric

aluminum nitride thin films for microelectromechanical systems, MRS Bull. 37 (2012) 1051–1061. https://doi.org/10.1557/mrs.2012.268.

[42] R.P. van Hove, I.N. Sierevelt, B.J. van Royen, P.A. Nolte, Titanium-Nitride Coating of Orthopaedic Implants: A Review of the Literature, BioMed Res. Int. 2015 (2015) 485975. https://doi.org/10.1155/2015/485975.

[43] K.K. Ho, G.P. Carman, Sputter deposition of NiTi thin film shape memory alloy using a heated target, Thin Solid Films 370 (2000) 18–29. https://doi.org/10.1016/S0040-6090(00)00947-0.

[44] T.M. Adams, S.R. Kirkpatrick, Z. Wang, A. Siahmakoun, NiTi shape memory alloy thin films deposited by co-evaporation, Mater. Lett. 59 (2005) 1161–1164. https://doi.org/10.1016/j.matlet.2004.12.019.

[45] H. Cicek, I. Efeoglu, Y. Totik, K.V. Ezirmik, E. Arslan, A low temperature in-situ crystalline TiNi shape memory thin film deposited by magnetron sputtering, Surf. Coat. Technol. 284 (2015) 90–93. https://doi.org/10.1016/j.surfcoat.2015.08.068.

[46] Y. Fu, H. Du, S. Zhang, Adhesion and interfacial structure of magnetron sputtered TiNi films on Si/SiO2 substrate, Thin Solid Films 444 (2003) 85–90. https://doi.org/10.1016/S0040-6090(03)01029-0.

[47] E. Quandt, C. Halene, H. Holleck, K. Feit, M. Kohl, P. Schloβmacher, A. Skokan, K.D. Skrobanck, Sputter deposition of TiNi, TiNiPd and TiPd films displaying the two-way shape-memory effect, Sens. Actuators Phys. 53 (1996) 434–439. https://doi.org/10.1016/0924-4247(96)01147-8.

[48] S. Miyazaki, K. Nomura, Development of perfect shape memory effect in sputter-deposited Ti-Ni thin films, Proc. IEEE Micro Electro Mech. Syst. (1994) 176–181.

[49] N. Cameron, Z. Farhat, Investigation into the wear and dent resistance of Ni/Ti nanolaminates and superelastic NiTi coating, J. Mater. Eng. Perform. 28 (2019)

6033–6041. https://doi.org/10.1007/s11665-019-04377-5.

[50] M. Mansoob Khan, 11 - Electrochemical deposition synthesis methods, in: M. Mansoob Khan (Ed.), Photocatal. Synth. Charact. Methods, Elsevier, 2025: pp. 113–123. https://doi.org/10.1016/B978-0-443-28913-2.00012-5.

[51] S. Pinate, E. Ghassemali, C. Zanella, Strengthening mechanisms and wear behavior of electrodeposited Ni–SiC nanocomposite coatings, J. Mater. Sci. 57 (2022) 16632–16648. https://doi.org/10.1007/s10853-022-07655-1.

[52] A. López-Ortega, R. Bayón, J.L. Arana, Evaluation of protective coatings for offshore applications. Corrosion and tribocorrosion behavior in synthetic seawater, Surf. Coat. Technol. 349 (2018) 1083–1097. https://doi.org/10.1016/j.surfcoat.2018.06.089.

[53] M.S. Safavi, S. Soleimanzadeh Ghazijahani, A. Rasooli, Pulsed electroplating of ZrO2-reinforced Ni-Cr alloy coatings from the duplex complexing agents-containing bath for engineering applications: Importance of operating conditions, Heliyon 10 (2024) e37631. https://doi.org/10.1016/j.heliyon.2024.e37631.

[54] Electroplating and Electroless Plating, (2014) 277–306. https://doi.org/10.1016/B978-0-08-096532-1.00413-1.

[55] A.A. Ojo, I.M. Dharmadasa, Electroplating of Semiconductor Materials for Applications in Large Area Electronics: A Review, Coatings 8 (2018) 262. https://doi.org/10.3390/coatings8080262.

[56] H.S. G., A.C. Hegde, Electrochemical deposition and characterisation of NiTi alloy coatings for better corrosion protection, Can. Metall. Q. 63 (2024) 1392–1399. https://doi.org/10.1080/00084433.2023.2295210.

[57] V. Hasannaeimi, T. Shahrabi, S. Sanjabi, Fabrication of NiTi layer via co-electrodeposition of nickel and titanium, Surf. Coat. Technol. 210 (2012) 10–14.

https://doi.org/10.1016/j.surfcoat.2012.07.054.

[58] S. Cooke, K. Ahmadi, S. Willerth, R. Herring, Metal additive manufacturing: Technology, metallurgy and modelling, J. Manuf. Process. 57 (2020) 978–1003. https://doi.org/10.1016/j.jmapro.2020.07.025.

[59] L.E. Murr, E. Martinez, K.N. Amato, S.M. Gaytan, J. Hernandez, D.A. Ramirez, P.W. Shindo, F. Medina, R.B. Wicker, Fabrication of Metal and Alloy Components by Additive Manufacturing: Examples of 3D Materials Science, J. Mater. Res. Technol. 1 (2012) 42–54. https://doi.org/10.1016/S2238-7854(12)70009-1.

[60] J. Gockel, J. Beuth, K. Taminger, Integrated control of solidification microstructure and melt pool dimensions in electron beam wire feed additive manufacturing of Ti-6Al-4V, Addit. Manuf. 1–4 (2014) 119–126. https://doi.org/10.1016/j.addma.2014.09.004.

[61] A. Bandyopadhyay, B. Heer, Additive manufacturing of multi-material structures, Mater. Sci. Eng. R Rep. 129 (2018) 1–16. https://doi.org/10.1016/j.mser.2018.04.001.

[62] S. Mao, D.Z. Zhang, Z. Ren, G. Fu, X. Ma, Effects of process parameters on interfacial characterization and mechanical properties of 316L/CuCrZr functionally graded material by selective laser melting, J. Alloys Compd. 899 (2022) 163256. https://doi.org/10.1016/j.jallcom.2021.163256.

[63] F. Bartolomeu, M.M. Costa, N. Alves, G. Miranda, F.S. Silva, Additive manufacturing of NiTi-Ti6Al4V multi-material cellular structures targeting orthopedic implants, Opt. Lasers Eng. 134 (2020) 106208. https://doi.org/10.1016/j.optlaseng.2020.106208.

Chapter 2

Electron-beam melting behavior of metallic materials

2.1 Introduction

As described in Chapter 1, the main objective of this study is the fabrication of NiTi-coating by EB-melting of Ni-plate on CP-Ti. For conducting the study it is essential to understand the common aspects of EB-melting of metals. In this chapter, the fundamental melting and solidification behavior of metallic materials under electron-beam irradiation is investigated using 316L stainless steel as one of the most commonly used metal. This chapter provides the fundamental information which is required in the following chapters. Electron-beam has attracted increasing attention as a high-energy-density processing technique capable of producing metallic components with complex geometries [1]. In the field of welding, it has been commonly recognized that EB irradiation provides deep penetration compered to laser welding [2]. However, the difference is attributed to the large power of electron beam machine [3]. In the field of AM process, it is commonly recognized that the melt pool formed by the electron beam is shallower than those obtained by laser powder bed fusion [4], which is abbreviated as L-PBF while the used of the term “PBF-LB” is recommended by ISO standard.

The characteristics of electron-beam melting — very rapid, localized heating from a high-energy electron beam and operation in high vacuum — make EB-based processes especially suitable for processing reactive metals (e.g. Ti, Zr, Hf) and high-melting-point/refractory alloys (e.g. Nb, Ta, W, Mo) [5]. Regardless of the material system, knowledge of the fundamental physics of electron beam (EB) melting, particularly the formation of melt pools and the evolution of the thermal-fluid behaviour of the processed region, is crucial. Therefore, understanding the melt-pool geometry and

associated flow fields under EB irradiation is essential for controlling subsequent solidification phenomena and achieving reliable material synthesis.

In this chapter, the fundamental melting behavior of 316L stainless steel under EB irradiation is investigated as a representative model system. Although the material differs from the titanium–nickel system treated in the subsequent chapters, EB-induced melt-pool formation, surface morphology, and Marangoni-driven flow share common features across metallic alloys. Thus, the results presented here provide essential physical insight for understanding melting, mixing, and resolidification processes relevant to the *in situ* formation of NiTi coatings presented in Chapters 3–6.

2.2 Experimental and Simulation Methods

2.2.1 Material

Commercial 316L austenitic stainless steel (JIS SUS316L) was used as a model material for examining fundamental melting behavior under electron beam (EB) irradiation. Cylindrical rods with a diameter of 10 mm and a length of 40 mm were prepared. Prior to EB irradiation, the top surface of each specimen was mechanically ground using SiC papers up to #1200 grit and subsequently polished with colloidal silica to obtain a smooth and reproducible initial surface condition.

2.2.2 Electron-Beam Irradiation

Electron-beam irradiation was performed using a commercial EB machining system (EBM-6LB-1, Mitsubishi Electric). The acceleration voltage and convergence current were fixed at 60 kV and 1150 mA, respectively. To systematically study the effects of beam energy input, four beam powers (300 W, 600 W, 900, and 1200 W) and four scan

speeds (100, 300, 1000, and 3000 mm/s) were used. A single-line scan of 10 mm length was applied for each irradiation condition. The line energy density E_{L} was defined as:

$$E_{\mathrm{L}} = \frac{P}{V} \tag{2.1}$$

where P is the beam power (W) and V is the scanning speed (mm/s). The melt tracks generated under these conditions were used for subsequent surface and cross-sectional analyses.

2.2.3 Surface Profilometry

The morphology of the irradiated surface was examined using a laser confocal microscope (VK-X200/210, Keyence, Japan). Surface profiles were extracted to quantify:

- melt-track width
- track height (material accumulation)
- heigh difference: elevation difference between peak and valley positions

These parameters were evaluated as functions of line energy density to characterize how EB parameters influence melt-pool geometry.

2.2.4 Cross-Sectional Microstructural Characterization

After melt-track formation, the specimens were sectioned perpendicular to the scanning direction. Cross-sections were prepared using standard metallographic procedures, including mechanical grinding, polishing with diamond suspensions, and final polishing with colloidal silica.

The melt-pool geometry (depth, width, and aspect ratio) was observed using a field-emission scanning electron microscope (FE-SEM; JSM 6500, JEOL, Japan).

2.3 Results

2.3.1 Surface Morphology of Melt Tracks

Fig. 2.1 shows representative laser confocal micrographs of melt tracks produced under various combinations of beam power and scan speed, while Fig. 2.2 presents the corresponding surface height maps. Note that melt tracks C, D, H, L, and P (with line energy $\leqslant$ 0.6) exhibited negligible melting, preventing the identification of their positions and geometry.

As shown in the first column of Fig. 2.1, the melt tracks processed at a scanning speed of 100 mm/s formed chevron-like patterns on their surfaces. This implies that solidification occurred immediately after melting, freezing the surface topography that was significantly affected by the hydrodynamic waves generated by the moving electron beam (EB) and the melt pool.

Fig. 2.2 reveals that the center of the melt track is elevated relative to the sides. Moreover, a droplet-like protrusion is observed at the start of the track, whereas a depression (or crater) formed at the end. These accumulations and concavities are attributed to the redistribution of molten material driven by thermocapillary flow (Marangoni flow) [6] as well as shrinkage induced by resolidification [7]. These observations confirm that the melt-track geometry under EB irradiation is strongly governed by the balance among heat input, heat conduction, thermal diffusion, and fluid flow within the molten region.

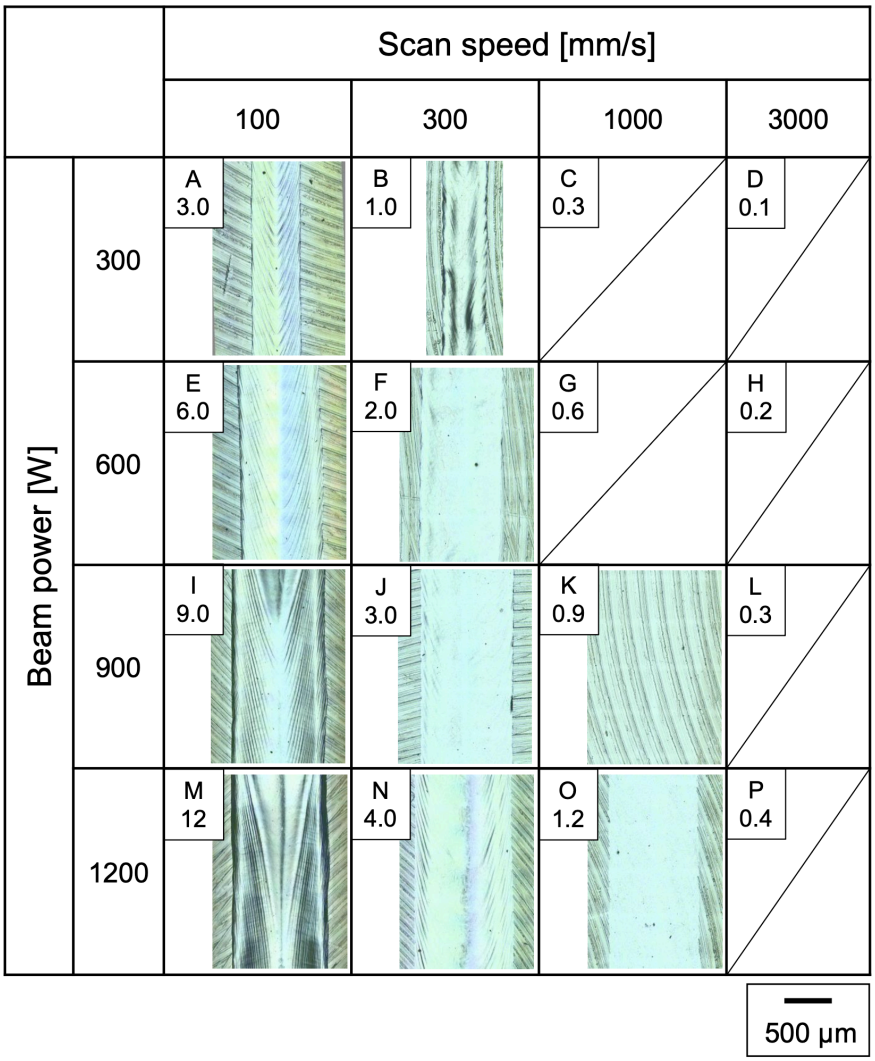

Fig 2.1. Laser microscope images of the surface of melt track formed by scanning electron beam with various condition on SUS316L steel. The scanning was carried out in the vertical direction, from bottom to top, in the images. Capital letter and values indicate label of condition and line energy density (E_L), respectively.

	A	B	E	F	I	J	K	M	N	O
Beam power [W]	300	300	600	600	900	900	900	1200	1200	1200
Scan speed [mm/s]	100	300	100	300	100	300	1000	100	300	1000
Line energy [J/mm]	3.0	1.0	6.0	2.0	9.0	3.0	0.9	12	4.0	1.2
500 μm	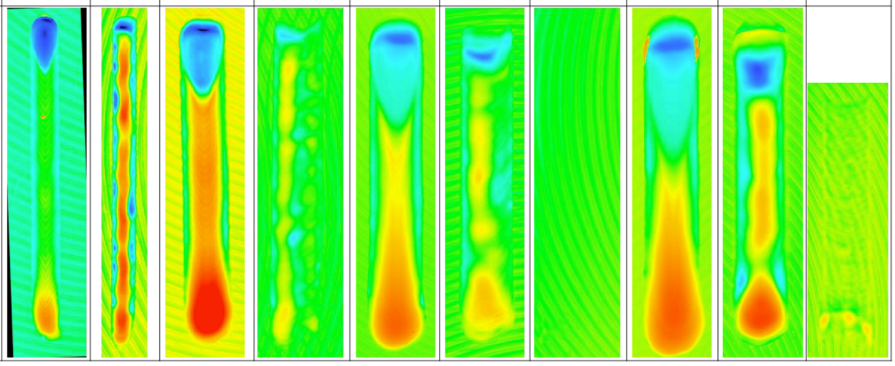									

Fig 2.2. Laser microscope height images of the surface of melt track formed by scanning electron beam with various on SUS316L steel. The scanning was carried out in the vertical direction, from bottom to top, in the images.

Fig. 2.3 plots the melt track width, height, and height difference as a function of line energy density (E_L). Generally, the melt-track width increased with increasing E_L. As shown in Fig. 2.3a, for a fixed scan speed, higher beam power resulted in broader melting. Conversely, at a fixed beam power, higher scan speeds led to narrower tracks due to the reduced energy input per unit length. Regarding track height (defined as the maximum elevation above the original surface), Fig. 2.3b shows a monotonic increase with line energy at 100 mm/s. However, at 300 mm/s, the track height initially decreases before increasing. The height difference, defined as the elevation difference between the peak and valley regions, is shown in Fig. 2.3c. At 100 mm/s, the height difference increased monotonically with line energy, indicating stronger melt-pool convection at higher heat inputs.

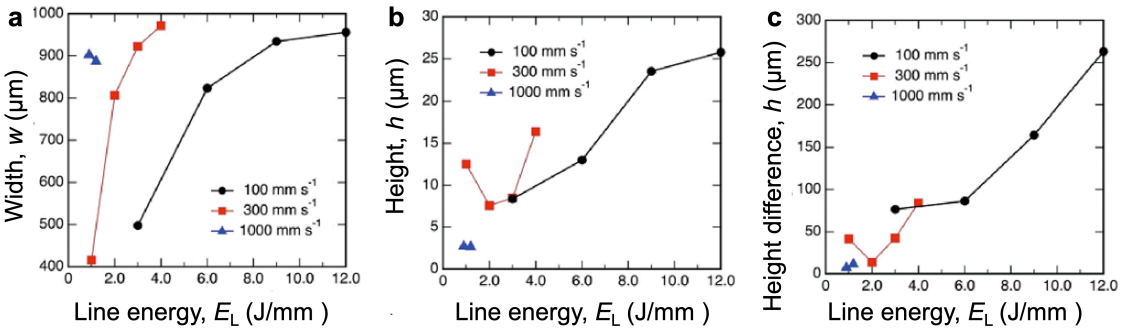

Fig. 2.3. Width, height, and height differences evaluated from laser microscope analysis of melt tracks formed by scanning electron beam.

2.3.2 Cross-Sectional Melt-Pool Geometry

SEM images of the melt-pool cross-sections are shown in Fig. 2.4. The microstructure consists of elongated grains in the melt-pool interior and finer, equiaxed grains near the pool boundary. Since the primary purpose of this chapter is to characterize melt-pool geometry and fluid flow, a detailed discussion of grain-transition mechanisms is omitted here. Qualitatively, however, the observed grain morphologies are consistent with directional solidification under steep thermal gradients and strong convective flow. In particular, the grain refinement near the boundary suggests local undercooling and rapid solidification influenced by thermocapillary-driven (Marangoni) flow.

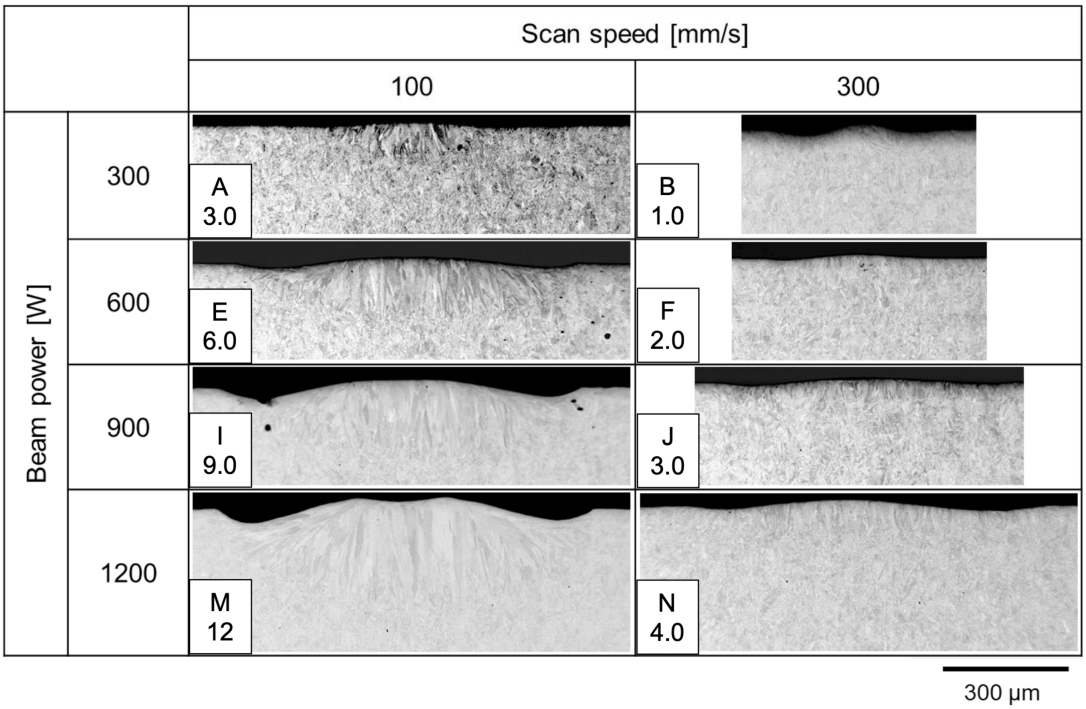

Fig 2.4. Scanning Electron Microscope (SEM) images of cross section of melt tracks formed by scanning electron beam with various condition on SUS316L steel. Capital letter and values indicate label of condition and line energy, respectively.

The melt track depths at a scanning speed of 100 mm/s were extracted from the cross-sections and are summarized in Fig. 2.5. The melt track depth exhibits a positive correlation with line energy. Combining these depth results with the width data from Fig. 2.3a, the aspect ratio (depth/width) increased more sharply than the width alone, especially under high-power and low-scan-speed conditions. This suggests that vertical heat penetration is enhanced more significantly than lateral spreading when the local temperature gradient becomes steep.

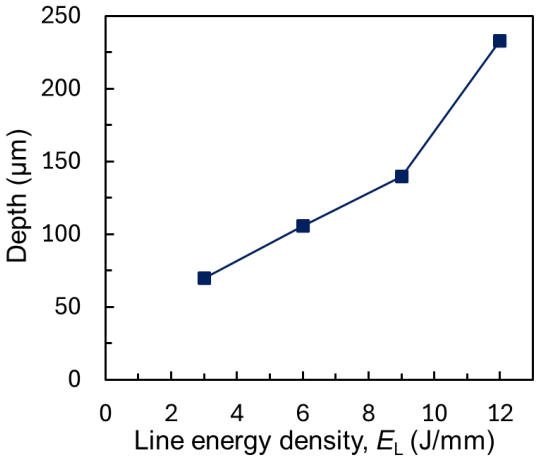

Fig 2.5. Depth of the melt tracks scanned by EB at the scanning speed of 100 mm/s with various condition on SUS316L steel.

2.4 Conclusions

316L stainless steel were irradiated with the EB in a combination of four beam powers (300 W, 600 W, 900, and 1200 W) and four scan speeds (100, 300, 1000, and 3000 mm/s) to investigate the effect of parameters on the surface morphology, and melt-pool geometry of the melt tracks. We observed the surface and cross-section of the melt track after irradiation and analyzed the variation in melt track width, height and depth. The key findings and conclusions are summarized below.

- The geometry of the electron beam melt tracks is sensitively governed by the line energy density. Increasing the energy input results in a monotonic increase in track width and depth, with the depth increasing more rapidly than the width at higher energy levels.
- The observation of chevron patterns and height variations along the melt tracks confirms the dominance of thermocapillary forces in redistributing the molten material prior to rapid resolidification.
- The non-linear increase in the melt-track aspect ratio suggests a transition in the heat transfer mechanism, where vertical heat dissipation becomes enhanced

relative to lateral diffusion as the local temperature gradient steepens.

Reference

[1] C. Körner, Additive manufacturing of metallic components by selective electron beam melting — a review, Int. Mater. Rev. 61 (2016) 361–377. https://doi.org/10.1080/09506608.2016.1176289.

[2] Electron-Beam Welding, (1993). https://doi.org/10.31399/asm.hb.v06.a0001369.

[3] T. Lienert, T. Siewert, S. Babu, V. Acoff, eds., Introduction to High Energy Density Electron and Laser Beam Welding, in: Weld. Fundam. Process., ASM International, 2011: pp. 507–513. https://doi.org/10.31399/asm.hb.v06a.a0005627.

[4] T. Ishimoto, T. Nakano, Review — Microstructural Control and Functional Enhancement of Light Metal Materials via Metal Additive Manufacturing, Mater. Trans. 64 (2023) 10–16. https://doi.org/10.2320/matertrans.MT-MLA2022007.

[5] V. Sonkamble, N. Phafat, A current review on electron beam assisted additive manufacturing technology: recent trends and advances in materials design, Discov. Mech. Eng. 2 (2023) 1. https://doi.org/10.1007/s44245-022-00008-x.

[6] T. Matsushita, I. Belov, D. Siafakas, A.E.W. Jarfors, M. Watanabe, Interfacial phenomena between molten iron and molten slag–Effect of nitrogen on the Marangoni convection, J. Mater. Sci. 56 (2021) 7811–7822. https://doi.org/10.1007/s10853-020-05730-z.

[7] C. Wang, C.-N. Sun, L. Zhang, S. Feih, P. Wang, Improving component dimensional accuracy in electron beam powder bed fusion by addressing nonlinear deformations with 3D compensation strategies, Virtual Phys. Prototyp. 19 (2024) e2430319. https://doi.org/10.1080/17452759.2024.2430319.

Chapter 3

In Situ Synthesis of NiTi via Single-Track Electron Beam Scanning on Ni-Plated Ti

3.1 Introduction

Commercially pure titanium (CP-Ti) is widely used in biomedical [1], aerospace [2], chemical [3], marine [4], and nuclear industries [5] owing to its good corrosion resistance, biocompatibility, low weight, and high specific strength [6]. However, the poor wear resistance of the CP-Ti limits its mechanical performance [7,8] and its use in transmission components, such as engines and pumps.

Nickel titanium (NiTi/Nitinol) is a widely used shape memory alloy composed of nickel and titanium in nearly equal atomic ratios [9]. It is widely used in the automotive [10], aerospace [11,12] industries and medical devices [13,14]. However, it also exhibit good wear resistance [15], even better than cobalt-based wear-resistant alloy [16]. Therefore, depositing NiTi coatings onto CP-Ti surfaces emerge as a viable strategy.

Several studies have been conducted on NiTi coatings using traditional coating methods such as low-pressure plasma spraying [17], vacuum plasma spraying [18,19], atmospheric plasma spraying [20,21], cold spraying [22–24], and physical vapor deposition [25–31]. These studies have demonstrated the potential of NiTi coatings as wear-resistant coatings. However, inherent flaws in conventional coating fabrication methods have resulted in issues such as oxidation [17], porosity [17,23], thickness non-uniformity [23], poor adhesion [31], and insufficient thickness [31]. Consequently, their wear resistance and load-bearing capacity remain below the levels achievable with bulk Nitinol. To overcome the disadvantages of traditional coating method, a new method

combining electroplating and additive manufacturing (AM) technology (specifically electron beam melting, EBM) was proposed to produce NiTi coatings on CP-Ti substrate. This method consists of two primary steps: electroplating pure Ni onto the CP-Ti and scanning the Ni plating layer with an electron beam (EB).

The objective of Chapter 2 is to confirm the feasibility of this new fabrication method prior to conducting a thorough investigation into it. Therefore, experiments involving single-track EB scanning on a Ni-plated CP-Ti substrate were conducted in this chapter. The effect of scanning parameters on the morphology, composition and elemental distribution of the melt tracks was investigated based on the analysis of surface and cross-sectional observation results. The formation of specific microstructure and inhomogeneities is discussed in view of phenomena such as melting, solidification and diffusion.

3.2 Methods

3.1.1 Preparation of substrate and Ni-plate

A slab of CP-Ti (99.5% purity; Nilaco, Tokyo, Japan) was cut into specimens of 25 × 25 × 10 mm^3 by electric discharge machining. A CP-Ti specimen of 25 × 25 mm^2 area was used as the working electrode. The CP-Ti specimen was given a four-stage pretreatment: (1) mechanical grinding using P120–P2400-grit SiC abrasive papers; (2) immersion in ethanol at RT for 5 min; (3) immersion 10 wt.% HCl solution at RT for 5 min, with a 9 V DC power applied to promote the removal of surface oxides and contaminants and (4) washing with ultrapure water.

A pure Ni anode (ϕ6 × 20 mm) of 405 mm^2 area was used with an interelectrode gap of 8 cm. In this study, a thicker pure Ni layer was required to enable subsequent processing. Therefore, a nickel sulfamate solution was used as the plating bath. This

type of bath tolerates high current density and produces plated layers with lower internal stress, making it suitable for applications that demand greater coating thickness [32]. The compositions of the solutions and the electroplating parameters that adopted from a electrochemical handbook [32] are listed in Table 3.1. Electroplating was conducted for 4 h to obtain a plating layer with sufficient thickness. After plating, the layer was ground using P120–P2000 grit SiC abrasive papers to a final thickness of 45 μm.

Table 3.1. Composition of Ni-plating solution and plating parameters.

	Compound/Parameter	**Value**
Composition	$NiCl_2 \cdot 6H_2O$	0.10–0.13 mol/L
	$Ni(SO_3NH_2)_2$	1.70–1.79 mol/L
	H_3BO_3	0.49–0.73 mol/L
Parameters	Temperature	50–60 °C
	pH	3.0–5.0
	Cathodic current density	3.0 A/dm^2
	Current mode	DC plating

3.1.2 Electron beam irradiation

The plated specimens were irradiated with EB and scanned along 4-mm long straight lines using an EB machine (Mitsubishi Electric, EBM-6LB-1) under a helium atmosphere at 0.5 Pa. The acceleration voltage and convergence current were fixed at 60 kV and 1150 mA, respectively. The irradiations were conducted under six levels of beam power, P: 100, 200, 300, 400, 500, and 600 W (i.e., beam currents, I : 1.67, 3.33, 5.00, 6.67, 8.33, and 10 mA, respectively), and a scanning speed of 100 mm/s.

3.2.3 Microstructural characterization

The top surfaces of the EB-irradiated samples were observed using a laser microscope (Keyence, VK-X200/210) to measure the widths and surface topographies of the melt tracks. A scanning electron microscope (Keyence, VE-8800) equipped with energy dispersive X-ray spectroscopy was used to analyze the elemental composition of the melt tracks on the surface. Furthermore, the samples were cut perpendicular to the beam-scanning direction for cross-sectional observations using field-emission scanning electron microscopy (FE-SEM, JEOL, JSM 6500). In addition, Vickers harnesses of the melt tracks were measured using a Vickers hardness tester (Shimadzu, HMV-G31) with a 200 g load for 15 s. The test was conducted seven times for the cross-sections of each sample, and the results were averaged.

In order to discuss the formation process of the observed phases resulting from the dissolution of Ni from the Ni-plate into the Ti melt formed by melting the substrate, we need to consider Ni as the solute and Ti as the solvent. To create Ni-Ti phase diagram, we used Thermodynamic calculation software (Thermo-Calc Software AB, Thermo-Calc 2022b) and relied on the thermodynamic database for Titanium alloys (TCTI4) [33].

3.3 Results

3.3.1 Surface morphology

Fig. 3.1 shows SEM images of the melt track surfaces after electron beam (EB) scanning, where the EB was scanned downward. The surface topography of the melt track is influenced by the value of P [W]. At P = 100 W (Fig. 3.1a), the melt track formed a chevron-like patterned surface, which did not appear at higher beam powers. This implies that solidification occurred immediately after melting when the surface

topography was still significantly affected by the wave generated by the irradiation of the moving EB and moving melt pool. In addition, a teardrop-shaped concave surface forms at the end of the melt track. These morphological features closely resemble the surface melt tracks observed on 316L stainless steel in Chapter 2. At P = 200 W (Fig. 3.1b), the surface of the melt track was smooth compared with that at P = 100 W. However, cracks were observed, as indicated by the arrows. Moreover, a hole were occasionally observed, as indicated by the white triangle. The smoothest surface was obtained at P = 300 W (Fig. 3.1c). It is worth noting that some irregular patterns distributed along the middle edges of the tracks formed by 400–600 W EB irradiation (Fig. 3.1d, 3.1e and 3.1f), as indicated by black triangles and the magnified images are shown as Fig. 3.2. The EDS analysis revealed the patterns consist of almost 100 at.% Ti, as shown in Table 3.2.

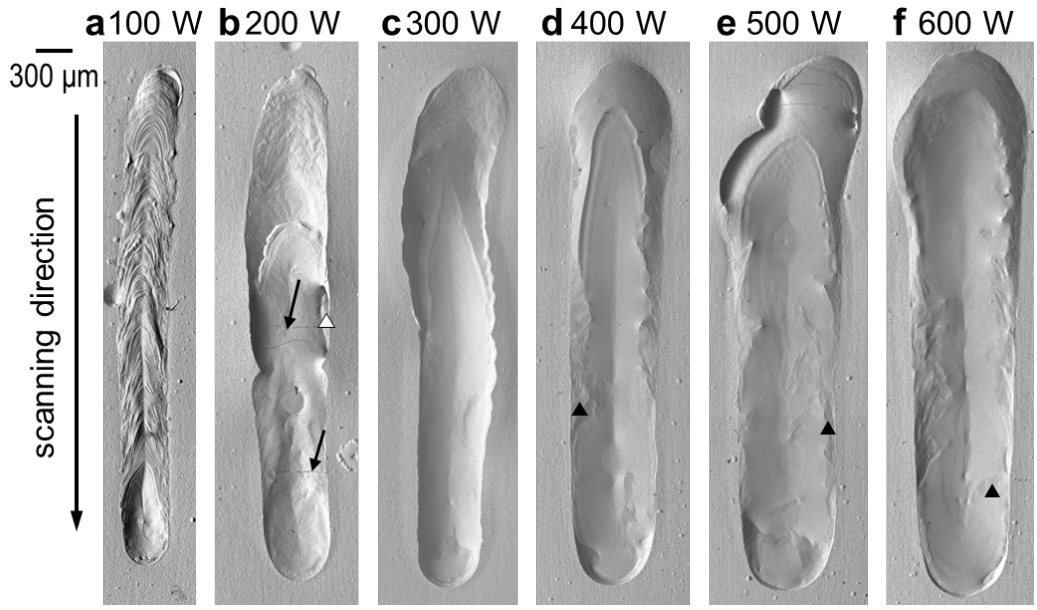

Fig. 3.1. SEM images of the melt track surfaces formed by EB scanning with a constant scanning speed of 100 mm/s and various powers of (a) 100 W, (b) 200 W, (c) 300 W, (d) 400 W, (e) 500 W, and (f) 600 W. The arrows indicate cracks, the white triangle indicates a hole, and the black triangles indicate irregular surface patterns.

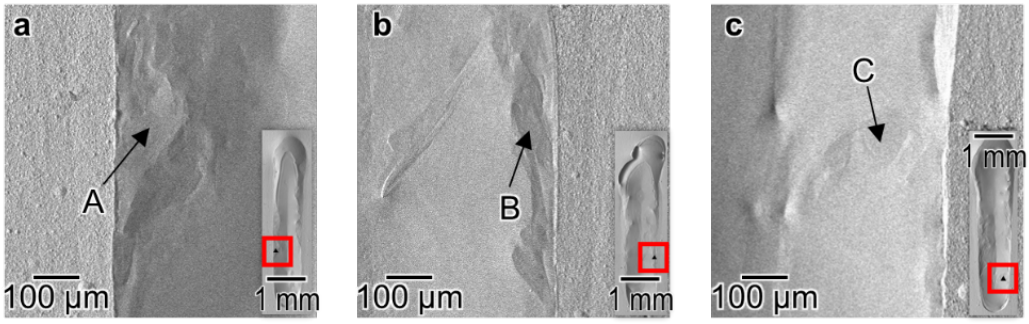

Fig. 3.2. Magnified SEM images of the area with irregular patterns on the surface of the melt tracks formed by EB scanning with the beam power of (a) 400 W, (b) 500 W, (c) 600 W, and a scanning speed of 100 mm/s .

Table 3.2. Compositions of the selected position in Fig. 3.2.

Selected Area	**Composition (at.%)**	
	Ni	Ti
A	0.2	99.8
B	0.0	100.0
C	1.8	98.2

The widths and lengths of the melt tracks were measured and plotted against the EB power (*P*), as shown in Fig. 3.3. The width significantly increased with an increase in *P* from 100 to 200 W, but was almost the same from 200 to 300 W. Moreover, the width increased significantly again from 300 to 600 W. On the other hand, the length exhibited a monotonic and gradual increase with increasing *P* without a tendency to saturate.

Miyata et al. [34] evaluated the shape of melt-pools in stainless steels formed by single-track EB scanning with various *P* and found that the width and height increased as the *P* increased. The trend between the shape of the melt track and the *P* is the same as that in the Ni-plated CP-Ti observed in this study. Miyata et al. [34] also reported that the change in the width can be reproduced by computational thermal-fluid

dynamics using single absorption rates of 0.8. It is suggested that the difference in the shape of the melt track with the *P* is caused by the difference in the total amount of absorbed heat.

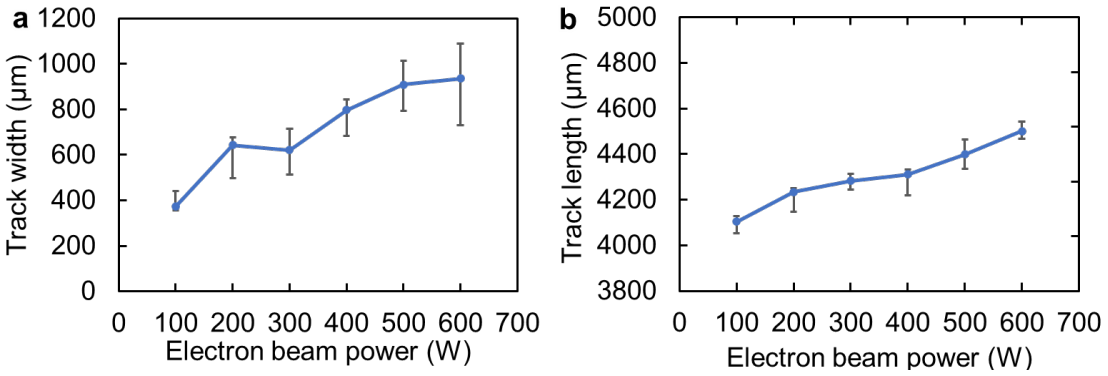

Fig. 3.3. (a) Width and (b) length of the melt track formed by EB scanning as a function of power. The scanning speed is fixed at 100 mm/s.

3.3.2 Cross-sectional observation and compositional analysis

Fig. 3.4 show the cross-sectional SEM images of the melt tracks corresponding to the top-view SEM images in Fig. 3.1. In general, melt tracks formed at all electron beam power (*P*) exhibit dense and porosity-free microstructure. The areas of the melted regions in cross-section increased with increasing EB power, in another word, the wider and deeper melt track is formed under the high-power EB irradiation. However, the melt track was not equally enlarged in every dimension and the curvatures of the fusion lines are varied by *P*: For *P* = 100 W (Fig. 3.4a) and 200 W (Fig. 3.4b), the width of the melt track was much greater than the depth, and the fusion lines appeared to be ellipse-like shape. With an increase in beam power from 300 to 600 W (Fig. 3.4c, 3.4d, 3.4e, 3.4f), the depth of the melt track increased more significantly than its width. As a result, the cross-section of the melt track evolved into a triangle-like shape. In addition, the fusion line appeared irregularly bent and blurred under these conditions.

The thickness of the electroplated Ni layer was less than 50 μm (45 μm on average),

and the side edges of the melt track for P = 200 W (Fig. 3.4b) and 300 W (Fig. 3.4c) were much thicker than the original Ni layer. In particular, the electroplated Ni layers beside the melt track detached from the Ti substrate, as shown in Fig. 3.4c. Moreover, the electroplated Ni layer is separated from the melt track on the right-hand side. Hydrogen inevitably emerges during the Ni plating process [35] and some of the hydrogens trapped at the interface between the plated layer and the substrate, as well as within the plated layer cause the formation of pores [36]. It has been reported that the pores weaken the bonding between the plating and the substrate [37], and cause localized separation of the plating from the substrate [38]. In this study, the pores are supposed to be also formed during the Ni plating and lead to cause the holes (Fig. 3.1b) and the plating to bulge (Fig. 3.4c and 3.4d). The separation of the electroplated Ni layer is also shown in Fig. 3.4a for P = 100 W. However, the effect of the separation distance in this case was not significant. The space can be filled by a subsequent EB scanning along an adjacent line with an offset of 200−300 μm in forming the NiTi layer, which will be presented in Chapter 4.

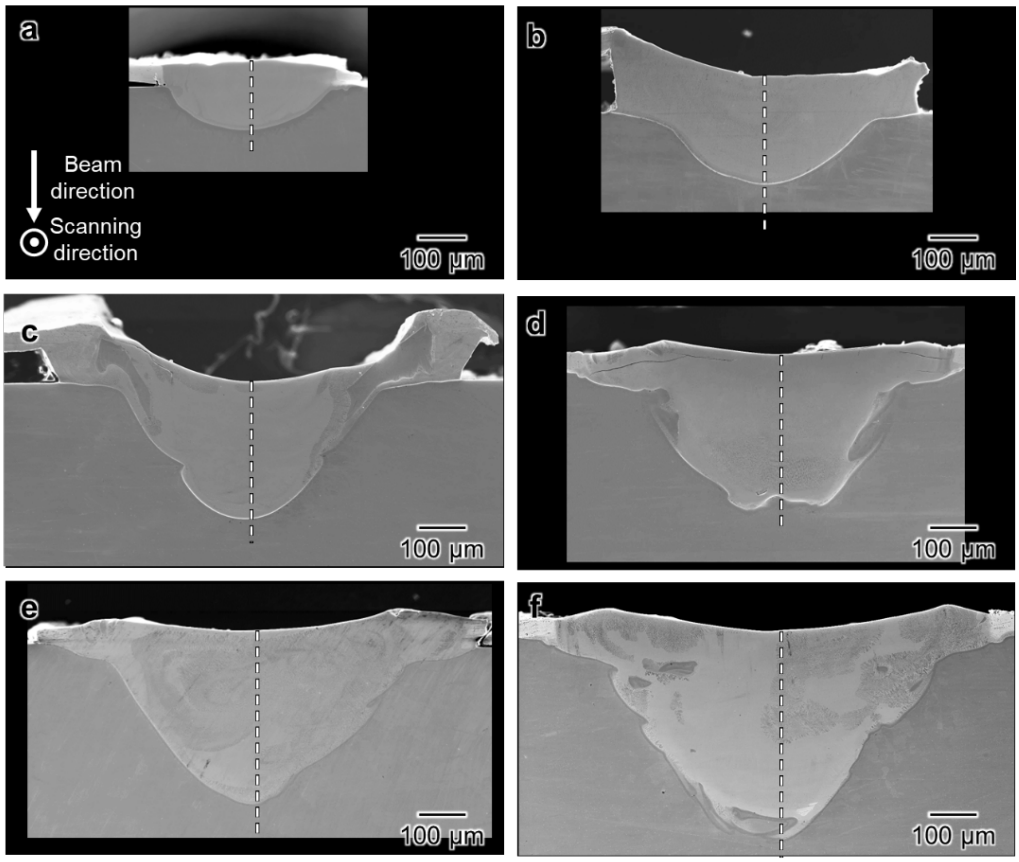

Fig. 3.4. SEM images of the cross-section of the melt tracks formed by EB scanning at a constant scanning speed of 100 mm/s and various levels of power (*P*): (a) 100 W, (b) 200 W, (c) 300 W, (d) 400 W, (e) 500 W and (f) 600 W.

Fig. 3.5 show the EDS line profiles of the melt tracks indicated by dashed lines in normal direction of the melt tracks in Fig. 3.4. The atomic ratio of Ni:Ti generally remains close to 1:1 throughout the melt tracks formed by EB irradiation with $P = 100$ and 200 W, which is the stoichiometric composition of the NiTi phase, as shown in Fig. 3.5a and 3.5b. The concentration distribution along the normal direction in the melt track is homogeneous at $P = 100$ W, but not completely homogeneous at $P = 200$ W. Notably, the Ti concentration at a distance of approximately 120 μm from the surface approaches 70 at.% (as indicated by the white arrow). This significant variation suggests local segregation within the melt track with $P = 200$ W. The ratios of Ni:Ti in the melt tracks formed with P = 300–600 W (Fig. 3.5c, 3.5d, 3.5e and 3.5f) are

approximately 1:3 with a uniform distribution along the normal direction of the melt tracks.

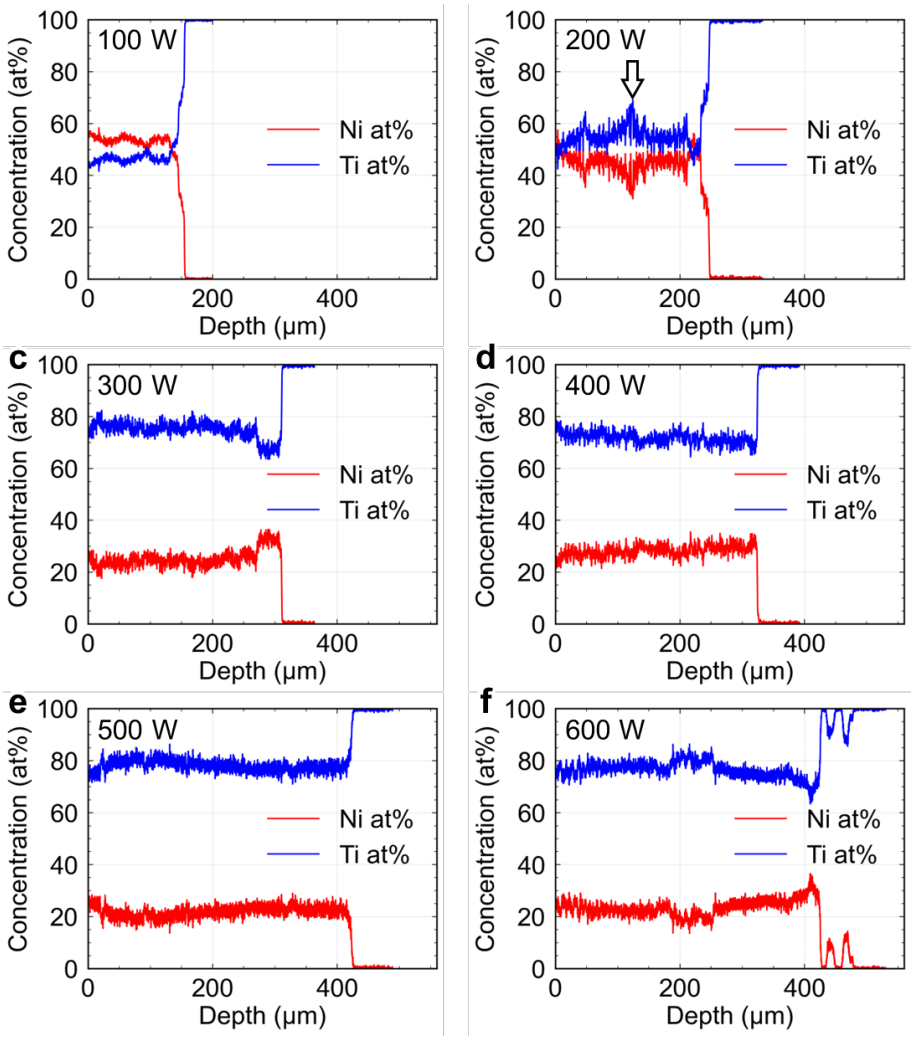

Fig. 3.5. EDS line profiles along the dashed line (indicated in Fig. 3.3) at the center of the melt tracks formed by EB scanning at a constant scanning speed of 100 mm/s and various levels of power (P): (a) 100 W; (b) 200 W; (c) 300 W; (d) 400 W; (e) 500 W; and (f) 600 W. The white arrow in (b) indicates the local inhomogeneity.

The average Ni concentrations of the melt tracks formed by various EB powers were calculated from the EDS line profiles (hereafter referred to as $C_{\mathrm{Ni}}^{\mathrm{EDS}}$) and shown in Fig. 3.6a as a function of P. The Ni concentration at P = 100 W was approximately 50 at.% , which is almost the stoichiometric composition of NiTi phase. The Ni concentration

decreased with the beam power. The decrease in Ni concentration is not linear, but decreases abruptly and then slows down, gradually approaching 20%.

Fig. 3.6b shows a sample cross-sectional SEM image of the melt track formed by EB irradiation at P = 100 W. The area enclosed by the red dashed line is the melted region of the electroplated Ni layer while the area enclosed by the blue dashed line is the melted region of the CP-Ti substrate. To analyze the elemental compositions in the melt tracks, we estimated Ni atomic concentrations ($C_{\mathrm{Ni}}^{\mathrm{Est}}$) through a calculation using the areas of Ni and Ti melting region of each melt track in the cross-section. First, the differential volume of the melting metal ΔV at the position of the plane shown in the cross-section image can be expressed by the following equation:

$$\Delta V_{\mathrm{Ni}} = A_{\mathrm{Ni}} \Delta L \tag{3.1}$$

$$\Delta V_{\mathrm{Ti}} = A_{\mathrm{Ti}} \Delta L \tag{3.2}$$

where A_{Ti} is the area of the Ti melting region in the cross-section, A_{Ni} is the area of the Ni melting region in the cross-section, and ΔL is the differential track length. Moreover, A_{Ti} can be obtained by directly measuring the area of the Ti-melted region in the cross-sectional image. A_{Ni} could not be measured directly in the cross-sectional image because the melt track surface did not maintain its shape after irradiation. However, the electroplated Ni layer is thin and uniform; therefore, the estimated value of A_{Ni} can be obtained by multiplying the melt track width by the thickness of the electroplated Ni layer. An electroplated Ni layer that was not irradiated with EB can also be observed in Fig. 3.6c. The thickness of the Ni layer was measured to be 45 μm as indicated by the double-headed arrow.

The differentiation of the amount of substance of melting metal Δn can be calculated using the volume differentiation.

$$\Delta n_{\mathrm{Ni}} = \frac{\Delta V_{\mathrm{Ni}} \rho_{\mathrm{Ni}}}{M_{\mathrm{Ni}}} \tag{3.3}$$

$$\Delta n_{\mathrm{Ti}} = \frac{\Delta V_{\mathrm{Ti}} \rho_{\mathrm{Ti}}}{M_{\mathrm{Ti}}} \tag{3.4}$$

Here, ρ_{Ti} and ρ_{Ni} are the densities of Ti and Ni, and M_{Ti} and M_{Ni} are the molar masses of Ti and Ni, respectively. The estimated Ni atomic concentration ($C_{\mathrm{Ni}}^{\mathrm{Est}}$) at the position of the plane shown in the cross-sectional image can be calculated combining the four equations from Eq. 3.1 to Eq. 3.4. Finally, the value of $C_{\mathrm{Ni}}^{\mathrm{Est}}$ is calculated using the following equation:

$$C_{\mathrm{Ni}}^{\mathrm{Est}} = \frac{\Delta n_{\mathrm{Ni}}}{\Delta n_{\mathrm{Ni}} + \Delta n_{\mathrm{Ti}}} \times 100\% \tag{3.5}$$

Comparing the $C_{\mathrm{Ni}}^{\mathrm{Est}}$ with the $C_{\mathrm{Ni}}^{\mathrm{EDS}}$ (Fig. 3.6a), both decreased abruptly and then gradually approached 20%.

The $C_{\mathrm{Ni}}^{\mathrm{Est}}$ and $C_{\mathrm{Ni}}^{\mathrm{EDS}}$ of the melt tracks formed by EB irradiations with P = 100 W and 200 W were very close to each other. On the other hand, $C_{\mathrm{Ni}}^{\mathrm{Est}}$ became higher than $C_{\mathrm{Ni}}^{\mathrm{EDS}}$ of the melt tracks formed by higher power EB irradiations. Despite the estimation error, it is supposed that the temperature in the melt pool exceeds the boiling point of Ti by the high-power EB irradiation and evaporation of Ti leads to an increase in the Ni concentrations in the melt pools.

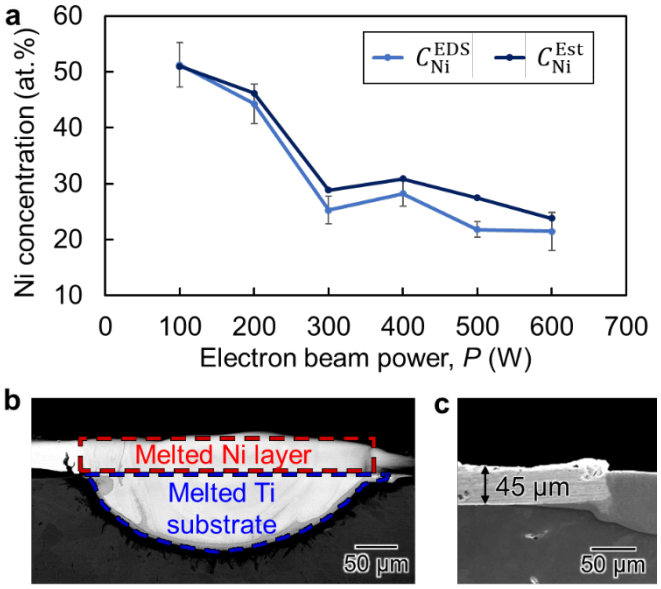

Fig. 3.6. (a) Ni concentration as a function of EB power (*P*). (b) Schematic of the melted area of Ni plating layer and CP-Ti substrate. (c) Cross-sectional SEM image of the Ni plating layer.

Since the elemental distribution in each melt track is generally uniform, their phase composition can be supposed from the Ni-Ti phase diagram [39] based on their average composition. As shown in Fig. 3.7, the melt track at P = 100 W is expected to consist mainly of the NiTi phase, with a small amount of the Ni_3Ti phase present. In contrast, the compositions of the four melt tracks at *P* = 300–600 W are similar, with the $NiTi_2$ phase predominating and a small admixture of the Ti phase present in all of them. The melt track at *P* = 200 W is the only one consisting of a mixture of the NiTi and $NiTi_2$ phases.

The differences in phase composition explain why cracks only appeared in the *P* = 200 W melt track. During cooling after electron beam scanning, tensile stresses developed within the melt track due to thermal contraction [40,41], directly causing the cracks. At high temperatures, the NiTi phase usually exists in the form of austenite (*B*2-NiTi) and has a coefficient of thermal expansion (CTE) of 11.0 $\times 10^{-6}$/K [42]. In contrast, the $NiTi_2$ phase has a CTE of only 6.3 $\times$ 10^{-6}/K [43]. The disparity in contraction rates

during cooling induces extra stresses at the phase boundary. Furthermore, the Young's modulus of the $NiTi_2$ phase is 150 GPa, which is significantly higher than the 83 GPa of the *B*2-NiTi phase and the 34 GPa of the *B*19' -NiTi phase [44]. This indicates that stresses generated at the phase boundary concentrate within the $NiTi_2$ phase, causing cracks to initiate within it. Driven by residual stresses within the melt track, these cracks propagate and eventually penetrate the surface, forming observable macroscopic cracks. Melt tracks formed by electron beams of other powers exhibit lower crack formation probabilities due to their simpler phase compositions.

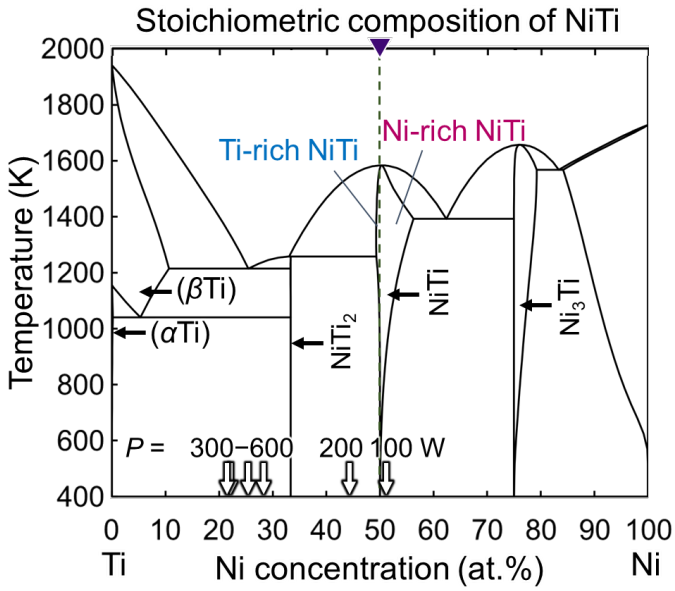

Fig. 3.7. Ni-Ti binary equilibrium phase diagram with concentration of Ni as horizontal axis. The melt track composition corresponding to each electron beam power (*P*) is marked with a white arrow on the horizontal axis.

Vickers hardness of the melt tracks formed by EB irradiation with various *P* are shown in Fig. 3.8, compared with the hardness of the CP-Ti substrate. All melt tracks except for the one with *P* = 200 W exhibit hardness values around 680 HV. The latter shows a Vickers hardness of 312 HV. Since the Ni concentration in the *P* = 200 W melt track is under 50 at.%, it is Ti-rich. Therefore, the NiTi phase within it should be

martensitic at room temperature, specifically the *B*19'-NiTi phase [45]. Conversely, the Ni concentration in the *P* = 100 W melt track exceeds 50 at.%, making it Ni-rich. Consequently, the NiTi phase within it is more likely to be austenitic, specifically the *B*2-NiTi phase [45]. The *B*2-NiTi phase exhibits greater resistance to deformation and higher hardness than the *B*19'-NiTi phase[46]. This explains why the *P* = 100 W melt track demonstrates significantly higher hardness despite similar compositions. The $NiTi_2$ phase in the *P* = 300–600 W melt tracks belongs to the Laves phase, which is characterized by high hardness and brittleness [47]. Consequently, these four melt tracks also exhibit elevated Vickers hardness values. However, even the Vickers hardness of the melt tracks at *P* = 200 W is significantly higher than the 180 HV of the CP-Ti substrate. The surface mechanical properties are expected to be improved by applying the EB irradiation method to the fabrication of NiTi coatings on CP-Ti.

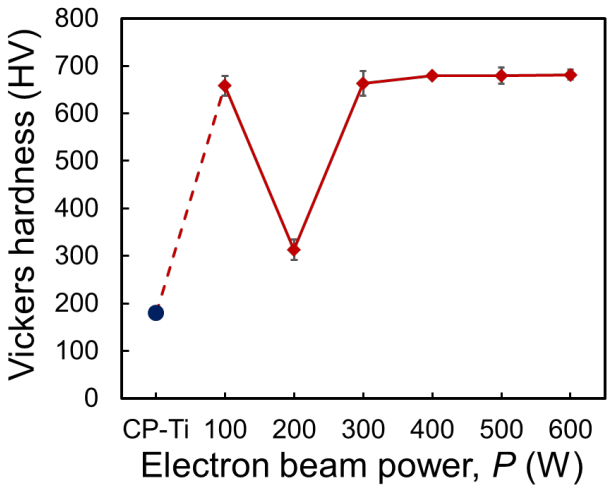

Fig. 3.8. Vickers hardness of melt track plotted as a function of EB power (*P*), in the range from 100 W to 600 W. The blue point on the far left represents the hardness of the CP-Ti substrate.

3.3.3 Microstructures and local inhomogeneities

Fig. 3.9 show the cross-sectional SEM back-scattered electron (BSE) images and the

corresponding EDS mapping image of the melt track for P = 100 W and 200 W, respectively. Both melt tracks consist of a fine dendrite microstructure as shown in Fig. 3.9a, 3.9b, 3.9c and 3.9d. In which, Fig. 3.9c and 3.9d show magnified images of the areas indicated by the red rectangular frames in Fig. 3.9a and 3.9b, respectively. The dendrite microstructure in the melt track formed by EB irradiation with P =100 W is finer than that with P = 200 W, and the widths are 0.9 μm and 1.2 μm, respectively. Miyata et al. [34] reported that the cooling rate of the regions melted by EB irradiation for AM process is higher with a smaller EB power condition. It is suggested that the higher cooling rate in the 100 W condition cause the finer microstructure in this study.

The relative brightness of the BSE image is positively correlated with the atomic weight of the elements in the local area. In this study, the observed brightness is suggested to be positively related to the Ni concentration within the melt tracks, since Ni has a higher atomic number than Ti. As seen in Fig. 3.9a and 3.9b, a dark layer is distributed along the fusion line of both melt tracks. It indicates that these layers have lower Ni concentrations that the interior region of the melt tracks. Fig. 3.9e and 3.9f show the EDS elemental maps corresponding to the BSE images in Fig. 3.9c and 3.9d, respectively. The EDS mapping data show that the concentration of Ni in the outermost layer is 25−35 at.%, which is lower than in the inner area in both melt tracks. It is also consistent with observations made using BSE images. Combining EDS mapping data (Fig. 3.9e and 3.9f) and referring to the Ni-Ti binary equilibrium phase diagram (Fig. 3.7) [39], the outermost layers formed with P = 100 and 200 W supposed to be the $NiTi_2$ phase. On the other hand, the inner area of the melt track consists of the NiTi phase. The formation of the $NiTi_2$ layer will be discussed in detail in *Section 3.4.1*.

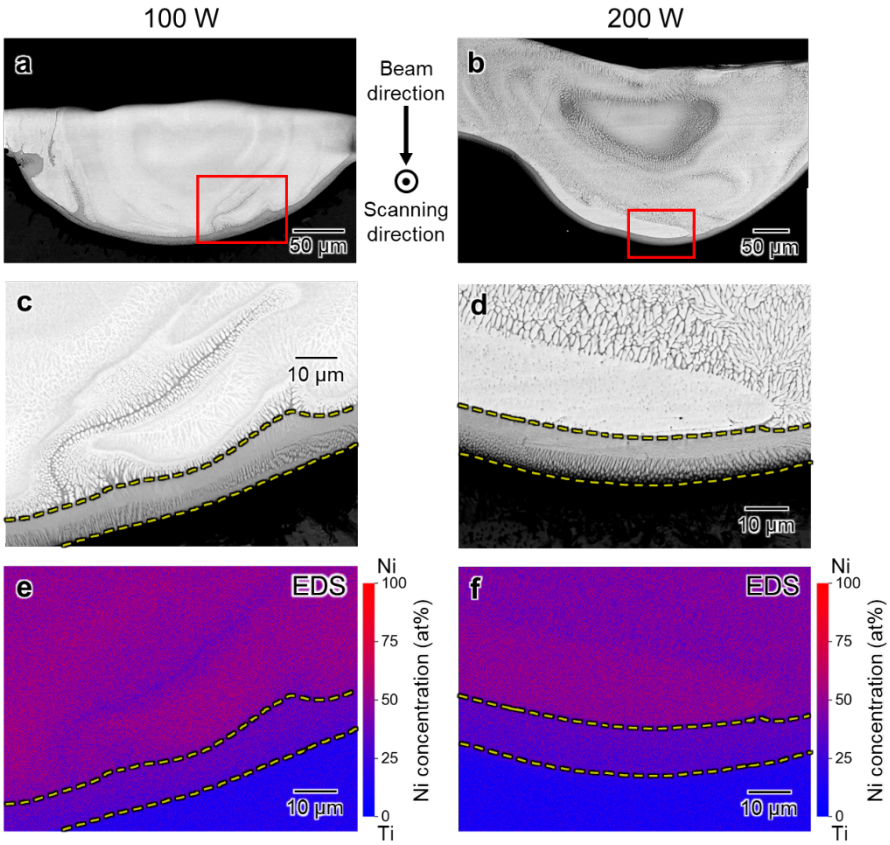

Fig. 3.9. (a, b) Cross-sectional BSE images of the melt track at P = 100 and 200 W. (c, d) Magnified images of the region near the fusion lines indicated by a red box in (a, b). (e, f) Ni and Ti elemental maps of the region in (c, d).

The brightness distribution at the center part of the melt tracks in Fig. 3.9a and 3.9b are different: the center part of the melt track at P = 100 W shows a uniform bright region, whereas that formed with P = 200 W has a dark region surrounded by bright regions. Fig. 3.10a and 3.10b show the BSE image and corresponding elemental distribution at the center part of the melt track with P = 200 W. The EDS data revealed that the dark phase in the central part had a Ni concentration of approximately 35 at.%, which indicated that it is the $NiTi_2$ phase, as well as a dark phase appearing on the fusion line. The brighter surrounding phase is suggested to be NiTi phase. The liquidus temperatures of the regions in Fig. 3.10a are calculated using the compositions and the Ni-Ti binary phase diagram, and mapped in Fig. 3.10c, for considering the formation

mechanism of the $NiTi_2$ phase. The liquidus temperature in the inner area of the yellow dashed line is significantly lower than that in the outer area. The $NiTi_2$ regions that appeared only in the melt track formed by EB irradiation at P = 200 W are suggested to be precipitated the final stage of solidification process due to its lower liquidus temperature. This will be discussed in detail in Section *3.4.1*.

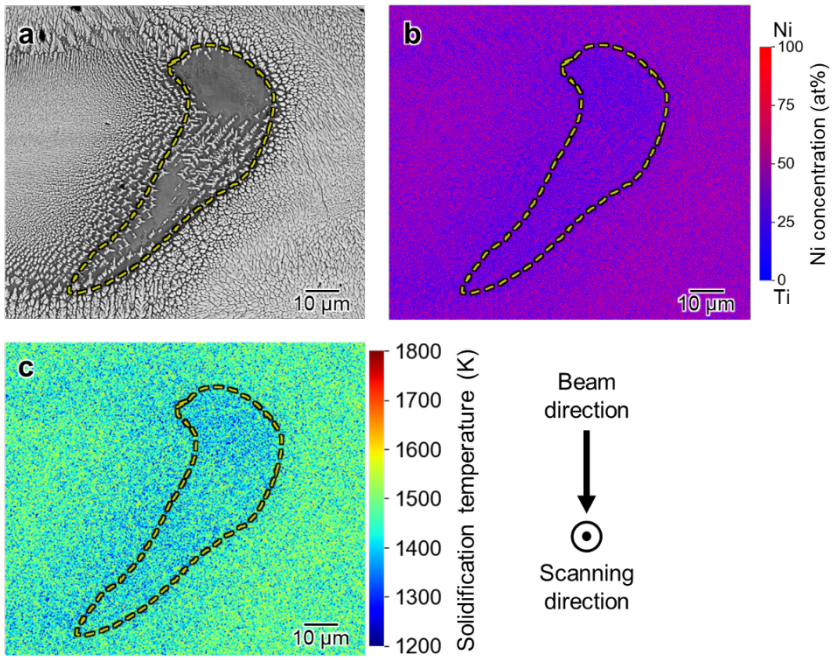

Fig. 3.10. (a) Cross-sectional BSE image at the center of the melt track formed with EB irradiation at P = 200 W. (b) Ni and Ti elemental mapping of the region in (a). (c) Solidification-point mapping of the region in (a).

Almost all the regions show uniform brightness and no obvious segregation is observed in the melt track at P = 300−600 W. However, several dark regions were observed near the side edge of the melt track at P = 300 W and 600 W, as shown in Fig. 3.11a and 3.11b. The magnified images of these dark regions are shown in Fig. 3.11c and 3.11d and corresponding EDS elemental maps are shown in Fig. 3.11e and 3.11f. The EDS data indicate that Ti concentration in the dark regions near the side edge of the melt track are 99-100 at.%, and in other regions of melt track are 72-76 at.%,

respectively. The phase composition of these regions are suggested to be $NiTi_2$ and Ti based on the Ni-Ti phase diagram in Fig. 3.7.

In the research about the additive manufacturing of Al-Si alloys [48], the rapid heating causes the partially melting and the Si phase with the high melting-point is remained even after the heating process. Fig. 3.11g and 3.11h show the liquidus-temperature distribution of the regions near the side edge of the melt track in Fig. 3.11c and 3.11d. The liquidus temperature of the dark regions indicated by yellow dashed lines in the BSE image, is much higher than that of the surrounding regions. It is suggested that some of the solid Ti remained in the melting pool after the EB irradiation because of the higher melting point of pure Ti than that of the intermetallic phases. The remained Ti particles is supposed to be flowed to the edge of the melt track by the Marangoni convection [49]. Notably, the position of these Ti particles corresponds to the irregularly patterned regions in Fig. 3.2, which also consist mostly of pure Ti.

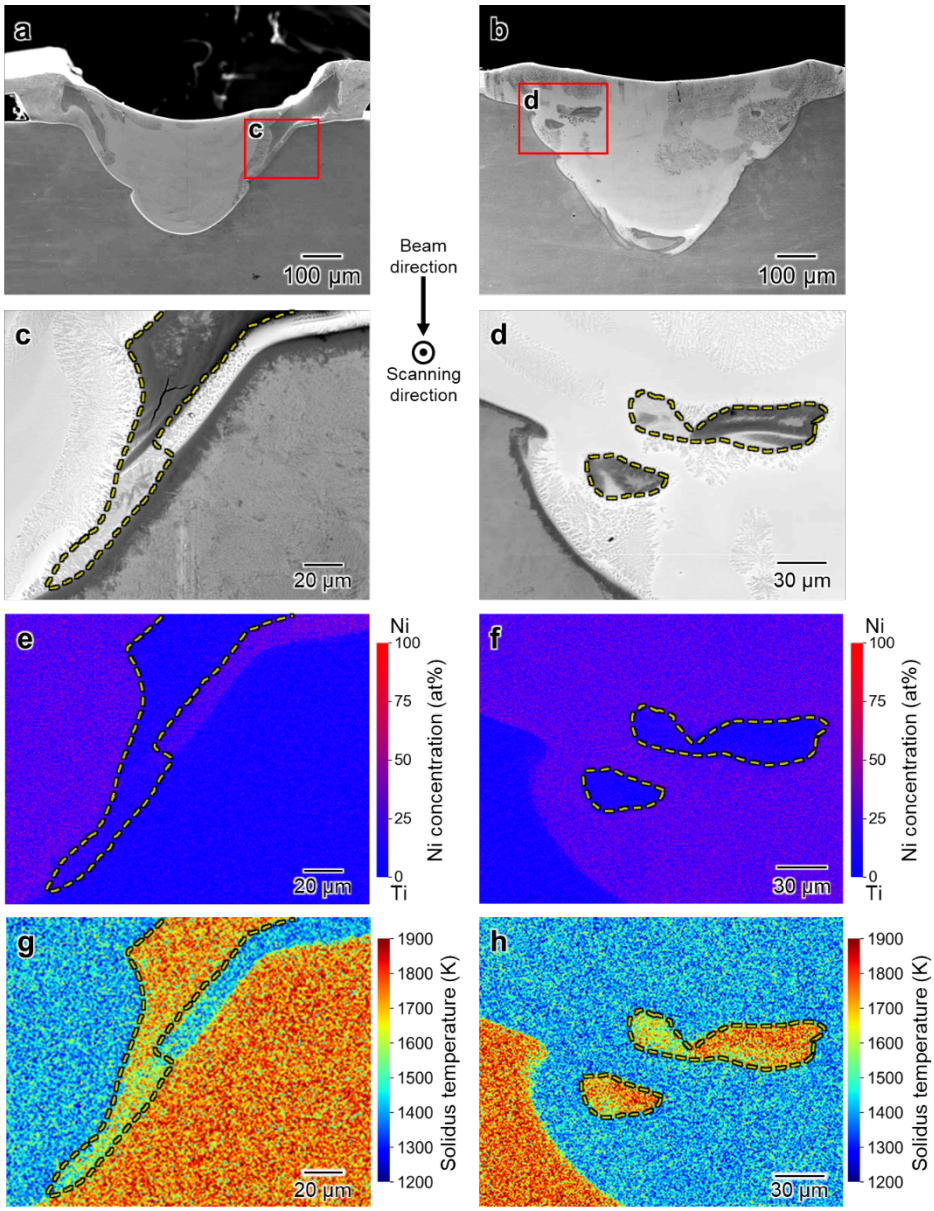

Fig. 3.11. (a, b) Cross-sectional BSE images of the melt track at P = 300 and 600 W. (c, d) Magnified images of the region indicated by a red box in (a, b). (e, f) Ni and Ti elemental maps of the region in (c, d). (g, h) Solidification-point mapping of the region in (c, d).

3.4 Discussion

3.4.1 Inhomogeneous formation under low beam power conditions

The melt tracks formed by the EB irradiation with P = 100 and 200 W have compositions close to that of the stoichiometric composition of NiTi phase. However,

the $NiTi_2$ phase is formed in the outermost layer of the melt tracks, in which Ni concentration is lower than the mean concentrations of the melt tracks of 51.3 at.% and 44.3 at.% obtained by the EDS analyses. Jiang et. al [50] investigated the influence of solid-liquid diffusion on the microstructure at the $Sn_{58}Bi$/Cu interface during welding. Their findings revealed that intermetallic compounds grew at the interface because of the diffusion of Cu from the substrate to the liquid during solidification. The abnormal microstructure formation due to the insufficient diffusion near the fusion line is also reported in the powder-bed fusion type AM process [51,52]. Moreover, researches about the diffusion from the substrate to the coating or thin film during the formation were also been reported [53–55]. In this study, the two sides of the fusion line consisted of a mixture of Ti, Ni, and pure Ti. Immediately after the melt pool formation, Ti tended to diffuse from the substrate to the melt pool owing to the difference in Ti concentration. This led to an increase in the Ti concentration near the fusion line in the melt track. As a result, the approximately 10 μm-thick layers of $NiTi_2$ are formed along the fusion line under the low *P* irradiation conditions. This process may also occur in the melt track under higher P conditions. However, the inner parts of these melt tracks also consist of the $NiTi_2$ phase, meaning the $NiTi_2$ layer cannot be distinguished from the inner part.

The formation of the $NiTi_2$ phase is observed also in the center of the melt track at *P* = 200 W condition, as shown in Fig. 3.10a. In the melting and solidification process induced by the EB irradiation, the melted liquid solidifies under a rapid cooling rate of 10^5–10^7 K/s, which prevents the system from reaching thermodynamic equilibrium [56]. In particular, the rapid cooling rate can suppress diffusion and segregation relaxation processes, leading to a frozen-in distribution of components [57–59]. Fig. 3.12 illustrates the composition transition during the solidification process in the Ni-Ti binary system, with a Ni content of 44.3 at.% which is the same as that in melt track of

P = 200 W. As the temperature of the melt pool decreased, the NiTi phase with a higher solidus temperature solidified from the liquid phase first, while the composition in the liquid phase transits along the liquid phase line toward the Ti-rich direction. Meanwhile, when the temperature decreased to the melting point of the $NiTi_2$ phase, the percentage of Ni concentration in the liquid phase also decreased to 33.3 at.%, and only then does the $NiTi_2$ phase start to precipitate from the liquid phase. In the cross-section of the melt track, the solidification process started from the fusion line, and the solid-liquid interface then advanced toward the central part. During this process, owing to the high solidification rate of EB melting, the firstly precipitated NiTi grains grew rapidly and occupied the surrounding area, while the remaining Ti-rich solution was pushed to the central part and finally solidified in the $NiTi_2$ phase. This indicates that a Ni-rich composition in the melt pool can prevent segregation of the $NiTi_2$ phase in the centre of the melt track. This also explains the difference in microstructure at the centre of the melt track for P = 100 W and 200 W in Fig. 3.9a and 3.9b.

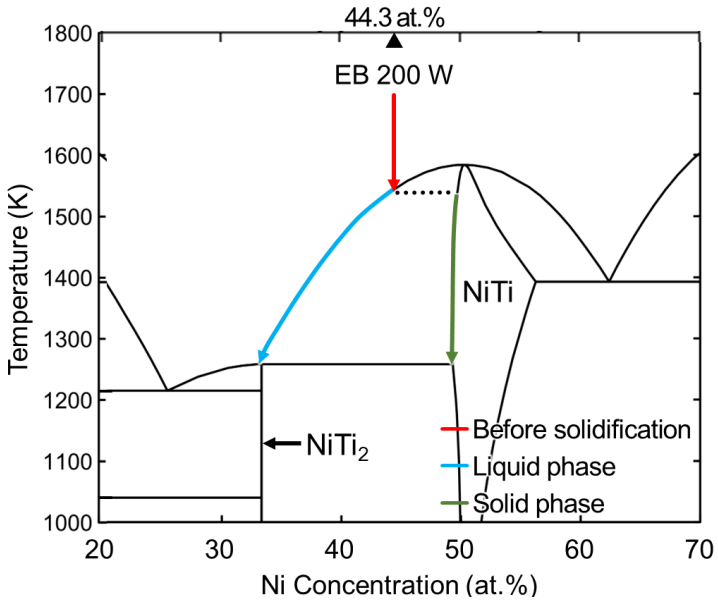

Fig. 3.12. Magnification of Ni-Ti binary equilibrium phase diagram and the schematic of the transition during the solidification process under P = 200 W condition.

3.4.2 Strategy for fabrication of NiTi coating

In this study the author demonstrates that the successful formation of the melt track with the almost stoichiometric composition of NiTi can be achieved by subjecting the Ni-plating layer on the Ti substrate to the EB scanning with the optimal EB irradiation conditions, resulting in melting and subsequent mixing of Ni and Ti. However, it should be noted that the local compositions of the melt tracks are inhomogeneous and the inhomogeneity in the composition must be eliminated for fabricating NiTi coating with shape memory effects or superelasticity.

The mixing of pure Ni and Ti is supposed to be caused by the diffusion and thermal convection in melting pool. In addition, the Marangoni effect also largely affects the melting and solidification behavior induced by the EB irradiation, in which temperature gradient at the surface of melt pool is up to 10^8 K/m [34]. The Marangoni convection occurs at the surface, originating from the center of the melt track and extending outward. The flow velocity of the convection is high up to 300 mm/s as revealed by experimentally validified computational thermal-fluid dynamics simulations[34], and the convection is suggested to accelerate the mixing of the melted pure Ni and Ti. However, the presence of inhomogeneity in the alloy composition is observed in this study although the high-velocity flow was supposed to occur in the melting and solidification processes by the EB irradiation. The exceptionally short time span of the rapid melting process in the single-track irradiation is suggested to be not enough to mix the pure Ni and Ti completely, and repeating melting and solidification of the same region is supposed to remove the inhomogeneity in the local compositions. Therefore, it is proposed that a more uniform NiTi layer can be achieved through multi-track melting under appropriate conditions.

3.5 Conclusions

Ni-plated CP-Ti substrates were irradiated with the EB in six sets of parameters to investigate the effect of parameters on the morphology, composition and elemental distribution of the melt tracks. We observed the surface and cross-section of the melt track after irradiation and analyzed the variation in composition. The melt solidification behavior of the melt tracks was also discussed to reveal the mechanism of the formation of the microstructure. The key findings and conclusions are summarized below.

- EB scanning of CP-Ti substrates plated with Ni yields a dense and porosity-free microstructure within the formed melt track, exhibiting superior uniformity when compared to thermal spray coatings.
- Under optimal EB scanning conditions, the melt track attains an elemental composition close to Ni-50 at.%Ti, which represents the stoichiometric composition of the NiTi phase. In this study, the optimal condition is a Ni plating thickness of 45 μm, EB scanning speed of 100 mm/s, and EB power of 100 W.
- There is a good homogeneity of the elemental composition in the melt track under optimal scanning experimental conditions. This can be attributed to the intense local heating caused by EB irradiation, resulting in a significant temperature gradient at the free surface. Consequently, the enhanced Marangoni convection vigorously stirs the liquid within the melt pool.
- EB Multi-Track Scanning emerges as a highly efficient technique for fabricating NiTi Self-Healing Shape Memory Coatings through the fusion of Ni-plate onto CP-Ti. This method holds the potential in achieving the desired outcome.

Reference

[1] F.A. Shah, M. Trobos, P. Thomsen, A. Palmquist, Commercially pure titanium (cp-

Ti) versus titanium alloy (Ti6Al4V) materials as bone anchored implants — Is one truly better than the other?, Mater. Sci. Eng. C 62 (2016) 960–966. https://doi.org/10.1016/j.msec.2016.01.032.

[2] R.R. Boyer, An overview on the use of titanium in the aerospace industry, Mater. Sci. Eng. -Struct. Mater. Prop. Microstruct. Process. 213 (1996) 103–114. https://doi.org/10.1016/0921-5093(96)10233-1.

[3] J.R.P. Jorge, V.A. Barão, J.A. Delben, L.P. Faverani, T.P. Queiroz, W.G. Assunção, Titanium in dentistry: Historical development, state of the art and future perspectives, J. Indian Prosthodont. Soc. 13 (2013) 71–77. https://doi.org/10.1007/s13191-012-0190-1.

[4] I.V. Gorynin, Titanium alloys for marine application, Mater. Sci. Eng. -Struct. Mater. Prop. Microstruct. Process. 263 (1999) 112–116. https://doi.org/10.1016/S0921-5093(98)01180-0.

[5] A. Kumar, M.K. Mahto, V.S. Rana, M. Vashista, M.Z.K. Yusufzai, Investigation of microstructure evolution and mechanical properties of gas tungsten arc welded dissimilar titanium (CP-Ti/Ti–6Al–4V) alloys, Proc. Inst. Mech. Eng. Part E J. Process Mech. Eng. (2022) 09544089221126431. https://doi.org/10.1177/09544089221126431.

[6] G. Welsch, R. Boyer, E.W. Collings, Materials Properties Handbook: Titanium Alloys, ASM International, 1993.

[7] Y. Qin, L. Geng, D. Ni, Dry sliding wear behavior of extruded titanium matrix composite reinforced by in situ TiB whisker and TiC particle, J. Mater. Sci. 46 (2011) 4980–4985. https://doi.org/10.1007/s10853-011-5415-x.

[8] H. Attar, K.G. Prashanth, A.K. Chaubey, M. Calin, L.C. Zhang, S. Scudino, J. Eckert, Comparison of wear properties of commercially pure titanium prepared by

selective laser melting and casting processes, Mater. Lett. 142 (2015) 38–41. https://doi.org/10.1016/j.matlet.2014.11.156.

[9] J. Mohd Jani, M. Leary, A. Subic, M.A. Gibson, A review of shape memory alloy research, applications and opportunities, Mater. Des. 1980-2015 56 (2014) 1078–1113. https://doi.org/10.1016/j.matdes.2013.11.084.

[10] D. Stoeckel, Shape memory actuators for automotive applications, Mater. Des. 11 (1990) 302–307. https://doi.org/10.1016/0261-3069(90)90013-A.

[11] D.J. Hartl, D.C. Lagoudas, Aerospace applications of shape memory alloys, Proc. Inst. Mech. Eng. Part G J. Aerosp. Eng. 221 (2007) 535–552. https://doi.org/10.1243/09544100JAERO211.

[12] L. McDonald Schetky, Shape memory alloy applications in space systems, Mater. Des. 12 (1991) 29–32. https://doi.org/10.1016/0261-3069(91)90089-M.

[13] O.N. Schipper, J.K. Ellington, Nitinol Compression Staples in Foot and Ankle Surgery, Orthop. Clin. North Am. 50 (2019) 391–399. https://doi.org/10.1016/j.ocl.2019.02.003.

[14] W.A. Brantley, Evolution, clinical applications, and prospects of nickel-titanium alloys for orthodontic purposes, J. World Fed. Orthod. 9 (2020) S19–S26. https://doi.org/10.1016/j.ejwf.2020.08.005.

[15] D.Y. Li, A new type of wear-resistant material: pseudo-elastic TiNi alloy, Wear 221 (1998) 116–123. https://doi.org/10.1016/S0043-1648(98)00269-5.

[16] J. Jin, H. Wang, WEAR RESISTANCE OF Ni-Ti ALLOY, Acta Metall. Sin. 24 (1988) 66–70.

[17] M. Bitzer, N. Rauhut, G. Mauer, M. Bram, R. Vaßen, H.-P. Buchkremer, D. Stöver, M. Pohl, Cavitation-resistant NiTi coatings produced by low-pressure plasma spraying (LPPS), Wear 328–329 (2015) 369–377.

https://doi.org/10.1016/j.wear.2015.03.003.

[18] A.P. Jardine, Y. Field, H. Herman, Shape memory effect in vacuum plasma sprayed NiTi, J. Mater. Sci. Lett. 10 (1991) 943–945. https://doi.org/10.1007/BF00722140.

[19] M. Bram, A. Ahmad-Khanlou, H.P. Buchkremer, D. Stöver, Vacuum plasma spraying of NiTi protection layers, Mater. Lett. 57 (2002) 647–651. https://doi.org/10.1016/S0167-577X(02)00847-9.

[20] B. Swain, S. Mantry, S.S. Mohapatra, S.C. Mishra, A. Behera, Investigation of tribological behavior of plasma sprayed NiTi coating for aerospace application, J. Therm. Spray Technol. 31 (2022) 2342–2369. https://doi.org/10.1007/s11666-022-01452-7.

[21] N. Cinca, A. Isalgué, J. Fernández, J.M. Guilemany, Structure characterization and wear performance of NiTi thermal sprayed coatings, Smart Mater. Struct. 19 (2010) 085011. https://doi.org/10.1088/0964-1726/19/8/085011.

[22] S. Tria, O. Elkedim, W.Y. Li, H. Liao, Ball milled Ni–Ti powder deposited by cold spraying, J. Alloys Compd. 483 (2009) 334–336. https://doi.org/10.1016/j.jallcom.2008.08.092.

[23] S. Tria, O. Elkedim, R. Hamzaoui, X. Guo, F. Bernard, N. Millot, O. Rapaud, Deposition and characterization of cold sprayed nanocrystalline NiTi, Powder Technol. 210 (2011) 181–188. https://doi.org/10.1016/j.powtec.2011.02.026.

[24] G. Mauer, K.-H. Rauwald, Y.J. Sohn, T.E. Weirich, Cold gas spraying of nickel-titanium coatings for protection against cavitation, J. Therm. Spray Technol. 30 (2021) 131–144. https://doi.org/10.1007/s11666-020-01139-x.

[25] K.K. Ho, G.P. Carman, Sputter deposition of NiTi thin film shape memory alloy using a heated target, Thin Solid Films 370 (2000) 18–29. https://doi.org/10.1016/S0040-6090(00)00947-0.

[26] T.M. Adams, S.R. Kirkpatrick, Z. Wang, A. Siahmakoun, NiTi shape memory alloy thin films deposited by co-evaporation, Mater. Lett. 59 (2005) 1161–1164. https://doi.org/10.1016/j.matlet.2004.12.019.

[27] H. Cicek, I. Efeoglu, Y. Totik, K.V. Ezirmik, E. Arslan, A low temperature in-situ crystalline TiNi shape memory thin film deposited by magnetron sputtering, Surf. Coat. Technol. 284 (2015) 90–93. https://doi.org/10.1016/j.surfcoat.2015.08.068.

[28] Y. Fu, H. Du, S. Zhang, Adhesion and interfacial structure of magnetron sputtered TiNi films on Si/SiO2 substrate, Thin Solid Films 444 (2003) 85–90. https://doi.org/10.1016/S0040-6090(03)01029-0.

[29] E. Quandt, C. Halene, H. Holleck, K. Feit, M. Kohl, P. Schloβmacher, A. Skokan, K.D. Skrobanck, Sputter deposition of TiNi, TiNiPd and TiPd films displaying the two-way shape-memory effect, Sens. Actuators Phys. 53 (1996) 434–439. https://doi.org/10.1016/0924-4247(96)01147-8.

[30] S. Miyazaki, K. Nomura, Development of perfect shape memory effect in sputter-deposited Ti-Ni thin films, Proc. IEEE Micro Electro Mech. Syst. (1994) 176–181.

[31] N. Cameron, Z. Farhat, Investigation into the wear and dent resistance of Ni/Ti nanolaminates and superelastic NiTi coating, J. Mater. Eng. Perform. 28 (2019) 6033–6041. https://doi.org/10.1007/s11665-019-04377-5.

[32] Denki Kagaku Kai (Ed.), Denki kagaku benran [Electrochemical Handbook], 6th ed., Maruzen Publishing, Tōkyō, 2013.

[33] Thermo-Calc Software, Titanium and TiAl-based Alloys Databases, Version 4(TCTI4), (2022). https://thermocalc.com/products/databases/ (accessed October 1, 2023).

[34] Y. Miyata, M. Okugawa, Y. Koizumi, T. Nakano, Inverse Columnar-Equiaxed Transition (CET) in 304 and 316L Stainless Steels Melt by Electron Beam for

Additive Manufacturing (AM), Crystals 11 (2021) 856. https://doi.org/10.3390/cryst11080856.

[35] N. Zech, D. Landolt, The influence of boric acid and sulfate ions on the hydrogen formation in Ni□Fe plating electrolytes, Electrochimica Acta 45 (2000) 3461–3471. https://doi.org/10.1016/S0013-4686(00)00415-1.

[36] H. Hoffmann, M.C. Paulisch-Rinke, M. Gernhard, Y. Jännsch, J. Timm, C. Brandmeir, S. Lechner, R. Marschall, R. Moos, I. Manke, C. Roth, Multi-scale morphology characterization of hierarchically porous silver foam electrodes for electrochemical CO2 reduction, Commun. Chem. 6 (2023) 1–14. https://doi.org/10.1038/s42004-023-00847-z.

[37] X. Fan, Y. Wang, B. Zou, L. Gu, W. Huang, X. Cao, Preparation and corrosion resistance of MAO/Ni–P composite coat on Mg alloy, Appl. Surf. Sci. 277 (2013) 272–280. https://doi.org/10.1016/j.apsusc.2013.04.044.

[38] M. Yang, Y. Liu, A.M. Nolan, Y. Mo, Interfacial Atomistic Mechanisms of Lithium Metal Stripping and Plating in Solid-State Batteries, Adv. Mater. 33 (2021) 2008081. https://doi.org/10.1002/adma.202008081.

[39] Titanium & titanium aluminide based alloys, Thermo-Calc Softw. (n.d.). https://thermocalc.com/products/databases/titanium-and-titanium-aluminide-based-alloys/ (accessed June 19, 2023).

[40] A. Takase, T. Ishimoto, R. Suganuma, T. Nakano, Surface residual stress and phase stability in unstable β-type Ti–15Mo–5Zr–3Al alloy manufactured by laser and electron beam powder bed fusion technologies, Addit. Manuf. 47 (2021) 102257. https://doi.org/10.1016/j.addma.2021.102257.

[41] C. Li, Z.Y. Liu, X.Y. Fang, Y.B. Guo, Residual Stress in Metal Additive Manufacturing, Procedia CIRP 71 (2018) 348–353.

https://doi.org/10.1016/j.procir.2018.05.039.

[42] S. Tang, Y. Li, Y. Gao, Q. Zheng, Z. Liu, X. Ren, First-Principles Investigations of the Structural, Anisotropic Mechanical, Thermodynamic and Electronic Properties of the AlNi2Ti Compound, Crystals 8 (2018) 93. https://doi.org/10.3390/cryst8020093.

[43] C.M. Jackson, H.J. Wagner, R.J. Wasilewski, The alloy with a memory, 55-Nitinol: Its physical metallurgy, properties, and applications, (1972). https://ntrs.nasa.gov/citations/19720022818 (accessed January 8, 2026).

[44] B. Terry, A. Shelton, A. Strauss, Microstructure and mechanical properties of dissimilar friction stir welding between butted, thin sheet NiTi and Ti-6Al-4V, Weld. World (2025). https://doi.org/10.1007/s40194-025-02162-8.

[45]K. Otsuka, X. Ren, Physical metallurgy of Ti–Ni-based shape memory alloys, Prog. Mater. Sci. 50 (2005) 511–678. https://doi.org/10.1016/j.pmatsci.2004.10.001.

[46] X. Huang, J. Nohava, B. Zhang, A.G. Ramirez, Nanoindentation of NiTi shape memory thin films at elevated temperatures, Int. J. Smart Nano Mater. 2 (2011) 39–49. https://doi.org/10.1080/19475411.2011.558179.

[47] Y. Tian, Z. Liang, Y. Cai, H. Jiang, M. Chen, J. Han, Microstructure and mechanical properties of Ti2Ni alloy fabricated by direct energy deposition, Sci. Technol. Weld. Join. 29 (2024) 47–51. https://doi.org/10.1177/13621718231216674.

[48] N. Kang, P. Coddet, L. Dembinski, H. Liao, C. Coddet, Microstructure and strength analysis of eutectic Al-Si alloy in-situ manufactured using selective laser melting from elemental powder mixture, J. Alloys Compd. 691 (2017) 316–322. https://doi.org/10.1016/j.jallcom.2016.08.249.

[49] Md.R.. . U. Ahsan, M. Cheepu, R. Ashiri, T.-H. Kim, C. Jeong, Y.-D. Park,

Mechanisms of weld pool flow and slag formation location in cold metal transfer (CMT) gas metal arc welding (GMAW), Weld. World 61 (2017) 1275–1285. https://doi.org/10.1007/s40194-017-0489-y.

[50] N. Jiang, L. Zhang, W. Long, S. Zhong, L. Zhang, Influence of doping Ti particles on intermetallic compounds growth at Sn58Bi/Cu interface during solid–liquid diffusion, J. Mater. Sci. Mater. Electron. 32 (2021) 3341–3351. https://doi.org/10.1007/s10854-020-05082-z.

[51] M. Okugawa, Y. Ohigashi, Y. Furishiro, Y. Koizumi, T. Nakano, Equiaxed grain formation by intrinsic heterogeneous nucleation via rapid heating and cooling in additive manufacturing of aluminum-silicon hypoeutectic alloy, J. Alloys Compd. 919 (2022) 165812. https://doi.org/10.1016/j.jallcom.2022.165812.

[52] M. Okugawa, Y. Furushiro, Y. Koizumi, Effect of Rapid Heating and Cooling Conditions on Microstructure Formation in Powder Bed Fusion of Al-Si Hypoeutectic Alloy: A Phase-Field Study, Materials 15 (2022) 6092. https://doi.org/10.3390/ma15176092.

[53] K. Rubacha, E. Godlewska, K. Zawadzka, J. Dąbrowa, Formation of silicide layers on a Ti-46Al-8Ta alloy in pack cementation and diffusion couple experiments, Surf. Coat. Technol. 429 (2022) 127860. https://doi.org/10.1016/j.surfcoat.2021.127860.

[54] K. Wang, B. Zhu, Z. Wang, Y. Liu, L. Wang, Y. Zhang, S. Li, Successive phase and morphology evolution of galvannealed coating in hot stamping and diffusion modeling of α-Fe(Zn)/steel system considering the effect of Zn concentration, Surf. Coat. Technol. 380 (2019) 125036. https://doi.org/10.1016/j.surfcoat.2019.125036.

[55] C. Pan, C. Fang, J. Shi, K. Ma, H. Yang, P. He, Synthesis and properties of Ti-Al

coating by high-frequency induction heated combustion, J. Alloys Compd. 939 (2023) 168739. https://doi.org/10.1016/j.jallcom.2023.168739.

[56] Y. Koizumi, M. Okugawa, Digital Twin Science of Metal Powder Bed Fusion Additive Manufacturing: A Selective Review of Simulations for Integrated Computational Materials Engineering and Science, ISIJ International 62 (2022) 2183–2196. https://doi.org/10.2355/isijinternational.isijint-2022-184.

[57] K. Sato, S. Takagi, S. Ichikawa, T. Ishimoto, T. Nakano, Microstructure and Solute Segregation around the Melt-Pool Boundary of Orientation-Controlled 316L Austenitic Stainless Steel Produced by Laser Powder Bed Fusion, Materials 16 (2023) 218. https://doi.org/10.3390/ma16010218.

[58] M. Okugawa, D. Izumikawa, Y. Koizumi, Simulations of Non-Equilibrium and Equilibrium Segregation in Nickel-Based Superalloy Using Modified Scheil-Gulliver and Phase-Field Methods, Mater. Trans. 61 (2020) 2072–2078. https://doi.org/10.2320/matertrans.MT-MA2020005.

[59] Y. Liu, K. Nose, M. Okugawa, Y. Koizumi, T. Nakano, Fabrication and Process Monitoring of 316L Stainless Steel by Laser Powder Bed Fusion with μ-Helix Scanning Strategy and Narrow Scanning Line Intervals, Mater. Trans. 64 (2023) 1135–1142. https://doi.org/10.2320/matertrans.MT-ME2022006.

Chapter 4

Formation of NiTi Coatings on Ti via Multi-Track Electron Beam Scanning for Enhanced Wear Resistance

4.1 Introduction

Single-track experiments were performed to examine the feasibility of this method for forming NiTi coatings in Chapter 2. A NiTi layer with a nearly stoichiometric composition was successfully obtained by optimizing the EB irradiation conditions. However, a single-track NiTi layer cannot be directly used as a practical coating. Only by arranging multiple tracks in parallel and close to each other to completely cover the material surface can NiTi coatings with practical applications be produced [1]. Moreover, the multi-track scanning process is not simply a repetition of single-track scanning; the interactions between neighboring tracks must be considered. Therefore, the EB irradiation conditions used in single-track scanning cannot be directly applied to the multi-track scanning process, which requires dedicated study and optimization. This then becomes the main objective of this chapter.

In Chapter 3, NiTi coatings were fabricated by multi-track EB scanning of Ni-plated CP-Ti substrates under various EB irradiation conditions. The relationship between the process conditions and the quality of coatings, including compositional homogeneity, constituent phases, and mechanical properties, was investigated from the perspective of melting, mixing, solidification, and solid-state diffusion.

4.2 Methods

4.2.1 Preparation of substrate and Ni-plate

A slab of CP-Ti (99.5% purity; Nilaco, Tokyo, Japan) was cut into specimens of 25 × 25 × 10 mm^3 by electric discharge machining. A CP-Ti specimen of 25 × 25 mm^2 area was used as the working electrode. The CP-Ti specimen was given a four-stage pretreatment: (1) mechanical grinding using P120–P2400-grit SiC abrasive papers; (2) immersion in ethanol at RT for 5 min; (3) immersion 10 wt.% HCl solution at RT for 5 min, with a 9 V DC power applied to promote the removal of surface oxides and contaminants and (4) washing with ultrapure water.

A pure Ni anode (ϕ6 × 20 mm) of 405 mm^2 area was used with an interelectrode gap of 8 cm. In this study, a thicker pure Ni layer was required to enable subsequent processing. Therefore, a nickel sulfamate solution was used as the plating bath. This type of bath tolerates high current density and produces plated layers with lower internal stress, making it suitable for applications that demand greater coating thickness [2]. The compositions of the solutions and the electroplating parameters that adopted from a electrochemical handbook [2] are listed in Table 4.1. Electroplating was conducted for 4 h to obtain a plating layer with sufficient thickness. After plating, the layer was ground using P120–P2000 grit SiC abrasive papers to a final thickness of 45 μm.

Table 4.1. Composition of Ni-plating solution and plating parameters.

	Compound/Parameter	**Value**
Composition	$NiCl_2 \cdot 6H_2O$	0.10–0.13 mol/L
	$Ni(SO_3NH_2)_2$	1.70–1.79 mol/L
	H_3BO_3	0.49–0.73 mol/L
Parameters	Temperature	50–60 °C
	pH	3.0–5.0
	Cathodic current density	3.0 A/dm^2
	Current mode	DC plating

4.2.2 Electron beam irradiation

The plated specimens were irradiated with EB using an EBM machine (EBM-6LB-1, Mitsubishi Electric) in a helium atmosphere at 0.5 Pa. Multi-track scanning was performed over a 3 × 4 mm^2 area using a serpentine scanning process (Fig. 4.1). The electron beam power (P) was set at four levels of 126, 132, 138, and 144 W, representing the electron beam current of 2.1, 2.2, 2.3 and 2.4 mA in the EBM machine. The line offset (l_{off}) and scanning speed (V) were fixed at 300 μm and 100 mm/s, respectively. The multi-track scanning experiments were conducted using two scanning modes—continuous scanning and intermittent scanning—to regulate the thermal effect induced by the preceding scanning. Continuous scanning mode had no intervals between consecutive track scans (t_{int} = 0 s), whereas intermittent scanning mode included a 60-s interval between scans (t_{int} = 60 s). In the intermittent scanning mode, the specimens were cooled before the subsequent beam scan. Although the interval of 60 s might be too long for an actual process, it was employed to perform experiments under near-ideal conditions with sufficient cooling time.

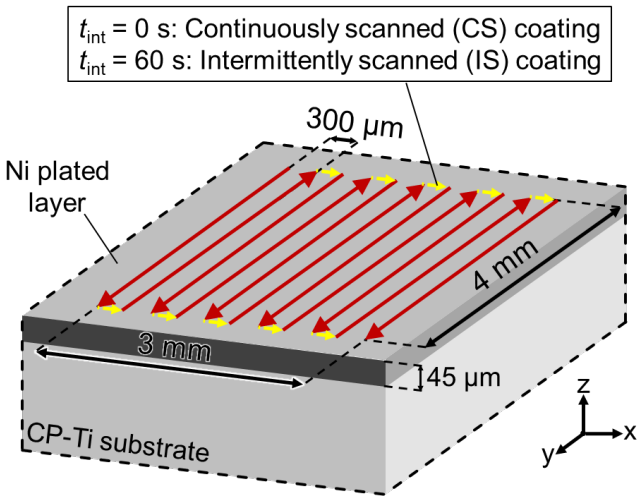

Fig. 4.1. Schematic of a Ni-plated CP-Ti substrate subjected to EB scanning.

4.2.3 Microstructural characterization

The top surfaces of the multi-scanned specimens were observed using a confocal laser scanning microscope (VK-X200/210, Keyence, Japan). The samples were then cut perpendicular to the beam-scanning direction for cross-sectional observation by field-emission scanning electron microscopy (FE-SEM; JSM 6500, JEOL, Japan). The elemental distributions were analyzed by energy-dispersive X-ray spectroscopy (EDS). X-ray diffractometry (XRD; SmartLab SE diffractometer, Rigaku, Japan) identified the crystallographic phases of the coatings. In the XRD tests, the ray source was Cu Kα and the 2theta scanning range was 20°–80° with a step size of 0.01°. The test for each sample was conducted by 3 times in the same condition. The formed Ni-Ti intermetallic phases were studied by evaluating the equilibrium phase characteristics of the Ni-Ti binary alloy using Thermo-Calc Software (version 2022b) with a thermodynamic database for Ti alloys (TCTI4) [3].

4.2.4 Nanoindentation tests

Nanoindentation tests were performed using a nanoindentation tester (ENT-1100a, Elionix, Japan) equipped with a Berkovich indenter to evaluate the indentation

properties of the EB-scanned coating. Before the tests, the surfaces of specimens were ground using P120–P4000-grit SiC abrasive papers and then polished using 50 nm alkaline colloidal silica suspension. The Nanoindentation tests were performed at 26 °C inside the device equipped with a shield case to prevent thermal drift. A total of 50 equally spaced points were selected on each sample to repeat the test under identical parameters. Then, the results were averaged to eliminate the effect of randomness. The peak load was 50 mN, and the loading rate was 5 mN/s. The Berkovich indenter[4] with an apex angle of 65.03° was used, and the following relationship between the indenter contact area (A) and indentation depth (h) was employed:

$$A = 3\sqrt{3}\tan^2(65.03°)\cdot(h+\Delta h)^2\,. \tag{4.1}$$

Here, Δh is the indenter tip correction value calculated using the Sawa–Tanaka method [5] based on the indentation results of a standard fused silica sample. From the obtained results, Young's modulus (E) and hardness (H) were calculated according to the ISO 14577-1 protocol [6]. Moreover, depth recovery ratio ($\eta_{d,h}$) is defined as the ratio of recoverable indentation depth to indenter displacement at maximum load[7]. It was calculated as follows:

$$\eta_{d,h} = \frac{h_{\max} - h_{\mathrm{p}}}{h_{\max}}, \tag{4.2}$$

where $h_{\max}$ and h_{p} are the maximum penetration depth of the indenter during the indentation tests and the permanent depth after load removal, respectively.

4.2.5 Sliding wear tests

Sliding wear tests were conducted according to the ASTM G133-22 standard [8] on an oscillation sliding tester (OST3000, Rhesca, Japan) to evaluate the wear resistance of the intermittently scanned (IS) coating. Before the tests, the surfaces of specimens were ground using P120–P4000-grit SiC abrasive papers and then polished using 50

nm alkaline colloidal silica suspension. The tests were conducted under a constant load (L) of 50 N using an alumina ceramic indenter. The diameter of the indenter is 9.5 mm and the hardness is 2085 $HV_{0.1}$ [9]. The specimens were subjected to a 1 Hz oscillation with an 8 mm amplitude. The test duration for each specimen was 625 s, resulting in a total sliding distance (D) of 10 m (= 8 mm × 2 × 625 s). The temperature inside the tester during the test was maintained at 26 °C and the relative humidity was maintained at 50%. The same wear test was conducted 2 times on each specimen. The friction coefficient (μ) was evaluated as follows:

$$\mu = \frac{F_Z}{F_T}, \tag{4.3}$$

where F_Z and F_T are normal and tangential loads, respectively. Both were measured and continuously recorded by the integrated sensor during the tests.

Specific wear rate (W_s) is an indicator of the wear resistance of a material[10]. The W_s of specimens was evaluated as follows:

$$W_s = \frac{V}{LD}, \tag{4.4}$$

where V, L, and D are volume loss, applied load, and sliding distance, respectively. V was measured by the confocal laser scanning microscope after the sliding test. The worn surfaces were also observed using SEM and EDS. A commercially available superelastic Nitinol (Ni 50.6 at. %, Ti 49.4 at. %; Seemine Keli, Lanzhou, China) as well as the substrate, CP-Ti, were also tested as control specimens.

4.3 Results and discussion

4.3.1 Surface morphology and roughness

Fig. 4.2 shows surface morphology optical images and height maps obtained from the coatings formed by multi-track EB scanning under various conditions. The scanning

direction of each track is parallel to the *y*-axis while the tracks fill the area along the x-axis in the positive direction.

In Figs. 4.2a–d, all height maps of continuous scanned (CS) coatings (t_{int} = 0 s) show sunken regions at the center of each coating. Protruding regions appeared at the right side of the CS-coatings at P = 132 W and 144 W (Figs. 2b2 and d2). These protrusions can be attributed to the rapid heating of the substrate caused by the continuous scanning of the EB. The thermal stress generated by the large temperature gradient caused warping deformation of the Ni layer near the melt track and debonding with the substrate. Then, the liquid metal in the melt pool flows into the crevices under the debonded Ni-plating layer, forming a protruding surface after solidification. In Figs. 4.2e–h, the height maps of the intermittently scanned (IS) coatings (t_{int} = 60 s) show remarkably flat surfaces, without significant protrusion and sinkage. Notably, corrugated patterns are observed on the surfaces of the IS-coating (Figs. 4.2f2 and h2), whose patterns are similar to those of the single-track melt formed by EB irradiation in Chapter 3. Cracks were generated perpendicular to the melt tracks on most CS-coatings (white triangles in Figs. 4.2a–d), while cracks did not appear on the IS-coatings. These cracks are presumably generated by residual stresses induced by the EB irradiation, as suggested by Li et al. [11] and Takase et al. [12], who reported that residual stresses up to hundreds of MPa could be generated in Ti alloys by EB-irradiation-induced melting and solidification in AM.

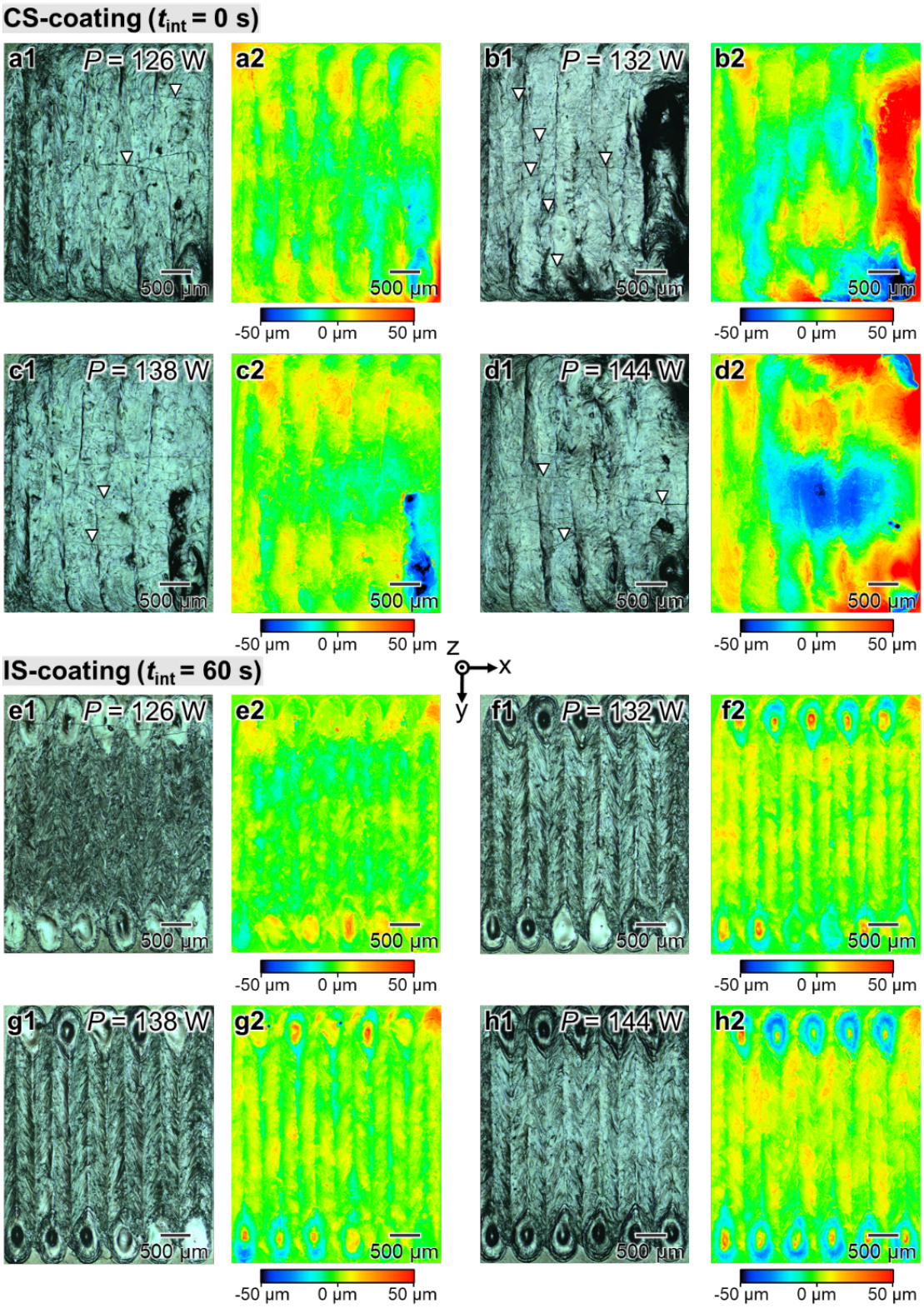

Fig. 4.3. Optical images and height maps of coatings fabricated by multi-track EB scanning under various conditions with: time intervals (t_{int}) of 0 s (a, b, c, d) and 60 s (e, f, g, h); EB power (P) of 126 W (a, e), 132 W (b, f), 138 W (c, g), and 144 W (d, h); scanning speed of 100 mm/s. The white triangles show the location of the cracks. "CS-coating" and "IS-coating" refer to continuously and intermittently scanned coatings, respectively.

Fig. 4.3 shows the variation in the surface roughness of the coatings with P. The CS-coatings have significantly rougher surfaces and have more significance fluctuation in roughness than those of the IS-coatings. Among the experimental conditions, the IS-coating at P = 126 W has the lowest surface roughness (R_a = 3.36 μm), i.e., the smoothest surface.

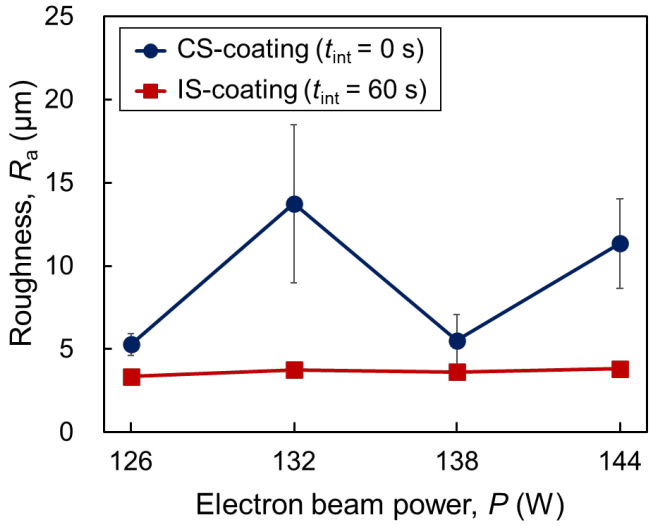

Fig. 4.3. Surface roughness (R_a) of EB-scanned coating fabricated under various scanning conditions as a function of EB power (P) with a constant scanning speed of 100 mm/s.

The significant difference in surface topography and roughness between CS- and IS-coatings originates from the distinct melting and solidification processes in continuous and intermittent scanning modes. In continuous scanning (CS) mode, the electron beam scans adjacent tracks sequentially in a serpentine pattern. Track #n+1 begins immediately after track #n, causing the melt pools to merge into a larger liquid zone. This larger melt pool leads to stronger liquid flow and steeper temperature gradients, resulting in pronounced macroscopic bumps and depressions after solidification. Consequently, CS-coated surfaces exhibit frequent surface undulations and high, fluctuating roughness values as electron beam power changes. In contrast, intermittent

scanning (IS) mode introduces sufficient cooling time after each track, allowing the material to return nearly to room temperature and minimizing heat transfer to subsequent tracks. The melt pool remains localized within the current scanning area, leading to weaker fluid flow, smaller temperature gradients, and more uniform surface solidification. As a result, IS coatings are flatter, with consistently low roughness across different electron beam powers.

4.3.2 Cross-sectional morphology and elemental distribution

Fig. 4.4 shows the cross-sectional backscattered electron (BSE) images (Figs. 4.4a1, 4.4a2, 4.4b1, and 4.4b2) and the corresponding elemental distributions analyzed by SEM-EDS (Figs. 4.4a3 and 4.4b3) of EB-scanned coatings with processed data (Figs. 4.4c, 4.4d and 4.4e) from BSE images and EDS mapping images. The BSE images show regions with dark and bright contrasts. The dark regions at the bottom correspond to the CP-Ti substrate. The bright areas at the center of the images represent the coatings formed by multi-track scanning. The scanning sequence is from left to right. Unmelted Ni plates can be seen at the left edges where the surface was not irradiated with EB. Ni and Ti are mixed in the coatings formed by EB irradiation under both conditions presumably due to convection and diffusion in the liquid metals. Marangoni convection is considered to have played a crucial role in the mixing of pure Ni and Ti as indicated by the marble pattern. The Marangoni effect can significantly influence melting and solidification during EB irradiation because of the steep temperature gradient along the melt pool surface, which can be as high as 10^7 K/m. This gradient arises from localized heating by the EB, which has a diameter of approximately 100 μm [13].

The influence of process parameters on the cross-sectional morphology of the melt region and coating composition was then analyzed. For this, the Ti-melt depth (d_{Ti}) and

Ni concentration (C_{Ni}) were quantified for each melt track. d_{Ti} represents the melt penetration depth into the CP-Ti substrate, defined as the vertical distance between the Ni-plate/Ti-substrate interface and the melt-track bottom (Figs. 4.4a2 and 4.4b2). C_{Ni} values were determined using EDS analysis of the melt-track regions in the elemental mapping images (Figs. 4.4a3 and 4.4b3).

Figs. 4.4c and 4.4d summarize the d_{Ti} and C_{Ni} data of the EB-scanned coatings under all scanning conditions. Fig. 4.4c shows the variation in d_{Ti} while Fig. 4.4d shows the variation in C_{Ni} with track number. Regardless of P, the d_{Ti} of continuously scanned (CS) coatings increases significantly with the number of melt tracks, showing an average rise of 60 μm from Track #1 to #11. As observed in laser powder bed fusion processes, continuous scanning is expected to cause heat accumulation [14]. A similar effect likely occurred in this study, leading to the increase in d_{Ti}. The growth in d_{Ti} is rapid from Track #1 to #4; however, it gradually stabilizes after Track #4, although the overall trend remains upward. In contrast, the d_{Ti} of intermittently scanned (IS) coatings remains relatively stable, fluctuating only slightly within a range of approximately 15 μm from Track #1 to #11. The C_{Ni} of CS-coatings is negatively correlated to d_{Ti}, gradually decreasing from Track #1 to #11 by an average of 13 at.%. This trend is consistent with predictions based on mass conservation. Specifically, the Ni in the melt track originates from Ni plating, and as the thickness of the Ni plating is uniform, the amount of Ni in the melt track remains constant. Conversely, Ti in the melt track is supplied from the Ti substrate. As d_{Ti} increases, a larger amount of Ti enters the melt track, causing a relative decrease in C_{Ni}, as evidenced in the data. This indicates that the composition of the melt track changes as the scanning progresses during continuous scanning, leading to variations in the mechanical properties of the formed coating. Hence, the CS-coating becomes inhomogeneous among melt tracks, rendering

controlling its properties through adjustments to the scanning parameters challenging. Conversely, C_{Ni} of IS-coatings exhibits a minor decreasing trend from Track #1 to #3. From Track #4, C_{Ni} stabilizes and fluctuates within a range of approximately 1 at.%. The EB-induced temperature accumulation is considered to have decreased during the 60-s interval. This suggests that the melting and solidification behaviors in all tracks of IS-coatings are essentially the same as those in single-track scanning. Therefore, IS-coatings demonstrate a stable composition and structure across all tracks, facilitating more precise control over the coating composition and properties.

Fig. 4.4e summarizes the average values of d_{Ti} and C_{Ni} across all melt tracks of every EB-scanned coating, showing the variation in the structure and composition of coatings in general. C_{Ni} decreases monotonically with increasing d_{Ti} in both CS- and IS-coatings. Generally, d_{Ti} is higher in CS-coatings than in IS-coatings. Conversely, C_{Ni} is lower in CS-coatings than in IS-coatings, which is closer to the target value of 50 at.%, i.e., the stoichiometric composition of the NiTi phase. The C_{Ni} of the IS-coating scanned at P = 126 W is higher than 50 at.%, approximately 50 at.% at 132 W, and lower than 50 at.% at 138 and 144 W. Fig. 4.4f shows the equilibrium phase diagram of the Ni-Ti binary system. At temperatures around 1400 K, the NiTi monophase can be stable at 49.3–56.7 at.% Ni concentration. However, when the temperature is lowered to 400 K, the NiTi monophase can occur predominantly at Ni concentration equal to 50 at.%. This means that a slight deviation in Ni concentration from 50 at.% in NiTi alloys may lead to phase separation during the equilibrium solidification process. However, the melt pool undergoes non-equilibrium solidification due to the steep temperature gradient and rapid solidification rate during EB scanning process, reaching up to 10^7 K/m and 10 m/s, respectively [13]. Therefore, the rapid solidification process enables higher Ni or Ti concentrations in the NiTi phase compared to the equilibrium state, preventing phase

separation [15]. This indicates that IS-coatings contain a higher amount of the NiTi primary phase and a lower amount of secondary phases ($NiTi_2$ and Ni_3Ti) compared to cast Ni-Ti alloy with the same composition. In contrast, the C_{Ni} in CS-coatings is 8 at.% lower than 50 at.% or less, inevitably leading to the formation of a significant amount of $NiTi_2$ phase.

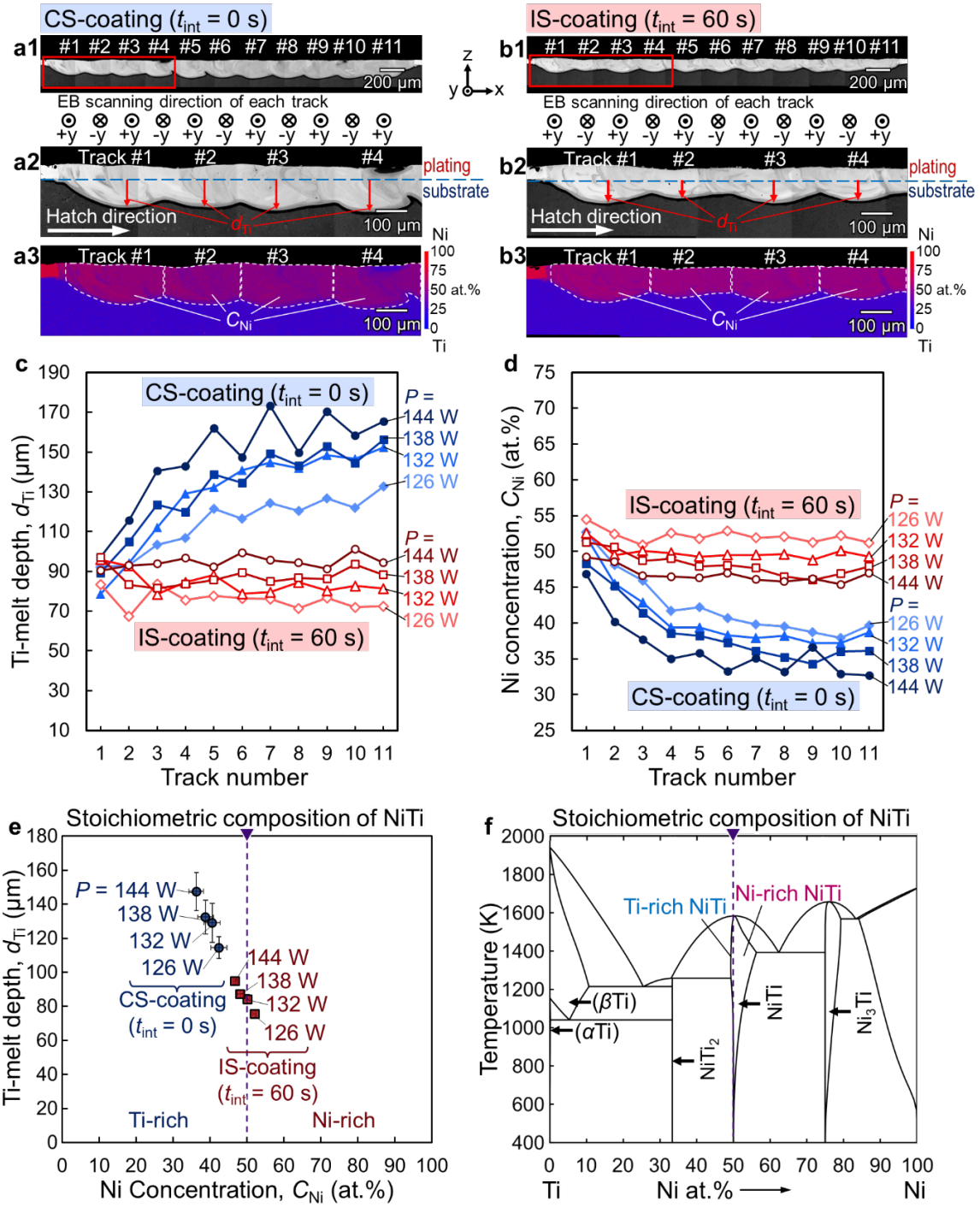

Fig. 4.4. Cross-sectional BSE images (a1, a2, b1, b2) and corresponding EDS mapping (a3, b3) of melt tracks in (a) continuously scanned (CS) coating: t_{int} = 0 s, P = 126 W; (b) intermittently scanned (IS) coating: t_{int} = 60 s, P = 126 W. The scanning speed of these coatings is fixed at 100 mm/s. (c) Variation in Ti-melt depth (d_{Ti}) with the track number in EB-scanned coatings. (d) Variation in the Ni concentration (C_{Ni}) with the track number in EB-scanned coatings. (e) Plot of d_{Ti} versus C_{Ni} in the EB-scanned coating with various scanning conditions. (f) Ni-Ti binary equilibrium phase diagram.

Fig. 4.5 shows the cross-sectional morphology (BSE images) and corresponding elemental composition distribution (EDS maps) from Track #6 to #7 of coatings fabricated by multi-track EB scanning under various conditions. In general, the brightness of BSE images is associated with the atomic mass of the elements present in the observed material. Specifically, higher atomic masses result in brighter images. In this study, a higher content of the element nickel (Ni) shows a higher brightness. The BSE images (Figs. 4.5a1, 4.5b1, 4.5c1, and 4.5d1) of the CS-coatings show noticeable variations in brightness across different regions. This suggests that the coatings experienced micrometer-scale segregation during the solidification process, resulting in an uneven distribution of elements. This observation is supported by the corresponding EDS mapping (Figs. 4.5a3, 4.5b3, 4.5c3, and 4.5d3). The magnified BSE images of the CS-coatings (Figs. 4.5a2, 4.5b2, 4.5c2, and 4.5d2) show that the microstructure evolves with increasing electron beam power (P). Phase identification was supported by the corresponding EDS mappings (Figs. 4.5a4, 4.5b4, 4.5c4, and 4.5d4). At P = 126 W, the microstructure consists of NiTi dendrites with $NiTi_2$ phases distributed between them. At P = 132 W, 138 W, and 144 W, the matrix is predominantly composed of $NiTi_2$, with a small amount of NiTi dendrites remaining in localized areas. In addition, a darker phase appears between $NiTi_2$ dendrites in regions with significantly lower Ni concentration. Detailed examination of EDS data reveals that the Ni concentration in these regions is close to 25 at.%, which marks the (α-Ti+$NiTi_2$) eutectic point in the Ni–Ti binary system (Fig. 4.4f). Additionally, cracks are visible in the cross-section of the CS-coatings, as indicated by the red arrows, which aligns with the findings from the surface observation (Fig. 4.2). These cracks primarily appear in the (α-Ti + $NiTi_2$) eutectic areas according to BSE images in Fig. 4.5.

The BSE images (Figs. 4.5e1, 4.5f1, 4.5g1, and 4.5h1) of the IS-coatings show that

the IS-coatings under all four levels of P have more uniform brightness distributions than the CS-coatings. This suggests that the elemental distributions are also more homogeneous in the IS-coatings. However, some dark streaks can be seen at the junction of the melt tracks as indicated by black arrows. These dark streaks are less frequent and narrower at P = 126 W and 132 W. Conversely, they are wider and more frequent at the junction region between every two tracks at P = 138 W and 144 W. Additionally, EDS mappings (Figs. 4.5e3, 4.5f3, 4.5g3, and 4.5h3) show lower Ni concentration (~33 at.%) in the regions corresponding to these dark streaks compared to the average composition of the coating. The magnified BSE images of the IS coatings (Figs. 4.5e3, 4.5f3, 4.5g3, and 4.5h3) reveal significant changes in microstructure with increasing electron beam power. Phase identification is supported by the corresponding EDS mappings (Figs. 4.5e4, 4.5f4, 4.5g4, and 4.5h4). At P = 126 W and 132 W, the coating matrix exhibits a cellular NiTi structure, with dark streaks—less than 1 μm wide—identified as $NiTi_2$ phase. When the power increases to 138 W, the cellular structure disappears. In this case, the dark regions consist of NiTi dendrites with $NiTi_2$ phase filling the spaces between them. At P = 144 W, both the matrix and the dark regions contain NiTi dendrites and inter-dendritic $NiTi_2$, but the dendrites in the dark regions are more widely spaced. These observations suggest that IS-coatings fabricated at P = 126 W and 132 W, which retain a cellular structure and have a lower $NiTi_2$ content, are expected to exhibit superior mechanical properties compared to those fabricated at P = 138 W and 144 W, as well as all CS-coatings.

Notably, cracks appear near these dark regions with relatively low Ni concentration (Ti-rich) in the CS-coatings exclusively. This observation is proposed to be attributed to liquation cracking owing to the lower melting temperature of the Ti-rich regions. Furthermore, heat accumulation during the continuous scanning process will promote

cracking. According to the Ni-Ti phase diagram (Fig. 4.4f), the composition of the Ti-rich region corresponds to the lower liquid-phase temperature. This indicates that most of the coating had already solidified and begun to cool and contract when the Ti-rich region started to solidify, leading to tensile stress concentration in the Ti-rich regions and increasing the probability of cracking [16]. Conversely, the absence of cracks in the IS-coatings can be attributed to two factors. First, intermittently scanning prevents excessive heat buildup, lowering the maximum melt-pool temperature and reducing thermal stresses. Second, the Ti-rich regions (dark contrast region) in the IS-coatings are significantly smaller.

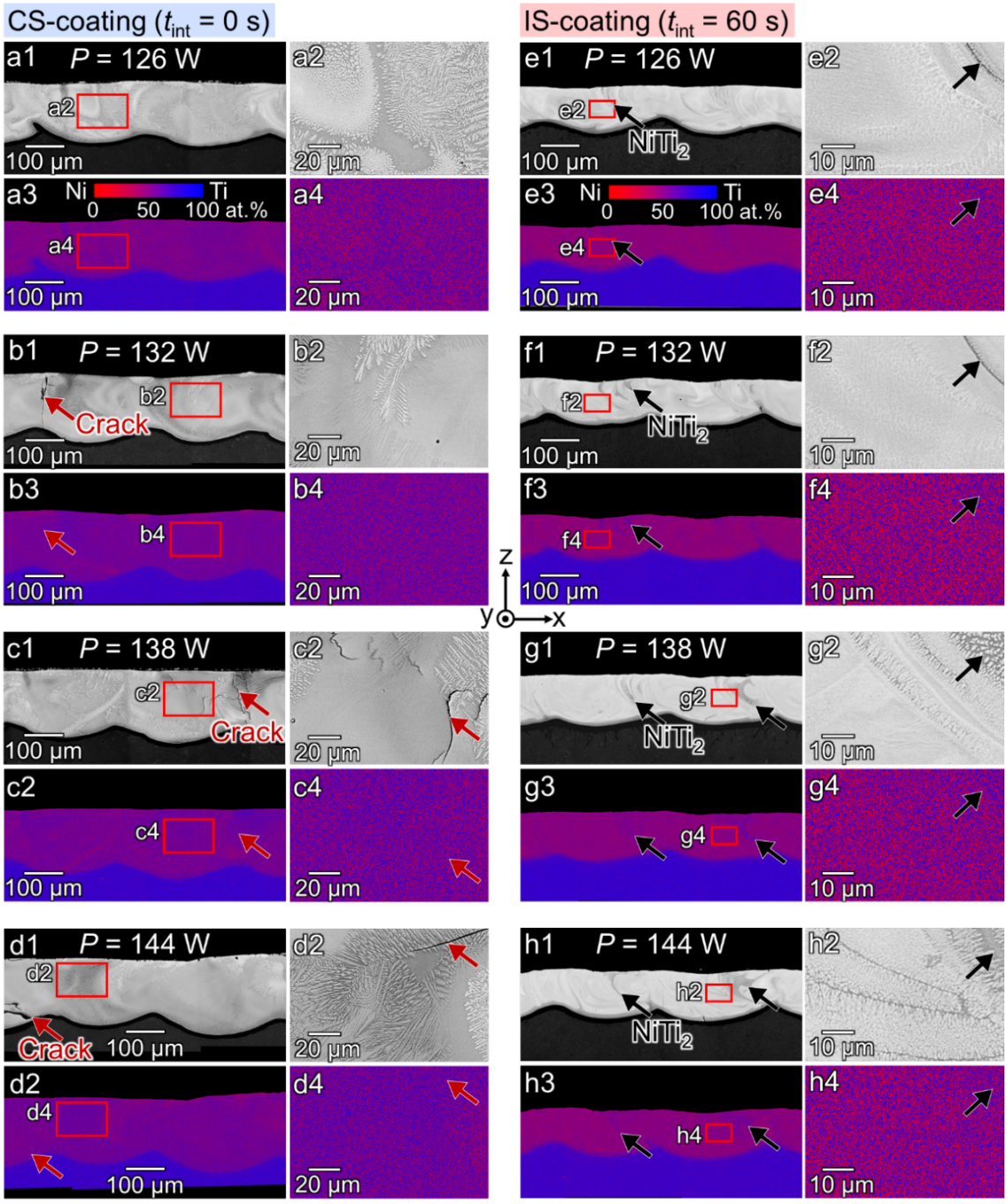

Fig. 4.5. (a–h) BSE images and EDS mapping of the cross-section of Track #6 to #7 in the continuously scanned (CS) coatings (left) and intermittently scanned (IS) coatings (right). *P* of each coating are (a, e) 126 W, (b, f) 132 W, (c, g) 138 W and (d, h) 144 W. The scanning speed of these coatings is fixed at 100 mm/s. Red arrows indicate cracks while black arrows indicate $NiTi_2$ phases.

4.3.3 Phase identification

Fig. 4.6 shows the XRD profiles of the EB-scanned coating and the variation in

intensity of selected characteristic peaks with P in continuously scanned (CS) and intermittently scanned (IS) coatings. The positions of the characteristic peaks were compared with 6 PDF cards to identify the phases: #00-001-1260 (cubic $A1$-Ni), #01-076-3614 (cubic $B2$-NiTi), #01-078-4618 (cubic $B2$-NiTi), #01-072-8488 (monoclinic $B19'$-NiTi), #01-075-0878 (hexagonal $D0_{24}$-Ni_3Ti), #00-005-0687 (cubic $C15$-$NiTi_2$). Data from other studies[17–19] were also referenced to assist in phase identification. The five profiles in Fig. 4.6a, from top to bottom, represent the as-deposited Ni plating (control) and the CS-coating with P of 126 W, 132 W, 138 W, and 144 W, respectively. The characteristic peaks of $C15$-$NiTi_2$, $B19'$-NiTi and $B2$-NiTi phases are observed on the profiles of CS-coatings. Owing to the low C_{Ni} in CS-coatings, the intensity of the $C15$-$NiTi_2$ characteristic peaks is significantly higher than that of the NiTi peaks across all profiles. The variation in intensity of $B2$-NiTi (110) and $C15$-$NiTi_2$ (511) (Figs. 4.6c and 4.6d) indicates that the small amount of $B2$-NiTi phase in the CS-coatings decreases further with increasing P. The $B2$-NiTi phase nearly disappears at P = 144 W, leaving $C15$-$NiTi_2$ as the dominant phase in the coatings. This observation is consistent with the cross-sectional BSE images (Fig. 4.5) discussed in Section *4.3.2*.

Fig. 4.6b shows the profiles of the IS-coatings with P of 126 W, 132 W, 138 W, and 144 W. Similar to the profiles in Fig. 4.6a, no characteristic peaks of Ni or Ti phases are observed in any of the coating profiles. This indicates that EB scanning fully mixes the Ni plating and CP-Ti substrate to form an alloy phase, regardless of the scanning parameters. Examining the four profiles of the IS-coatings alongside the variation in the $B2$-NiTi (110), $C15$-$NiTi_2$ (511), and $D0_{24}$-Ni_3Ti ($20\bar{2}1$) peaks (Figs. 4.6c, 4.6d, and 4.6e) reveals that the $B2$-NiTi phase is predominant in all four coatings and reaches its highest concentration at P = 132 W. As P increases, the $NiTi_2$ phase, which is absent at P = 126 W, first appears at P = 132 W and then grows rapidly. Meanwhile, the $D0_{24}$-

Ni_3Ti phase, present at P = 126 W, decreases and eventually disappears as P increases beyond 138 W. These variations in the phase content within the coating essentially align with the trends in the binary Ni-Ti phase diagram (Fig. 4.4f).

Typically, the martensitic transformation start temperature (M_s) of NiTi phases increases as the Ni content decreases. When the Ni concentration falls below 50 at.%, Ms is generally considered to be around 350 K [20]. This implies that NiTi phases with such compositions should be martensitic (i.e. *B*19'-NiTi) at room temperature. However, in this study, the average Ni concentrations in the IS coatings at P = 138 W and P = 144 W are only 47.1 and 45.7 at.%, respectively, yet they still contain significant amounts of the *B*2-NiTi phase. This is because the distribution of Ni elements in these two IS-coatings is not microscopically uniform: the presence of the $NiTi_2$ phase at the melt track junctions lowered the average Ni concentration. Consequently, the Ni concentration in the remaining coating regions exceeds the average value, with some areas potentially maintaining concentrations above 50 at.%. In these Ni-rich regions, the NiTi phase retains its *B*2 structure. Furthermore, the martensitic transformation of the NiTi phase depends not only on composition, but also on thermal history. The extremely high cooling rates during electron beam scanning suppress the *B*2 → *B*19' transformation of the NiTi phase. At the same time, lattice defects and residual stresses generated during cooling inhibit this transformation by increasing the friction between the *B*2 and *B*19' phases at the interfaces, ultimately preserving the *B*2 phase within the IS-coating [21]. Together, these two factors account for the retention of the *B*2-NiTi phase in IS-coatings scanned at P = 138 W and P = 144 W.

The *B*2-NiTi phase is the primary phase in superelastic Nitinol, contributing to the superelastic properties [22]. In addition, $D0_{24}$-Ni_3Ti exhibits the highest hardness and

mechanical strength among all Ni–Ti intermetallic compounds [23] and is typically considered a strengthening phase in Nitinol. In contrast, *C*15-$NiTi_2$ has lower hardness than Ni_3Ti and is prone to brittle fracture [24]. Owing to the heat accumulation effect, the C_{Ni} of the CS-coatings is significantly lower than that of the IS-coatings, even though both are scanned at P = 126 W. Therefore, as shown by the comparison of the intensities of the *B*2-NiTi (110) and *C*15-$NiTi_2$ (511) peaks between CS- and IS-coatings, CS-coatings are mainly composed of the $NiTi_2$ phase, whereas IS-coatings have a superior structure with *B*2-NiTi as the primary phase and $D0_{24}$-Ni_3Ti as the reinforcing phase. Thus, IS-coatings could be inferred to have better toughness, mechanical strength, and wear resistance than CS-coatings.

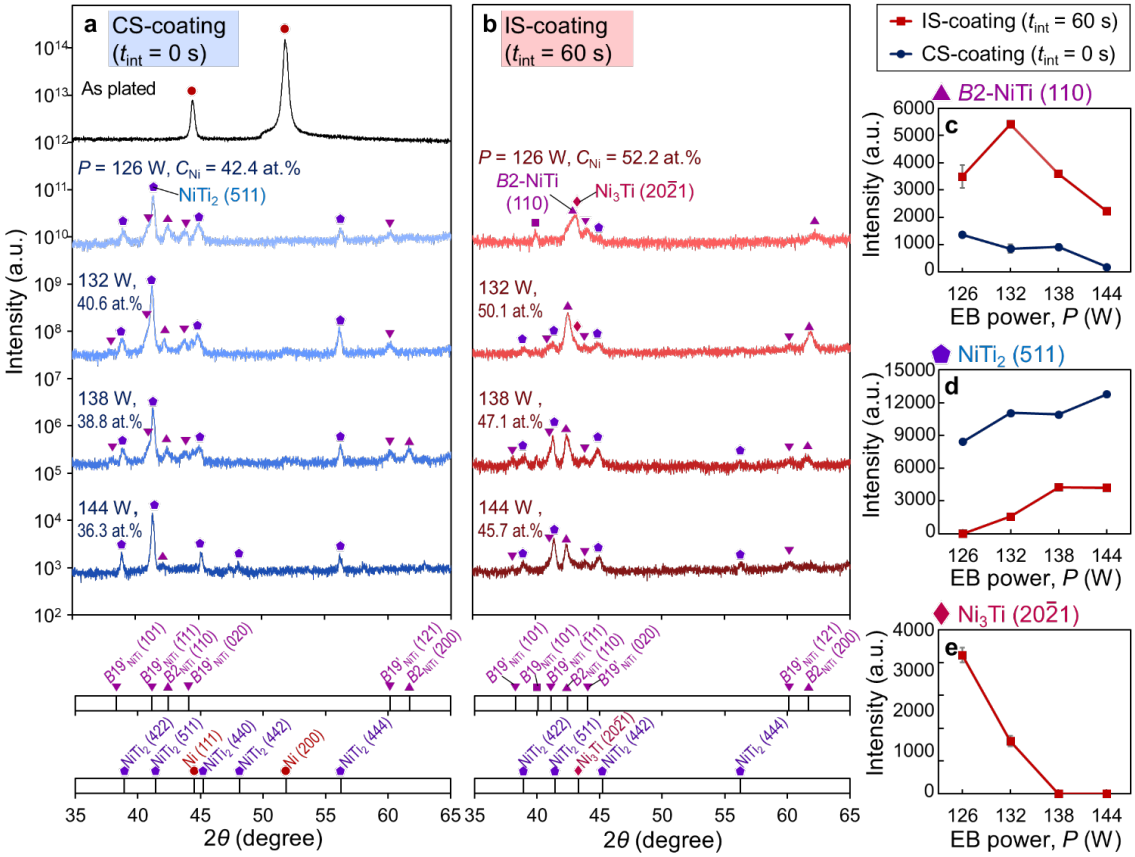

Fig. 4.6. X-ray diffraction (XRD) patterns of the EB-scanned coatings. (a) Results for the continuously scanned (CS) coatings with the as-plated specimen as control. (b) Results for the intermittently scanned (IS) coatings. Variation in intensity of (c) *B*2-NiTi (110) peak, (d) $NiTi_2$ (511) peak, and (e) Ni_3Ti (20$\bar{2}$1) peak with EB power in CS- and IS-coatings.

4.3.4 Indentation properties

4.3.4.1 Nanoindentation test results

Fig. 4.7a shows the load–displacement curves from the indentation tests of EB-scanned coatings, superelastic Nitinol (SE-NiTi), and CP-Ti. Overlapping curves are avoided by presenting only the data for continuously scanned (CS) and intermittently scanned (IS) coatings produced at P = 126 W. The maximum indenter penetration depth during loading (h_{max}) and the permanent indentation depth after unloading (h_p) can be intuitively inferred from these curves. Fig. 4.7b shows the hardness (H) versus depth recovery ratio ($\eta_{d,h}$) plot of EB-scanned coatings. $\eta_{d,h}$ is defined as the ratio of the

recoverable indentation depth to the maximum indentation depth, as given by Eq (4.2). This index characterizes the elastic recovery properties of the material and has been shown to positively correlate with wear resistance in materials such as nanocomposites [25] and 60NiTi alloy [19,26]. For the CS-coating, both H and $\eta_{d,h}$ are generally lower and display minimal variation as P changes. Consequently, the results obtained from all four levels of P can be represented by a single data point in the figure. Conversely, the IS-coatings exhibit gradual increase in H and $\eta_{d,h}$ as P decreases, such that the coating produced at P = 126 W achieves the highest H and $\eta_{d,h}$ among all coatings. This trend may be attributed to the increasing fractions of Ni_3Ti and $B2$–NiTi phases and a decreasing fraction of $NiTi_2$ (Fig. 4.6). All EB-scanned coatings show considerably higher H and $\eta_{d,h}$ than CP-Ti. The IS-coatings exhibit higher H and $\eta_{d,h}$ than the CS-coatings.

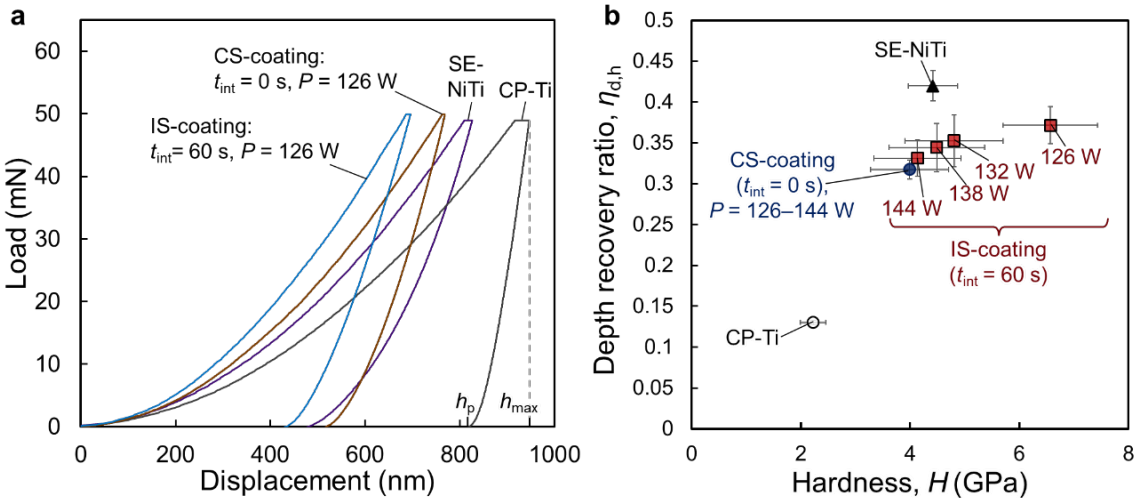

Fig. 4.7. (a) Load–displacement curve of Berkovich indentation tests on CP-Ti, Superelastic Nitinol (SE-NiTi), and EB-scanned coatings. (b) Depth recovery ratio ($\eta_{d,h}$) vs. hardness (H) plot of CP-Ti, SE-NiTi, and EB-scanned coatings. "CS-coating" and "IS-coating" refer to continuously and intermittently scanned coatings, respectively.

Fig. 4.8a shows the variation of H and E in EB-scanned coatings with respect to P.

For CS-coatings, H is lower than that of SE-NiTi and remains nearly constant regardless of P. In contrast, for IS-coatings, H increases as P decreases and exceeds that of the SE-NiTi when $P < 138$ W. A similar trend is observed for E: it remains stable for CS-coatings but increases with decreasing P for IS-coatings. Notably, E is higher for IS-coatings compared to CS-coatings at all P values; it is slightly above SE-NiTi but well below CP-Ti. Fig. 4.8b shows the hardness-to-modulus ratio (H/E) of all EB-scanned coatings. The H/E ratios of all EB-scanned coatings are significantly higher than CP-Ti. CS-coatings exhibit H/E ratios of approximately 0.06, regardless of P. In contrast, H/E for IS-coatings increases as P decreases, surpassing CS-coating at $P = 126$ W and 132 W. Although the H/E ratios of most coatings are slightly lower than those of SE-NiTi, the IS-coating at $P = 126$ W matches or even exceeds them. Higher hardness generally indicates improved wear resistance [27]; however, several recent studies [28–30] have suggested that the H/E ratio is a more reliable indicator, as it better correlates with wear resistance indicator than hardness alone. Therefore, higher H/E ratio of EB-scanned coatings indicates that the coating could significantly improve the wear resistance of CP-Ti substrates.

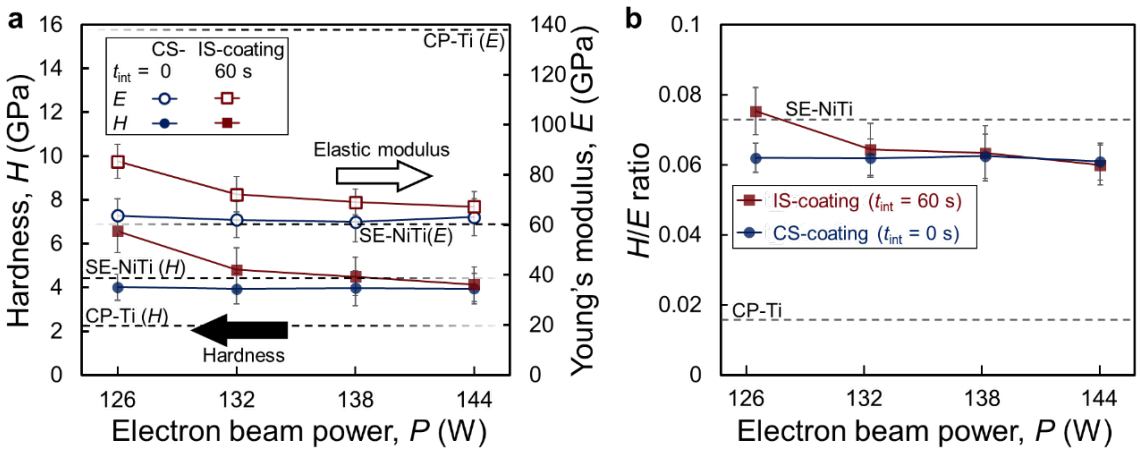

Fig. 4. 8. (a) Variation in hardness (H) and Young's modulus (E) of coatings with increasing EB power (P) and constant beam scan speed (V) of 100 mm/s. The dashed lines represent the H and E of the reference superelastic Nitinol (SE-NiTi) and CP-Ti. (b) Variation in H/E ratio of coatings with increasing P. The dashed lines represent the H/E ratio of the reference SE-NiTi and CP-Ti.

4.3.4.2 Comparative analysis of indentation properties in EB-scanned coatings

Figs. 4.9a and 4.9b compare the parameters H/E ratio, H, and E of EB-scanned coatings with other materials such as structural metal (SM), superelastic Nitinol (SE-NiTi), wear resistant (WR) coating, and NiTi coating from other studies. Commonly used SMs have hardness in the range 1–10 GPa and Young's moduli of approximately 100–300 GPa. WR-coatings are typically used for surface protection of SMs, and their hardness and H/E ratios are higher than those of most SMs. Although SE-NiTi does not exhibit a hardness higher than SM or WR-coating, its lower Young's modulus gives it a considerably higher H and H/E ratio than that of SM or WR-coating. The EB-scanned coatings in this study have H and E values similar to those of SE-NiTi, resulting in improved H/E ratios compared to those of SM and WR-coatings. In particular, the IS-coating at P = 126 W shows an H/E ratio higher than that of most SE-NiTi alloys. The EB-scanned coatings exhibit a considerably higher H/E ratio than those of NiTi coatings fabricated by magnetron sputtering in other studies [31,32]. This is due to their

significantly lower E, despite having H values within the same range.

Fig. 4.9c compares the $\eta_{d,h}$ of each material. The results show that the $\eta_{d,h}$ of SE-NiTi is considerably higher than that of SM and WR-coatings. This difference arises from the superelastic properties of SE metals, which enable a high reversible strain limit exceeding the elastic strain limit of conventional metals [33,34], leading to significantly higher $\eta_{d,h}$ values. In our study, the $\eta_{d,h}$ of the EB-scanning coatings is higher than that of the SM and WR-coatings and is similar to that of SE-NiTi. In particular, the IS-coating with P = 126 W shows the highest $\eta_{d,h}$ in EB-scanned coatings, although it is slightly lower than the average value for SE-NiTi. Similarly, the $\eta_{d,h}$ values reported for NiTi coatings in other studies [31,32] fall within a comparable range. Although the IS-coatings are mainly composed of the superelastic $B2$-NiTi phase, similar to SE-NiTi, their $\eta_{d,h}$ is reduced due to a higher level of defects compared to that in bulk SE-NiTi and the presence of the $NiTi_2$ phase.

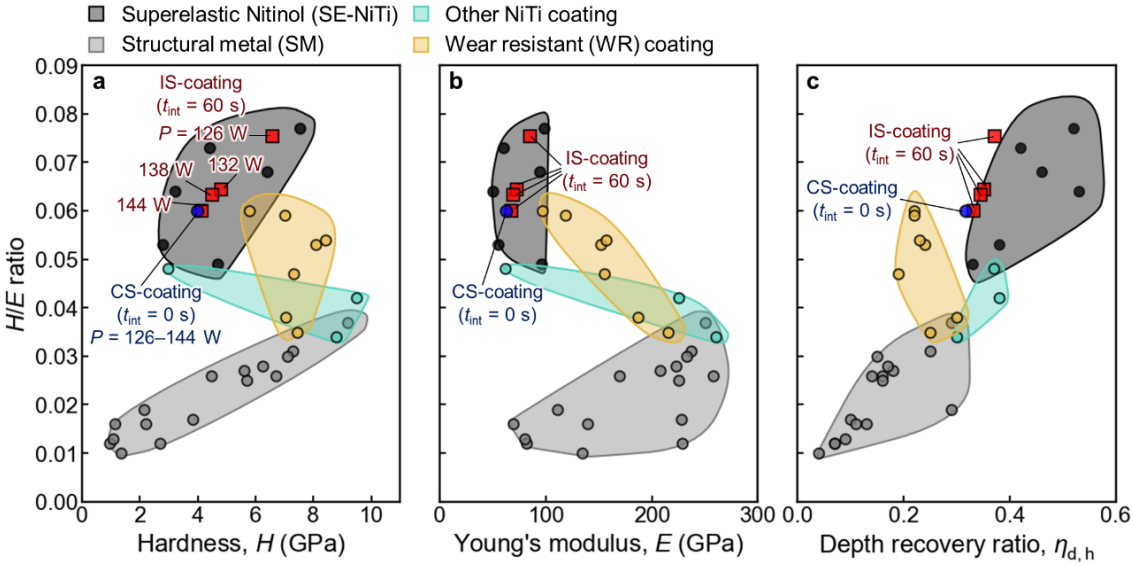

Fig. 4.9. Comparison of the indentation properties among the IS-coating/CS-coating in the present study, superelastic Nitinol (SE-NiTi) [18,26,28,35], structural metal (SM) [18,28,35–43], other NiTi coatings [31,32], and wear resistant (WR) coating [44–47]. Plot of H/E ratio vs. (a) hardness (H), (b) Young's modulus (E), and (c) depth recovery ratio ($\eta_{d,h}$).

4.3.5 Frictional wear properties

4.3.5.1 Sliding wear test results

To further evaluate the wear resistance of the intermittently scanned (IS) coating for practical applications, we conducted friction and wear tests. Fig. 4.10a presents the friction coefficient curves of IS-coating at P = 126 W and 138 W, comparing them with that of superelastic Nitinol (SE-NiTi) and CP-Ti. The friction coefficients of the two IS-coatings and SE-NiTi are similar. These coefficients drop sharply to approximately 0.6 within the initial 500–1,000 mm of sliding, then fluctuate between 0.5 and 0.7 throughout the remaining sliding distance, showing no indication of stabilization by the end of the test. In contrast, CP-Ti shows the lowest coefficient of friction during the test. It decreases during the initial 2,000 mm of sliding, then gradually increases over the sliding distance from 2,000 mm to 10,000 mm, stabilizing to around 0.5. The higher friction coefficients of IS-coatings are possibly due to the much lower elastic modulus. This lower modulus leads to a larger contact area between the indenter and the IS-coating during abrasion testing [48], resulting in increased friction. In contrast, the IS-coating has a similar composition, elastic modulus, and phase structure to SE-NiTi, leading to comparable friction coefficients.

Fig. 4.10b compares the specific wear rates (W_s) of the two IS-coatings, SE-NiTi, and CP-Ti. The IS-coating produced at P = 138 W, despite having a higher friction coefficient, exhibits a W_s considerably lower than that of the CP-Ti substrate—approximately 33% W_s of CP-Ti. The IS-coating at P = 126 W shows a further reduction in W_s, reaching only 20% W_s of CP-Ti. These results confirm that EB-scanned coatings significantly enhance the wear resistance. Elemental and phase composition analyses show that the IS-coating fabricated at P = 126 W contains a higher concentration of C_{Ni},

more Ni_3Ti phases, and fewer $NiTi_2$ phases compared to the coating produced at P = 138 W. The high hardness of Ni_3Ti enhances the mechanical strength of the coating [23], while the reduced presence of $NiTi_2$ phases minimizes damage from localized stress concentrations[24], thereby improving wear resistance. These wear test results are aligning with the predictions based on the $\eta_{d,h}$ and H/E ratio data presented in Section *4.3.4*.

Additionally, the W_s of the IS-coating at P = 126 W remains slightly higher than that of SE-NiTi, despite the similarity in elemental composition. The IS-coating at P = 126 W still contains a small amount of the $NiTi_2$ phase due to compositional inhomogeneity (Figs. 4.5 and 4.6), although its primary phase is *B*2-NiTi phase. The $NiTi_2$ compound is hard, brittle, and prone to fracture. Cracks tend to initiate at $NiTi_2$ phases [23,24], which is detrimental to the coating's wear resistance. Therefore, the presence of the $NiTi_2$ phase is assumed to reduce the overall wear resistance of the IS-coating.

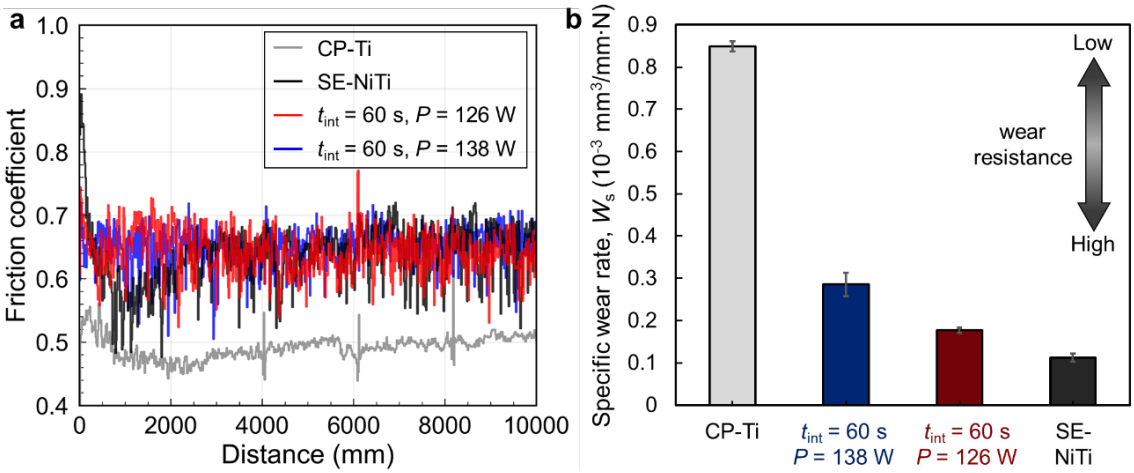

Fig. 4.10. (a) Friction coefficient curves of two intermittently scanned (IS) coatings, CP-Ti, and superelastic Nitinol (SE-NiTi) during the sliding wear test. (b) Comparison of specific wear rate (W_s) of IS-coating with CP-Ti and SE-NiTi.

Fig. 4.11 shows the secondary electron (SE) images and corresponding EDS mapping of the worn surfaces of CP-Ti, IS-coating at P = 126 W, and superelastic Nitinol (SE-

NiTi). The SE images reveal a common phenomenon of scratching and plate-like particle adhesion on the worn surfaces of the three materials. However, the origin of the particles are completely different. EDS mapping of the CP-Ti surface shows only Ti element, indicating that the plate-like particles result from delaminated CP-Ti rather than adhered substances. This suggests that the wear of CP-Ti is caused by both abrasive wear and delamination. The surface delamination of CP-Ti during sliding friction is caused by severe plastic deformation, which induces crack nucleation and propagation parallel to the surface, ultimately leading to delamination [49]. This mechanism contributes to the high W_s and poor wear resistance of CP-Ti.

In contrast, EDS mapping of the EB-scanned coating reveals particles rich in Al, indicating alumina particles detached from the indenter. The SE-NiTi exhibits a similar pattern, with adhered alumina particles observed on its worn surface. Therefore, the EB-scanned coatings and SE-NiTi do not exhibit delamination under indenter compression. This indicates that the wear of the EB-scanned coatings and SE-NiTi is caused by abrasive wear. In addition, adhesive wear [50] occurring on the alumina indenter side leads to the transfer of alumina debris particles from the indenter, explaining their higher friction coefficients but significantly lower W_s.

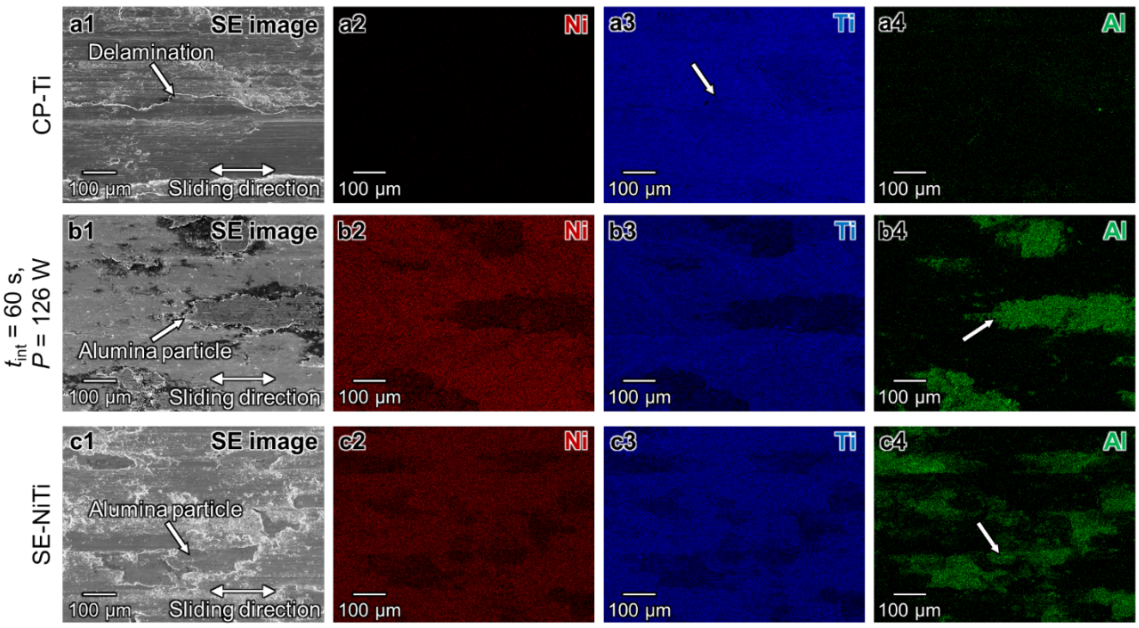

Fig. 4.11. SE images and EDS elemental mapping of the worn surface on (a) CP-Ti substrate, (b) IS-coating (t_{int} = 60 s, P = 126 W), and (c) superelastic Nitinol (SE-NiTi).

4.3.5.2 Correlation between indentation properties and frictional wear properties

In Fig. 4.12a, W_s of IS-coating, superelastic Nitinol (SE-NiTi), and CP-Ti show a weak negative correlation with H. Hardness, a key result of indentation testing, is often considered a reference indicator of a material's wear resistance. As discussed in section *4.3.4.1*, higher hardness is generally assumed to correspond to better wear resistance, meaning a lower wear rate under identical conditions. However, the results of this study challenge this assumption. SE-NiTi has the lowest W_s among the four materials, yet it does not have the highest H. Figs. 4.12b and 4.12c reveal a clearer linear negative correlation between W_s and both the H/E ratio and $\eta_{d,h}$. These results consistent with the discussion in section *4.3.4.1* that the H/E ratio and $\eta_{d,h}$ are more reliable indicators of wear resistance than H alone.

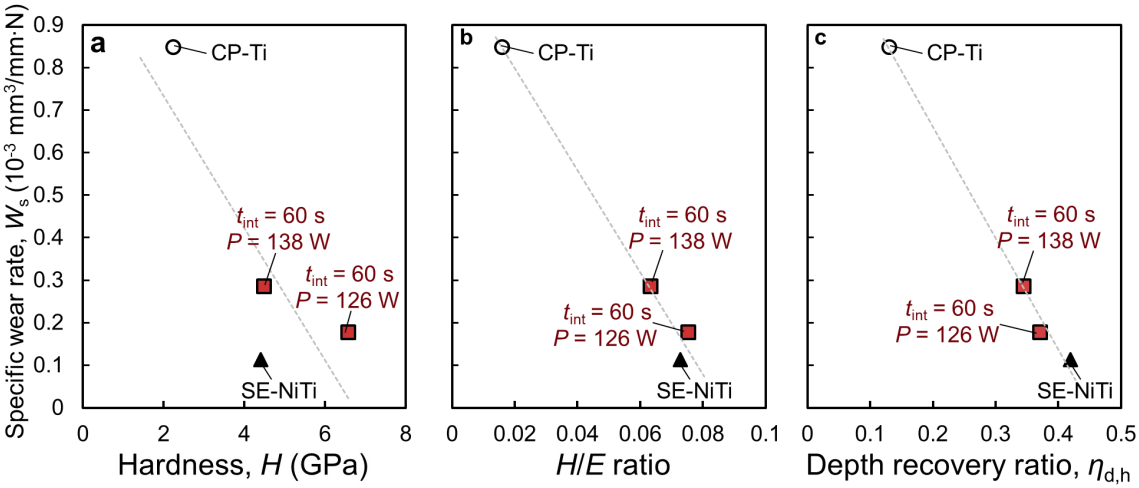

Fig. 4.12 Plot of specific wear rate (W_s) versus (a) Hardness (H), (b) H/E ratio and (c) Depth recovery ratio ($\eta_{d,h}$) among EB-scanned coatings, superelastic Nitinol (SE-NiTi), and CP-Ti.

According to the classical wear theory, one significant cause of wear is localized fracture due to severe plastic deformation of the material surface [50]. Therefore, minimizing plastic deformation is crucial for reducing wear. The relationship between H/E and $\eta_{d,h}$, and the deformation behavior of the material in surface contact provide the mechanism by which these two factors can serve as indicators of wear resistance.

Greenwood and Williamson [51] introduced a "plasticity index" (ψ) for rough contact. In this research, it was concluded that the contact surface deforms plastically under even minimal loads when $\psi > 1$, whereas it deforms predominantly elastically when $\psi < 0.6$. The value of ψ is determined by multiplying E_r/H with geometric factors:

$$\psi = \frac{E_r}{H}\sqrt{\frac{\sigma}{\beta}}. \tag{4.5}$$

Here, E_r is a reduced modulus, and σ and β are geometric factors dependent only on the contact surface morphology. E_r is defined based on the modulus (E) and Poisson's ratio (ν) of the specimen, along with the modulus (E_i) and Poisson's ratio (ν_i) of the indenter, as follows:

$$\frac{1}{E_{\mathrm{r}}}=\frac{(1-\nu^{2})}{E}+\frac{(1-\nu_{\mathrm{i}}^{2})}{E_{\mathrm{i}}}. \tag{4.6}$$

The value of E_{r} is primarily determined by E when contact occurs between a specimen and a rigid indenter with a large E_{i}, as is commonly the case in indentation tests and friction wear tests. This indicates that under constant load and contact surface morphology, a larger H/E ratio results in a smaller ψ, which favors elastic deformation. Y.T. Cheng and C.M. Cheng [52–54] investigated in detail the numerical relationships between work, indenter displacement, and material properties such as H and E_{r} in indentation experiments. From their findings, the following two scaling relationships can be summarized:

$$\frac{W_{\mathrm{e}}}{W_{\mathrm{tot}}}\propto\frac{H}{E_{\mathrm{r}}} \tag{4.7}$$

and

$$\frac{W_{\mathrm{e}}}{W_{\mathrm{tot}}}\propto\frac{h_{\mathrm{max}}-h_{\mathrm{p}}}{h_{\mathrm{max}}}=\eta_{d,h}. \tag{4.8}$$

Here, W_{e} is the reversible work, representing the work done by the specimen on the indenter during unloading, and W_{tot} is the total work, representing the work done by the indenter on the specimen during loading. W_{e} corresponds to the elastic deformation work, while the difference between W_{tot} and W_{e} represents the irreversible work consumed in plastic deformation. A larger H/E_{r} or $\eta_{\mathrm{d,h}}$ indicates a higher proportion of reversible work to total work, meaning a greater proportion of elastic to total deformation.

These studies suggest that under constant contact conditions, a material with a higher H/E or $\eta_{\mathrm{d,h}}$ experiences less plastic deformation and consumes less deformation energy. Thus, it undergoes less surface wear in the friction wear test, resulting in improved wear resistance. The EB-scanned coatings fabricated in this study not only have considerably

higher hardness than the CP-Ti substrate, but also very high H/E and $\eta_{d,h}$ comparable to SE-NiTi. Therefore, the EB-scanned coatings achieve low W_s, i.e., excellent wear resistance.

4.4 Conclusion

A novel fabrication method for NiTi coating on CP-Ti has been developed utilizing Ni electro-plating and multi-track EB scanning for AM. Four levels of electron beam power (126 W, 132 W, 138 W, and 144 W) with constant scan speed of 100 mm/s were tested in each of the two scanning modes, continuous scanning and intermittent scanning, in order to evaluate the effects of processing parameters on the coating morphology, microstructure, composition, indentation properties, and frictional wear properties. The key findings and conclusions are summarized as follows:

- Implementing an intermittent scanning instead of continuous scanning strategy can produce coatings with reduced surface roughness.
- Intermittently scanned (IS) coatings exhibit improved composition and microstructure compared to continuously scanned (CS) coatings. In particular, the IS-coating scanned at an optimum EB power exhibited a Ni concentration exceeding 50 at.%, with a microstructure primarily composed of the superelastic $B2$-NiTi phase, reinforced by the $D0_{24}$-Ni_3Ti phase.
- All EB-scanned coatings exhibit improved indentation properties compared to uncoated CP-Ti. Among them, the IS-coatings outperform the CS-coatings, showing higher hardness-to-elastic modulus (H/E) ratios and greater depth recovery rates. The IS-coatings demonstrate an even higher H/E ratio than the superelastic Nitinol at its maximum level.
- The IS-coatings demonstrate most enhanced wear resistance compared to uncoated

CP-Ti, approaching closely those of the superelastic Nitinol.

- Local compositional inhomogeneities resulted in the formation of *C*15-$NiTi_2$ phase at the melt track junctions of the IS-coating. This reduces the coating's wear resistance. This is thought to explain why the wear resistance of the IS coating does not match that of superelastic Nitinol equally well. Therefore, measures such as heat treatment or optimized scanning strategies should be considered to eliminate these inhomogeneities.

References

[1] Y. Huang, M.B. Khamesee, E. Toyserkani, A new physics-based model for laser directed energy deposition (powder-fed additive manufacturing): From single-track to multi-track and multi-layer, Opt. Laser Technol. 109 (2019) 584–599. https://doi.org/10.1016/j.optlastec.2018.08.015.

[2] Denki Kagaku Kai (Ed.), Denki kagaku benran [Electrochemical Handbook], 6th ed., Maruzen Publishing, Tōkyō, 2013.

[3] Thermo-Calc Software, Titanium and TiAl-based Alloys Databases, Version 4(TCTI4), (2022). https://thermocalc.com/products/databases/ (accessed October 1, 2023).

[4] E.S. Berkovich, The three-faceted diamond pyramid for microhardness testing, Zavod. Lab. 16 (1950) 345.

[5] A. Shimamoto, K. Tanaka, Y. Akiyma, H. Yoshizaki, Nanoindentation of glass with a tip-truncated Berkovich indenter, Philos. Mag. A 74 (1996) 1097–1105. https://doi.org/10.1080/01418619608239710.

[6] International Organization for Standardization, Metallic materials — Instrumented indentation test for hardness and materials parameters — Part 1: Test method (ISO

Standard No. 14577-1:2015), (2015). https://www.iso.org/standard/56626.html.

[7] W. Ni, Y.-T. Cheng, D.S. Grummon, Microscopic superelastic behavior of a nickel-titanium alloy under complex loading conditions, Appl. Phys. Lett. 82 (2003) 2811–2813. https://doi.org/10.1063/1.1569984.

[8] ASTM International, Test Method for Linearly Reciprocating Ball-on-Flat Sliding Wear, (2022). https://doi.org/10.1520/G0133-22.

[9] J.F. Shackelford, W. Alexander, eds., CRC Materials Science and Engineering Handbook, 3rd ed., CRC Press, Boca Raton, 2000. https://doi.org/10.1201/9781420038408.

[10] S.K. Ray, A. Banerjee, B.K. Bhangi, D. Pyne, B. Dutta, 2 - Tribological analysis—general test standards, in: S.C. George, J.T. Haponiuk, S. Thomas, R. Reghunath, S. P. s. (Eds.), Tribol. Polym. Polym. Compos. Polym. Nanocomposites, Elsevier, 2023: pp. 17–50. https://doi.org/10.1016/B978-0-323-90748-4.00001-7.

[11] C. Li, Z.Y. Liu, X.Y. Fang, Y.B. Guo, Residual Stress in Metal Additive Manufacturing, Procedia CIRP 71 (2018) 348–353. https://doi.org/10.1016/j.procir.2018.05.039.

[12] A. Takase, T. Ishimoto, R. Suganuma, T. Nakano, Surface residual stress and phase stability in unstable β-type Ti–15Mo–5Zr–3Al alloy manufactured by laser and electron beam powder bed fusion technologies, Addit. Manuf. 47 (2021) 102257. https://doi.org/10.1016/j.addma.2021.102257.

[13] Y. Miyata, M. Okugawa, Y. Koizumi, T. Nakano, Inverse Columnar-Equiaxed Transition (CET) in 304 and 316L Stainless Steels Melt by Electron Beam for Additive Manufacturing (AM), Crystals 11 (2021) 856. https://doi.org/10.3390/cryst11080856.

[14] L.E. Criales, Y.M. Arısoy, B. Lane, S. Moylan, A. Donmez, T. Özel, Predictive

modeling and optimization of multi-track processing for laser powder bed fusion of nickel alloy 625, Addit. Manuf. 13 (2017) 14–36. https://doi.org/10.1016/j.addma.2016.11.004.

[15] Y. Cheng, G. Wang, Z. Qiu, Z. Zheng, D. Zeng, X. Tang, R. Shi, M. Uddagiri, I. Steinbach, Multi-physics simulation of non-equilibrium solidification in Ti-Nb alloy during selective laser melting, Acta Mater. 272 (2024) 119923. https://doi.org/10.1016/j.actamat.2024.119923.

[16] S. Katayama, 12 - Defect formation mechanisms and preventive procedures in laser welding, in: S. Katayama (Ed.), Handb. Laser Weld. Technol., Woodhead Publishing, 2013: pp. 332–373. https://doi.org/10.1533/9780857098771.2.332.

[17] G. Baigonakova, E. Marchenko, T. Chekalkin, J. Kang, S. Weiss, A. Obrosov, Influence of Silver Addition on Structure, Martensite Transformations and Mechanical Properties of TiNi–Ag Alloy Wires for Biomedical Application, Materials 13 (2020) 4721. https://doi.org/10.3390/ma13214721.

[18] Z.N. Farhat, C. Zhang, The role of reversible martensitic transformation in the wear process of TiNi shape memory alloy, Tribol. Trans. 53 (2010) 917–926. https://doi.org/10.1080/10402004.2010.510620.

[19] Z. Pang, Q. Zeng, Z. Ning, W. He, Z. Wang, J. Wang, L. Li, Ultralow friction and low wear behavior of in-situ formed NiTiO3 from 60NiTi alloy at 350 °C, Intermetallics 168 (2024) 108271. https://doi.org/10.1016/j.intermet.2024.108271.

[20]K. Otsuka, X. Ren, Physical metallurgy of Ti–Ni-based shape memory alloys, Prog. Mater. Sci. 50 (2005) 511–678. https://doi.org/10.1016/j.pmatsci.2004.10.001.

[21] J. Ge, B. Yuan, H. Chen, J. Pan, Q. Liu, M. Yan, Z. Lu, S. Zhang, L. Zhang, Anisotropy in microstructural features and tensile performance of laser powder bed fusion NiTi alloys, J. Mater. Res. Technol. 24 (2023) 8656–8668.

https://doi.org/10.1016/j.jmrt.2023.05.046.

[22] K. Otsuka, K. Shimizu, Pseudoelasticity and shape memory effects in alloys, Int. Met. Rev. 31 (1986) 93–114. https://doi.org/10.1179/imtr.1986.31.1.93.

[23] Z. Liu, L. Zhang, C. Fu, C. Zeng, X. Wu, W. Li, X. Ma, Structural, mechanical, and thermodynamic properties of Ni–Ti intermetallic compounds: First-principle calculation, J. Appl. Phys. 134 (2023) 085107. https://doi.org/10.1063/5.0159431.

[24] Y. Tian, Z. Liang, Y. Cai, H. Jiang, M. Chen, J. Han, Microstructure and mechanical properties of Ti2Ni alloy fabricated by direct energy deposition, Sci. Technol. Weld. Join. 29 (2024) 47–51. https://doi.org/10.1177/13621718231216674.

[25] L. Yang, M. Wen, X. Dai, G. Cheng, K. Zhang, Ultrafine Ceramic Grains Embedded in Metallic Glass Matrix: Achieving Superior Wear Resistance via Increase in Both Hardness and Toughness, ACS Appl. Mater. Interfaces 10 (2018) 16124–16132. https://doi.org/10.1021/acsami.8b02338.

[26] R. Neupane, Z. Farhat, Wear Resistance and Indentation Behavior of Equiatomic Superelastic TiNi and 60NiTi, Mater. Sci. Appl. 6 (2015) 694–706. https://doi.org/10.4236/msa.2015.67071.

[27] R.C.D. Richardson, The wear of metals by relatively soft abrasives, Wear 11 (1968) 245–275. https://doi.org/10.1016/0043-1648(68)90175-0.

[28] W. Ni, Y.-T. Cheng, M. Lukitsch, A.M. Weiner, L.C. Lev, D.S. Grummon, Novel layered tribological coatings using a superelastic NiTi interlayer, Wear 259 (2005) 842–848. https://doi.org/10.1016/j.wear.2005.01.015.

[29] A. Leyland, A. Matthews, On the significance of the H/E ratio in wear control: a nanocomposite coating approach to optimised tribological behaviour, Wear 246 (2000) 1–11. https://doi.org/10.1016/S0043-1648(00)00488-9.

[30] B.D. Beake, The influence of the H/E ratio on wear resistance of coating systems – Insights from small-scale testing, Surf. Coat. Technol. 442 (2022) 128272. https://doi.org/10.1016/j.surfcoat.2022.128272.

[31] N. Cameron, Z. Farhat, Investigation into the wear and dent resistance of Ni/Ti nanolaminates and superelastic NiTi coating, J. Mater. Eng. Perform. 28 (2019) 6033–6041. https://doi.org/10.1007/s11665-019-04377-5.

[32] K.L. Ng, Q.P. Sun, M. Tomozawa, S. Miyazak, Wear behavior of NiTi thin film at micro-scale, Int. J. Mod. Phys. B 24 (2010) 85–93. https://doi.org/10.1142/S0217979210064010.

[33] H. Tobushi, K. Tanaka, T. Hori, T. Sawada, T. Hattori, Pseudoelasticity of TiNi shape memory alloy : Dependence on maximum strain and temperature, JSME Int. J. Ser Mech. Mater. Eng. 36 (1993) 314–318. https://doi.org/10.1299/jsmea1993.36.3_314.

[34] L. Hou, D.S. Grummon, Transformational superelasticity in sputtered titanium-nickel thin films, Scr. Metall. Mater. 33 (1995) 989–995. https://doi.org/10.1016/0956-716X(95)00311-I.

[35] C. Zhang, Z.N. Farhat, Sliding wear of superelastic TiNi alloy, Wear 267 (2009) 394–400. https://doi.org/10.1016/j.wear.2008.12.093.

[36] H. Vafaeenezhad, S. Aliakbari-Sani, S.H. Seyedein, A. Ghosh, A.R. Eivani, Flow behavior and strain rate sensitivity assessment of γ and γ′ phases in Co–Al–W-based superalloy using experimental and computational approaches, J. Mater. Res. Technol. 18 (2022) 4617–4630. https://doi.org/10.1016/j.jmrt.2022.03.166.

[37] W. Xiufang, Y. Xiaoping, G. Zhendan, Z. Yinchang, S. Hongwei, Nanoindentation characterization of mechanical properties of ferrite and austenite in duplex stainless steel, Adv. Mater. Res. 24–25 (2007) 1165–1170.

[38] Z. Wang, J. Zhang, H.U. Hassan, J. Zhang, Y. Yan, A. Hartmaier, T. Sun, Coupled effect of crystallographic orientation and indenter geometry on nanoindentation of single crystalline copper, Int. J. Mech. Sci. 148 (2018) 531–539. https://doi.org/10.1016/j.ijmecsci.2018.09.007.

[39] L. Zhu, B. Xu, H. Wang, C. Wang, D. Yang, Measurement of mechanical properties of 1045 steel with significant pile-up by sharp indentation, J. Mater. Sci. 46 (2011) 1083–1086. https://doi.org/10.1007/s10853-010-4876-7.

[40] A. Liu, Q. Pan, M. Chen, W. Xu, W. Chen, An investigation on the relationships between hardness, elas- ticmodulus and the work of 7075 aluminium alloy by nanoindentation, J. Phys. Conf. Ser. 2044 (2021) 012106. https://doi.org/10.1088/1742-6596/2044/1/012106.

[41] X.Y. Li, J.R. Ye, B. Tang, Study of the Ion Nitrided Layer on Ti-6Al-4V substrate, Adv. Mater. Res. 79–82 (2009) 695–698. https://doi.org/10.4028/www.scientific.net/AMR.79-82.695.

[42] M. Liu, Q. Zheng, X. Wang, C. Xu, Characterization of Distribution of Microstructure and Micro-mechanical Properties of Nickel-Based Single Crystal Superalloy Within the Shot-Peened Layer, Met. Mater. Int. 29 (2023) 2257–2286. https://doi.org/10.1007/s12540-023-01388-9.

[43] M. Zhang, F. Li, B. Chen, S. Wang, Investigation of micro-indentation characteristics of P/M nickel-base superalloy FGH96 using dislocation-power theory, Mater. Sci. Eng. A 535 (2012) 170–181. https://doi.org/10.1016/j.msea.2011.12.060.

[44] J. Nohava, B. Bonferroni, G. Bolelli, L. Lusvarghi, Interesting aspects of indentation and scratch methods for characterization of thermally-sprayed coatings, Surf. Coat. Technol. 205 (2010) 1127–1131.

https://doi.org/10.1016/j.surfcoat.2010.08.086.

[45] J.G. La Barbera-Sosa, Y.Y. Santana, M.H. Staia, D. Chicot, J. Lesage, J. Caro, G. Mesmacque, E.S. Puchi-Cabrera, Microstructural and mechanical characterization of Ni-base thermal spray coatings deposited by HVOF, Surf. Coat. Technol. 202 (2008) 4552–4559. https://doi.org/10.1016/j.surfcoat.2008.04.041.

[46] C. Leither, J. Risan, M. Bashirzadeh, F. Azarmi, Determination of the elastic modulus of wire arc sprayed alloy 625 using experimental, analytical, and numerical simulations, Surf. Coat. Technol. 235 (2013) 611–619. https://doi.org/10.1016/j.surfcoat.2013.08.033.

[47] P. Poza, C.J. Múnez, M.A. Garrido-Maneiro, S. Vezzù, S. Rech, A. Trentin, Mechanical properties of Inconel 625 cold-sprayed coatings after laser remelting. Depth sensing indentation analysis, Surf. Coat. Technol. 243 (2014) 51–57. https://doi.org/10.1016/j.surfcoat.2012.03.018.

[48] J.A. Greenwood, Analysis of elliptical Hertzian, Tribol. Int. 30 (1997) 235–237.

[49] N. P. Suh, The delamination theory of wear, Wear 25 (1973) 111–124. https://doi.org/10.1016/0043-1648(73)90125-7.

[50] K.G. Budinski, Surface engineering for wear resistance, Englewood Cliffs, N.J. : Prentice Hall, 1988. http://archive.org/details/surfaceengineeri0000budi (accessed December 30, 2024).

[51] J.A. Greenwood, J.B.P. Williamson, Contact of nominally flat surfaces, Proc. R. Soc. Lond. Ser. Math. Phys. Sci. 295 (1966) 300–319. https://doi.org/10.1098/rspa.1966.0242.

[52] Y.-T. Cheng, C.-M. Cheng, Relationships between hardness, elastic modulus, and the work of indentation, Appl. Phys. Lett. 73 (1998) 614–616. https://doi.org/10.1063/1.121873.

[53] Y.-T. Cheng, Z. Li, C.-M. Cheng, Scaling relationships for indentation measurements, Philos. Mag. A 82 (2002) 1821–1829. https://doi.org/10.1080/01418610208235693.

[54] Y.-T. Cheng, C.-M. Cheng, Scaling, dimensional analysis, and indentation measurements, Mater. Sci. Eng. R Rep. 44 (2004) 91–149. https://doi.org/10.1016/j.mser.2004.05.001.

Chapter 5

Heat Treatment of NiTi Coatings for Compositional Homogenization and Wear Resistance Improvement

5.1 Introduction

Chapter 4 described the fabrication of NiTi coatings on the surface of Ti using a multi-track electron beam scanning method. However, multi-track scanned coatings still exhibit issues with non-uniform composition distribution, which is considered to be detrimental to wear resistance. To improve the homogeneity and further enhance the wear resistance, post-process is required for these coatings.

Heat treatment is a common post-processing method for coatings such as thermal spray coatings, cold spray coatings, and magnetron sputtered coatings. This can improve coating properties by eliminating residual stresses within the coating [1–3], achieving a more uniform phase distribution and an ordered crystal structure [4–6], improving mechanical properties such as hardness and interface bonding [7,2,5], increasing wear resistance [5,6] and enhancing corrosion resistance [2].

Furthermore, studies indicate that the microstructure and mechanical properties of additive-manufactured NiTi can be modulated through heat treatment. Following annealing and aging treatment, the recoverable strain of additive-manufactured superelastic NiTi increases [8,9] and strain cycling stability improves [10]. These effects both contribute to the wear resistance of NiTi. Therefore, heat treatment is expected to be a proper post-process to mitigate the non-uniformity issues observed in multi-tack scanned coatings and further improve their wear resistance.

This chapter investigates the effects of heat treatment on the microstructure, phase

composition and wear resistance of multi-track scanned NiTi coatings. These coatings were fabricated as described in Chapter 4. The changes that occurred in the annealed and age-treated coatings were then compared with the original coatings. Additionally, these two types of coating are referred to as Ni-rich and Ti-rich EB-scanned coatings in this chapter, according to their respective compositions.

In this chapter, the effects of heat treatment on the microstructure, phase composition, and wear resistance of multi-track scanned NiTi coatings are presented and discussed.

5.2 Methods

5.2.1 Preparation of multi-track scanned NiTi coatings

The multi-track scanned coatings fabricated in Chapter 4 using 126 W and 138 W electron beams were used as samples for heat treatment and subsequent investigations in this chapter. Detailed preparation procedures and parameter settings are described in Chapter 4.

5.2.3 Heat treatment

To reduce the inhomogeneity and residual stress in the coating, the EB-scanned coatings were sealed in an evacuated quartz tube and then annealed at 900 ℃ for 10 minutes, followed by quenching in ice water. To induce Ni_4Ti_3 precipitation for strengthening, the annealed specimens were subjected to aging at 400 ℃ for 60 minutes using identical sealing and quenching procedures as in annealing.

5.2.4 Microstructural characterization

The coating samples were cut perpendicular to the beam-scanning direction for cross-sectional observation by field-emission scanning electron microscopy (FE-SEM;

JSM 6500, JEOL, Japan). The elemental distributions were analyzed by energy-dispersive X-ray spectroscopy (EDS). X-ray diffractometry (XRD; SmartLab SE diffractometer, Rigaku, Japan) identified the crystallographic phases of the coatings. In the XRD tests, the ray source was Cu Kα and the 2theta scanning range was 20°–80° with a step size of 0.01°. The test for each sample was conducted by 3 times in the same condition. The formed Ni-Ti intermetallic phases were studied by evaluating the equilibrium phase characteristics of the Ni-Ti binary alloy using Thermo-Calc Software (version 2022b) with a thermodynamic database for Ti alloys (TCTI4) [11].

5.2.5 Nanoindentation tests

Nanoindentation tests were performed using a nanoindentation tester (ENT-1100a, Elionix, Japan) equipped with a Berkovich indenter to evaluate the indentation properties of the EB-scanned coating. Before the tests, the surfaces of specimens were ground using P120–P4000-grit SiC abrasive papers and then polished using 50 nm alkaline colloidal silica suspension. The Nanoindentation tests were performed at 26 °C inside the device equipped with a shield case to prevent thermal drift. A total of 50 equally spaced points were selected on each sample to repeat the test under identical parameters. Then, the results were averaged to eliminate the effect of randomness. The peak load was 50 mN, and the loading rate was 5 mN/s. The Berkovich indenter[12] with an apex angle of 65.03° was used, and the following relationship between the indenter contact area (A) and indentation depth (h) was employed:

$$A = 3\sqrt{3}\tan^2(65.03°)\cdot(h+\Delta h)^2\,. \tag{5.1}$$

Here, Δh is the indenter tip correction value calculated using the Sawa–Tanaka method [13] based on the indentation results of a standard fused silica sample. From the obtained results, Young's modulus (E) and hardness (H) were calculated according

to the ISO 14577-1 protocol [14]. Moreover, depth recovery ratio ($\eta_{d,h}$) is defined as the ratio of recoverable indentation depth to indenter displacement at maximum load[15]. It was calculated as follows:

$$\eta_{d,h} = \frac{h_{\max} - h_{\mathrm{p}}}{h_{\max}}, \tag{5.2}$$

where $h_{\max}$ and h_{p} are the maximum penetration depth of the indenter during the indentation tests and the permanent depth after load removal, respectively.

5.2.6 Sliding wear tests

Sliding wear tests were conducted according to the ASTM G133-22 standard [16] on an oscillation sliding tester (OST3000, Rhesca, Japan) to evaluate the wear resistance of the coatings. Before the tests, the surfaces of specimens were ground using P120–P4000-grit SiC abrasive papers and then polished using 50 nm alkaline colloidal silica suspension. The tests were conducted under a constant load (L) of 50 N using an alumina ceramic indenter. The diameter of the indenter is 9.5 mm and the hardness is 2085 $HV_{0.1}$ [17].The specimens were subjected to a 1 Hz oscillation with an 8 mm amplitude. The test duration for each specimen was 625 s, resulting in a total sliding distance (D) of 10 m (= 8 mm × 2 × 625 s). The temperature inside the tester during the test was maintained at 26 °C and the relative humidity was maintained at 50%. The same wear test was conducted 2 times on each specimen. The friction coefficient (μ) was evaluated as follows:

$$\mu = \frac{F_{\mathrm{Z}}}{F_{\mathrm{T}}}, \tag{5.3}$$

where F_{Z} and F_{T} are normal and tangential loads, respectively. Both were measured and continuously recorded by the integrated sensor during the tests.

Specific wear rate (W_{s}) is an indicator of the wear resistance of a material[18]. The

W_s of specimens was evaluated as follows:

$$W_s = \frac{V}{LD}, \tag{5.4}$$

where V, L, and D are volume loss, applied load, and sliding distance, respectively. V was measured by the confocal laser scanning microscope after the sliding test. The worn surfaces were also observed using SEM and EDS. A commercially available superelastic nitinol (Ni 50.6 at. %, Ti 49.4 at. %; Seemine Keli, Lanzhou, China) as well as the substrate, CP-Ti, were also tested as control specimens.

5.3 Results and discussions

5.3.1 Phase evolution during heat treatment

Fig. 5.1 shows the XRD patterns of electron-beam (EB)-scanned coatings in three states: "as-scanned," "annealed", and "annealed, aged". Fig. 5.1a shows the XRD patterns of the Ni-rich EB-scanned coatings (electron beam power, P, of 126 W) in three heat treatment state. Fig. 5.1b shows the XRD patterns of the Ti-rich EB-scanned coatings (electron beam power, P, of 138 W). All EB-scanned coatings generally consist of the NiTi phase, regardless of the electron beam power or heat treatment state.

However, the relatively high Ni concentration resulted in a significant presence of the hexagonal $D0_{24}$-Ni_3Ti phase alongside the cubic $B2$-NiTi phase in the as-scanned Ni-rich coating, as demonstrated by the initial XRD pattern in Fig. 5.1a. The second pattern shown in Fig. 5.1a illustrates the annealed Ni-rich coating pattern, where the $D0_{24}$-Ni_3Ti peaks appear narrower and more intense, indicating coarsening and further $D0_{24}$-Ni_3Ti generation during annealing. The melt pool undergoes non-equilibrium solidification due to the steep temperature gradient and rapid solidification rate during EB scanning process, reaching up to 10^7 K/m and 10 m/s, respectively [19]. Therefore,

the rapid solidification process enables more Ni atoms trapped in the NiTi phase compared to the equilibrium state, preventing phase separation [20]. During annealing, the Ni atoms that are trapped start to precipitate during non-equilibrium solidification, leading to the formation of additional $D0_{24}$-Ni_3Ti. Notably, after annealing, peaks for Ni_4Ti_3—a metastable phase typically formed only during the aging of Ni-rich NiTi—also appear. The formation of this phase may stem from interfacial reactions between the $D0_{24}$-Ni_3Ti and NiTi or $C15$-$NiTi_2$ phases during high-temperature interdiffusion. A similar phenomenon was observed by Babaei-Dehkordi et al. [21] in Ni-Ti diffusion couples. The third pattern shown in Fig. 5.1a illustrates the annealed and aged Ni-rich coating pattern, with no new peaks compared to the annealed pattern. However, the intensities of the $D0_{24}$-Ni_3Ti and Ni_4Ti_3 peaks have slightly increased, indicating further precipitation of these phases from the Ni-supersaturated NiTi matrix during aging. The precipitation of Ni-rich phases lowers the Ni concentration in the matrix, promoting stress-induced martensitic transformation and thereby enhancing superelasticity in the NiTi phase [22]. Additionally, these phases are usually dispersed as fine particles, providing precipitation strengthening and increasing the mechanical strength and hardness of the coating [23].

The relatively high Ti concentration resulted in a high amount of cubic $C15$-$NiTi_2$ phase alongside the monoclinic $B19'$-NiTi phase in the as-scanned Ti-rich coating, as shown by the first XRD pattern in Fig. 5.1b. The second pattern shown in Fig. 5.1b illustrates the annealed Ti-rich coating pattern, where the peaks become narrower but retain their number and position, indicating that grain growth is the primary change. Notably, new peaks with low intensity appear for the $D0_{24}$-Ni_3Ti phase at $2\theta = 43.39°$. Though the coating is Ti-rich in total, due to inhomogeneity in the coating (as detailed in Section 5.3.2), small amounts of $D0_{24}$-Ni_3Ti still precipitated from Ni-rich NiTi

regions during annealing. The third pattern shown in Fig. 5.1b illustrates the annealed and aged Ti-rich coating pattern, where the $D0_{24}$-Ni_3Ti peak intensity increases significantly, and the peak for Ni_4Ti_3 newly appears. Since Ni solubility in the NiTi phase is minimal at 400 °C, supersaturated Ni in Ni-rich regions precipitates, forming $D0_{24}$-Ni_3Ti and Ni_4Ti_3 phases—consistent with the behavior in the Ni-rich coating during aging. As in Ni-rich coatings, these precipitated phases precipitated in Ti-rich coatings can also increase the mechanical strength and hardness of the coating.

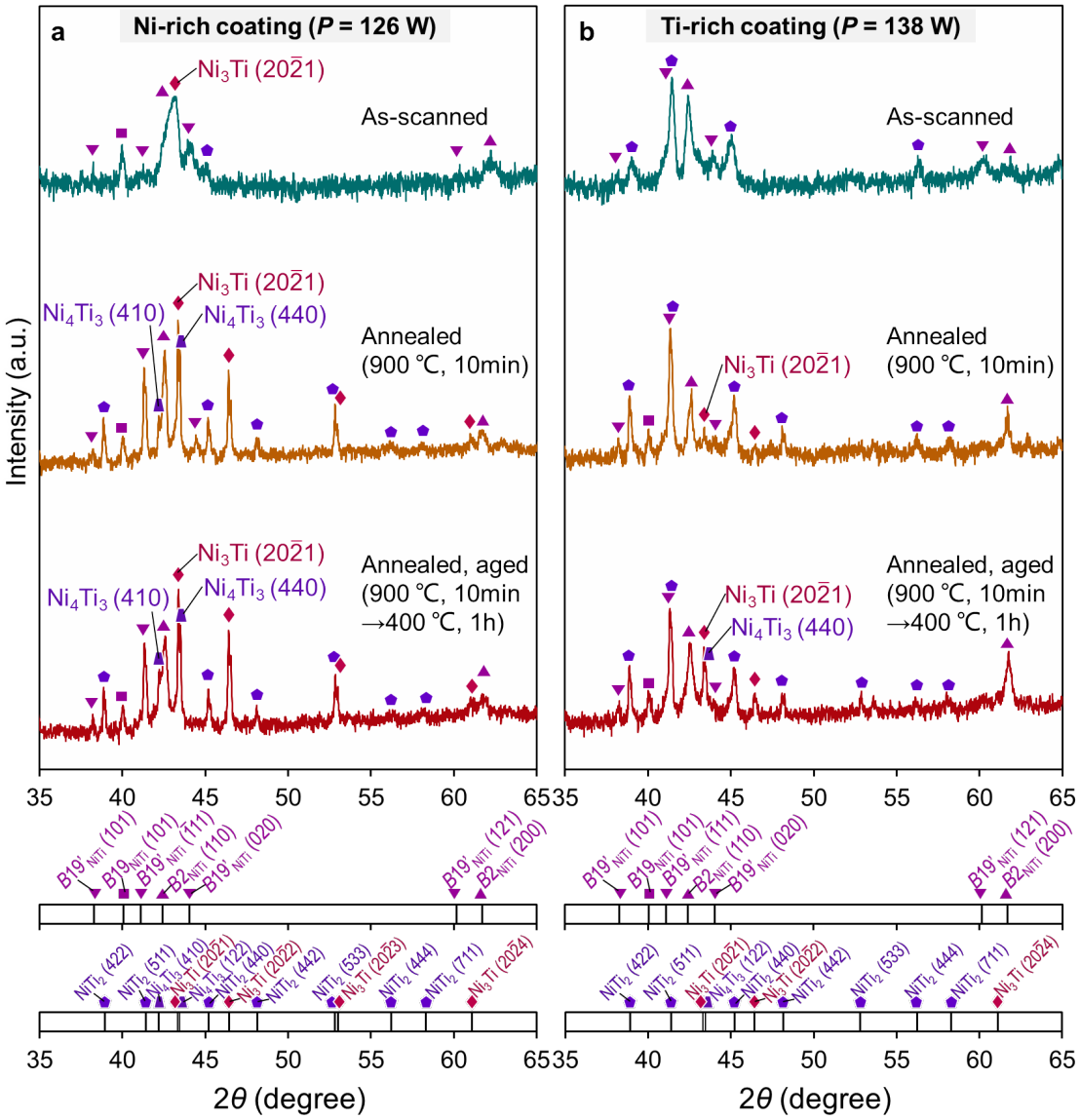

Fig. 5.1. XRD patterns of EB-scanned coatings under the state of as-scanned, annealed, annealed and aged. The scanning conditions for the as-scanned coatings are as follows: (a) P = 126 [W], resulting in a Ni-rich coating; and (b) P = 138 [W], resulting in a Ti-rich coating.

5.3.2 Evolution of microstructure and elemental distribution

Fig. 5.2 shows BSE and EDS mapping images of the cross-section of the electron-beam(EB)-scanned coating in its as-scanned, annealed, and annealed and aged states. The cross-section is perpendicular to the scanning melt track, and each image shows four melt tracks. As seen in Fig. 5.2a1, the brightness distribution of the as-scanned Ni-rich coating is uniform, indicating homogeneous elemental and microstructural

distributions. However, dark streaks (indicated by black arrows) are visible at some melt track junctions. The corresponding EDS mapping data (Fig. 5.2a2) reveal that these dark streaks have below-average Ni concentrations, approximately 33 at.%, and correspond to Ti concentrations around 66 at.%. Combined with XRD data, this confirms the presence of the $NiTi_2$ phase. The BSE image of the as-scanned Ti-rich coating (Fig. 5.2d1) shows that these dark regions are also present at every melt track junction and cover significantly larger areas than in the Ni-rich coating. The corresponding EDS mapping data (Fig. 5.2d2) shows that the Ti concentration in these dark regions is also around 66 at.%, which corresponds to the $NiTi_2$ phase identical to that in the Ni-rich coating. These results suggest that the $NiTi_2$ phase accumulates at melt track junctions during electron beam scanning, regardless of whether the coating is Ni-rich or Ti-rich. Furthermore, this accumulation becomes more pronounced as the Ti concentration in the coating increases. Although the $NiTi_2$ phases are harder than the NiTi phase matrix, they are prone to brittle fracture. Cracks also tend to initiate at these locations, which is harmful to the coating's wear resistance [24].

As shown in Fig. 5.2b1, the brightness distribution across the cross-section of the annealed Ni-rich coating has become more uniform, and the dark streak at the melt track junction (indicated by black arrows) has nearly disappeared. Corresponding EDS mapping also reveals a more uniform elemental distribution. This indicates that, during annealing, Ni atoms diffused from the NiTi phase into the $NiTi_2$ phase, where they reacted and transformed it into the same NiTi phase as the matrix. This improved the phase distribution within the coating. The annealed Ti-rich coating shown in Fig. 5.2e1 also exhibits significantly enhanced uniformity compared to the as-scanned coating. The dark streak area at the melt track junction has noticeably shrunk, and regions with Ti concentrations reaching 66 at.% in the EDS mapping image have also significantly

decreased. This is also presumed to result from phase reactions caused by solid-state diffusion during annealing, similar to those observed in the Ni-rich coating. However, due to the higher abundance of the $NiTi_2$ phase in the Ti-rich coating, it is difficult for all of the $NiTi_2$ phase to react, leaving some residual phases. As can be seen in Fig. 5.2c3 and 5.2f3, the cross-sectional morphology of the annealed and aged Ni-rich and Ti-rich coatings does not differ significantly from that of the annealed coatings. This is because, at an aging temperature of 400 °C, the diffusion coefficients of the Ni and Ti elements within the NiTi phase are extremely low [25]. This means that solid-state diffusion is insufficient to significantly change the cross-sectional morphology.

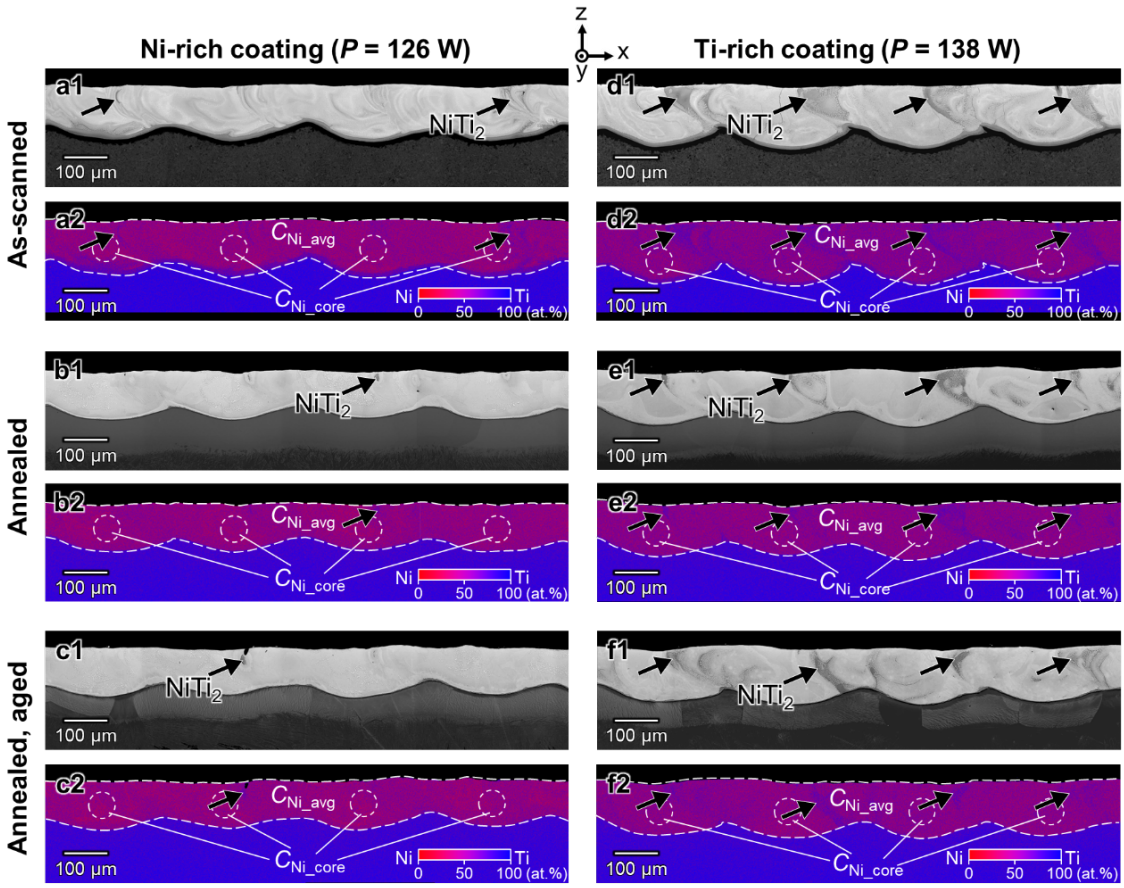

Fig. 5.2. BSE images (a1-f1) and EDS mapping (a2-f2) of the cross section of four melt tracks in (a–c) Ni-rich EB-scanned coatings (P = 126 W) and (d–f) Ti-rich EB-scanned coatings (P = 138 W) undergone different heat treatment states. (a, d) As-scanned coatings. (b, e) Annealed coatings. (c, f) Annealed and aged coatings. The black arrows in the BSE image indicate the dark streaks at the junctions of the melt tracks.

Fig. 5.3 shows the changes in the average Ni concentration (C_{Ni_avg}, at.%) and the core Ni concentration of melt track (C_{Ni_core}, at.%) within the EB-scanned coating during heat treatment. The regions selected for calculating these two characteristic values are indicated in Fig. 5.2. The value of C_{Ni_avg} is calculated using EDS data across all regions of each coating cross-section. The value of C_{Ni_core} is calculated using EDS data from a circular region measuring around 60 μm in diameter at the core of the melt tracks in the coating. It can be observed that C_{Ni_avg} increases in both Ni-rich and Ti-rich coatings after annealing, while remaining generally unchanged after aging.

However, C_{Ni_core} did not exhibit a trend similar to C_{Ni_avg}, showing no significant change after annealing or aging. This indicates that, although changes occurred in the coating's average composition, no large-scale solid-state diffusion altering the matrix composition of the coating occurred during annealing and aging. The specific reasons for this result will be analyzed below in the observation of the coating's microstructure (Fig. 5.4). In addition, even when the C_{Ni_avg} of the Ti-rich coating fell below 50 at.%, C_{Ni_core} remained slightly above 50 at.% throughout the entire heat treatment process. This explains why the $NiTi_2$ phase is reduced at melt track junctions after annealing, and why the Ni_3Ti and Ni_4Ti_3 phases precipitate after aging, in the Ti-rich coating.

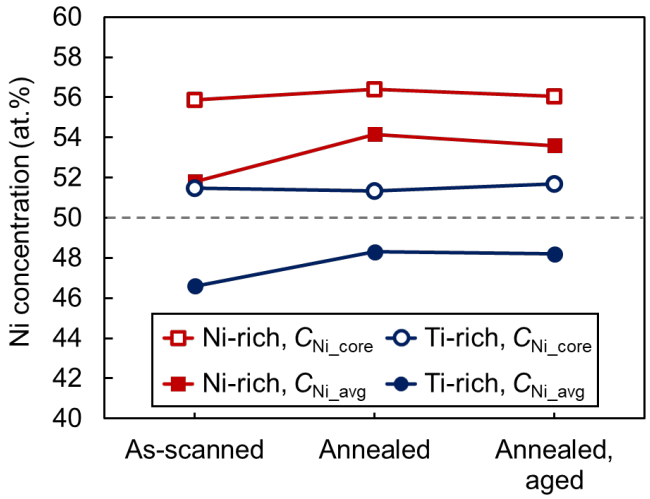

Fig. 5.3. Variation in the average Ni concentrations (C_{Ni_avg}, at.%) and the core Ni concentration of melt track (C_{Ni_core}, at.%) in the EB-scanned coatings under different heat treatment states. The area selected for calculating C_{Ni_avg} and C_{Ni_core} are shown in Fig. 5.2.

Fig. 5.4 shows magnified BSE images of the EB-scanned coating in its as-scanned, annealed and annealed and aged states, alongside EDS line-scanning data taken vertically across the cross-section. As can be seen in Fig. 5.4a3 and 5.4d3, a layer of dark structure is present at the edges of the Ni-rich and Ti-rich coatings in their as-scanned state. EDS data from Fig. 5.4a2 and 5.4d2 show that the Ni concentration in

this layer ranges from 30 to 40 at.%, indicating that it is primarily composed of the $NiTi_2$ phase. It is suggested that this layer is a reaction layer formed through reaction between the CP-Ti substrate and liquid metal in the molten pool during electron beam scanning. As can be seen in Fig. 5.4b3 and 5.4e3, the $NiTi_2$ phase reaction layer has disappeared after annealing treatment. Comparing the EDS line scan data in Fig. 5.4a2 and 5.4d2 with that in Fig. 5.4b2 and 5.4e2 shows that the coating thickness has decreased after annealing, with the reduction precisely matching the thickness of the reaction layer. This indicates that, during annealing, solid-state diffusion transformed the $NiTi_2$ phase in the reaction layer into a pure Ti phase identical to the substrate. Consequently, the original melt track edge became invisible and the boundary between the NiTi matrix and the $NiTi_2$ reaction layer became the new boundary between the coating and the substrate. This makes it appear as though the melt track depth has reduced. This explains why the C_{Ni_avg} of the coating increases after annealing. The region used to calculate the C_{Ni_avg} of the as-scanned coating includes the $NiTi_2$ reaction layer at the melt track boundary, whereas the region used to calculate the C_{Ni_avg} of the annealed coating excludes this reaction layer. Additionally, EDS line scan data reveal that the Ni concentration within the coating remains almost unchanged after annealing, which is consistent with the C_{Ni_core} trend shown in Fig. 5.3. Meanwhile, the substrate, which contained no Ni prior to annealing, develops a Ni-gradient layer approximately 80 μm thick post-annealing, with Ni concentration decreasing vertically. This occurs because, in the Ni-Ti system, Ni diffusion almost exclusively occurs in one direction, from Ni-rich regions to Ti-rich regions [21]. Furthermore, the integrated diffusion coefficient (calculated using the Wagner method) of the $NiTi_2$ phase (3.53×10^{-12} m^2/s) is significantly higher than that of the NiTi (18.1×10^{-15} m^2/s) and Ni_3Ti (6.2×10^{-15} m^2/s) phases [21].

As shown in Fig. 5.4a3 and 5.4a4, the as-scanned Ni-rich coating matrix exhibits a cellular structure. Reticular bright structures (indicated by white arrows) are distributed along the cell boundaries, suggesting that the Ni content of these structures is considerably higher than that of the NiTi phase matrix. Together with the XRD patterns from the previous section, these bright structures can be identified as the Ni_3Ti phase. In the annealed Ni-rich coating (Fig. 5.4b3 and 5.4b4), the reticular structures observed in the as-scanned state have disappeared. Instead, needle-like or granular bright structures appear in some area (indicated by white arrows). EDS line-scanning data (Fig. 5.4b2) reveal abrupt increases in Ni concentration where the scan line traverses these structures (indicated by white arrows). Together with the XRD patterns of the annealed state from the previous section, these needle-like or granular structures are also identified as the Ni_3Ti phase. The morphological transformation of the Ni_3Ti phase is the result of the Oswald ripening process occurring within the coating during annealing [26]. At 900 °C, this process manifests as dissolution of the Ni_3Ti phase in the NiTi phase matrix in certain regions of the coating, followed by re-precipitation on the surfaces of nearby Ni_3Ti particles. This leads to Ni_3Ti grain coarsening. The Ni_3Ti phase exhibits significantly higher hardness than the Ni_3Ti matrix, but inferior toughness [27]. It is speculated that converting the reticular Ni_3Ti phase distributed at cell boundaries into needle-like or granular structures could enhance the toughness of the coating and reduce the risk of cracking. Furthermore, these coarsened, needle-like Ni_3Ti phases provide a framework for the coating, thereby increasing hardness and improving wear resistance.

As discussed earlier, $NiTi_2$ phase at the melt track boundary of the as-scanned state layer can also be observed in Fig. 5.4a4 and 5.4d4. In the Ni-rich coating (Fig. 5.4a4), $NiTi_2$ phase streaks at the melt track boundary are embedded between NiTi dendrites,

exhibiting a width of less than 1 μm but extending tens of micrometers in length (indicated by black arrow). In the Ti-rich coating (Fig. 5.4d4), the gaps between the dendrites of the NiTi phase at the melt track junction are wider and are filled with the $NiTi_2$ phase exceeding 10 μm at their widest points. Additionally, Fig. 5.4d3 reveals a $NiTi_2$ phase branch protrudes from the reaction layer at the melt track boundary into the interior of the Ti-rich coating. Fig. 5.4b4 shows that after annealing, the $NiTi_2$ phase in the Ni-rich coating is significantly reduced, with the remaining phase coarsening to form a grain approximately 2 μm wide and 10 μm long. In Fig. 5.4e4, due to Ni diffusion, the $NiTi_2$ phase at the melt track junction in the Ti-rich coating also markedly decreased after annealing. NiTi phase dendrites integrated through coarsening, reducing the number of grain boundaries separated by $NiTi_2$ phases. Similarly, the $NiTi_2$ phase branch protruded from the melt track boundary also disappears. These results indicate that after annealing, the negative effects of $NiTi_2$ on the plasticity, toughness, and wear resistance of the EB-scanned coating are mitigated.

Finally, as shown in Fig. 5.4c and 5.4f, neither the Ni-rich coating nor the Ti-rich coating exhibited any microstructural or elemental distribution changes observable at the micrometer scale after aging compared to the annealed state.

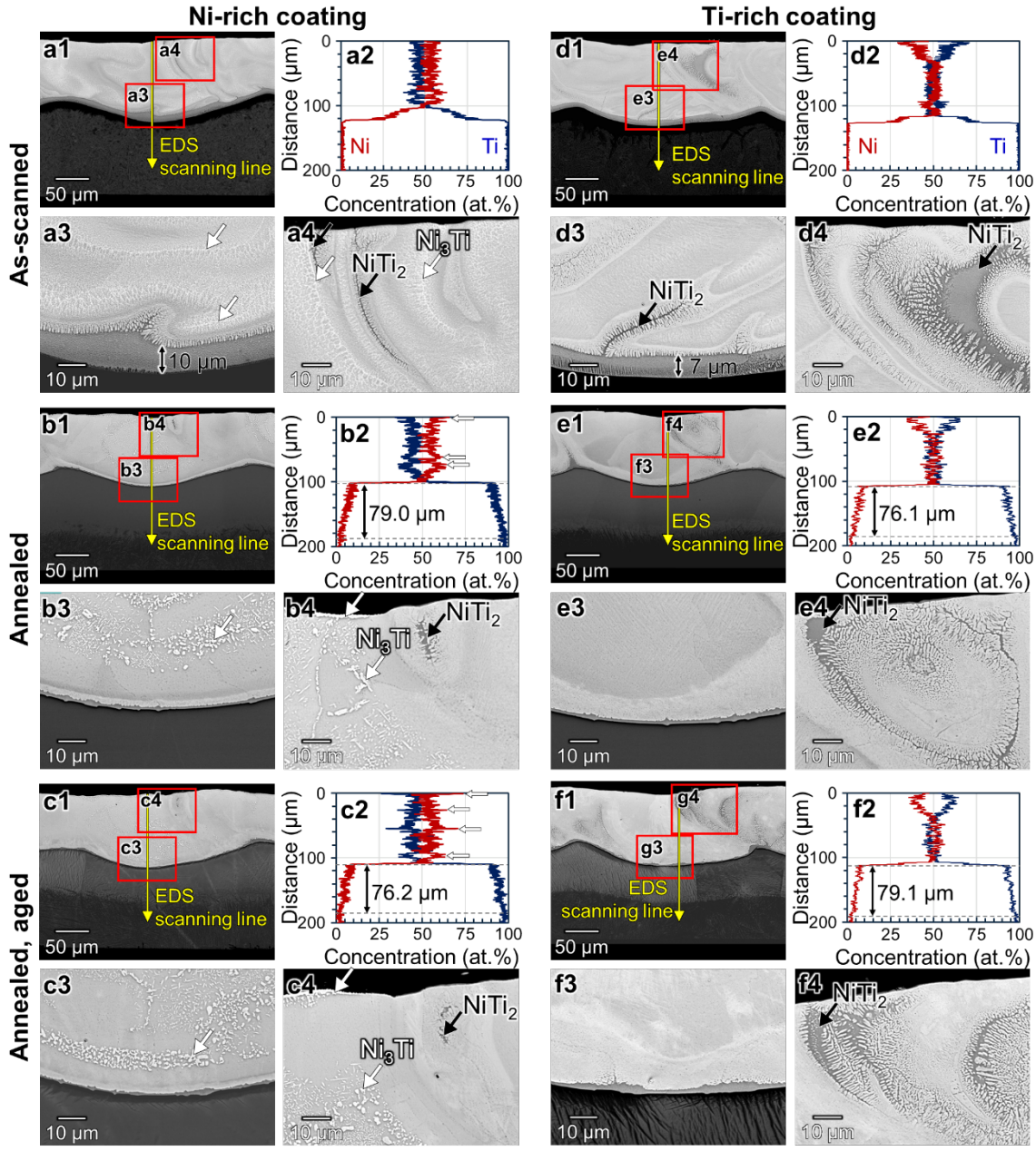

Fig. 5.4. Magnified BSE images and elemental distribution curve along a vertical line across the cross section of (a–c) Ni-rich EB-scanned coatings and (d–f) Ti-rich EB-scanned coatings in different heat treatment states. (a, d) As-scanned coatings. (b, e) Annealed coatings. (c, f) Annealed and aged coatings.

5.3.3 Enhancement of indentation properties by heat treatment

Fig. 5.5 shows the results of nanoindentation tests for Ni-rich and Ti-rich coatings under different heat treatment states. These results are compared with those of superelastic nitinol (SE-NiTi) and the substrate material, CP-Ti. Fig. 5.5a shows the

load-displacement curves from nanoindentation tests for the coatings, NiTi and CP-Ti. To avoid overlapping curves, only the data for the Ti-rich coatings are presented. The maximum indenter penetration depth during loading (h_{max}) and the permanent indentation depth after unloading (h_p) can be inferred from these curves. Fig. 5.5b shows the hardness/Young's modulus ratio (*H/E* ratio) versus the depth recovery ratio ($\eta_{d,h}$) plot for the coatings, SE-NiTi and CP-Ti. Both characteristic values of *H/E* ratio and $\eta_{d,h}$ can be obtained directly by analyzing the load-displacement curve. Hardness (*H*) and Young's modulus (*E*) were calculated using the method specified in ISO 14577-1, and $\eta_{d,h}$ is defined as the ratio of the recoverable indentation depth to the maximum indentation depth (given by Eq. (5.2)). Traditionally, higher hardness has generally been considered to indicate improved wear resistance [28]. However, several recent studies have suggested that the *H/E* ratio [29–31] and the $\eta_{d,h}$ [32–34] are better correlated with wear resistance than hardness alone. The mechanisms demonstrating the correlation between the two indicators and wear resistance is also elucidated in Chapter 4. Therefore, the *H/E* ratio and $\eta_{d,h}$ can be considered more reliable wear resistance indicators.

As shown in Fig. 5.5b, the *H/E* ratio and $\eta_{d,h}$ of as-scanned coatings are significantly higher than those of CP-Ti. Furthermore, each heat treatment step — annealing and aging — further enhances the *H/E* ratio and $\eta_{d,h}$ of the coating. Notably, after annealing and aging, the coating's *H/E* ratio exceeds that of SE-NiTi, and its $\eta_{d,h}$ becomes almost identical to that of SE-NiTi. This suggests that EB-scanned coatings exhibit significantly higher wear resistance than CP-Ti even before heat treatment. The wear resistance of coatings can be further enhanced by both annealing and aging. Eventually, the annealed and aged coatings achieved a level of wear resistance comparable to that of SE-NiTi. Among Ni-rich and Ti-rich coatings, Ti-rich coatings exhibit greater wear

resistance improvement after heat treatment than Ni-rich coatings. At the as-scanned state, the Ni-rich coating has higher *H/E* ratio and $\eta_{d,h}$ than that of the Ti-rich coating. Following each stage of heat treatment, the *H/E* ratio and $\eta_{d,h}$ of both the Ni-rich and Ti-rich coatings improved. However, the increase in the Ni-rich coating was relatively minor, while the increase in the Ti-rich coating was more pronounced. Consequently, after annealing and aging, the *H/E* ratio and $\eta_{d,h}$ of the Ti-rich and Ni-rich coatings were almost identical. This confirms that annealing homogenizes the coating and coarsens the Ni_3Ti phase, while aging promotes Ni_4Ti_3 phase precipitation, collectively enhancing wear resistance. Furthermore, this demonstrates that annealing and aging can narrow the performance gap between Ni-rich and Ti-rich coatings. If applied to large-scale production of coatings, this technique could help to eliminate performance inconsistencies caused by regional variations in coating composition.

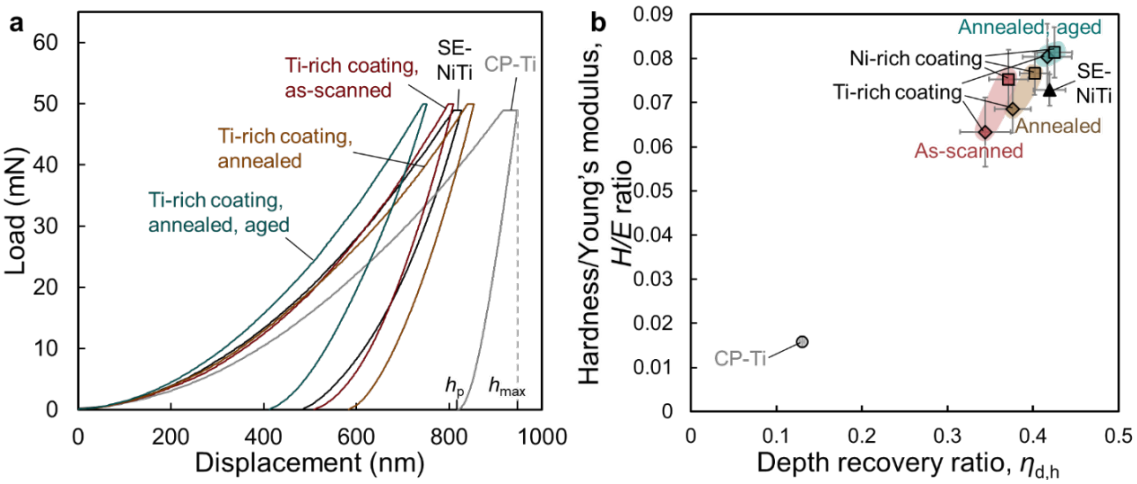

Fig. 5.5. (a) Load-displacement curve and (b) plot of hardness/Young's modulus ratio (*H/E* ratio) versus depth recovery ratio ($\eta_{d,h}$) of CP-Ti, superelastic nitinol (SE-NiTi) and EB-scanned coatings at various heat treatment states.

Fig. 5.6a and 5.6b compares the parameters *H/E* ratio, *H*, and *E* of EB-scanned and heat-treated coatings with other materials such as superelastic nitinol (SE-NiTi)

[29,33,35,36], structural metals (SM) [29,35–44], wear resistant (WR) coatings [45–48], and the NiTi coatings from other studies [5,49]. Commonly used SMs have hardness in the range 1–10 GPa and Young's moduli of approximately 100–300 GPa. WR-coatings are typically used for surface protection of SMs, and their hardness and *H*/*E* ratios are higher than those of most SMs. The *H/E* ratios of the other NiTi coatings, although higher than those of the SMs, are still lower than the average of the WR-coatings. Although SE-NiTi does not exhibit a higher *H* than SMs, WR coatings or other NiTi coatings, its lower *E* gives it a considerably higher *H/E* ratio. The *H/E* ratio of the EB-scanned coatings in this study reached or even exceeded the average level of SE-NiTi prior to heat treatment. This makes their *H/E* ratio higher than that of all SMs, WR-coatings, and other NiTi coatings. Although the *H* value of the EB-scanned coatings increased only slightly after annealing and aging, their *H/E* ratio surpassed that of all SE-NiTi due to the essentially unchanged *E* value after heat treatment.

Fig. 5.6c also shows a comparison of the depth recovery ratio ($\eta_{d,h}$) for different materials. The results show that WR-coatings exhibit a higher $\eta_{d,h}$ than the average level of SMs; however, the highest $\eta_{d,h}$ for either material only reaches 0.3. However, the $\eta_{d,h}$ of all SE-NiTi is greater than 0.3, meaning it is higher than that of all SMs and WR-coatings. This difference arises from the superelastic properties of SE-NiTi, which enable a high reversible strain limit exceeding the elastic strain limit of conventional metals [4,50], leading to significantly higher $\eta_{d,h}$ values. Although the $\eta_{d,h}$ values of other NiTi coatings are higher than those of SMs and WR-coatings, they only just reach the minimum level of SE-NiTi. The EB-scanned coating in this study was at the same level as other NiTi coatings before heat treatment. However, following annealing and aging treatment, the $\eta_{d,h}$ of the EB-scanned coating surpassed that of the other NiTi coatings, reaching the average level of SE-NiTi.

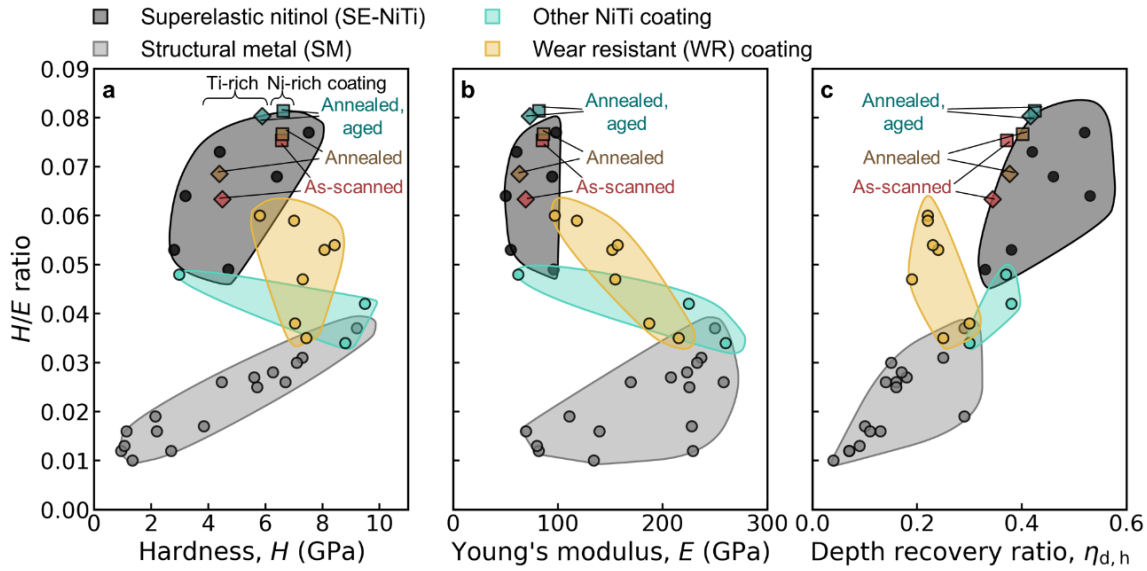

Fig. 5.6. Comparison of the indentation properties among the EB-scanned heat-treated coatings in the present study, superelastic nitinol (SE-NiTi) [29,33,35,36], structural metal (SM) [29,35–44], wear resistant (WR) coating [45–48], and other NiTi coating [5,49]. Plot of *H/E* ratio vs. (a) hardness (*H*), (b) Young's modulus (*E*), and (c) depth recovery ratio ($\eta_{d,h}$).

5.3.4 Improvement of wear resistance by heat treatment

Fig. 5.7 shows the results of the sliding wear test for CP-Ti, superelastic nitinol (SE-NiTi) and EB-scanned coatings in various heat treatment states. The results demonstrate that the specific wear rate (W_s) of the EB-scanned coating before heat treatment is notably lower than that of CP-Ti, but still slightly higher than that of SE-NiTi. Following annealing and aging treatment, the W_s of both the Ti-rich and the Ni-rich coatings decreased significantly. Notably, the W_s of the Ti-rich coating decreased by 51.8% after annealing and aging, compared to the as-scanned coating, while the W_s of the Ni-rich coating decreased by 26.5%. Both values approached the W_s of SE-NiTi. This indicates that heat treatment significantly enhances the wear resistance of EB-scanned coatings, achieving wear resistance nearly equivalent to SE-NiTi. Conversely, the coefficient of friction (CoF) for CP-Ti in sliding friction tests was 0.49; all EB-scanned coatings and SE-NiTi, however, exhibited CoF values of 0.6–0.7, which are

significantly higher than those of CP-Ti. Interestingly, the CoF of the annealed and aged EB-scanned coating decreased markedly compared to the as-scanned coating, dropping from 0.64 to 0.60.

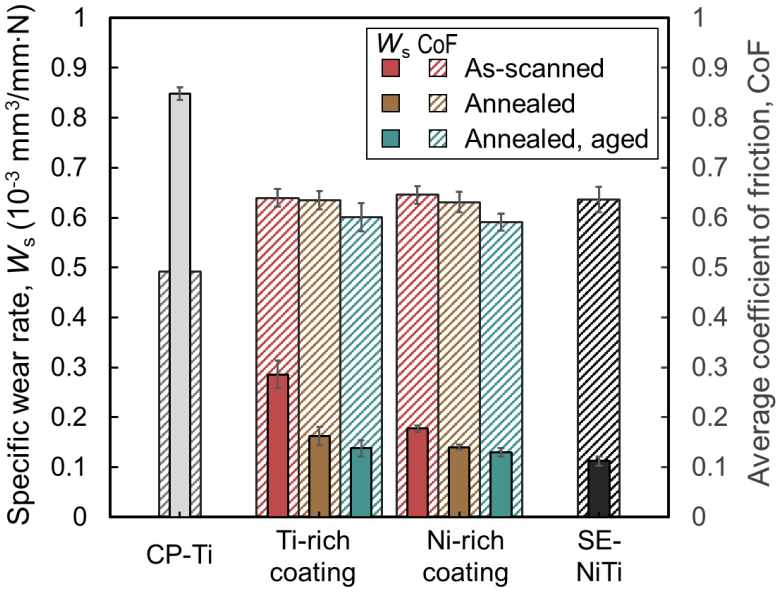

Fig. 5.7. Comparison of specific wear rate (W_s) and coefficient of friction (CoF) of CP-Ti and superelastic nitinol (SE-NiTi) with EB-scanning coatings at various heat treatment states.

Fig. 5.8 shows the worn surfaces of CP-Ti, SE-NiTi and EB-scanned coatings in all heat treatment states. Plate-like debris (indicated by white arrows) can be seen adhering to the worn surfaces of SE-NiTi and all EB-scanned coatings. However, no such debris is present on the CP-Ti wear surface. Corresponding EDS mapping images reveal that these particles contain aluminium, indicating that they originated from the aluminium oxide ceramic indenter and adhered to the surfaces of the SE-NiTi and EB-scanned coatings. This is due to adhesive wear [51] occurring on the alumina indenter side, which leads to alumina debris being transferred from the indenter to the SE-NiTi and EB-scanned coatings. This also explains why their friction coefficients are higher but their W_s are significantly lower.

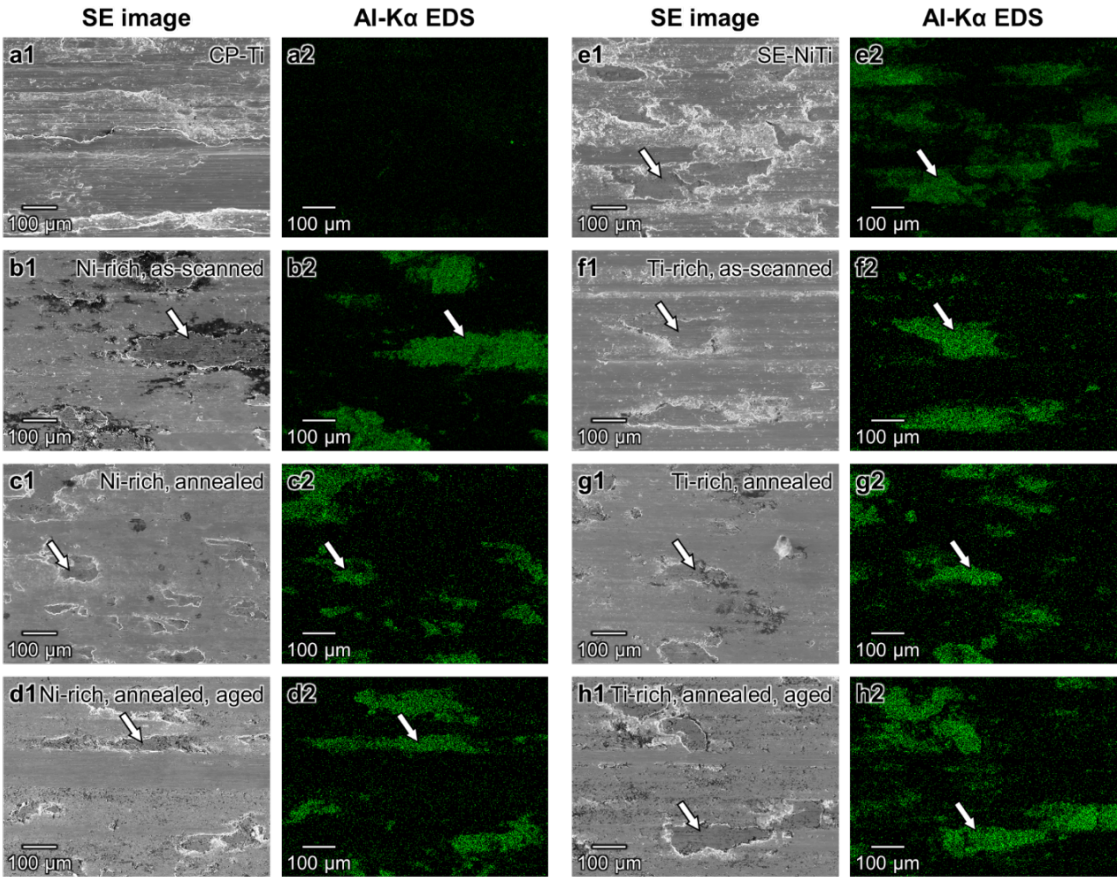

Fig. 5.8 SE images and Al-Kα EDS mapping of the worn surface on (a) CP-Ti substrate, (b) as-scanned Ni-rich coating, (c) annealed Ni-rich coating, (d) annealed and aged Ni-rich coating, (e) superelastic nitinol (SE-NiTi), (f) as-scanned Ti-rich coating, (g) annealed Ti-rich coating, (h) annealed and aged Ti-rich coating.

Fig. 5.9 shows magnified images of the wear surfaces of EB-scanned coatings in various heat treatment states. As can be seen in Fig. 5.9a and 5.9c, the worn surfaces of as-scanned coatings exhibit deep grooves (indicated by the black arrows). The grooves on the Ni-rich surface are shorter and more discontinuous than those on the Ti-rich surface, which are longer, deeper and wider. Fig. 5.9b and 5.9d show that the number of deep grooves on the annealed coating's worn surface has decreased, with a significant reduction in both width and depth. Fig. 5.9c and 5.9e show that the grooves on the worn surface of the coating after annealing and aging became fine and uniform with no individual deep grooves present.

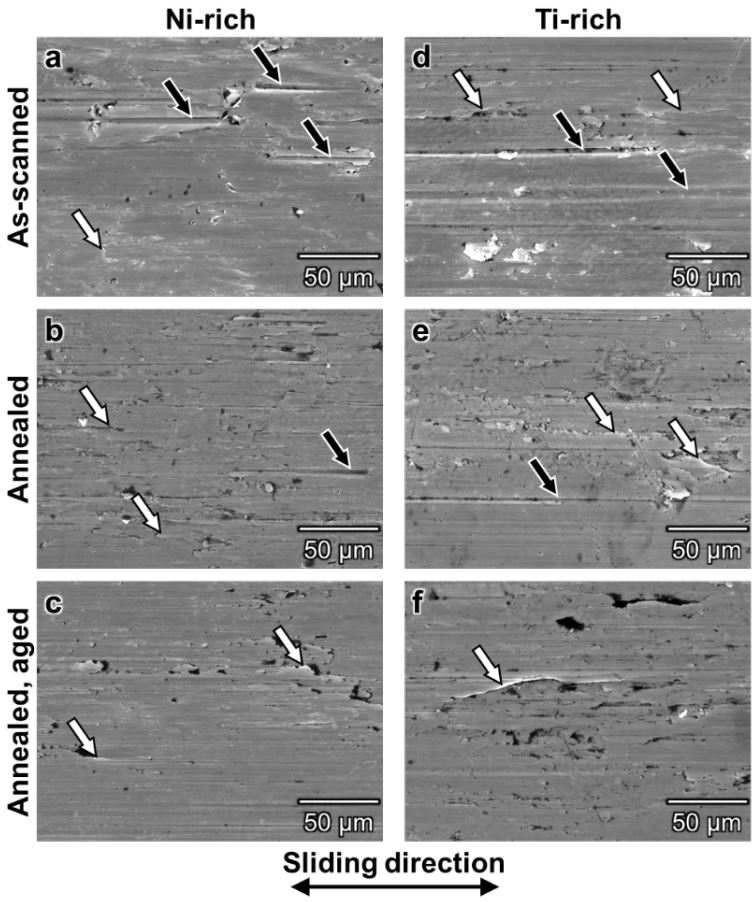

Fig. 5.9 Magnified SE images of worn surface on (a) as-scanned Ni-rich coating, (b) annealed Ni-rich coating, (c) annealed and aged Ni-rich coating, (d) as-scanned Ti-rich coating, (e) annealed Ti-rich coating, (f) annealed and aged coating. The white arrows show the deep grooves, and the black arrows show the delamination.

This indicates that, following heat treatment, the increased hardness/Young's modulus ratio (H/E) and depth recovery ratio ($\eta_{d,h}$) of the coating make it more difficult for abrasive particles to plow through the surface during sliding friction, resulting in decreased abrasive wear. This also explains the decrease in CoF after heat treatment. Additionally, minor delamination (indicated by white arrows) was observed on the worn surfaces of the coatings in all heat treatment states. This is due to shear deformation of the surface layer of the coatings by friction, which induces crack nucleation and propagation underneath the surface but parallel to it, ultimately leading to delamination [52]. This suggests that heat treatment may have a limited effect on

suppressing delamination in EB-scanned coatings.

Fig. 5.10 shows the correlation between W_s and H, the H/E ratio and the $\eta_{d,h}$ value for CP-Ti, SE-NiTi and EB-scanned coatings in various heat treatment states. As can be seen in Fig. 5.10a, there is a weak negative correlation between W_s and H for these materials. As discussed in *Section 5.3.3*, higher H is generally associated with superior wear resistance, i.e. lower wear rate under identical test conditions. While this conclusion holds some validity, it is often inaccurate. For example, Fig. 5.10a shows that the as-scanned Ti-rich coating, the annealed Ti-rich coating and the SE-NiTi coating have almost identical H values, yet their W_s values differ significantly. Conversely, Fig. 5.10b and 5.10c show that W_s exhibits a clear linear negative correlation with both the H/E ratio and the $\eta_{d,h}$. This aligns with the findings of other relevant studies cited in *Section 5.3.3*, which confirm that the H/E ratio and $\eta_{d,h}$ are more reliable indicators of wear resistance.

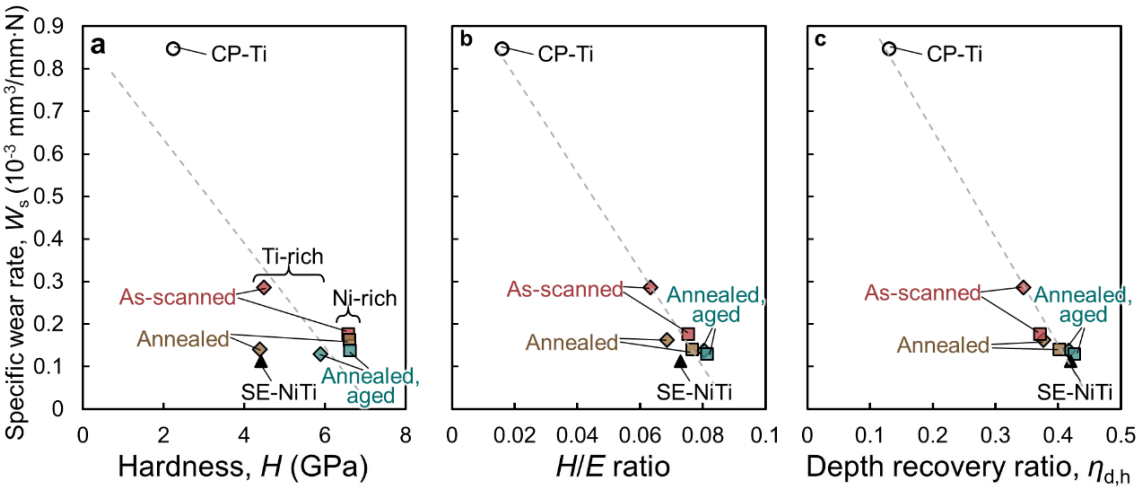

Fig. 5.10. Plot of specific wear rate (W_s) versus (a)hardness (H), (b) H/E ratio and (c)depth recovery ratio ($\eta_{d,h}$) of CP-Ti, superelastic nitinol (SE-NiTi) and EB-scanning coatings at various heat treatment states.

5.4 Conclusions

This chapter aims to improve the properties of the NiTi coatings scanned by electron beam (EB) and fabricated in Chapter 4, using heat treatment methods such as annealing and aging. Ti-rich and Ni-rich EB-scanned coatings were first annealed at 900 °C for 10 minutes, followed by aging at 400 °C for 60 minutes. The effects of the heat treatment on the performance of the coatings were evaluated by analyzing the phase composition, cross-sectional morphology, microstructure, indentation properties and friction-wear properties before and after the treatment. The key findings and conclusions are as follows:

- Annealing reduces the $NiTi_2$ phase in EB-scanned coatings. This phase almost disappears in Ni-rich coating, but remains to some extent, i.e., it is not completely eliminated in Ti-rich coating.
- Annealing causes the reticular Ni_3Ti phase in Ni-rich EB-scanned coatings to coarsen into needle-like or granular structures. These form a framework that supports the NiTi phase matrix and enhances the coating's mechanical properties.

- Subsequent aging after annealing promotes the precipitation of the Ni_4Ti_3 phase in the EB-scanned coating, leading to further strengthening by precipitation hardening.
- Annealing and ageing both enhance the hardness/Young's modulus (*H/E*) ratio and the depth recovery ($\eta_{d,h}$) ratio of EB-scanned coatings. Notably, the differences between the two coatings are significantly reduced after annealing and ageing, with both achieving *H/E* ratios that exceed those of superelastic nitinol and $\eta_{d,h}$ values that nearly match those of superelastic nitinol.
- Annealing and ageing also markedly improve the wear resistance of EB-scanned coatings while reducing their friction coefficient. After annealing and ageing, the disparity in wear rates between the two coatings was eliminated, resulting in performance comparable to that of superelastic nitinol.

References

[1] R. Huang, M. Sone, W. Ma, H. Fukanuma, The effects of heat treatment on the mechanical properties of cold-sprayed coatings, Surf. Coat. Technol. 261 (2015) 278–288. https://doi.org/10.1016/j.surfcoat.2014.11.017.

[2] N.V. Abhijith, D. Kumar, K. Rawat, Effect of Heat Treatment on Mechanical Properties and Corrosion Response of HVOF Sprayed High Entropy Alloy Coatings, Key Eng. Mater. 982 (2024) 3–8. https://doi.org/10.4028/p-UVGG3f.

[3] L. Liu, H. Xu, J. Xiao, X. Wei, G. Zhang, C. Zhang, Effect of heat treatment on structure and property evolutions of atmospheric plasma sprayed NiCrBSi coatings, Surf. Coat. Technol. 325 (2017) 548–554. https://doi.org/10.1016/j.surfcoat.2017.07.011.

[4] L. Hou, D.S. Grummon, Transformational superelasticity in sputtered titanium-nickel thin films, Scr. Metall. Mater. 33 (1995) 989–995. https://doi.org/10.1016/0956-716X(95)00311-I.

[5] N. Cameron, Z. Farhat, Investigation into the wear and dent resistance of Ni/Ti nanolaminates and superelastic NiTi coating, J. Mater. Eng. Perform. 28 (2019) 6033–6041. https://doi.org/10.1007/s11665-019-04377-5.

[6] T. Abubakar, M. Rahman, J. Stokes, Effect of Annealing Treatment on the Wear Properties of Ni Rich NiTi Alloy Coatings, Adv. Mater. Res. 686 (2013) 192–200. https://doi.org/10.4028/www.scientific.net/AMR.686.192.

[7] L. Wang, M. Okugawa, Y. Liu, K. Cho, H.Y. Yasuda, T. Nakano, Y. Koizumi, NiTi coating formation on Ti for enhanced wear resistance utilizing electron-beam additive manufacturing technique, Surf. Interfaces 72 (2025) 107024. https://doi.org/10.1016/j.surfin.2025.107024.

[8] G. Carlucci, L. Patriarca, A.G. Demir, J.N. Lemke, A. Coda, B. Previtali, R. Casati, Building Orientation and Heat Treatments Effect on the Pseudoelastic Properties of NiTi Produced by LPBF, Shape Mem. Superelasticity 8 (2022) 235–247. https://doi.org/10.1007/s40830-022-00391-0.

[9] J.J. Marattukalam, V.K. Balla, M. Das, S. Bontha, S.K. Kalpathy, Effect of heat treatment on microstructure, corrosion, and shape memory characteristics of laser deposited NiTi alloy, J. Alloys Compd. 744 (2018) 337–346. https://doi.org/10.1016/j.jallcom.2018.01.174.

[10] H.Z. Lu, Z.J. Zhou, Y. Yang, R.C. Wang, H.W. Ma, W.S. Cai, D.Z. Zhu, C. Yang, Effect of heat treatment on the microstructure and superelasticity of NiTi alloy via selective laser melting, J. Mater. Res. Technol. 30 (2024) 1044–1055. https://doi.org/10.1016/j.jmrt.2024.03.148.

[11] Thermo-Calc Software, Titanium and TiAl-based Alloys Databases, Version 4(TCTI4), (2022). https://thermocalc.com/products/databases/ (accessed October 1, 2023).

[12] E.S. Berkovich, The three-faceted diamond pyramid for microhardness testing, Zavod. Lab. 16 (1950) 345.

[13] A. Shimamoto, K. Tanaka, Y. Akiyma, H. Yoshizaki, Nanoindentation of glass with a tip-truncated Berkovich indenter, Philos. Mag. A 74 (1996) 1097–1105. https://doi.org/10.1080/01418619608239710.

[14] International Organization for Standardization, Metallic materials — Instrumented indentation test for hardness and materials parameters — Part 1: Test method (ISO Standard No. 14577-1:2015), (2015). https://www.iso.org/standard/56626.html.

[15] W. Ni, Y.-T. Cheng, D.S. Grummon, Microscopic superelastic behavior of a nickel-titanium alloy under complex loading conditions, Appl. Phys. Lett. 82 (2003) 2811–2813. https://doi.org/10.1063/1.1569984.

[16] ASTM International, Test Method for Linearly Reciprocating Ball-on-Flat Sliding Wear, (2022). https://doi.org/10.1520/G0133-22.

[17] J.F. Shackelford, W. Alexander, eds., CRC Materials Science and Engineering Handbook, 3rd ed., CRC Press, Boca Raton, 2000. https://doi.org/10.1201/9781420038408.

[18] S.K. Ray, A. Banerjee, B.K. Bhangi, D. Pyne, B. Dutta, 2 - Tribological analysis—general test standards, in: S.C. George, J.T. Haponiuk, S. Thomas, R. Reghunath, S. P. s. (Eds.), Tribol. Polym. Polym. Compos. Polym. Nanocomposites, Elsevier, 2023: pp. 17–50. https://doi.org/10.1016/B978-0-323-90748-4.00001-7.

[19] Y. Miyata, M. Okugawa, Y. Koizumi, T. Nakano, Inverse Columnar-Equiaxed Transition (CET) in 304 and 316L Stainless Steels Melt by Electron Beam for

Additive Manufacturing (AM), Crystals 11 (2021) 856. https://doi.org/10.3390/cryst11080856.

[20] Y. Cheng, G. Wang, Z. Qiu, Z. Zheng, D. Zeng, X. Tang, R. Shi, M. Uddagiri, I. Steinbach, Multi-physics simulation of non-equilibrium solidification in Ti-Nb alloy during selective laser melting, Acta Mater. 272 (2024) 119923. https://doi.org/10.1016/j.actamat.2024.119923.

[21] A. Babaei-Dehkordi, M. Soltanieh, M. Mirjalili, M. Asherloo, A. Mostafaei, Understanding Interfacial Reactions in Ti–Ni Diffusion Couple, Materials 16 (2023) 2267. https://doi.org/10.3390/ma16062267.

[22]K. Otsuka, X. Ren, Physical metallurgy of Ti–Ni-based shape memory alloys, Prog. Mater. Sci. 50 (2005) 511–678. https://doi.org/10.1016/j.pmatsci.2004.10.001.

[23] E.E. Timofeeva, N.Yu. Surikov, A.I. Tagiltsev, A.S. Eftifeeva, A.A. Neyman, E.Yu. Panchenko, Yu.I. Chumlyakov, The superelasticity and shape memory effect in Ni-rich Ti-51.5Ni single crystals after one-step and two-step ageing, Mater. Sci. Eng. A 796 (2020) 140025. https://doi.org/10.1016/j.msea.2020.140025.

[24] Y. Tian, Z. Liang, Y. Cai, H. Jiang, M. Chen, J. Han, Microstructure and mechanical properties of Ti2Ni alloy fabricated by direct energy deposition, Sci. Technol. Weld. Join. 29 (2024) 47–51. https://doi.org/10.1177/13621718231216674.

[25] S. Divinski, I. Stloukal, L. Král, C. Herzig, Diffusion of Titanium and Nickel in B2 NiTi, Defect Diffus. Forum 289 (2009) 377–382. https://doi.org/10.4028/www.scientific.net/DDF.289-292.377.

[26] M. Lifshitz, V.V. Slezov, KINETICS OF DIFFUSIVE DECOMPOSITION OF SUPERSATURATED SOLID SOLUTIONS, Sov. Phys. Jetp Ussr 35 (1958) 331–339.

[27] Z. Liu, L. Zhang, C. Fu, C. Zeng, X. Wu, W. Li, X. Ma, Structural, mechanical, and thermodynamic properties of Ni–Ti intermetallic compounds: First-principle calculation, J. Appl. Phys. 134 (2023) 085107. https://doi.org/10.1063/5.0159431.

[28] R.C.D. Richardson, The wear of metals by relatively soft abrasives, Wear 11 (1968) 245–275. https://doi.org/10.1016/0043-1648(68)90175-0.

[29] W. Ni, Y.-T. Cheng, M. Lukitsch, A.M. Weiner, L.C. Lev, D.S. Grummon, Novel layered tribological coatings using a superelastic NiTi interlayer, Wear 259 (2005) 842–848. https://doi.org/10.1016/j.wear.2005.01.015.

[30] A. Leyland, A. Matthews, On the significance of the H/E ratio in wear control: a nanocomposite coating approach to optimised tribological behaviour, Wear 246 (2000) 1–11. https://doi.org/10.1016/S0043-1648(00)00488-9.

[31] B.D. Beake, The influence of the H/E ratio on wear resistance of coating systems – Insights from small-scale testing, Surf. Coat. Technol. 442 (2022) 128272. https://doi.org/10.1016/j.surfcoat.2022.128272.

[32] Z. Pang, Q. Zeng, Z. Ning, W. He, Z. Wang, J. Wang, L. Li, Ultralow friction and low wear behavior of in-situ formed NiTiO3 from 60NiTi alloy at 350 °C, Intermetallics 168 (2024) 108271. https://doi.org/10.1016/j.intermet.2024.108271.

[33] R. Neupane, Z. Farhat, Wear Resistance and Indentation Behavior of Equiatomic Superelastic TiNi and 60NiTi, Mater. Sci. Appl. 6 (2015) 694–706. https://doi.org/10.4236/msa.2015.67071.

[34] L. Yang, M. Wen, X. Dai, G. Cheng, K. Zhang, Ultrafine Ceramic Grains Embedded in Metallic Glass Matrix: Achieving Superior Wear Resistance via Increase in Both Hardness and Toughness, ACS Appl. Mater. Interfaces 10 (2018) 16124–16132. https://doi.org/10.1021/acsami.8b02338.

[35] C. Zhang, Z.N. Farhat, Sliding wear of superelastic TiNi alloy, Wear 267 (2009)

394–400. https://doi.org/10.1016/j.wear.2008.12.093.

[36] Z.N. Farhat, C. Zhang, The role of reversible martensitic transformation in the wear process of TiNi shape memory alloy, Tribol. Trans. 53 (2010) 917–926. https://doi.org/10.1080/10402004.2010.510620.

[37] H. Vafaeenezhad, S. Aliakbari-Sani, S.H. Seyedein, A. Ghosh, A.R. Eivani, Flow behavior and strain rate sensitivity assessment of γ and γ′ phases in Co–Al–W-based superalloy using experimental and computational approaches, J. Mater. Res. Technol. 18 (2022) 4617–4630. https://doi.org/10.1016/j.jmrt.2022.03.166.

[38] W. Xiufang, Y. Xiaoping, G. Zhendan, Z. Yinchang, S. Hongwei, Nanoindentation characterization of mechanical properties of ferrite and austenite in duplex stainless steel, Adv. Mater. Res. 24–25 (2007) 1165–1170.

[39] Z. Wang, J. Zhang, H.U. Hassan, J. Zhang, Y. Yan, A. Hartmaier, T. Sun, Coupled effect of crystallographic orientation and indenter geometry on nanoindentation of single crystalline copper, Int. J. Mech. Sci. 148 (2018) 531–539. https://doi.org/10.1016/j.ijmecsci.2018.09.007.

[40] L. Zhu, B. Xu, H. Wang, C. Wang, D. Yang, Measurement of mechanical properties of 1045 steel with significant pile-up by sharp indentation, J. Mater. Sci. 46 (2011) 1083–1086. https://doi.org/10.1007/s10853-010-4876-7.

[41] A. Liu, Q. Pan, M. Chen, W. Xu, W. Chen, An investigation on the relationships between hardness, elas- ticmodulus and the work of 7075 aluminium alloy by nanoindentation, J. Phys. Conf. Ser. 2044 (2021) 012106. https://doi.org/10.1088/1742-6596/2044/1/012106.

[42] X.Y. Li, J.R. Ye, B. Tang, Study of the Ion Nitrided Layer on Ti-6Al-4V substrate, Adv. Mater. Res. 79–82 (2009) 695–698. https://doi.org/10.4028/www.scientific.net/AMR.79-82.695.

[43] M. Liu, Q. Zheng, X. Wang, C. Xu, Characterization of Distribution of Microstructure and Micro-mechanical Properties of Nickel-Based Single Crystal Superalloy Within the Shot-Peened Layer, Met. Mater. Int. 29 (2023) 2257–2286. https://doi.org/10.1007/s12540-023-01388-9.

[44] M. Zhang, F. Li, B. Chen, S. Wang, Investigation of micro-indentation characteristics of P/M nickel-base superalloy FGH96 using dislocation-power theory, Mater. Sci. Eng. A 535 (2012) 170–181. https://doi.org/10.1016/j.msea.2011.12.060.

[45] J. Nohava, B. Bonferroni, G. Bolelli, L. Lusvarghi, Interesting aspects of indentation and scratch methods for characterization of thermally-sprayed coatings, Surf. Coat. Technol. 205 (2010) 1127–1131. https://doi.org/10.1016/j.surfcoat.2010.08.086.

[46] J.G. La Barbera-Sosa, Y.Y. Santana, M.H. Staia, D. Chicot, J. Lesage, J. Caro, G. Mesmacque, E.S. Puchi-Cabrera, Microstructural and mechanical characterization of Ni-base thermal spray coatings deposited by HVOF, Surf. Coat. Technol. 202 (2008) 4552–4559. https://doi.org/10.1016/j.surfcoat.2008.04.041.

[47] C. Leither, J. Risan, M. Bashirzadeh, F. Azarmi, Determination of the elastic modulus of wire arc sprayed alloy 625 using experimental, analytical, and numerical simulations, Surf. Coat. Technol. 235 (2013) 611–619. https://doi.org/10.1016/j.surfcoat.2013.08.033.

[48] P. Poza, C.J. Múnez, M.A. Garrido-Maneiro, S. Vezzù, S. Rech, A. Trentin, Mechanical properties of Inconel 625 cold-sprayed coatings after laser remelting. Depth sensing indentation analysis, Surf. Coat. Technol. 243 (2014) 51–57. https://doi.org/10.1016/j.surfcoat.2012.03.018.

[49] K.L. Ng, Q.P. Sun, M. Tomozawa, S. Miyazak, Wear behavior of NiTi thin film at

micro-scale, Int. J. Mod. Phys. B 24 (2010) 85–93. https://doi.org/10.1142/S0217979210064010.

[50] H. Tobushi, K. Tanaka, T. Hori, T. Sawada, T. Hattori, Pseudoelasticity of TiNi shape memory alloy : Dependence on maximum strain and temperature, JSME Int. J. Ser Mech. Mater. Eng. 36 (1993) 314–318. https://doi.org/10.1299/jsmea1993.36.3_314.

[51] K.G. Budinski, Surface engineering for wear resistance, Englewood Cliffs, N.J. : Prentice Hall, 1988. http://archive.org/details/surfaceengineeri0000budi (accessed December 30, 2024).

[52] N. P. Suh, The delamination theory of wear, Wear 25 (1973) 111–124. https://doi.org/10.1016/0043-1648(73)90125-7.

Chapter 6

Point-Wise Electron Beam Scanning Strategy for Homogeneous NiTi Coatings and Improved Mechanical Performance

6.1 Introduction

The heat treatment method described in Chapter 5 is an effective way of addressing inhomogeneity issues in multi-track scanned NiTi coatings. However, this process is complex and time-consuming, involving both annealing and ageing steps. This chapter therefore focuses on the electron beam (EB) scanning process itself, aiming to achieve homogeneous coatings directly after scanning through an improved scanning strategy, eliminating the need for post-processing.

Scanning strategies have always played a key role in additive manufacturing processes, whether lasers or electron beams are used as heat sources. In selective laser melting (SLM) research, in addition to the conventional uni-directional and bi-directional scanning strategies [1], researchers have also developed unique strategies such as island/chessboard scanning [2] and rotation of the scan between successive layers [1]. Scanning strategies suitable for SLM are generally compatible with electron beam melting (EBM). Here, SLM and EBM are respectively categorized as powder bed fusion–laser beam (PBF-LB) and powder bed fusion–electron beam (PBF-EB) according to ISO/ASTM 52900. However, leveraging the electron beam's capability for high-speed deflection and point-wise dwell, point-wise scanning strategies have also been developed [3,4]. Using these unconventional scanning strategies and optimizing parameters enables the control of various material properties, including grain size [4,5], crystallographic orientation [4–6], ductility [7] and hardness [8].

Additionally, bringing localized remelting into scanning strategies enhances material homogeneity [9]. Consequently, these novel strategies hold significant potential for further development.

After drawing insights from the above studies, we found that the point-wise scanning strategy inherently enables strong localized remelting. This is because the scanning process easily achieves mutual isolation between molten pools — specifically, the current point has already solidified by the time adjacent points are melted. Consequently, applying this scanning strategy to EB scanning for NiTi coating fabrication is expected to improve coating homogeneity. Furthermore, by rationally configuring the distribution of points along the scanning route, heat distribution can be made more uniform to prevent thermal accumulation. This implies that, unlike in Chapter 4, the point-wise scanning strategy does not require intervals to be introduced into the scanning process to avoid overheating. Instead, it enables the entire area to be scanned continuously, reducing the time consumed in the scanning process.

In this chapter, a novel EB point-wise scanning strategy suitable for NiTi coating fabrication was developed based on prior research. The coatings produced using this new strategy were compared with those fabricated in Chapter 4. Additionally, the effects of various scanning parameters on coating surface roughness, microstructure and compositional homogeneity, and nanoindentation properties were thoroughly investigated.

6.2 Methods

6.2.1 Preparation of substrate and Ni-plate

A slab of CP-Ti (99.5% purity; Nilaco, Tokyo, Japan) was cut into specimens of 25 × 25 × 10 mm^3 by electric discharge machining. A CP-Ti specimen of 25 × 25 mm^2

area was used as the working electrode. The CP-Ti specimen was given a four-stage pretreatment: (1) mechanical grinding using P120–P2400-grit SiC abrasive papers; (2) immersion in ethanol at RT for 5 min; (3) immersion in 10 wt.% HCl solution at RT for 5 min, with a 9 V DC power applied to promote the removal of surface oxides and contaminants and (4) washing with ultrapure water.

A pure Ni anode (ϕ6 × 20 mm) of 405 mm^2 area was used with an interelectrode gap of 8 cm. In this study, a thicker pure Ni layer was required to enable subsequent processing. Therefore, a nickel sulfamate solution was used as the plating bath. This type of bath tolerates high current density and produces plated layers with lower internal stress, making it suitable for applications that demand greater coating thickness [10]. The compositions of the solutions and the electroplating parameters adopted from a electrochemical handbook [10] are listed in Table 1. Electroplating was conducted for 4 h to obtain a plating layer with sufficient thickness. After plating, the layer was ground using P120–P2000 grit SiC abrasive papers to a final thickness of 45 μm.

Table 3.1. Composition of Ni-plating solution and plating parameters.

	Compound/Parameter	**Value**
Composition	$NiCl_2 \cdot 6H_2O$	0.10–0.13 mol/L
	$Ni(SO_3NH_2)_2$	1.70–1.79 mol/L
	H_3BO_3	0.49–0.73 mol/L
Parameters	Temperature	50–60 °C
	pH	3.0–5.0
	Cathodic current density	3.0 A/dm^2
	Current mode	DC plating

6.2.2 Electron beam point-wise scanning

6.2.2.1 Design of point-wise scanning strategy

Initially, we intended to use the point-wise scanning strategy developed by Kirka et al. [4] for additive manufacturing research in our electron beam scanning experiments on Ni-plated CP-Ti specimens. A schematic of this scanning strategy is shown in Fig. 6.1. Two geometric parameters control the scanning grid: the step size (l_s) and the point spacing (l_t). This scanning strategy fills the entire grid in the following steps: 1. Fill the first points in each row of the first row set along a zigzag route (Fig. 6.1a). 2. Repeat the basic zigzag route, shifting it to the right by l_t, until the first-row set is filled (Fig. 6.1b). 3. Repeat the first-row set, shifting it down by l_t, until the grid is filled (Fig. 6.1c). However, when this scanning strategy was applied to the experiments in this study, the central region of the scanned area exhibited significantly more intense melting than the surrounding areas (as indicated by the red arrow in Fig. 6.2a1), and cracks appeared on the surface of the specimens that were scanned. This suggests that, during scanning, the central region accumulated substantially more heat than the surrounding areas, resulting in excessive melting and significant residual stresses [11].

To analyze the heat input distribution within the scanned region, we used an analytical solution of temperature field for a two-dimensional transient point heat source to estimate the temperature history on the surface during the electron beam scanning process. The temperature field induced by a transient point heat source can be obtained by integrating the two-dimensional Green's function of the heat equation [12]:

$$G(r,t) = \frac{1}{4\pi\alpha t}\exp\left(-\frac{r^2}{4\alpha t}\right), \qquad t > 0. \tag{6.1}$$

Where α, t, and r are thermal diffusivity, time, and distance to the heat source, respectively.

Based on this fundamental solution, the temperature evolution after the irradiation of a single spot was analytically derived as:

$$T(r,t) = \frac{P}{4\pi\alpha}\left[E_1\left(\frac{r^2}{4\alpha(t-t_0)}\right) - E_1\left(\frac{r^2}{4\alpha(t-t_1)}\right)\right], t > t_1 > t_0 \geq 0. \quad (6.2)$$

where T is the temperature, r the radial distance from the heat source, t the time, t_0 and t_1 the start and end times of irradiation, and P the electron beam power. E_1 represents exponential integral, which is defined as $E_1(x) = \int_1^\infty \frac{e^{-tx}}{t} dt,\ x > 0$. The value of thermal diffusivity α is obtained through this equation: $\alpha = k/\rho c_p$, in which k is the heat conductivity coefficient, ρ is the density, c_p is the specific heat capacity of the material (nickel in this study).

The temperature history at each point within the scanning area was calculated using Eq. 6.2. Then, the peak temperature (H) in the temperature history was normalized and plotted H as a heat map. As shown in Fig. 6.1a1, the heat map indicates that the peak temperature at the center of the scanned area is significantly higher than in the surrounding regions and that the distribution of peak temperatures within the area is highly non-uniform. This confirms the experimental results.

To improve the uniformity of heat input in the scanning area, we modified the original scanning strategy. After screening candidate strategies using peak temperature heat maps and conducting extensive electron beam scanning experiments, we selected the strategy shown in Fig. 6.3 for this study. This modified strategy is also governed by the two geometric parameters, step size (l_s) and point spacing (l_t), which control the scanning grid. This modified strategy fills the entire grid in the following steps： 1. Fill the first points in each row of the first row set along a zigzag route (Fig. 6.3a). 2. Repeat the basic zigzag route, shifting it to the right by $2l_t$, until first row set in the 1st-quarter grid is filled (Fig. 6.3b). 3. Repeat the first-row set, shifting it down by $2l_t$, until the 1st-

quarter grid is filled (Fig. 6.3c). 4. Shift the 1st-quarter grid down to fill the 2nd-quarter grid (Fig. 6.3d). 5. Shift the 1st-quarter grid to the right to fill the 3rd-quarter grid (Fig. 6.3e). 6. Shift the 3rd-quarter grid down to fill the 4th-quarter grid (Fig. 6.3f). This modified strategy accomplishes four scans of the entire area in the same amount of time as the original strategy by dividing the original grid into four nested quarter grids. Each scan delivers only one-quarter of the original heat input, resulting in a more uniform thermal distribution across the scanning area. The result of the scanning experiment (Fig. 6.2b1) shows uniform melting across the scanning area. The estimated peak temperature heatmap (Fig. 6.2b2) shows that the modified scanning strategy achieves lower peak temperatures at the center of the area with identical geometric parameters. Additionally, comparing the probability density distributions on the right side of the two heat maps (Fig. 6.2a2 and 6.2b2) reveals that the range of peak temperatures for the modified strategy narrows from 0.5–9.8 to 3.0–9.0, resulting in a significantly more concentrated probability distribution. This demonstrates that the modified strategy achieves a more uniform distribution of heat input within the area.

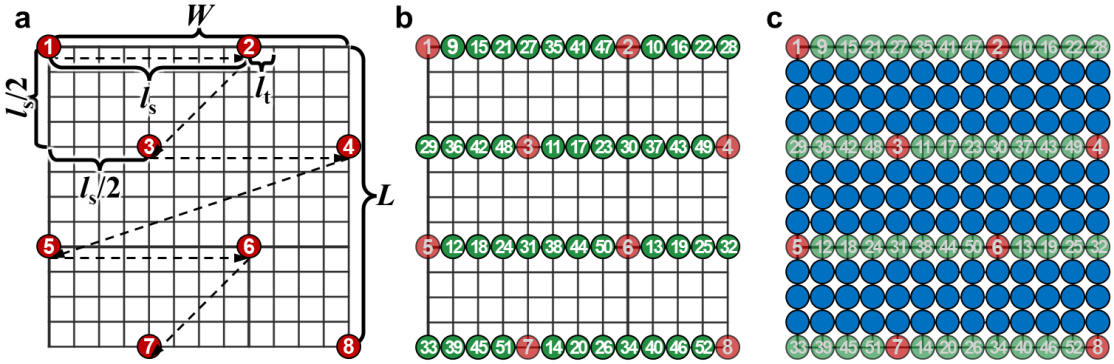

Fig. 6.1. Schematic of original point-wise scanning strategy [4] in exploded view. (a) The fill of the first points of each row in the first row set, (b) the fill of the first row set, (c) the fill of subsequent rows. Symbol definition: l_s, step distance; l_t, point spacing; W, width of scanning area; L, length of scanning area.

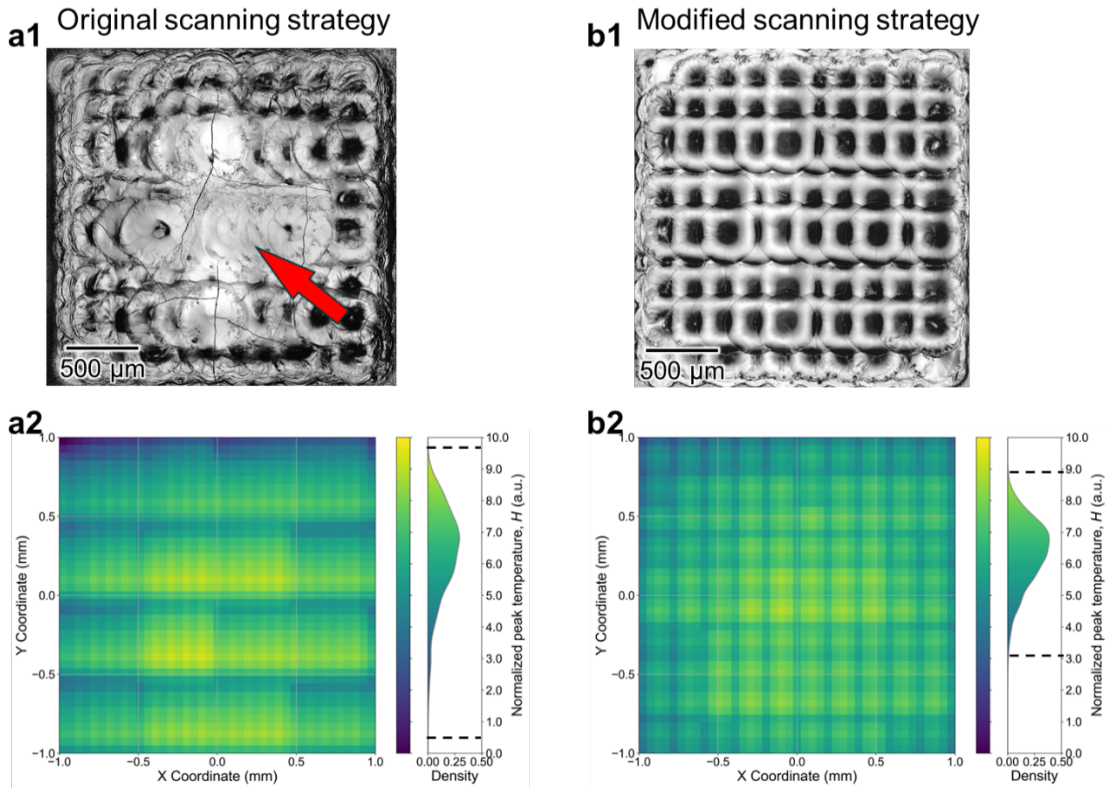

Fig. 6.2. Comparison of the original and modified scanning strategies with the same geometry parameter, step size (l_s) and point spacing (l_t), in (a1, b1) of the results of the scanning experiment on Ni-plated CP-Ti and (a2, b2) of the heat maps of estimated peak temperature in scanning process. The red arrow indicates intensively melting in the center of the scanning area.

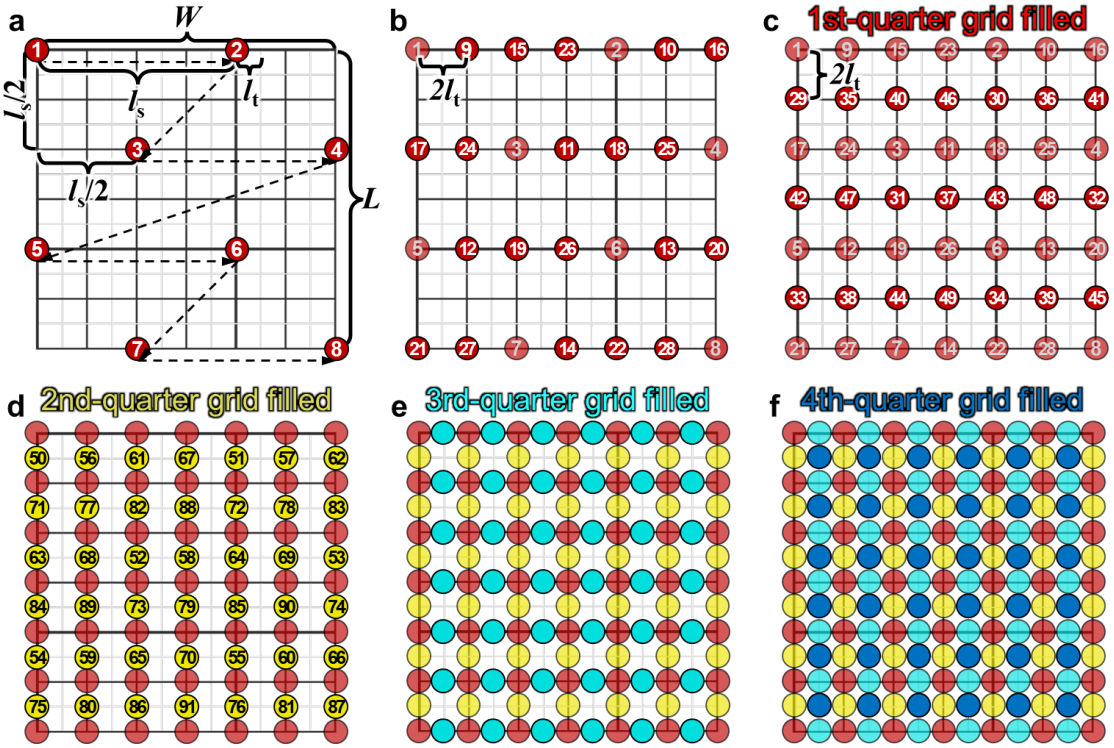

Fig. 6.3. Schematic of modified point-wise scanning in exploded view. (a) The fill of the first points of each row in the first row set, (b) the fill of the first row set in the 1st-quarter grid, (c) the fill of the 1st-quarter grid (in red), (d) the fill of the 2nd-quarter grid (in yellow), (e) the fill of the 3rd-quarter grid (in cyan), (f) the fill of the 3rd-quarter grid (in blue). Symbol definition: l_s, step distance; l_t, point spacing; W, width of scanning area; L, length of scanning area.

6.2.2.2 Parameters for point-wise scanning experiments

The plated specimens were irradiated with EBs using an EBM machine (EBM-6LB-1, Mitsubishi Electric) in a helium atmosphere at 0.5 Pa. Point-wise scanning was performed over a 2 × 2 mm^2 area using the modified scanning strategy described in *Section 6.2.2.1*. The coordinates of each point in the scanning grid were generated in scanning order using the program shown in Fig. 6.4.

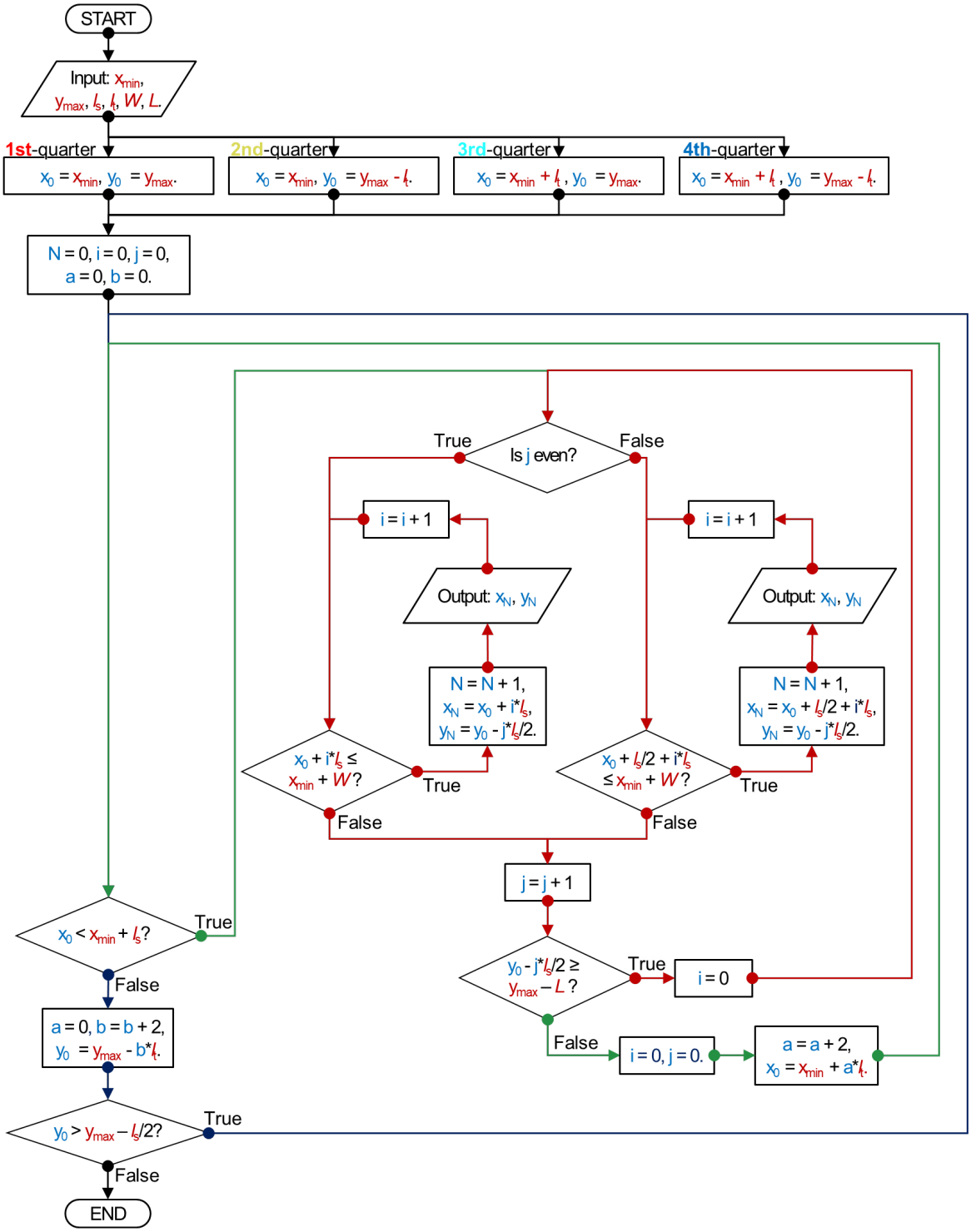

Fig. 6.4. Flow chart of the program for generating the coordinates of spots in the scanning order in the modified scanning strategy. Definitions of the input parameters: x_{min}, minimum x coordinate in the scanning area; y_{max}, maximum y coordinate in the scanning area; l_s, step distance; l_t, point spacing; W, width of scanning area; L, length of scanning area.

The step size (l_s) for scanning grid was fixed at 1 mm, while the point spacing (l_t)

was set at four levels: 83, 100, 125 and167 μm. These represent 1/12, 1/10, 1/8 and 1/6 of the l_s, respectively. The cycle time (τ) for each point in the point-wise scanning was fixed at 10 ms, while the EB dwell time (t_d) at each point was set at three levels: 2 ms, 5 ms and 10 ms. These represent 20%, 50% and 100% of the τ, respectively. As shown in Fig. 6.5, when t_d is shorter than τ, the actual power (P) during electron beam scanning does not remain constant, but instead rises and falls within a cycle time of τ. Therefore, the average electron beam power (P_{avg}) per cycle was adopted as the experimental parameter. The relationship between P and P_{avg} is given by Eq. 6.3. The range of P_{avg} values for each parameter set is summarized in Table 6.2.

$$P_{\text{avg}} = \frac{\int_0^{\tau} P dt}{\tau} \tag{6.3}$$

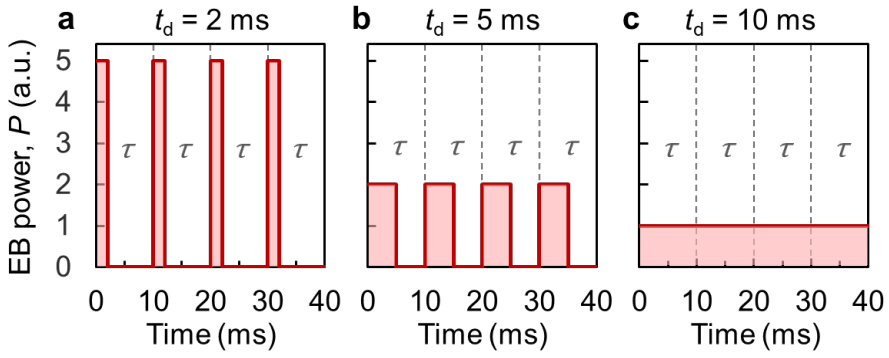

Fig. 6.5. Schematics showing the variation of electron beam power (P) over time during scanning for (a) a dwell time (t_d) of 2 ms, (b) a t_d of 5 ms, and (c) a t_d of 10 ms, when the average EB power (P_{avg}) is held constant.

Table 6.2. Parameters of EB point-wise scanning experiment. Symbol definition: t_d, dwell time; l_t, point spacing; P_{avg}, average EB power.

P_{avg} (W)		t_d (ms)		
		2	5	10
l_t (µm)	83	20–50	20–50	20–50
	100	30–60	30–60	30–60
	125	30–60	30–60	30–60
	167	40–60	40–60	40–60

6.2.3 Microstructural characterization

The top surfaces of the point-wise scanned (PWS) specimens were observed using a confocal laser scanning microscope (VK-X200/210, Keyence, Japan). The samples were then cut for cross-sectional observation by field-emission scanning electron microscopy (FE-SEM; JSM 6500, JEOL, Japan). The elemental distributions were analyzed by energy-dispersive X-ray spectroscopy (EDS). The crystal orientation and microstructure statistics are analyzed by Electron backscatter diffraction (EBSD). The formed Ni-Ti intermetallic phases were studied by evaluating the equilibrium phase characteristics of the Ni-Ti binary alloy using Thermo-Calc Software (version 2022b) with a thermodynamic database for Ti alloys (TCTI4) [13].

6.2.4 Training of machine learning model

A machine learning model was trained using the results of experiments conducted on all parameter sets to predict the Ni concentration at the center of the coating (C_{Ni_cnt}). The model included four features: l_t, t_d, P_{avg} and t_{Ni} (the Ni-plating thickness). Although t_{Ni} was set as a constant in the experimental design, minor fluctuations in t_{Ni} still existed across specimens due to processing errors and affected C_{Ni_cnt}. Therefore, to reduce

unexplained variance and improve prediction accuracy, t_{Ni} was incorporated into the training as a covariate. All the data were split into training (80%) and testing (20%) sets. Prior to training, features were standardized based on training set statistics. Both Lasso and Ridge linear regression models were employed during training, utilizing hyperparameter grid search with 5-fold cross-validation. The final model was determined by the highest validation R^2 value.

6.2.5 Nanoindentation tests

Nanoindentation tests were performed using a nanoindentation tester (ENT-1100a, Elionix, Japan) equipped with a Berkovich indenter to evaluate the indentation properties of the EB-scanned coatings. Before the tests, the surfaces of specimens were ground using P120–P4000-grit SiC abrasive papers and then polished using 50 nm alkaline colloidal silica suspension. The Nanoindentation tests were performed at 26 °C inside the device equipped with a shield case to prevent thermal drift. A total of 50 equally spaced points were selected on each sample to repeat the test under identical parameters. Then, the results were averaged to eliminate the effect of randomness. The peak load was 50 mN, and the loading rate was 5 mN/s. The Berkovich indenter[14] with an apex angle of 65.03° was used, and the following relationship between the indenter contact area (A) and indentation depth (h) was employed:

$$A = 3\sqrt{3}\tan^2(65.03°)\cdot(h+\Delta h)^2\,. \tag{6.4}$$

Here, Δh is the indenter tip correction value calculated using the Sawa–Tanaka method [15] based on the indentation results of a standard fused silica sample. From the obtained results, Young's modulus (E) and hardness (H) were calculated according to the ISO 14577-1 protocol [16]. Moreover, depth recovery ratio ($\eta_{d,h}$) is defined as the

ratio of recoverable indentation depth to indenter displacement at maximum load [17]. It was calculated as follows:

$$\eta_{d,h} = \frac{h_{\max} - h_{\mathrm{p}}}{h_{\max}}, \tag{6.5}$$

where $h_{\max}$ and h_{p} are the maximum penetration depth of the indenter during the indentation tests and the permanent depth after load removal, respectively.

6.3 Results and discussion

6.3.1 Surface morphology and roughness

Fig. 6.6 shows the optical surface images, surface profiles and height maps of a multi-track intermittently scanned (IS) coating fabricated in Chapter 4, as well as a point-wise scanned (PWS) coating fabricated in this chapter. The processing parameters for the IS-coating were as follows: melt track line offset (l_{off}) = 300 μm; time interval (t_{int}) = 60 s; and electron beam power (P) = 126 W. The processing parameters for the PWS-coating were as follows: point spacing (l_{t}) = 100 μm; dwell time of electron beam (t_{d}) = 5 ms; and average electron beam power (P_{avg}) = 36 W. Firstly, it is worth noting that multi-track intermittent scanning takes 360 seconds in the same 2 × 2 mm^2 area, whereas point-wise scanning takes just 4.4 seconds. This indicates that the scanning strategy has become much more efficient by switching from multi-track to point-wise scanning. However, the surface morphology of these two coatings differs significantly. Fig. 6.6a1 and 6.6b1 show that the surface of the IS-coating exhibits a matte texture, whereas the surface of the PWS-coating is very glossy. The height maps and profiles (Fig. 6.6a2, 6.6b2, Fig. 6.6a3 and 6.6b3) show that the PWS-coating exhibit more concave and convex features than the IS-coating. This is because 15-μm-height bumps

appear at the center of melt spots on PWS-coating. Although these bumps may cause stress concentration and accelerate wear during the initial stage under dry friction conditions [18], the periodic texture composed of protrusions and depressions under lubricated friction conditions may facilitate oil film formation and retention [19,20]. However, the specific constraints are complex and require further investigation, which is beyond the scope of this discussion.

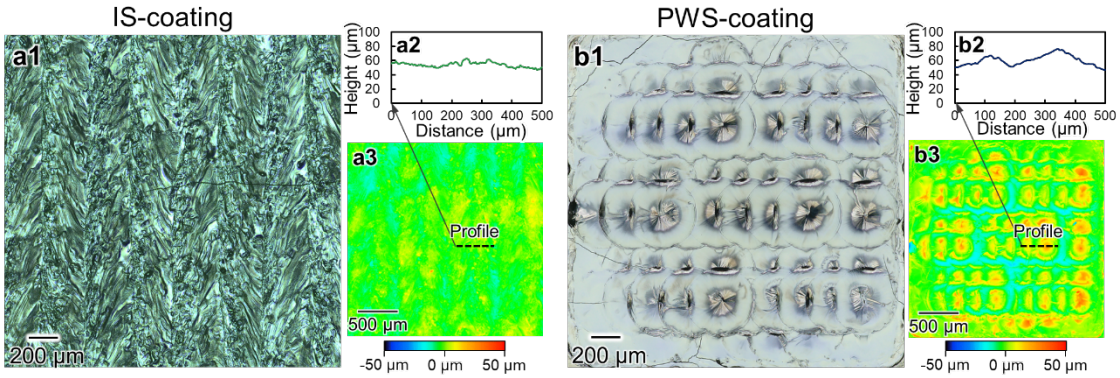

Fig. 6.6. Comparison of multi-track intermittently scanned (IS, in Chapter 4) and point-wise scanned (PWS) coatings in terms of (a1, b1) optical surface images, (a2, b2) surface profiles and (a3, b3) height maps.

In Fig. 6.7 shows box plots of roughness of the PWS-coatings with various l_t, compared with those of the continuously scanned (CS) and intermittently scanned (IS) coatings fabricated by multi-track scanning in Chapter 4. As l_t increases, the roughness of the PWS-coating increases slightly. This is because the spacing between melt spots widens as l_t increases, resulting in the central protrusions of melt spots being covered less by surrounding spots. Consequently, the undulations on the coating surface become more pronounced, leading to increased roughness. Compared to the CS-coating, which exhibits high roughness and significant fluctuations, the PWS-coating maintains roughness at a relatively low and stable level. The combined fluctuation range of the PWS-coating, resulting from dozens of different scanning parameter sets, remains less

than half that of the CS-coating. However, the PWS-coating's roughness is still slightly higher than that of the IS-coating. As the roughness of the PWS-coating originates primarily from the protrusions at the centers of the melt spots, roller or ball burnishing [21] can rapidly reduce the coating's roughness if necessary.

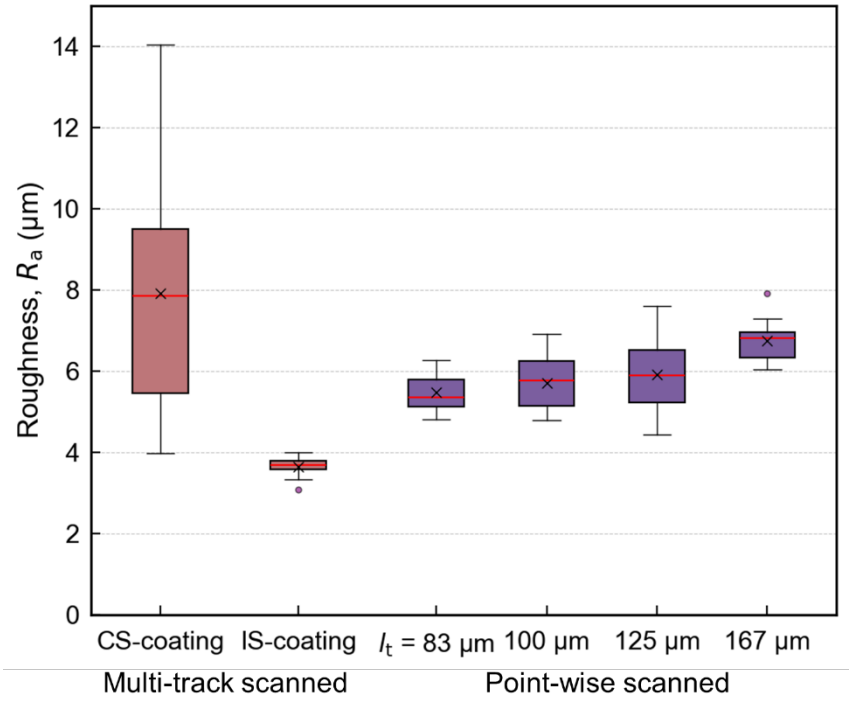

Fig. 6.7. Box plots of roughness of the point-wise scanned (PWS) coatings with various point spacing (l_t), compared with those of the continuously scanned (CS) and intermittently scanned (IS) coatings fabricated by multi-track scanning in Chapter 4.

6.3.2 Phase distribution and homogeneity

6.3.2.1 Effect of dwell time on phase distribution and homogeneity

To thoroughly investigate the melt-pool dynamics (i.e., the melting and solidification behavior within the melt pool) during the point-wise scanning process, and to specifically analyze the remelting effect of subsequent melt spots on phase distribution and homogeneity of the coatings, we applied an additional setting on the scanning

strategy. This setting involved dividing the scanning area into four distinct quadrants, each with a unique activation pattern for the scanning points, as shown by the colored points in Fig. 6.8a:

Upper left quadrant: Only points belonging to the 1st-quarter scanning grid were activated; points from the other three quarter grids were skipped. The results in this quadrant represent the state of post-1st-quarter-scan coating.

Upper right quadrant: Points from the 1st and 2nd-quarter grids were activated; the 3rd and 4th-quarter grids were skipped. The results in this quadrant represent the state of post-2nd-quarter-scan coating.

Lower left quadrant: Points from the 1st, 2nd, and 3rd-quarter grids were activated; the 4th-quarter grid was skipped. The results in this quadrant represent the state of post-3rd-quarter-scan coating.

Lower right quadrant: All four quarter grids (1st, 2nd, 3rd, and 4th) were activated. The results in this quadrant represent the state of post-4th-quarter-scan coating.

Fig. 6.8, 6.9 and 6.10 show the surface morphology and cross-sectional microstructure, along with the corresponding EDS elemental maps of three point-wise scanned (PWS) coatings. These coatings were applied with the aforementioned settings. The dwell times (t_d) of the electron beams for the three coatings are 2 ms, 5 ms and 10 ms, respectively. Meanwhile, the point spacing (l_t) and the average electron beam power (P_{avg}) are fixed at 100 µm and 36 W, respectively. The melt pool dynamics of these three coatings differ significantly at various stages of the scanning process. Fig. 6.8a shows that, for the coating with t_d = 2 ms, the post-1st-quarter-scan melt spots exhibit a rough surface with a central depression, while the other melt spots appear smoother. This is because the low temperature of the melt pool formed during the 1st-quarter grid scan results in poor wettability, leading to a rough melt spot [22]. As scanning

progressed to the 2nd-quarter grid and beyond, the melt pool temperature increased, improving wettability and reducing Rayleigh instability. With the help of Marangoni convection, the surface of the melt spot began to smooth out [22]. As shown in Fig. 6.9a, some of the post-1st-quarter-scan melt spots in the t_d = 5 ms coating had already become smooth. This suggests that the melt pool temperature during the 1st-quarter scan at t_d = 5 ms is higher than at t_d = 2 ms. Fig. 6.9a shows that, for the coating with t_d = 10 ms, both the post-1st-quarter-scan and post-2nd-quarter-scan melt spots remain rough. Only some of the post-3rd-quarter-scan melt spots began to smooth out, and all melt spots did not become smooth until the 4th-quarter scan. This indicates that the material surface was heated more slowly during the t_d = 10 ms scan, with temperatures only reaching the level of the t_d = 5 ms 1st-quarter scan by the time the 3rd-quarter scan was completed.

The results of the cross-sectional observations corroborate the conclusions drawn from the analysis of the surface morphology. Fig. 6.8b1 shows the BSE image of the coating cross-section after the 1st-quarter scan at t_d = 2 ms. This reveals the irregular shapes of the melt spot boundary and the black particles at the bottom. Combined with the EDS data in Fig. 6.8b2, these particles are identified as Ti phases. This suggests that, during the 1st-quarter scan of the t_d = 2 ms coating, the melt pool temperature was insufficient to completely melt the underlying Ti substrate, resulting in particles of the substrate entering the melt pool. Fig. 6.9b1 shows the cross-section of the coating after the 1st-quarter scan at t_d = 5 ms, where the melt spot boundary is clearly observed. In contrast, the cross-section of coating after the 1st-quarter scan at t_d = 10 ms (Fig. 6.10b1) shows minimal fusion between the Ni coating and Ti substrate. EDS data (Fig. 6.10b2) reveal a surface Ni concentration approaching 100 at.%. In the post-2nd-quarter-scan cross-sections of the 10 ms coating (Fig. 6.10c1 and 6.10c2), the Ni coating still shows

almost no fusion with the Ti substrate. It is only in the post-3rd-quarter-scan cross-sections (Fig. 6.10d1 and 6.10d2) that a melt spot composed of mixed Ni and Ti can be observed. This suggests that the 1st-quarter grid scan at t_d = 5 ms can fuse the Ni-plating layer with the Ti substrate, whereas the scan at t_d = 10 ms requires the third-quarter grid scan to achieve effective fusion.

Although point-wise scans with t_d = 2 ms, 5 ms and 10 ms effectively fused the Ni coating and Ti substrate after reaching the 3rd-quarter grid, the resulting coatings exhibit differences in microstructure and homogeneity. Fig. 6.8e1 shows the post-4th-quarter-scan cross-section of the coating with t_d = 2 ms. While the surface layer of the coating appears highly uniform, dark streaks are observed at regular intervals near the coating-substrate interface. EDS data (Fig. 6.8e2) reveal that these streaks have a Ni concentration of approximately 34 at.%, which corresponds to the $NiTi_2$ phase. These $NiTi_2$ phases were already present in the coating's post-3rd-quarter-scan cross-section (Fig. 6.8d1), distributed along the edges of the 3rd-quarter-scan melt spot. Subsequent scan of the 4th-quarter grid failed to eliminate these phases. These $NiTi_2$ phases belong to the hard phase with negligible ductility [23]. If they were distributed in streak-like structures, they would serve as crack sources within the coating, thereby compromising its mechanical properties. Fig. 6.9e1 shows the post-4th-quarter-scan cross-section of the coating with t_d = 5 ms. The coating exhibits a highly uniform composition with only a few $NiTi_2$ particles near the coating-substrate interface. By contrast, the post-3rd-quarter-scan cross-section (Fig. 6.9d1) of the t_d = 5 ms coating also exhibits streak-like $NiTi_2$ phases similar to those in the t_d = 2 ms coating. Evidently, the 4th-quarter scan at t_d = 5 ms partially eliminated these streak-like $NiTi_2$ phases. Fig. 6.10e1 shows the post-4th-quarter-scan cross-section of the coating with t_d = 10 ms. The coating exhibits an overall uniform composition, but several elongated $NiTi_2$ phases extend almost from

the interface to the coating surface. These phases also formed during the 3rd-quarter scan, as they were already present in the post-3rd-quarter-scan cross-section (Fig. 6.10d1).

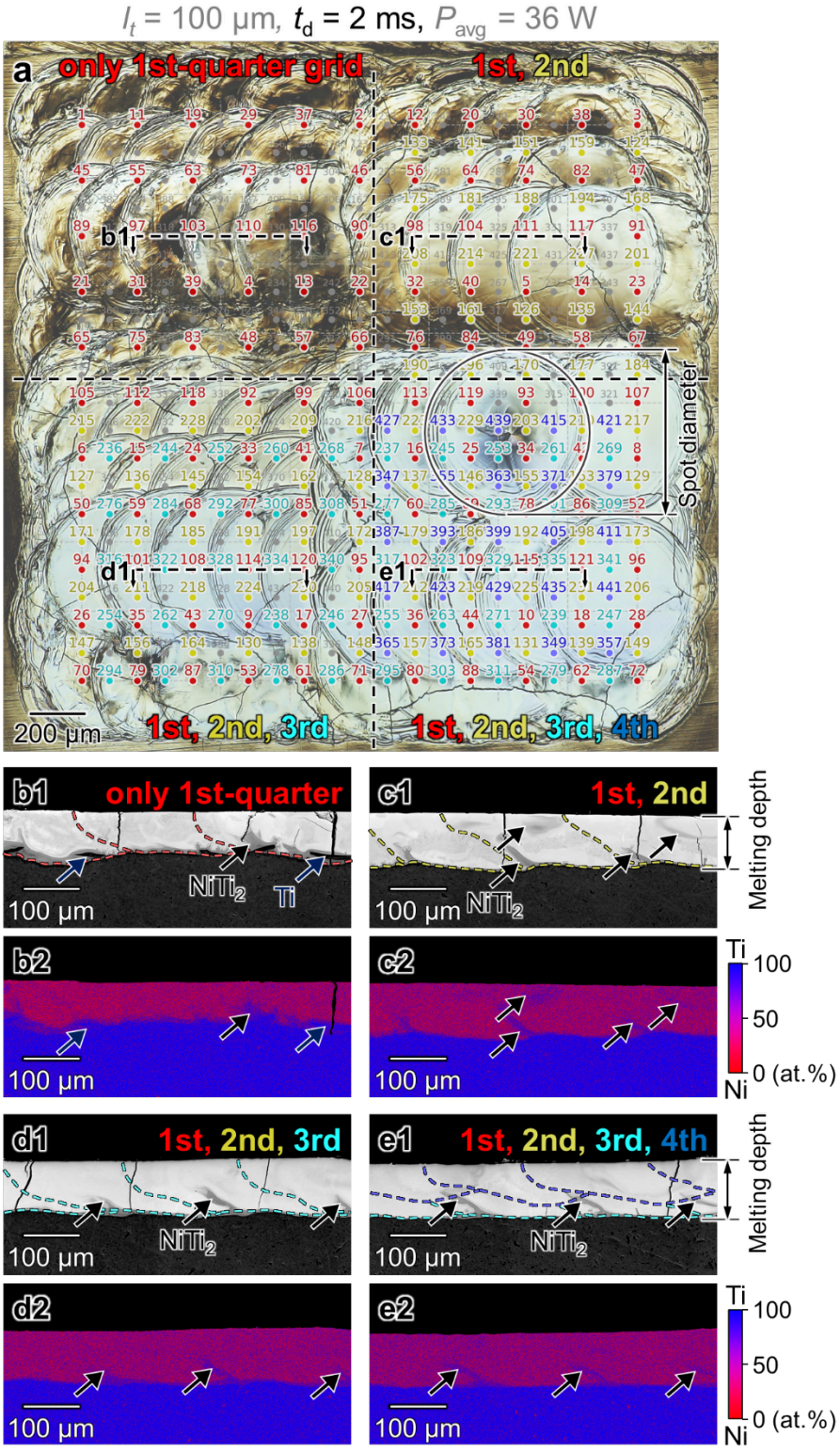

Fig. 6.8. (a) Optical surface image, (b1, c1, d1, e1) cross-sectional BSE images and (b2, c2, d2, e2) corresponding EDS elemental maps obtained from a point-wise scanned (PWS) coating fabricated with: point spacing (l_t) = 100 µm, EB dwell time (t_d) = 2 ms and average EB power (P_{avg}) = 36 W. The colored dots and numbers in (a) represent the scanning points that were activated during the scanning process, along with their respective sequence numbers.

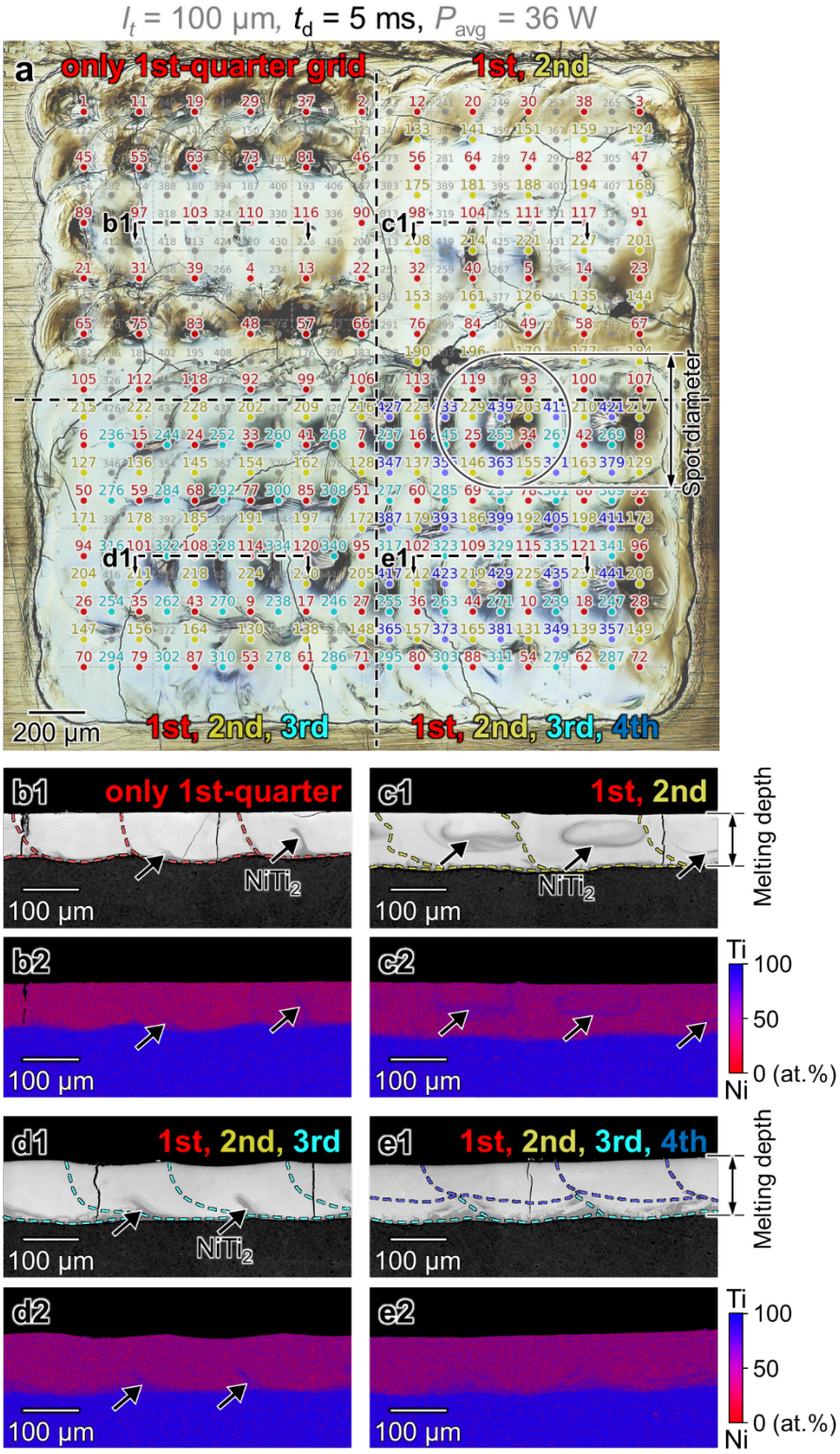

Fig. 6.9. (a) Optical surface image, (b1, c1, d1, e1) cross-sectional BSE images and (b2, c2, d2, e2) corresponding EDS elemental maps obtained from a point-wise scanned (PWS) coating fabricated with: point spacing (l_t) = 100 µm, EB dwell time (t_d) = 5 ms and average EB power (P_{avg}) = 36 W. The colored dots and numbers in (a) represent the scanning points that were activated during the scanning process, along with their respective sequence numbers.

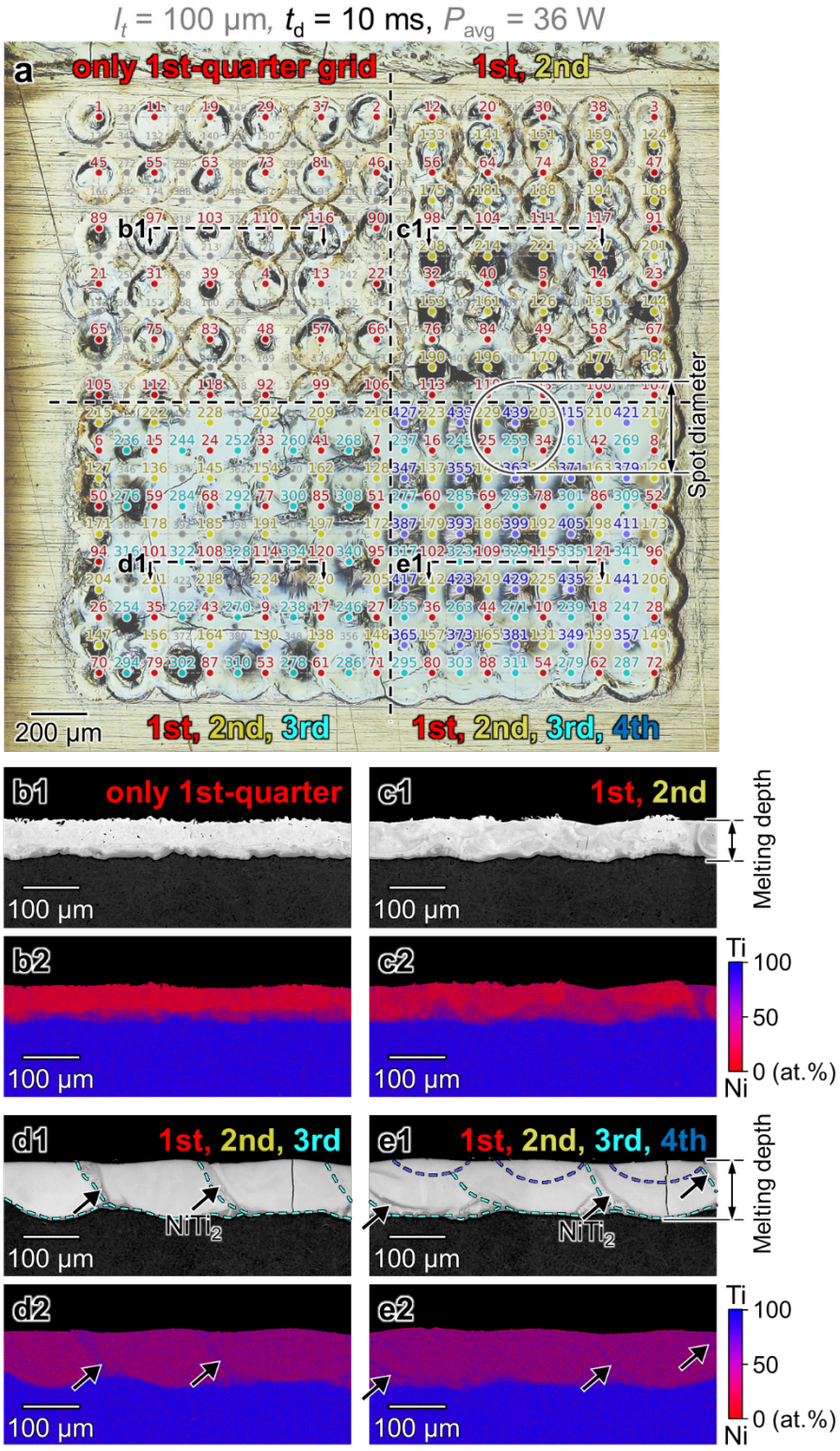

Fig. 6.10. (a) Optical surface image, (b1, c1, d1, e1) cross-sectional BSE images and (b2, c2, d2, e2) corresponding EDS elemental maps obtained from a point-wise scanned (PWS) coating fabricated with: point spacing (l_t) = 100 µm, EB dwell time (t_d) = 10 ms and average EB power (P_{avg}) = 36 W. The colored dots and numbers in (a) represent the scanning points that were activated during the scanning process, along with their respective sequence numbers.

The variation in the distribution of the $NiTi_2$ phase in the coating obtained from point-wise scanning at different t_d values primarily stems from differences in melt pool dynamics and thermal history during scanning. As shown in Fig. 6.11a, the melt spot diameter slightly increased with scanning progression; it is largest for t_d = 2 ms, intermediate for t_d = 5 ms and smallest for t_d = 10 ms in scans of all quarter grids. Fig.6.11b shows that in the scan of the 3rd- and 4th-quarter grids, the melting depths of the three conditions show almost no difference, although the melt depth at t_d = 10 ms was initially significantly lower than the other two due to slower heating. This results in a significant difference in the melt pool width-to-depth ratio between the three conditions. The melt pool width-to-depth ratio is largest for t_d = 2 ms. However, as shown in the cross-sectional BSE image (Fig. 6.8d1) and the schematic (Fig. 6.12a), the maximum melt depth is only achieved in a small central region of the melt pool. This indicates that the melt spot boundaries have a gentle gradient, causing the streak-like $NiTi_2$ phase distributed along the melt spot boundary to incline outward. Furthermore, as the points in the 4th-quarter grid are spaced distance of a l_t apart from those in the 3rd-quarter grid (see Fig. 6.12), the peripheral region of the 4th-quarter-scan melt pool lacks sufficient depth to remelt the $NiTi_2$ phase inclined in the post-3rd-quarter scan coating (see Fig. 6.12a). With t_d = 10 ms, the melt pool has the smallest width-to-depth ratio of the three conditions and, as can be seen in the cross-sectional BSE image (Fig. 6.10d1), it also has the steepest melt spot boundary. However, with a melt spot diameter of only around 300 μm, the depth of the peripheral region of the 4th-quarter-scan melt pool can only remelt the $NiTi_2$ phase in the surface layer of the post-3rd-quarter-scan coating, failing to remelt it entirely (see Fig. 6.12c). In contrast, at t_d = 5 ms, the melt spot diameter reaches 460 μm and the boundary is relatively steep. Consequently, the peripheral region of the 4th-quarter-scan melt pool can remelt the

upper portion of the streak-like $NiTi_2$ phase in the post-3rd-quarter-scan coating (Fig. 6.12b).

However, the cross-sectional BSE image (Fig. 6.9e1) shows no streak-like $NiTi_2$ phase remained in the post-4th-quarter-scan coating. It was therefore assumed that the 4th-quarter scan with t_d = 5 ms induced *in situ* heat treatment [24,25], causing the lower portion of the streak-like $NiTi_2$ phases to break into $NiTi_2$ phase particles. In contrast, the t_d = 2 ms scan spends only 20% of its duration in the heating state. While the short duration of the high-power electron beam (180 W in this example) can heat the melt pool to very high temperatures, the remaining 80% of the time that the electron beam is idle allows the temperature to drop below the threshold required for *in situ* heat treatment. As discussed earlier, the scan with t_d = 10 ms, featuring the lowest electron beam power (36 W in this example), heats the material too slowly. Therefore, it is difficult to reach the required temperatures for *in situ* heat treatment. Only the scan with t_d = 5 ms combines a sufficiently long heating duration with a sufficiently high electron beam power to induce *in situ* heat treatment effects within the coating.

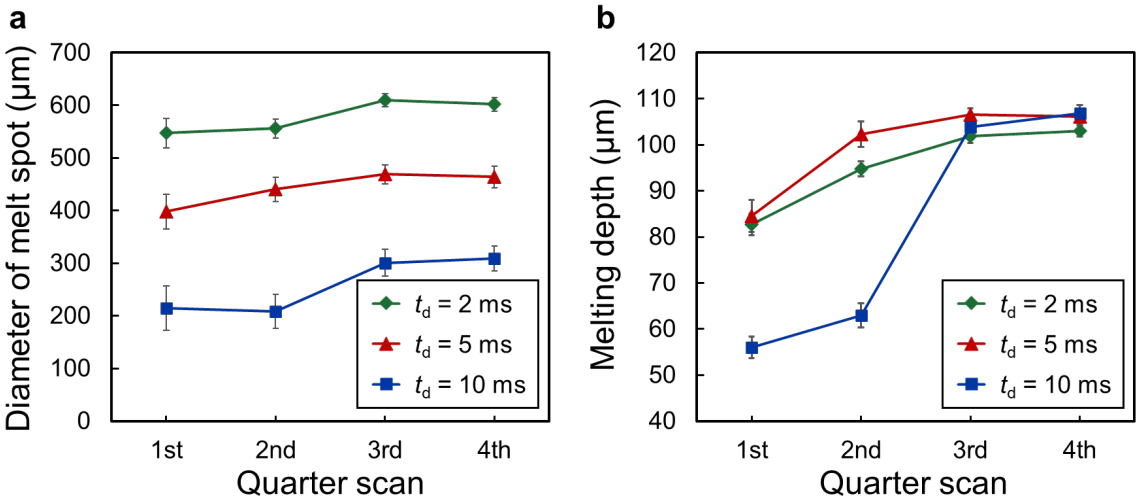

Fig. 6.11. Variation in diameter of melt spot and melting depth of the coatings in Fig. 6.8 (t_d = 2 ms), Fig. 6.9 (t_d = 5 ms) and Fig. 6.10 (t_d = 10 ms) with the progress in point-wise scanning.

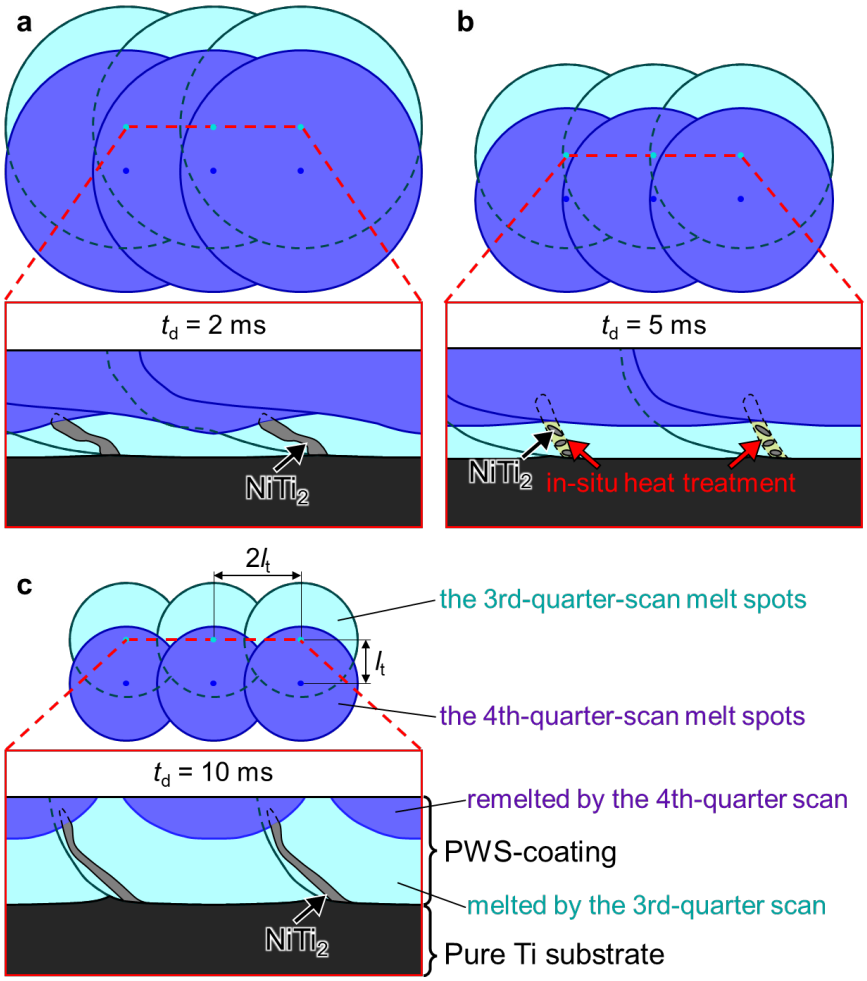

Fig. 6.12. Schematic diagrams of remelting effects in the point-wise scanned (PWS) coatings fabricated with EB dwell times (t_d) of (a) 2 ms, (b) 5 ms, and (c) 10 ms, under fixed point spacing and average EB power.

6.3.2.2 Comparison between IS-coating and PWS-coating

Fig. 6.13 shows the cross-sectional BSE images and corresponding EDS elemental maps of a PWS-coating fabricated by without additional four-quadrant settings, compared with a multi-track intermittently scanned (IS) coating fabricated in Chapter 4. The processing parameters for the PWS-coating were as follows: l_t = 100 μm; t_d = 5 ms; and P_{avg} = 36 W. The processing parameters for the IS-coating were as follows: l_{off} = 300 μm; t_{int} = 60 s; and P = 126 W. According to the results in Chapter 4, the IS-coating matrix consists of the cubic *B*2-NiTi phase and contains a small amount of the

hexagonal $D0_{24}$-Ni_3Ti strengthening phase. However, due to compositional inhomogeneity at the melt track junctions in the IS-coatings, the cubic $C15$-$NiTi_2$ phase is still present. These are the dark streaks that can be observed in Fig. 6.13a1. The corresponding EDS data (Fig. 6.13a2) confirmed that these streaks consist of the $NiTi_2$ phase. By contrast, Fig. 6.13b1 shows only a few particles of the $NiTi_2$ phase distributed near the coating-substrate interface within the PWS-coating. EDS data in Fig. 6.13b2 shows that the PWS-coating has an average Ni concentration of 52.9 at.%, which is very close to 52.2 at.% of the IS-coating. Therefore, it is most likely that the PWS-coating still consists of the $B2$-NiTi and $D0_{24}$-Ni_3Ti phases. This suggests that point-wise scanning under optimized parameters is able to effectively eliminate coating inhomogeneities while ensuring consistent coating composition, compared to multi-track scanning. Another noteworthy observation is that the IS-coating in Fig. 6.13a1 is thicker at the melt track center and thinner at the melt track junctions. By contrast, the PWS coating in Fig. 6.13b1 demonstrates a consistent thickness across all locations. This suggests that point-wise scanning also has the advantage of ensuring uniform coating thickness.

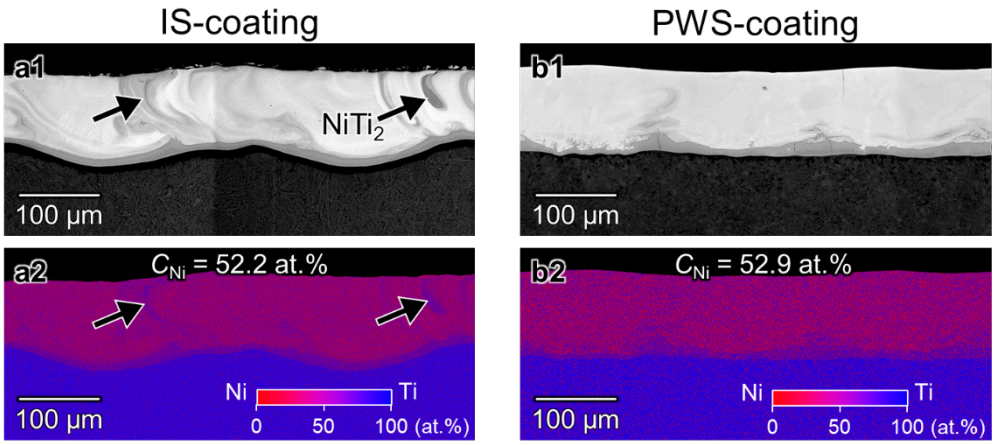

Fig. 6.13. Comparison of multi-track intermittently scanned (IS, in Chapter 4) and point-wise scanned (PWS) coatings in terms of (a1, b1) cross-sectional BSE images and (a2, b2) corresponding EDS elemental maps.

6.3.3 Elemental composition

Fig. 6.14 shows the variation of the central Ni concentration (C_{Ni_cnt}) in point-wise scanned (PWS) coatings with average electron beam power (P_{avg}) for all 12 parameter combinations. The concentration range for the NiTi single phase in the Ni-Ti binary phase diagram [13] is extremely narrow. Even a slight compositional deviation can lead to the formation of a secondary phase in the alloy. Furthermore, the martensitic thermoelastic phase transformation behaviour of the NiTi phase is influenced by the Ni concentration in the alloy [26]. Therefore, restricting the composition of PWS coatings to levels close to those of bulk Nitinol is essential for ensuring good mechanical properties. Therefore, it is necessary to analyze the influence of each experimental parameter on coating composition in point-wise scanning to achieve control over the composition of PWS coatings. The most notable observation from Fig. 6.14 is that C_{Ni_cnt} in PWS coatings decreases as P_{avg} increases across all parameter sets. This phenomenon has the same cause as the decrease in Ni concentration in the coatings observed in Chapter 4 with increasing electron beam power: with a fixed Ni coating thickness, a higher P_{avg} increases the melt depth and the amount of molten Ti substrate, resulting in a relative decrease in the Ni content of the coating. Secondly, comparing the results within a single parameter column (e.g. Fig. 6.14a, 6.14d, 6.14g and 6.14j) reveals that C_{Ni_cnt} increases with growing point spacing (l_t). This is because increased lt means reduced energy area density during scanning; thus, the mechanism by which it affects C_{Ni_cnt} is similar to that of P_{avg}. However, comparing results within the same parameter row (e.g. Fig. 6.14g, 6.14h and 6.14i) reveals that electron beam dwell time (t_d) appears to have a negligible impact on C_{Ni_cnt}.

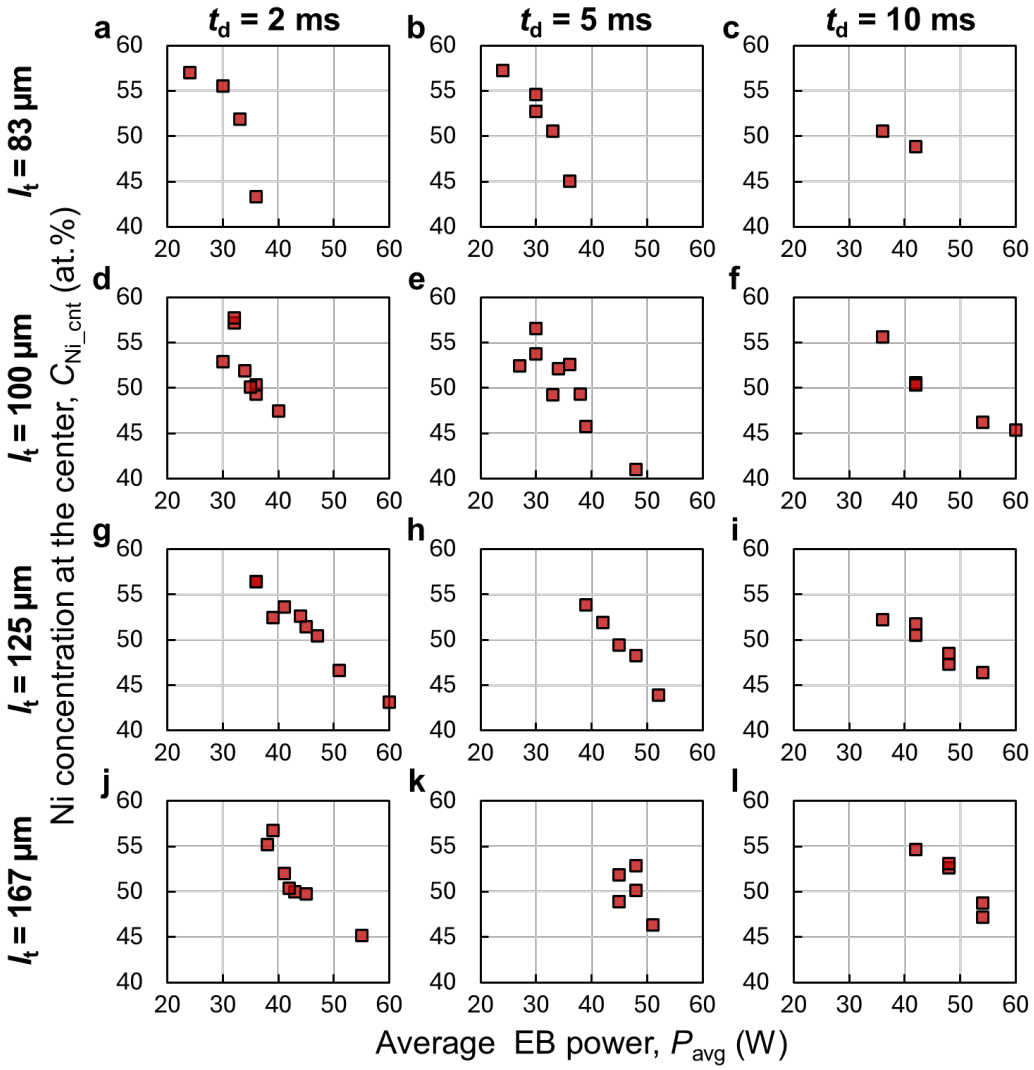

Fig. 6.14. Ni concentration at the center (C_{Ni_cnt}) as a function of average EB power (P_{avg}) plots of point-wise scanned (PWS) coatings under all 12 parameter sets of 4 levels of point spacing (l_t) × 3 levels of EB dwell time (t_d). The corresponding process parameters for each sub-figure are indicated within the figures as follows: (a) l_t = 83 µm, t_d = 2 ms; (b) l_t = 83 µm, t_d = 5 ms; (c) l_t = 83 µm, t_d = 10 ms; (d) l_t = 100 µm, t_d = 2 ms; (e) l_t = 100 µm, t_d = 5 ms; (f) l_t = 100 µm, t_d =10 ms; (g) l_t = 125 µm, t_d = 2 ms; (h) l_t = 125 µm, t_d = 5 ms; (i) l_t = 125 µm, t_d = 10 ms; (j) l_t = 167 µm, t_d = 2 ms; (k) l_t = 167µm, t_d = 5 ms; (l) l_t = 167 µm, t_d = 10 ms.

Direct observation of raw data only enables the qualitative analysis of the effects of these parameters. Mathematical modelling is a more suitable approach for quantitative analysis of each parameter's effect. Therefore, we used all the data from Fig. 6.14 to train a machine learning model to predict Ni concentration in the PWS-coating. As

shown in Fig. 6. 15a, the model yielded a test-set coefficient of determination (R^2) of 0.8, and a prediction mean square error (MSE) of 3.2. Fig. 6.15b shows all the coefficients of the machine learning model. P_{avg} has the largest absolute linear coefficient value among them and is negative, indicating that an increase in P_{avg} reduces C_{Ni_cnt} when the other parameters remain constant. The absolute value of the linear coefficient of l_t ranks second and is positive, suggesting that C_{Ni_cnt} tends to increase as l_t rises. In contrast, all terms containing t_d have smaller coefficients, indicating weaker contributions from t_d. These findings are consistent with the conclusions drawn from the direct observation of the data in Fig. 6.14. Furthermore, the coefficients for the $l_t \times P_{avg}$ and P_{avg}^2 terms also have large absolute values, indicating that the non-linear and interaction effects of the experimental parameters on C_{Ni_cnt} are also significant. This model enables control over coating composition across various parameter combinations and provides a means of controlling variables when investigating the impact of experimental parameters on mechanical properties.

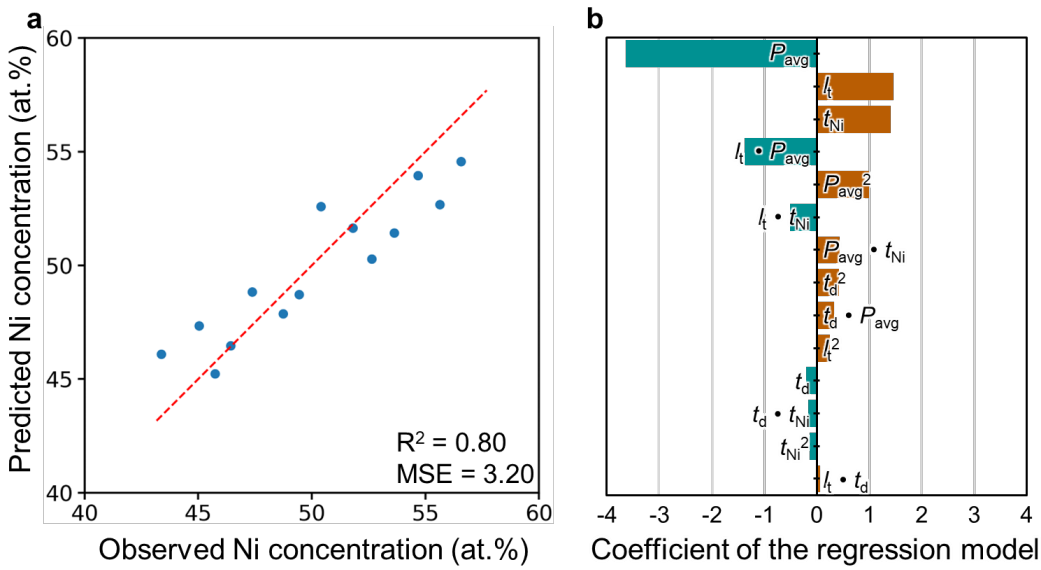

Fig. 6.15. (a) Prediction of Ni concentrations of the point-wise scanned (PWS) coatings on the test set by the machine learning model. (b) Coefficients of the ridge regression model. Symbol definitions: P_{avg}, average EB power; l_t, point spacing in scanning grid; t_d, EB dwell time in point-wise scanning; t_{Ni}, thickness of Ni-plating layer before scanning.

6.3.4 Microstructural size and crystal orientation

Fig. 6.16 presents the EBSD analysis results obtained from the *x*–*y* plane of the intermittently scanned (IS) coatings in the as-scanned and heat-treated conditions. Fig. 6.16a2 shows the band contrast (BC) image the as-scanned IS-coating at P = 126 W, in which microstructure across three adjacent melt tracks can be seen. A finer microstructure is observed near the melt track boundaries, whereas coarser microstructural features are present in the central region of the melt tracks. This spatial variation in microstructural scale can be attributed to differences in the local solidification conditions during electron beam scanning. At the early stage of solidification, the cooling rate near the melt track boundaries is relatively high, which limits grain growth and results in finer grains. As solidification proceeds toward the melt track center, the cooling rate decreases, allowing grains to grow to larger sizes [27]. The inverse pole figure (IPF) map of the as-scanned coating and the corresponding

{100} pole figure (PF) of the *B*2-NiTi phase are shown in Fig. 6.16a3 and 6.16a4, respectively. The relatively dispersed distribution of orientation intensities in the pole figure indicates that no pronounced crystallographic texture is developed in the multi-track scanned coating. The EBSD results of the heat-treated (annealed and aged) IS-coating are shown in Fig. 6.16(b1−b4). The heat-treated coating exhibits a similar spatial microstructural and crystallographic orientation distribution to the as-scanned condition. This suggests that, under the heat-treatment conditions employed in this study, no significant changes in crystallographic texture occurred, and neither noticeable grain coarsening nor recrystallization was induced.

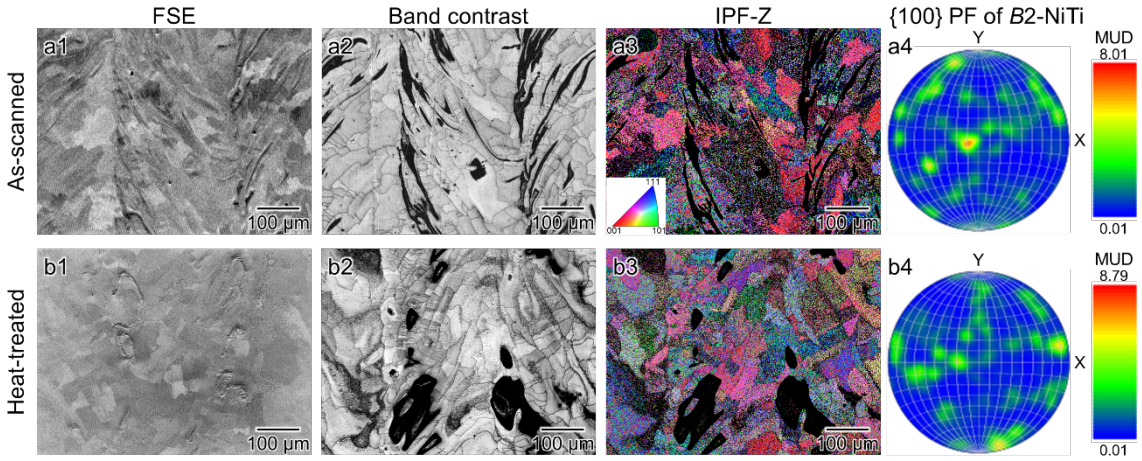

Fig. 6.16. Forescatter electron images, band contrast images, inverse pole figure maps and pole figures of *B*2-NiTi phase of multi-track scanned coatings in (a) as-scanned state and (b) heat-treated state.

Fig. 6.17 presents the EBSD analysis results on the *x*–*y* plane of point-wise scanned (PWS) coatings fabricated with three different electron beam dwell times (t_d). Figs. 6.17a2, 6.17b2, and 6.17c2 show the BC images of the PWS coatings produced with t_d values of 2 ms, 5 ms, and 10 ms, respectively, in which a single melt spot and its surrounding region can be identified. Similar to the spatial distribution observed in the IS-coatings, the microstructure near the edge of the melt spot is finer, whereas coarser

microstructural features are observed in the central region. Moreover, with increasing t_d, the microstructure within the melt spot becomes progressively finer. This trend can be attributed to the variation in energy input during electron beam scanning. When the average electron beam power (P_{avg}) is maintained constant, increasing t_d leads to a reduction in the peak instantaneous beam power during scanning. As demonstrated by the experimental results in Section 6.3.2, scanning with a lower effective beam power at t_d = 10 ms results in the smallest melt pool size. The reduced melt pool size enhances heat dissipation, thereby increasing the cooling rate during solidification, which ultimately leads to the formation of the finest microstructure [28]. In addition, no pronounced crystallographic orientation preference is observed in the IPF maps of the three PWS coatings (Figs. 6.17a3, 6.17b3, and 6.17c3). Consistently, the corresponding {100} PFs of the *B*2-NiTi phase (Figs. 6.17a4, 6.17b4, and 6.17c4) do not exhibit any significant orientation intensity concentration, indicating that no strong crystallographic texture is formed in the PWS coatings.

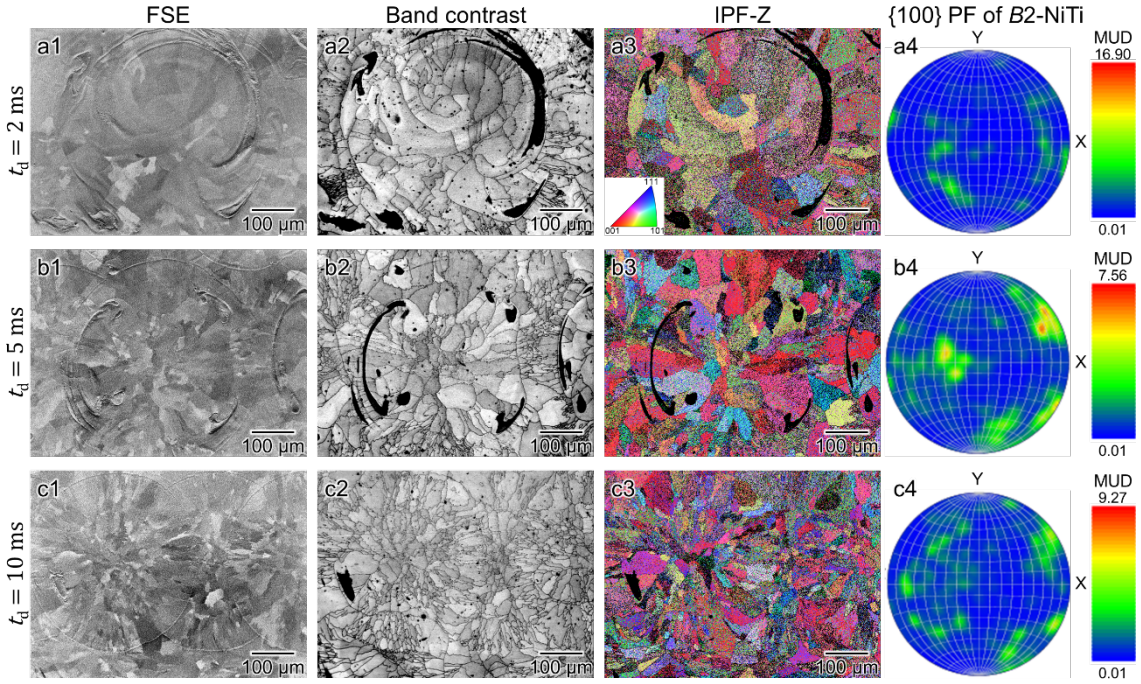

Fig. 6.17. Forescatter electron images, band contrast images, inverse pole figure maps and pole figures of *B*2-NiTi phase of point-wise scanned coatings at dwell time (t_d) of (a) 2 ms, (b) 5 ms and (c) 10 ms.

Fig. 6.18 shows the fractions of the *B*2-NiTi and *B*19'-NiTi phases in multi-track, heat-treated and point-wise scanned coatings, respectively, as analyzed based on EBSD results. The *B*2-NiTi phase accounts for approximately 67% in all three types of coating, while the *B*19'-NiTi phase constitutes around 33%. This indicates that changing the scanning strategy from multi-track to point-wise, or whether heat treatment is performed, has essentially no effect on the phase fractions within the coating.

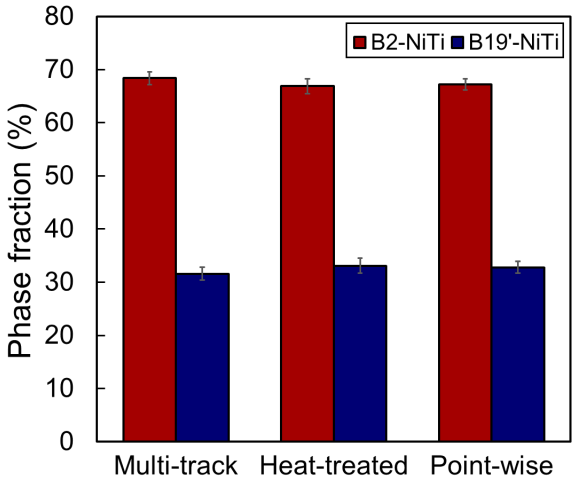

Fig. 6.18. Phase fraction based on EBSD analysis of *B*2- and *B*19'-NiTi phases in multi-track scanned, heat-treated and point-wise scanned coatings.

Fig. 6.19 compares the statistical distributions of characteristic microstructural sizes in IS-coatings under different heat-treatment conditions and in PWS-coatings fabricated with different t_d. Due to the limited EBSD indexing quality, grain size determination based on orientation data was not reliable. Therefore, the characteristic microstructural size was evaluated using BC-domains extracted from EBSD band contrast images, which serve as a consistent comparative length scale rather than an absolute grain size.

A slight increase in both mean and median domain sizes is observed in the IS-coating after heat treatment, indicating slight microstructural coarsening. In contrast, all PWS coatings exhibit significantly finer microstructure than the IS coatings. Moreover, the characteristic domain size in PWS coatings decreases monotonically with increasing t_d, as reflected by the reduction in both mean and median values. This is consistent with the observations shown in Fig. 6.17. Both IS- and PWS-coatings exhibit right-skewed distributions in characteristic domain size, with a mean value that exceeds the median. This suggests that a small number of large microstructures significantly increase the average size. In contrast, the difference between the mean and median values is smaller

in PWS-coatings than in IS-coatings, which suggests that the proportion of large microstructures is lower in PWS-coatings. Additionally, the standard deviation (σ) of characteristic domain sizes in the PWS-coating gradually decreases with increasing t_d and remains lower than in the as-scanned IS-coating. This suggests that the point-wise scanning strategy produces microstructures with a more concentrated size distribution, i.e. greater microstructural uniformity, than multi-track scanning.

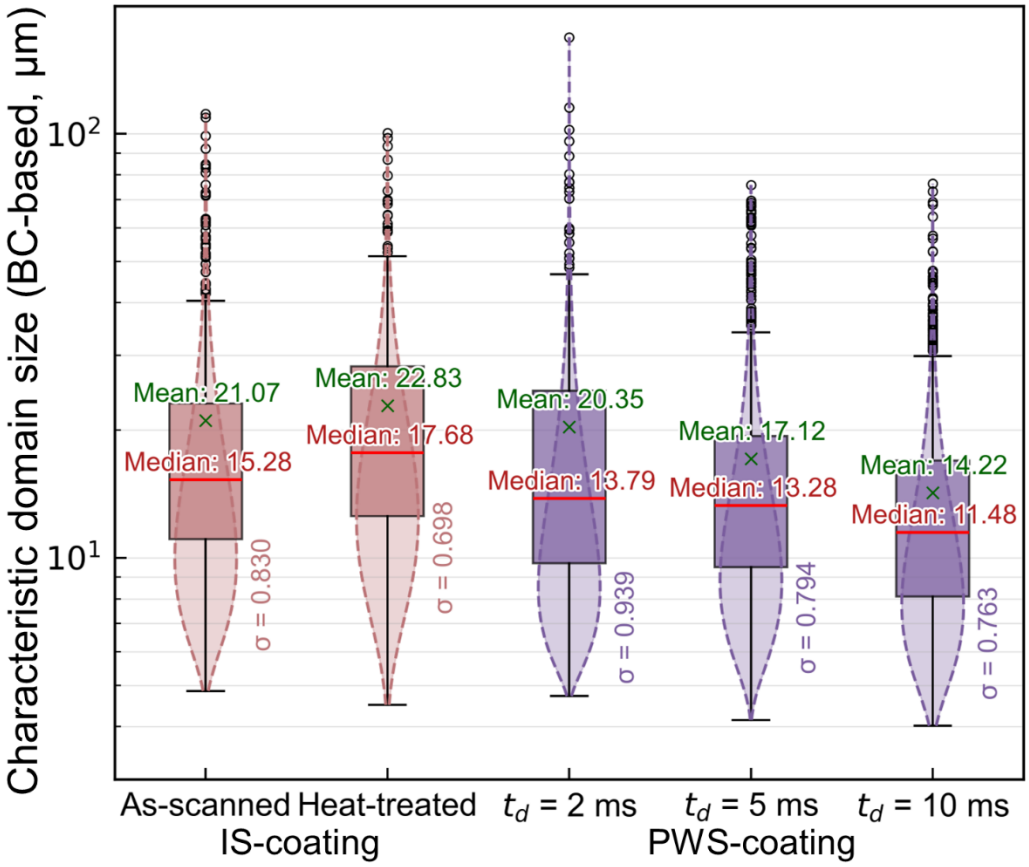

Fig. 6.19. Statistics on the characteristic domain size of intermittently scanned (IS) and point-wise scanned (PWS) coatings, obtained with different heat treatment and dwell times (t_d) , respectively. The characteristic domain size was quantified using the equivalent circular diameter calculated from the segmented band contrast images.

6.3.5 Indentation properties

In nanoindentation testing, the hardness parameter (H, GPa) and Young's modulus

parameter (E, GPa) tend to receive the most attention. This is because a strong positive correlation is generally believed to exist between a material's H and its strength and wear resistance [29], while E is thought to reflect the material's rigidity [30]. However, recent studies [31–36] and the results presented in Chapters 4 and 5 demonstrate that the H/E ratio and the indentation depth recovery rate ($\eta_{d,h}$) are more strongly correlated with wear resistance. Specifically, higher H/E ratios and higher $\eta_{d,h}$ values indicate superior wear resistance. Therefore, Fig. 6.20 shows how the H/E ratio and $\eta_{d,h}$ vary for point-wise scanned (PWS) coatings as a function of point spacing (l_t) and electron beam dwell time (t_d). Although the changes are small, distinct trends can still be discerned. As shown in Fig. 6.20a, both the H/E ratio and the indentation depth recovery rate of the PWS coating initially increase and then decrease with increasing l_t, reaching their maximum values at l_t = 125 µm. As shown in Fig. 6.20b, the H/E ratio and $\eta_{d,h}$ of the PWS-coating initially increase and then decrease with increasing t_d, reaching their maximum values at t_d = 5 ms.

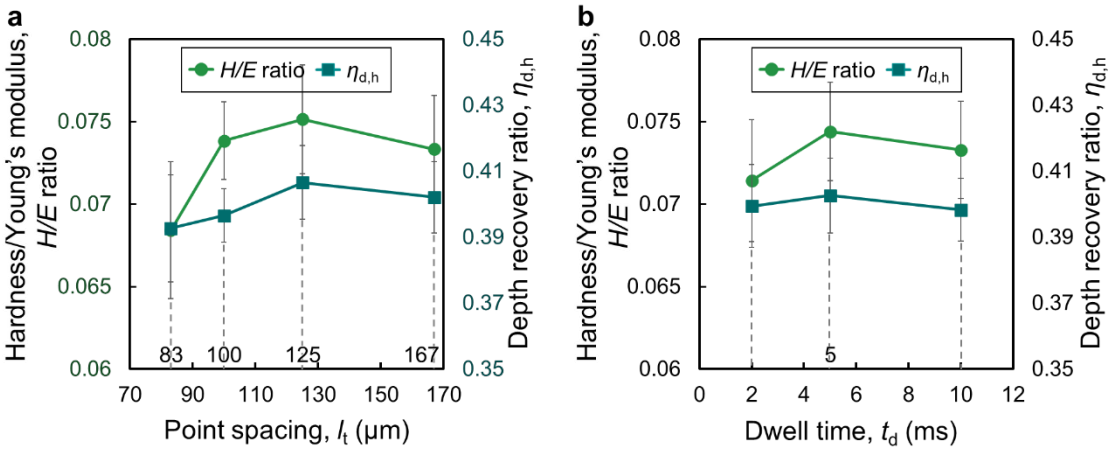

Fig. 6.20. Variation on Hardness/Young's modulus ratio (H/E ratio) and depth recovery ratio ($\eta_{d,h}$) with (a) point spacing (l_t) and (b) dwell time of EB (t_d) in point-wise scanned coatings.

Fig. 6.21 shows the H/E ratio and the $\eta_{d,h}$ of the PWS-coatings produced using all

the parameter sets. These are compared with the results obtained for the multi-track, intermittently scanned (IS) coatings in Chapter 4, the heat-treated IS coatings in Chapter 5 and the superelastic Nitinol (SE-NiTi) bulk material. Thanks to the machine learning model trained in Section 6.3.3, the Ni concentration in all PWS coatings was controlled to approximately 52 at.%, matching that of the IS coatings. Consequently, all differences in indentation properties stem from variations in scanning methodology.

As shown in Fig. 6.21a, the PWS coating exhibits a significantly higher $\eta_{d,h}$ compared to the as-scanned IS-coating, while the *H/E* ratio shows only a slight improvement. Compared to the heat-treated IS-coating, the *H/E* ratio and $\eta_{d,h}$ of the PWS-coating generally fell between the values for the annealed and aged IS-coatings. The PWS-coating with l_t = 125 µm and t_d = 5 ms achieved the highest *H/E* ratio and $\eta_{d,h}$ values. Its $\eta_{d,h}$ value was markedly higher than that of the annealed IS-coating and reached levels comparable to those of the aged IS-coatings and SE-NiTi. This suggests that PWS-coatings are likely to be as resistant to wear as, or even more resistant than, annealed IS-coatings without requiring heat treatment. Another noteworthy point is that, as shown in Fig. 6.21b, the average standard deviation of the *H/E* ratio and $\eta_{d,h}$ for the PWS-coating decreased significantly compared to the IS-coating, reaching essentially the same levels to those of the SE-NiTi. Although heat treatment slightly reduced the average standard deviation of the IS-coating, the magnitude of this reduction was markedly less than that observed for the PWS-coating. According to Furgiuele et al.[18], the estimated diameter of the deformation zone in the nanoindentation tests performed in this study is approximately 17 µm. This is higher than the median characteristic domain size of the PWS-coatings shown in Fig. 6.18. Therefore, the measured nanoindentation response is more likely to represent the behavior of multiple grains or sub-grains than that of a single grain in the PWS-coatings. This suggests that point-

wise scanning substantially improves the uniformity of the mechanical properties of the coating compared to multi-track scanning by enhancing the homogeneity of both the microstructure and composition.

During wear, debris often originates from more vulnerable areas on the material surface [37,38]. These debris enters the friction interface and acts as a third body, causing cutting, embedding and ploughing and thereby accelerating wear [39,40]. Enhanced uniformity reduces such vulnerable sites and should significantly improve the coating's wear resistance.

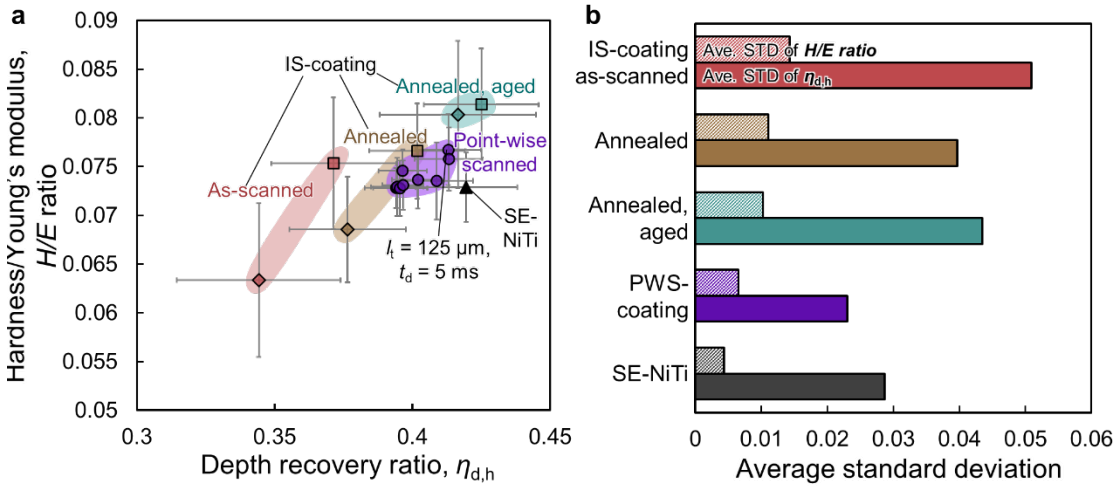

Fig. 6.21. (a) Plot of hardness/Young's modulus ratio (*H/E* ratio) versus depth recovery ratio ($\eta_{d,h}$) of multi-track intermittently scanned (IS) coatings at various heat treatment states (results in Chapter 4 and 5) and point-wise scanned (PWS) coatings fabricated under all parameter sets, compared with superelastic nitinol (SE-NiTi). (b) Average standard deviations of *H/E* ratio and $\eta_{d,h}$ of multi-track scanned coatings, PWS-coatings and SE-NiTi.

6.4 Conclusions

To explore a efficient improvement methods to homogenize coatings and eliminate inhomogeneities, this chapter focuses on electron beam (EB) scanning strategies. Drawing insights from additive manufacturing researches, a novel point-wise scanning strategy has been designed. The point-wise EB scanning experiments involved five

parameters: the step size (l_s) for scanning grid, the spacing between points (l_t) in the scanning grid, the cycle time (τ) for each point, the dwell time (t_d) of the EB at each point and the average EB power (P_{avg}) during scanning. The l_t was varied across four levels (83, 100, 125 and 167 μm), while the t_d was varied across three levels (2, 5 and 10 ms) with l_s and τ fixed at 1 mm and 10 ms, respectively. The general range of P_{avg} is 20–60, though it varies specifically in each parameter set. The effects of the parameters on the point-wise scanned (PWS) coatings were evaluated by analyzing surface and cross-sectional morphology, microstructure, elemental composition and indentation properties. The key findings and conclusions are as follows:

- When the parameters are optimized, point-wise scanning eliminated $NiTi_2$ phases while achieving Ni concentrations of around 52 at.%, which is comparable to multi-track scanned coatings. The t_d = 5 ms scan produced the most effective coating homogenization.
- To quantify the effects of the numerous parameters involved in point-wise scanning and to control the composition of coating, a machine learning model was developed to predict the Ni concentration in the coating. The model coefficients indicate that P_{avg} and l_t significantly contribute to variations in Ni concentration, whereas t_d's contribution is negligible.
- PWS-coatings have a finer microstructure than multi-track scanned coatings. The microstructure of PWS coatings becomes more refined with increasing td, and the size distribution of the microstructure becomes more uniform.
- The nanoindentation results of PWS-coatings were compared with those of multi-track scanned and heat-treated coatings in Chapter 4 and 5. It revealed that point-wise scanning effectively enhances the hardness/Young's modulus ratio (*H/E* ratio) and indentation depth recovery ratio ($\eta_{d,h}$), achieving levels comparable to or

exceeding those of multi-track scanned coatings after annealing.

- Moreover, point-wise scanning significantly reduced the average standard deviation of both the *H/E* ratio and $\eta_{d,h}$, indicating that improved microstructural and composition uniformity enhances uniformity of mechanical properties and contributes to the improved wear resistance of the coatings.

References

[1] H. Jia, H. Sun, H. Wang, Y. Wu, H. Wang, Scanning strategy in selective laser melting (SLM): a review, Int. J. Adv. Manuf. Technol. 113 (2021) 2413–2435. https://doi.org/10.1007/s00170-021-06810-3.

[2] Q. Chen, H. Taylor, A. Takezawa, X. Liang, X. Jimenez, R. Wicker, A.C. To, Island scanning pattern optimization for residual deformation mitigation in laser powder bed fusion via sequential inherent strain method and sensitivity analysis, Addit. Manuf. 46 (2021) 102116. https://doi.org/10.1016/j.addma.2021.102116.

[3] R.R. Dehoff, M.M. Kirka, W.J. Sames, H. Bilheux, A.S. Tremsin, L.E. Lowe, S.S. Babu, Site specific control of crystallographic grain orientation through electron beam additive manufacturing, Mater. Sci. Technol. 31 (2015) 931–938. https://doi.org/10.1179/1743284714Y.0000000734.

[4] M.M. Kirka, Y. Lee, D.A. Greeley, A. Okello, M.J. Goin, M.T. Pearce, R.R. Dehoff, Strategy for Texture Management in Metals Additive Manufacturing, JOM 69 (2017) 523–531. https://doi.org/10.1007/s11837-017-2264-3.

[5] B. AlMangour, D. Grzesiak, J.-M. Yang, Scanning strategies for texture and anisotropy tailoring during selective laser melting of TiC/316L stainless steel nanocomposites, J. Alloys Compd. 728 (2017) 424–435. https://doi.org/10.1016/j.jallcom.2017.08.022.

[6] L. Thijs, K. Kempen, J.-P. Kruth, J. Van Humbeeck, Fine-structured aluminium products with controllable texture by selective laser melting of pre-alloyed AlSi10Mg powder, Acta Mater. 61 (2013) 1809–1819. https://doi.org/10.1016/j.actamat.2012.11.052.

[7] C.Y. Liu, J.D. Tong, M.G. Jiang, Z.W. Chen, G. Xu, H.B. Liao, P. Wang, X.Y. Wang, M. Xu, C.S. Lao, Effect of scanning strategy on microstructure and mechanical properties of selective laser melted reduced activation ferritic/martensitic steel, Mater. Sci. Eng. A 766 (2019) 138364. https://doi.org/10.1016/j.msea.2019.138364.

[8] E. Onal, A.E. Medvedev, M.A. Leeflang, A. Molotnikov, A.A. Zadpoor, Novel microstructural features of selective laser melted lattice struts fabricated with single point exposure scanning, Addit. Manuf. 29 (2019) 100785. https://doi.org/10.1016/j.addma.2019.100785.

[9] F. Huber, M. Rasch, M. Schmidt, Laser Powder Bed Fusion (PBF-LB/M) Process Strategies for In-Situ Alloy Formation with High-Melting Elements, Metals 11 (2021) 336. https://doi.org/10.3390/met11020336.

[10] Denki Kagaku Kai (Ed.), Denki kagaku benran [Electrochemical Handbook], 6th ed., Maruzen Publishing, Tōkyō, 2013.

[11] C. Li, Z.Y. Liu, X.Y. Fang, Y.B. Guo, Residual Stress in Metal Additive Manufacturing, Procedia CIRP 71 (2018) 348–353. https://doi.org/10.1016/j.procir.2018.05.039.

[12] H.S. Carslaw, J.C. Jaeger, H.S. Carslaw, J.C. Jaeger, Conduction of Heat in Solids, Second Edition, Second Edition, Oxford University Press, Oxford, New York, 1986.

[13] Thermo-Calc Software, Titanium and TiAl-based Alloys Databases, Version

4(TCTI4), (2022). https://thermocalc.com/products/databases/ (accessed October 1, 2023).

[14] E.S. Berkovich, The three-faceted diamond pyramid for microhardness testing, Zavod. Lab. 16 (1950) 345.

[15] A. Shimamoto, K. Tanaka, Y. Akiyma, H. Yoshizaki, Nanoindentation of glass with a tip-truncated Berkovich indenter, Philos. Mag. A 74 (1996) 1097–1105. https://doi.org/10.1080/01418619608239710.

[16] International Organization for Standardization, Metallic materials — Instrumented indentation test for hardness and materials parameters — Part 1: Test method (ISO Standard No. 14577-1:2015), (2015). https://www.iso.org/standard/56626.html.

[17] W. Ni, Y.-T. Cheng, D.S. Grummon, Microscopic superelastic behavior of a nickel-titanium alloy under complex loading conditions, Appl. Phys. Lett. 82 (2003) 2811–2813. https://doi.org/10.1063/1.1569984.

[18] B.N.J. Persson, Surface Roughness-Induced Stress Concentration, Tribol. Lett. 71 (2023) 66. https://doi.org/10.1007/s11249-023-01741-4.

[19] D. Gropper, L. Wang, T.J. Harvey, Hydrodynamic lubrication of textured surfaces: A review of modeling techniques and key findings, Tribol. Int. 94 (2016) 509–529. https://doi.org/10.1016/j.triboint.2015.10.009.

[20] W. Tang, Y. Zhou, H. Zhu, H. Yang, The effect of surface texturing on reducing the friction and wear of steel under lubricated sliding contact, Appl. Surf. Sci. 273 (2013) 199–204. https://doi.org/10.1016/j.apsusc.2013.02.013.

[21] G.V. Jagadeesh, S. Gangi Setti, A review on latest trends in ball and roller burnishing processes for enhancing surface finish, Adv. Mater. Process. Technol. 8 (2022) 4499–4523. https://doi.org/10.1080/2374068X.2022.2077534.

[22] M. Khorasani, A. Ghasemi, U.S. Awan, E. Hadavi, M. Leary, M. Brandt, G.

Littlefair, W. O'Neil, I. Gibson, A study on surface morphology and tension in laser powder bed fusion of Ti-6Al-4V, Int. J. Adv. Manuf. Technol. 111 (2020) 2891–2909. https://doi.org/10.1007/s00170-020-06221-w.

[23] Y. Tian, Z. Liang, Y. Cai, H. Jiang, M. Chen, J. Han, Microstructure and mechanical properties of Ti2Ni alloy fabricated by direct energy deposition, Sci. Technol. Weld. Join. 29 (2024) 47–51. https://doi.org/10.1177/13621718231216674.

[24] J. Günther, F. Brenne, M. Droste, M. Wendler, O. Volkova, H. Biermann, T. Niendorf, Design of novel materials for additive manufacturing - Isotropic microstructure and high defect tolerance, Sci. Rep. 8 (2018) 1298. https://doi.org/10.1038/s41598-018-19376-0.

[25] D. Schimbäck, L. Kaserer, P. Mair, M.S. Mohebbi, P. Staron, V. Maier-Kiener, I. Letofsky-Papst, T. Kremmer, F. Palm, I. Montes, H.W. Höppel, G. Leichtfried, S. Pogatscher, Advancements in metal additive manufacturing: In-situ heat treatment of aluminium alloys during the laser powder bed fusion process, Mater. Sci. Eng. A 905 (2024) 146102. https://doi.org/10.1016/j.msea.2024.146102.

[26]K. Otsuka, X. Ren, Physical metallurgy of Ti–Ni-based shape memory alloys, Prog. Mater. Sci. 50 (2005) 511–678. https://doi.org/10.1016/j.pmatsci.2004.10.001.

[27] A. Prasad, L. Yuan, P. Lee, M. Patel, D. Qiu, M. Easton, D. StJohn, Towards understanding grain nucleation under Additive Manufacturing solidification conditions, Acta Mater. 195 (2020) 392–403. https://doi.org/10.1016/j.actamat.2020.05.012.

[28] C.M. Cepeda-Jiménez, F. Potenza, E. Magalini, V. Luchin, A. Molinari, M.T. Pérez-Prado, Effect of energy density on the microstructure and texture evolution of Ti-6Al-4V manufactured by laser powder bed fusion, Mater. Charact. 163

(2020) 110238. https://doi.org/10.1016/j.matchar.2020.110238.

[29] R.C.D. Richardson, The wear of metals by relatively soft abrasives, Wear 11 (1968) 245–275. https://doi.org/10.1016/0043-1648(68)90175-0.

[30] W.C. Oliver, G.M. Pharr, An improved technique for determining hardness and elastic modulus using load and displacement sensing indentation experiments, J. Mater. Res. 7 (1992) 1564–1583. https://doi.org/10.1557/JMR.1992.1564.

[31] Z. Pang, Q. Zeng, Z. Ning, W. He, Z. Wang, J. Wang, L. Li, Ultralow friction and low wear behavior of in-situ formed NiTiO3 from 60NiTi alloy at 350 °C, Intermetallics 168 (2024) 108271. https://doi.org/10.1016/j.intermet.2024.108271.

[32] R. Neupane, Z. Farhat, Wear Resistance and Indentation Behavior of Equiatomic Superelastic TiNi and 60NiTi, Mater. Sci. Appl. 6 (2015) 694–706. https://doi.org/10.4236/msa.2015.67071.

[33] W. Ni, Y.-T. Cheng, M. Lukitsch, A.M. Weiner, L.C. Lev, D.S. Grummon, Novel layered tribological coatings using a superelastic NiTi interlayer, Wear 259 (2005) 842–848. https://doi.org/10.1016/j.wear.2005.01.015.

[34] A. Leyland, A. Matthews, On the significance of the H/E ratio in wear control: a nanocomposite coating approach to optimised tribological behaviour, Wear 246 (2000) 1–11. https://doi.org/10.1016/S0043-1648(00)00488-9.

[35] B.D. Beake, The influence of the H/E ratio on wear resistance of coating systems – Insights from small-scale testing, Surf. Coat. Technol. 442 (2022) 128272. https://doi.org/10.1016/j.surfcoat.2022.128272.

[36] L. Yang, M. Wen, X. Dai, G. Cheng, K. Zhang, Ultrafine Ceramic Grains Embedded in Metallic Glass Matrix: Achieving Superior Wear Resistance via Increase in Both Hardness and Toughness, ACS Appl. Mater. Interfaces 10 (2018) 16124–16132. https://doi.org/10.1021/acsami.8b02338.

[37] R. Aghababaei, D.H. Warner, J.-F. Molinari, On the debris-level origins of adhesive wear, Proc. Natl. Acad. Sci. 114 (2017) 7935–7940. https://doi.org/10.1073/pnas.1700904114.

[38] Q. Cheng, P. Zhang, X. Ma, S. Wan, Jialin chen, W. Hu, W. Wang, G. Yi, J. Zhao, Microstructure evolution and wear mechanism of in situ prepared Ti–TiN cermet layers at high temperature, Compos. Part B Eng. 242 (2022) 110028. https://doi.org/10.1016/j.compositesb.2022.110028.

[39] R.S. Dwyer-Joyce, R.S. Sayles, E. Ioannides, An investigation into the mechanisms of closed three-body abrasive wear, Wear 175 (1994) 133–142. https://doi.org/10.1016/0043-1648(94)90176-7.

[40] Q. Hu, D. Ji, M. Shen, H. Zhuang, H. Yao, H. Zhao, H. Guo, Y. Zhang, Three-Body Abrasive Wear Behavior of WC-10Cr3C2-12Ni Coating for Ball Mill Liner Application, Materials 15 (2022) 4569. https://doi.org/10.3390/ma15134569.

Chapter 7

Concluding remarks

The author developed a processing method for the *in situ* synthesis of NiTi coatings by electron beam irradiation on Ni-plated CP-Ti substrates, with the objective of enhancing CP-Ti's wear resistance by coating it with NiTi. Furthermore, in-depth investigations into electron beam parameters, post-processing and scanning strategies progressively refined the fabrication method for the NiTi coating. This ultimately yielded a NiTi coating with a uniform composition and properties comparable to those of Nitinol bulk material. The following summarizes the main findings of this study.

Chapter 1 described the background and the objectives of this study. Commercially pure titanium (CP-Ti) is a widely utilized material in aerospace and biomedical applications, valued for its biocompatibility, corrosion resistance, and excellent formability. However, its major drawback is inferior wear resistance, which restricts its use in critical components. In contrast, Nickel Titanium (NiTi/Nitinol), a shape memory alloy, exhibits superior wear and cavitation erosion resistance, particularly under heavy load, due to its unique superelasticity. A promising strategy is depositing a NiTi coating onto a CP-Ti substrate. Nevertheless, conventional techniques such as thermal spraying and physical vapor deposition are typically unable to produce high-quality NiTi layers, resulting in structural defects or inadequate film thickness. Therefore, this research proposes utilizing Additive Manufacturing (AM) technology for NiTi coating fabrication. AM offers superior control over microstructure and multi-material interface bonding, presenting a robust solution to overcome the limitations of traditional coating methods and develop high-performance NiTi/CP-Ti structures.

Chapter 2 described the melting behavior of 316L stainless steel under EB

irradiation by investigating the effect of parameters on the surface morphology, and melt-pool geometry of the melt tracks.

Surface and cross-sectional observation of the melt tracks revealed that the geometry of the electron beam melt tracks is sensitively governed by the line energy density. Increasing the energy input results in a monotonic increase in track width and depth, with the depth increasing more rapidly than the width at higher energy levels. The observation of chevron patterns and height variations along the melt tracks confirms the dominance of Marangoni flow in redistributing the molten material prior to rapid resolidification. The non-linear increase in the melt-track aspect ratio suggests a transition in the heat transfer mechanism, where vertical heat dissipation becomes enhanced relative to lateral diffusion as the local temperature gradient steepens. Despite material differences, these hydrodynamic insights are critical for understanding the NiTi formation processes explored in the later chapters.

Chapter 3 described the validation of the feasibility of *in situ* NiTi synthesis by investigating the morphology, composition, and elemental distribution of single EB melt tracks on Ni-plated CP-Ti substrates under varying EB power.

The experiments confirmed that Electron Beam Irradiation is a viable method for the *in situ* synthesis of NiTi coatings on CP-Ti substrates. By adjusting the EB power, the Ni concentration within the melt track can be precisely controlled, allowing for the formation of a composition close to the required NiTi stoichiometric ratio. Specifically, increasing the EB power leads to a gradual decrease in Ni concentration. Furthermore, observations of the cross-section demonstrated that the melt tracks exhibit generally uniform elemental distribution with no significant segregation. This uniformity confirms that the melt pool flow, driven by the Marangoni effect and thermal convection, effectively promotes the mixing of Ni and Ti atoms. These findings

successfully establish the necessary compositional and mixing conditions for the subsequent formation of the desired NiTi phase, paving the way for the development of a comprehensive NiTi coating fabrication method.

Chapter 4 described the preparation of practical NiTi coatings via multi-track EB scanning using continuous scanning (CS) and intermittent scanning (IS) modes. The control of surface roughness, composition, microstructure, and wear resistance through the adjustment of scanning parameters were also investigated.

The multi-track EB scanning successfully achieved the *in situ* synthesis of NiTi coatings on CP-Ti substrates, demonstrating that the scanning strategy is critical for controlling coating quality. IS-coatings exhibited significantly lower surface roughness compared to CS-coatings. More importantly, IS-coating resulted in Ni concentrations closer to the required NiTi stoichiometric ratio, leading to the formation of the desirable superelastic *B*2-NiTi phase and the strengthening $D0_{24}$-Ni_3Ti phase, whereas CS-coatings primarily formed the brittle *C*15-$NiTi_2$ phase. The optimal IS-coating showed substantial mechanical enhancement, with the hardness/Young's modulus ratio and indentation depth recovery ratio being significantly higher than those of CP-Ti. Consequently, the specific wear rate was reduced by a large margin, achieving wear resistance comparable to superelastic Nitinol. Despite this success, local compositional inhomogeneities persist, indicating a need for further optimization in subsequent chapters to fully match the performance of bulk superelastic Nitinol.

Chapter 5 described the application of a two-step heat treatment (annealing at 900 ℃ then ageing at 400 ℃) to Ni-rich and Ti-rich NiTi coatings fabricated in Chapter 3 to reduce inhomogeneities and enhance wear resistance.

The applied two-step heat treatment was highly effective in significantly improving the compositional and microstructural homogeneity of both the Ni-rich and Ti-rich

coatings. In the Ni-rich coating, the annealing caused the strengthening $D0_{24}$-Ni_3Ti phase to coarsen and uniformly redistribute. Subsequent ageing induced the precipitation of the Ni_4Ti_3 phase, further enhancing hardness and mechanical strength. Crucially, the heat treatment resulted in a substantial narrowing of the performance gap between the two coatings. While the Ni-rich coating showed moderate improvements in the hardness/Young's modulus ratio and indentation depth recovery ratio, the Ti-rich coating exhibited much more significant gains. This homogenization effect led to notable decreases in the specific wear rates for both coatings. Following heat treatment, the wear resistance of both coatings successfully approached that of superelastic Nitinol.

Chapter 6 described the development and optimization of a novel point-wise EB scanning strategy. The effects of the parameters on the point-wise scanned coatings were evaluated by analyzing surface and cross-sectional morphology, microstructure, elemental composition and indentation properties.

The optimized point-wise EB scanning effectively eliminated the undesirable $NiTi_2$ phase and achieved Ni concentrations around 52 at.%, comparable to multi-track scanned coatings. Significantly, the condition with EB dwell time of 5 ms yielded the best homogenization. The developed machine learning model quantified the parameter effects, showing that average EB power during scanning and point spacing in scanning grid are the most significant factors influencing the final Ni concentration, while EB dwell time had negligible impact. Compared to multi-track scanned coatings, point-wise scanned coatings exhibited finer microstructure. As the increase of EB dwell time, the microstructure in point-wise scanned coatings became more refined and more uniform. Coatings fabricated using optimized parameters exhibited hardness/Young's modulus ratio and indentation depth recovery ratio values comparable to or surpassing annealed multi-track scanned coatings. Crucially, point-wise scanning substantially

reduced the standard deviation of mechanical properties, confirming that the improved microstructural and composition uniformity leads to more uniform mechanical properties and consequently enhanced wear resistance.

Overall Conclusion The author successfully established a robust method for the *in situ* fabrication of high-performance NiTi coatings on CP-Ti substrates through the systematic optimization of electron beam processing parameters, scanning strategies, and post-heat treatments. The proposed approach offers a promising pathway for extending the application of CP-Ti into high-wear environments, including aerospace components, sports equipments, wear-resistant outer structures of humanoid and out-fielding robots, and wear-resistant wearable devices. Considering the presence of nickel, the developed NiTi coatings are particularly suited for external applications, such as wear-resistant wearable devices, timepiece components, and structural elements in exoskeleton robots, where both mechanical durability and functional reliability are critical.

Achievement

Publication

- **L. Wang**, M. Okugawa, Y. Liu, K. Cho, Y. Koizumi, H. Yasuda, T. Nakano, Microstructural evolution and wear resistance enhancement of electron-beam-fabricated nickel titanium coatings on titanium by heat treatment, *Materials Transactions*, in press.
- **L. Wang,** M. Okugawa, Y. Liu, K. Cho, H. Yasuda, T. Nakano, Y. Koizumi, NiTi coating formation on Ti for enhanced wear resistance utilizing electron-beam additive manufacturing technique, *Surfaces and Interfaces*, Vol. 72, 2025, 107024
- **L. Wang,** M. Okugawa, H. Konishi, Y. Liu, Y. Koizumi, T. Nakano, Fusion of Ni Plating on CP-Titanium by Electron Beam Single-Track Scanning: Toward A New Approach for Fabricating TiNi Self-Healing Shape Memory Coating, *Materials,* Vol. 16(15), 2023, 5449
- M. Okugawa, Y. Miyata, **L. Wang**, K. Nose, Y. Koizumi, T. Nakano, Melting and Solidification Behavior of 316L Steel Induced by Electron-Beam Irradiation for Additive Manufacturing, *Journal of Smart Processing*, Vol. 10(4), 2021, 208

Conference

- Electron Beam Fabrication of NiTi Coatings on Titanium Inspired by Additive Manufacturing Technique (Oral, English), **L. Wang**, M. Okugawa, Y. Liu, K. Cho, H. Yasuda, T. Nakano, Y. Koizumi, The 7th International Conference on Powder Metallurgy in Asia (APMA 2025), Session 4 (AM: Material & Process Development II), Qingdao, China, Oct. 21st, 2025
- TiNi coating on commercially pure Ti substrate by multi-track electron beam

scanning (Oral, English), **L. Wang**, M. Okugawa, Y. Koizumi, T. Nakano, Japan Institute of Metal and Materials Spring Conference, Tokyo, Japan, Mar. 9th, 2023

- Melting and Solidification of Ni Plating Layer on Ti Substrate by Electron beam Single-Track Scanning (Poster), **L. Wang**, M. Okugawa, H. Konishi, Y. Koizumi, T. Nakano, Alloys for Additive Manufacturing Symposium 2022 (AAMS22), München, Germany, Sep. 12th, 2022
- Synthesis of TiNi-layer by electron beam scanning on Ni plated CP-Ti-substrate (Oral, English), **L. Wang**, M. Okugawa, H. Konishi, Y. Koizumi, T. Nakano, Japan Institute of Metal and Materials Fall Conference, Fukuoka, Japan, Sep. 22nd, 2022
- Melting and Solidification of a Ti-6Al-4V/Cu Multi-Material Powder Bed Induced by Additive-Manufacturing-Compatible Electron Beam Irradiation (Oral, English), **L. Wang**, K. Hieda, M. Okugawa, H. Kawabata, Y. Koizumi, T. Nakano, Japan Institute of Metal and Materials Spring Conference, Online, Mar. 18th, 2021
- Electron Beam Single-Track Tests for Ti-6Al-4V/Copper Multi-Material Powder Bed Fusion Additive Manufacturing (Oral, English), **L. Wang**, K. Hieda, M. Okugawa, H. Kawabata, Y. Koizumi, T. Nakano, The 2nd Materials Physics and Engineering Colloquium, Kansai Branch of The Iron and Steel Institute of Japan & The Japan Institute of Metals and Materials, Online, Feb. 3rd, 2021

Acknowledgment

First and foremost, I would like to express my deepest respect and gratitude to my doctoral supervisor, Professor Yuichiro Koizumi. It was only through his patient guidance and unwavering support that I was able to complete my doctoral course. The knowledge and skills he has imparted to me are an invaluable asset that will benefit me for the rest of my life. I would also like to thank the members of my doctoral thesis examination committee: Professor Hiroshi Utsunomiya, Professor Hiroyuki Yasuda, and Professor Masakazu Tane. Their invaluable feedback and suggestions on my dissertation greatly improved the quality of my research.

I would like to express my gratitude to Assistant Professors Masayuki Okugawa and Yuheng Liu, Mr. Hirotoshi Kawabata and all the staffs and students at the Koizumi lab for their invaluable assistance and support throughout my research journey. I could never have completed this doctoral research on my own without this teamwork.

I would also like to thank the JSPS (Japan Society for the Promotion of Science) for funding my doctoral research through the “Research Fellowship for Young Scientists” project, and for recognizing my research abilities.

Last but not least, I would like to thank my parents and girlfriend for their financial and emotional support. Their encouragement kept me from giving up, enabling me to persevere and complete my doctoral research.